ISSN 0915-6348

NATIONAL INSTITUTE FOR FUSION SCIENCE

New Aspects of High Energy Density Plasma, Mar. 7-8, 2005, NIFS

Edited by E. Hotta

(Received - Sep. 20, 2005)

NIFS-PROC-61 Oct 2005

RESEARCH REPORT
NIFS-PROC Series

TOKI, JAPAN

New Aspects of High Energy Density Plasma

Edited by Eiki Hotta

March 7-8, 2005
National Institute for Fusion Science
Toki, Gifu, Japan

Abstract

The papers presented at the symposium on “New aspects of high energy density plasma” held at National Institute for Fusion Science are collected in this proceedings. The papers reflect the present status and recent progress in the experiments and theoretical works on high energy density plasma produced by pulsed power technology.

Keywords: high energy density plasma, z-pinch, pulsed power, soft x-ray, x-ray laser, high power particle beam, pulsed discharge, high power microwave, EUV, material processing

PREFACE

The collaborative research symposium on “New aspects of high energy density plasma” was held at National Institute for Fusion Science (NIFS), Toki, from 7 to 8 May, 2005. During the two days, 60 scientists and students attended from universities and institutes. Totally 31 papers were presented at the symposium on the physics and applications of Z-pinch plasmas, high power particle beams pulsed discharge and pulsed power technology. The proceedings contain most of the papers presented at the symposium. Great achievements were obtained by this symposium through fruitful discussions. I would like to express my sincere thanks to all of the authors, participants and stuff of National Institute for Fusion Science.

Eiki Hotta
Department of Energy Sciences
Interdisciplinary Graduate School of
Science and Engineering
Tokyo Institute of Technology

CONTENTS

List of Participants

S. Akiyoshi (Kumamoto University)
R. Ando (Kanazawa University)
S. Furuya ((Nagaoka University of Technology)
S. Hamada (Tokyo Institute of Technology)
T. Hayashi (Nihon University)
Y. Honma (Tokyo Institute of Technology)
K. Horioka (Tokyo Institute of Technology)
H. Horita (Kumamoto University)
E. Hotta (Tokyo Institute of Technology)
K. Igawa (Toyama University)
T. Ihara (Saga University)
K. Ikuta (Kawai Sekitan Kogyo Co., Ltd.)
J. Irisawa (Nagaoka University of Technology)
S. Ishii (Tokyo Institute of Technology)
H. Itoh (Toyama University)
W. Jiang (Nagaoka University of Technology)
Y. Kakuya (Tokyo Institute of Technology)
K. Kamada (Kanazawa University)
M. Kamada (Fukui University)
S. Katsuki (Kumamoto University)
T. Kikuchi (Utsunomiya University)
T. Kiyan (Kumamoto University)
N. Kobayashi (Tokyo Institute of Technology)
K. Kondo (Tokyo Institute of Technology)
Y. Kondo (Kumamoto University)
Y. Kubota (Nagaoka University of Technology)
T. Kurihara (Kanazawa University)
M. Masnavi (Tokyo Institute of Technology)
K. Masugata (Toyama University)
J. Mizuno (Gunma University)
S.R. Mohanty (Tokyo Institute of Technology)
K. Naito (Nagaoka University of Technology)
R. Nakajima (Kanazawa University)
T. Namihara (Kumamoto University)
Y. Nishimura (Kurita Seisakusho Co., Ltd.)
Y. Oka (University of Hyogo)
A.Okino (Tokyo Institute of Technology)
A. Osawa (Kanazawa University)

N. Oshima (Nagaoka University of Technology)

T. Sakugawa (Kumamoto University)

T. Sasaki (Tokyo Institute of Technology)

M. Sato (Gunma University)

S. Shirai (Tokyo Institute of Technology)

M. Shirota (Nihon University)

T. Someya (Utsunomiya University)

K. Takasugi (Nihon University)

D. Tanaka (Kanazawa University)

A. Tashiro (Tokyo Institute of Technology)

T. Tazima (Research Institute for Fusion Science)

N. Tomisawa (Kanazawa University)

T. Tomita (Toyama University)

T. Umeda (Nihon University)

M. Watanabe (Tokyo Institute of Technology)

Y. Yamaguchi (Nihon University)

K. Yatsui (Nagaoka University of Technology)

M. Yatsuzuka (University of Hyogo)

K. Yamamoto (Kanazawa University)

T. Yokoo (Nagaoka University of Technology)

H.R. Yousefi (Toyama University)

Study of Plasma Focus Device for EUV Source Development

Nobuaki Oshima, Yugo Kubota, Tomoyuki Yokoo, Weihua Jiang and Kiyoshi Yatsui
Extreme Energy-Density Research Institute, Nagaoka University of Technology
Nagaoka, Niigata 940-2188, Japan

Akira Tokuchi
Nichicon Corporation
2-3-1, Yagura, Kusatsu, Shiga, 525-0053, Japan

Abstract

Generation of extreme ultra-violet (EUV) emission was studied by using a plasma focus device driven by a pulsed high-current generator. The driving current pulse had a peak value of 31.7 kA and a full-width of 450 ns, with a current-rising rate of approximately 200 kA/μs. Visible light images of the source during discharge were obtained by a high-speed camera. The EUV spectra radiated from the plasma were measured by a spectrometer.

Keyword : pulsed power, magnetic pulse compression, EUV, plasma focus, IGBT

1. Introduction

Development of the advanced semiconductor technologies in recent years has greatly improved the computers and other information-processing instruments in both speed and capacity. The semiconductor lithography technology, which is the fine processing technology for projecting circuit patterns on to silicon wafer surface, is especially important in this development. The resolution of the lithography is determined by the following equation [(1)].

$$R = k_1 \frac{\lambda}{NA}$$

where k_1 is constant determined by the resist process conditions, λ is the wavelength of the light source, and NA is the numerical aperture of the optical system. It is seen that the resolution R is proportional to wavelength λ and the wavelength of the light source has to be reduced in order to achieve higher resolution of lithography.

The light source for the next generation lithography is demanded by the semiconductor industry. Among several potential candidates, extreme ultraviolet (EUV) light at 13.5 nm has been chosen due to the fact that there exists a multilayer coating [(2)] that has a relatively high reflectance near this wavelength. The required EUV source specifications includes an output power in the range of 100 W ~ 120 W, a bandwidth of 2 % at the wavelength of 13.5 nm, an energy stability of ± 0.3 %, and a lifetime of more than one year.

The EUV emission can be obtained from a high temperature and high density plasma. In order to generate such plasma, basically two approaches have been suggested. One is laser produced plasma (LPP)

and the other is discharge produced plasma (DPP). In LPP, a target is blasted out from a nozzle and irradiated by a high-power pulsed laser [3), 4)]. In DPP, pulsed high- current discharge is carried out in the source gas [5), 6)]. We are studying EUV generation by DPP for the reason that DPP has advantages of low cost and high efficiency compared to LPP. A pulsed high-current generator has been developed for EUV generation in our previous studies [7)]. In this paper, a plasma focus device is designed and tested on the high-current generator.

2. Experimental Setup

2.1 Pulsed power generator

Plasma focus systems were driven by large pulsed power generators with energy storage more than tens of kJ [8), 9)]. These generators are not applicable to EUV generation due to their disability in repetitive operation. We have developed a repetitive pulsed high-current generator as shown in Figs. 1 and 2 [7)]. The generator consists of two units. One is a resonant charging unit which is used to charge C_0 and the other is a magnetic pulse compression [10)] unit which compresses the pulsed output of C_0. A typical output current waveform on a shorted load is shown in Fig. 3. It has a peak value of 40.2 kA and a full-width of 397 ns. From this

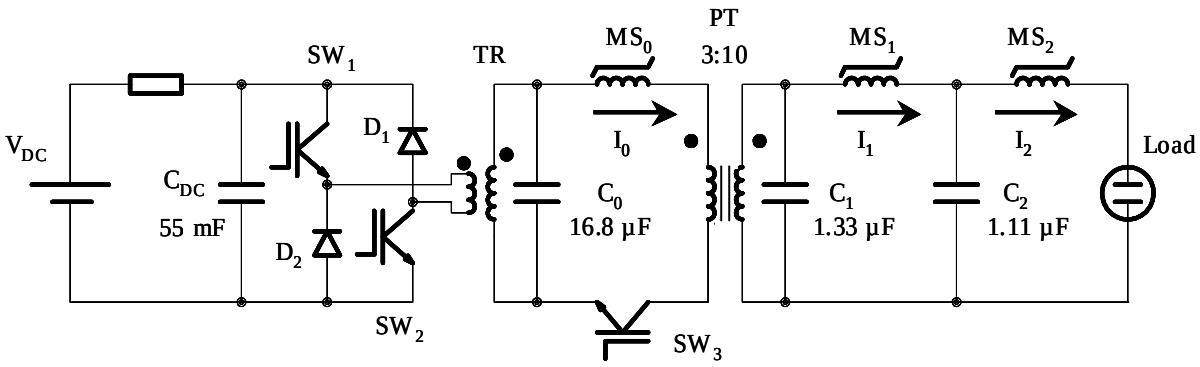

Fig.1 A schematic diagram of the generator.

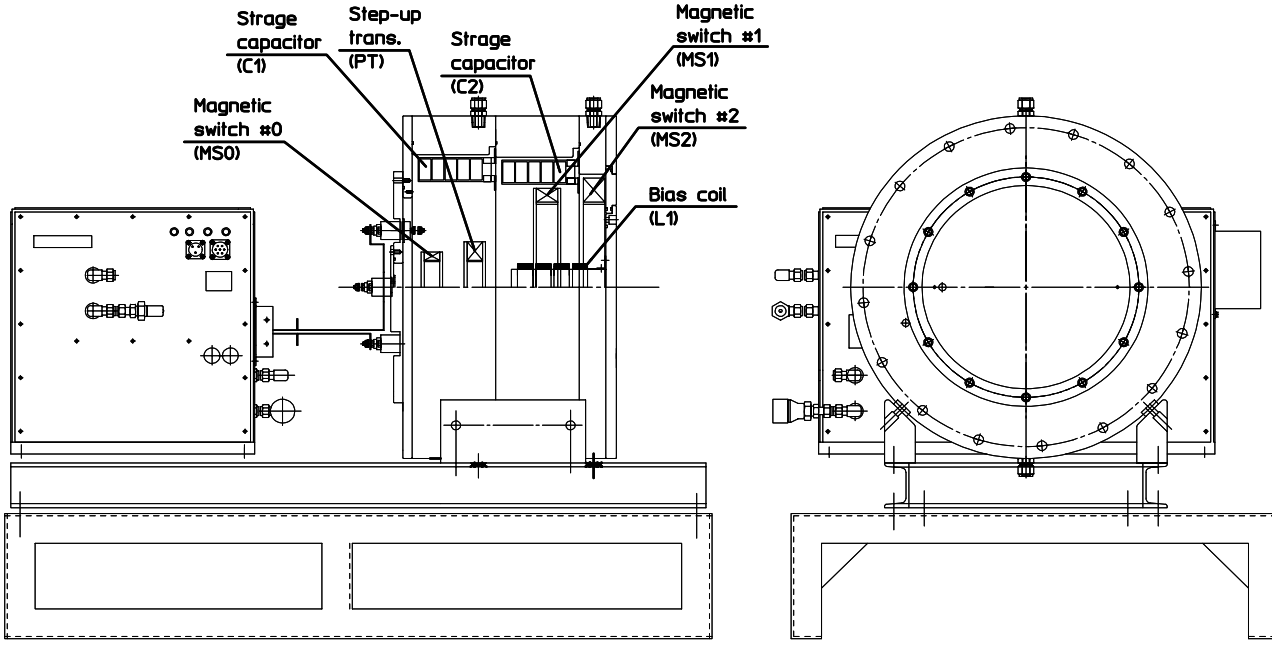

Fig.2 Cross-sectional view of designed generator.

waveform, the current rise rate is approximately 280 kA/μs and the inductance after C_2 is calculated to be 15.2 nH. The output voltage on an open load shown in Fig. 4 is measured in order to confirm the stored energy on C_2. From this waveform, the voltage on C_2 is 4 kV and the energy is calculated to be 8.9 J.

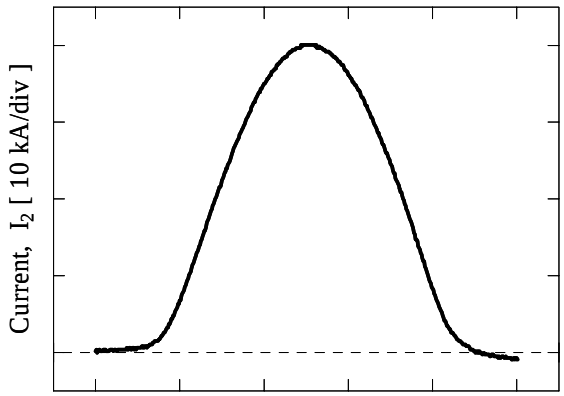

Fig.3 Typical output current on a shorted load.

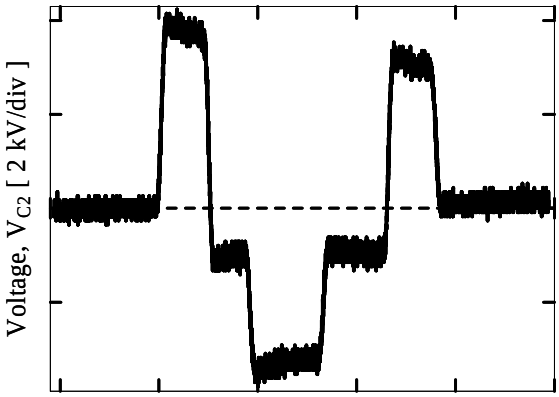

Fig.4 Output voltage on an open load.

2.2 Plasma focus system

The designed plasma focus diode is called Mather type [9] as shown in Fig. 5. The anode is made of stainless steel, with an outer diameter of 10mm. In order to feed Xe gas at the tip of the anode which is the focus point, the anode has an opening with diameter of 3 mm on the central axis. It is required that the melting point of the insulator should be high because it is exposed to a high temperature plasma. Therefore, an Al_2O_3 (melting point > 2000 °C) plate is used as the insulator. The cathode is made of copper, with an inner diameter is 13 mm.

The plasma focus diode is placed in the vacuum chamber. It is exhausted by a turbo-molecular-pump to 5×10^{-3} Pa. After that, Xe and He gases with flow rates of 50 sccm are injected into the chamber increasing the pressure to 10 Pa.

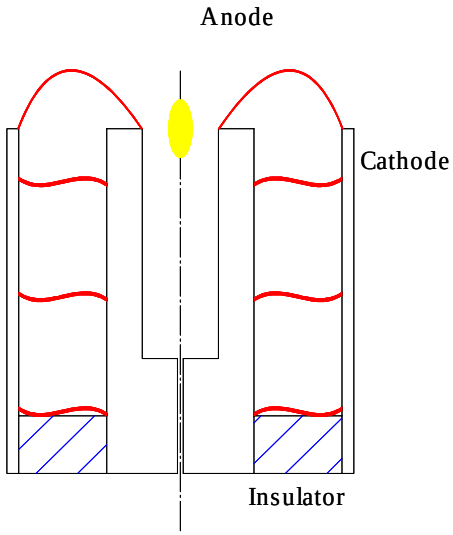

Fig.5 Schematic diagram of Mather type plasma focus.

3. Results and Discussions

3.1 Discharge current

Typical discharge current is shown in Fig. 6. The waveform has peak value of 31.7 kA and full-width of 450 ns. The current rise rate is approximately 200 kA/μs and the inductance after C_2, including the plasma focus diode, is calculated to be 18.5 nH. The plasma focus has caused the inductance increase of ~ 3.3 nH.

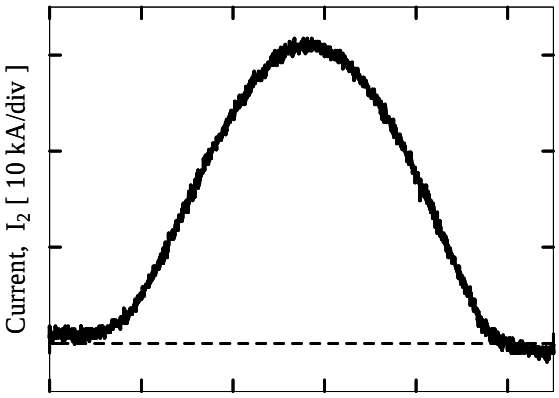

Fig.6 Typical output current on a shorted load.

3.2 Observation of source image

EUV is emitted from a high temperature and high density plasma. In order to generate such plasma, a plasma focus is developed in this study. Therefore, it is important that a high-temperature and high-density plasma is formed at the focus point. Shown in Figs. 7 and 8 are visible light images taken by a digital camera and a high-speed camera (UltraNAC FS501, of which the specification is shown in Table I).

Table I Technical specification of the high-speed camera.

Frame speed	$5 \times 10^3 \sim 20 \times 10^6$ frames/sec
Exposure time	10 ns ~ 200 μs
Inter-frame time	40 μs ~ 200 μs
Inner delay	30 ns ~ 40 ns
Photographic sensitivity	400 nm ~ 900 nm

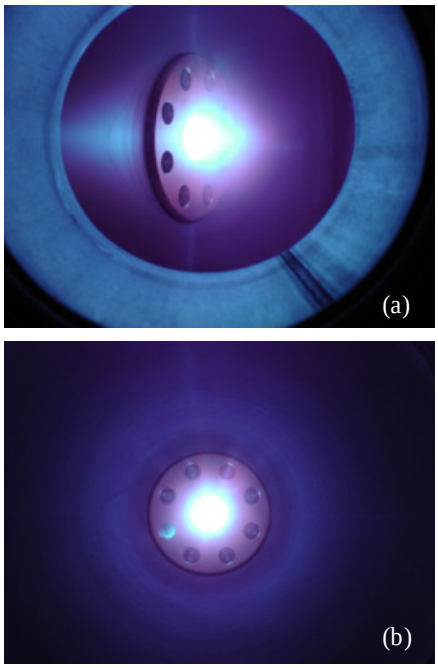

Fig. 7 Visible light images taken by digital camera.

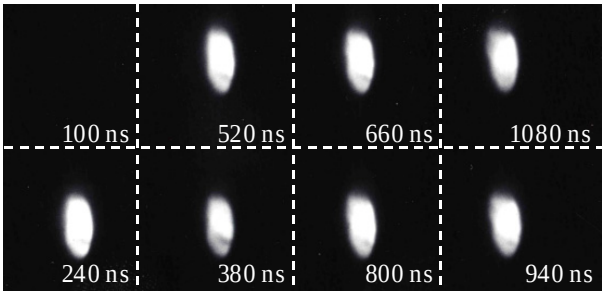

Fig. 8 Visible light images of the plasma focus diode during the discharge. The exposure time is 100 ns, the inter-frame time is 40 ns.

It is seen from Figs. 7 and 8 that very intense light emission is observed near the tip of the anode, indicating the existence of a discharge plasma. However, due to the high intensity of the light emission and the saturation of the exposure, it was not possible to quantitatively determine the spacial dimension of the light source. Therefore, it has not yet been directly confirmed that a dense focus did happen in our experiment.

3.3 Spectral characterization of the source

The EUV spectra were obtained using the grating incidence spectrometer, as shown in Fig. 9. It consists of a Zr filter, a slit, a diffraction grating with 1200 lines/mm, and a EUV-sensitive CCD. In this setup, the measurable range of wavelength is 5 nm to 50 nm. Figure 10 shows a spectrum emitted from the plasma focus. Since the spectrometer is not yet calibrated, the horizontal axis is the pixel number of the CCD. Although the absolute wavelength is not determined, the light emission in the wavelength range of 5-50 nm is confirmed.

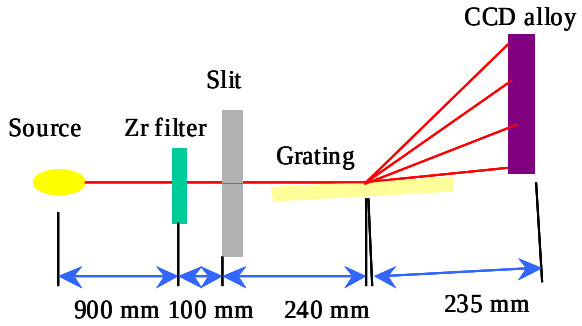

Fig. 9 Schematic of the transmission grating spectrometer.

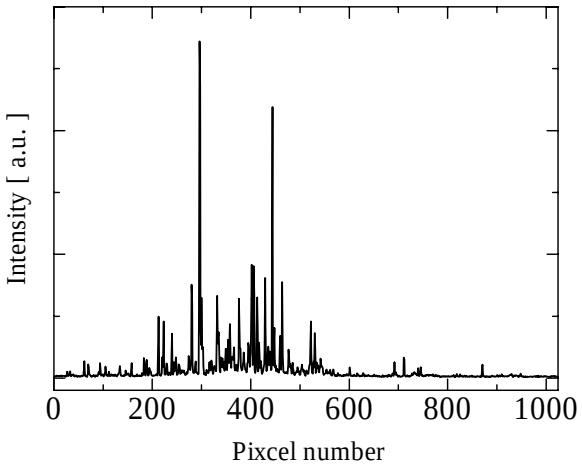

Fig. 10 Spectra emitted from the plasma focus.

4. Conclusions

A plasma focus diode has been driven by a pulsed high current generator. Visible light images of the light source and an EUV spectrum were obtained by a high-speed camera and a grating incidence spectrometer, respectively. The following conclusions have been obtained.

(1) The discharge current from C_2, which is charged to 4 kV, has a peak value of 31.7 kA and a full-width of 450 ns, with a current rise rate of 200 kA/μs.

(2) The focus point is not confirmed although intense light emission around the plasma focus diode is confirmed.

(3) Light emission in wavelength range from 5 ~ 50 nm is obtained.

References

(1) K. Murakami, T. Oshino, H. Kinoshita, T. Watanabe, M. Niibe, M. Ito, H. Oizumi and H. Yamanashi: Jpn. J. Appl. Phys. Vol.37, 6750-6755 (1998).

(2) M. Yamamoto: “Fabrication and use of soft X-ray multilayers”, OYO BUTURI [in Japanese] vol.62, No7, pp.676 – 682(1993).

(3) Richard H. Moyer, Harry Shields, Armondo Martos, Steven W. Fornaca, Randall J. St. Pierre, Michael B. Peach: Proc. of SPIE, vol.4343, 249 (2001).

(4) A. Endo: “High Average Power Laser Produced Plasma EUV Light Sources”, J. Plasma Fusion Res. [in Japanese] vol.79, No.3 (2003) 240-244.

(5) W.N. Partlo, I.V. Fomenkov, R.M. Ness, R.I. Oliver, S.T. Melnychuk, J.E. Rauch: “Progress Toward use of a Dense Plasma Focus as a Light Source for Production EUV Lithography”, Proc. of SPIE vol.4343 (2001).

(6) I.V. Fomenkov, N. Böwering, C. L. Retting, S.T. Melnychuk, I. R. Oliver, J. R. Hoffman, O. V. Khodykin, R. M. Ness and W. N. Partlo : “EUV discharge light source based on a dense plasma focus operated with positive and negative polarity”, J. Phys. D: Appl. Phys., 37, p.3266 (2004).

(7) N. Oshima, Y. Kubota, T. Yokoo, K. Shimada, A. Tokuchi, W. Jiang and K. Yatsui : IEEJ Trans. FM, Vol.125, No.1, p.25 (2005).

(8) N. V. Filipov, T. I. Filipova, and V. P. Vinogradov : Nuclear Fusion, **2**, p.577 (1962).

(9) J. W. Mather : Physics Fluids, **8**, p.366 (1965)

(10) W. S. Meliville : Proc. of IEE, 98, p.185 (1951)

Plasma Focus EUV Radiation Source

T. Hayashi and K. Takasugi

College of Science and Technology, Nihon University
1-8-14 Kanda-surugadai, Chiyoda-ku, Tokyo 101-8308, JAPAN

A small plasma focus device was constructed for the EUV radiation experiment. The storage energy of capacitor bank is 3.4 kJ, and the maximum discharge current is 125 kA. Although the device was not well optimized for strong pinch, EUV radiation was observed from bulk plasma. The plasma dynamics was affected by electrode material, and the use of Sn electrode was proved to be effective for producing Sn plasma.

Keywords: plasma focus, EUV, radiation source, Sn

I. Introduction

Self-contracting systems such as z-pinches and plasma focus are efficient for generating high density and high temperature plasma.[1] Among the systems the plasma focus has advantages as EUV radiation source to the conventional z-pinches. The plasma focus has a single radiation point, which is produced by 3-dimensional local concentration of stored energy. The location of the point (hot spot) is reproducible and the size is small. During the contraction process, the ambient gas is collected by snowplow, and the self-absorption of EUV emission by the gas is minimized. The focus plasma has a directed momentum due to the anti-symmetric configuration of discharge electrodes, and the exhaust of plasma after maximum pinch can be removed easily.

Recently EUV light source at the wavelength of 13.5 nm is strongly demanded for the next generation semiconductor lithography. The development of the light source using Xe or Sn has been undergoing. In a gas-puff z-pinch experiment EUV radiation from electrode material has been observed,[2] and this implies possibility for new source of radiation. We propose a method of producing Sn plasma in a small plasma focus device. Some new results on EUV radiation and metal plasma generation are presented.

II. Experimental Setup

Schematic drawing of the plasma focus device is shown in Fig. 1. The storage section consists of 7.5 μF fast capacitor bank which is charged up to 30 kV (3.4 kJ). The diameters of center conductor and chamber wall are 30 mm and 156 mm, respectively. The center conductor (anode) has a hole on its top in order to prevent concentration of discharge current. A Rogowski coil is used for the measurement of the discharge current. Ar or He gas is used in this experiment. The operating gas is supplied by a needle valve (gas nozzle).

A scintillation probe is used for detecting time dependent signal of soft x-ray emitted from the plasma. The probe is filtered by a 10 μm Be window,

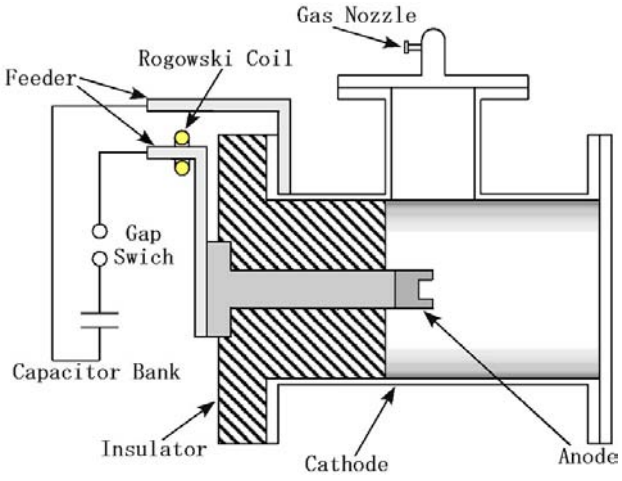

Fig. 1 Schematic drawing of the plasma focus device.

Parameters		Value
Maximum Current	[kA]	125
Quarter Period	[μs]	2.83
Decay Time	[μs]	30.0
Inductance	[nH]	430
Resistance.	[nΩ]	25.6

Table 1. Circuit parameters of the discharge system.

and it is sensitive to x-ray whose energy is above 1 keV. The sensitive range of the probe contains both K-shell radiation of Ar ions and K_α radiation of impurity metals coming from Hot Spots. The EUV light emitted from the plasma is detected by an x-ray diode (XRD) with Al photocathode. The XRD covers wide range of energy from UV to soft x-ray (1 – 100 nm).

Table 1 shows circuit parameters of the discharge system measured by short-circuiting the electrodes. The peak current at the charged voltage of 30 kV is 125 kA. The quarter period of the oscillating current is 2.83 μs and the decay time of the envelope is 30 μs. From those measurements the circuit inductance is obtained as 430 nH, and the circuit resistance is 25.6 nΩ. The inductance is rather high for conventional plasma focus device, and it is not well optimized for strong pinch.

III. Experimental Results

First we made Ar discharge with Al electrode, as we have experiences on Ar z-pinch. If we have hot spots, we can detect soft x-ray from He-like Ar ion, and also we can have EUV emission from Ne-like (Ar X) or Na-like (Ar IX) ions.

Figure 2 (a) shows typical discharge current and EUV signal of Ar discharge, and Figure 2 (b) shows a dependence of EUV intensity with gas pressure. Current peak occurs at the time nearly equal 2.83 μs. The EUV signal comes from highly ionized Ar ions, and is the evidence of hot plasma formation. The signal is spread over few microseconds, and the intensity decreases slowly with the pressure. As the amount of gas is proportional to the gas pressure, the decreasing tendency indicates the decrease of electron temperature. Soft x-ray signal was not observed in the experiment.

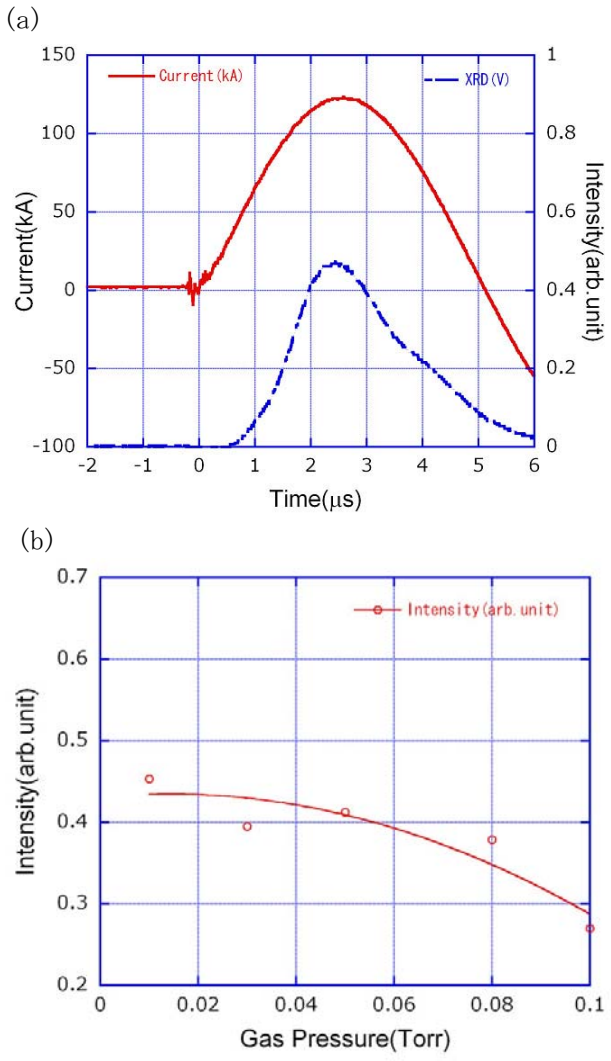

Fig. 2 (a) Discharge current and EUV signal of Ar z-pinch plasma with Al electrode. (b) Gas pressure dependence of EUV intensity.

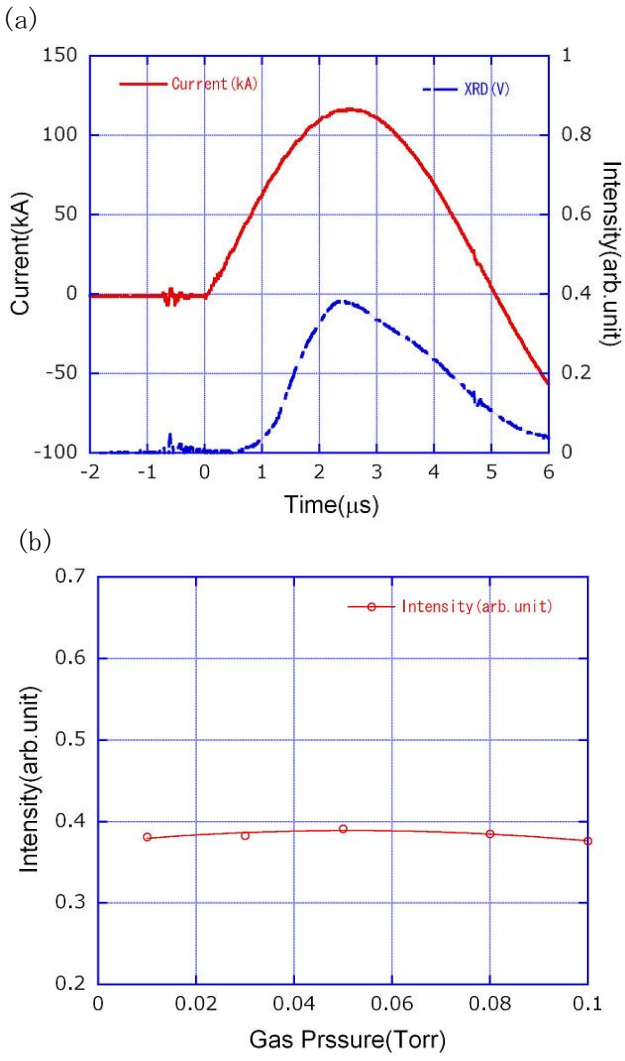

Fig. 3 (a) Discharge current and EUV signal of He z-pinch plasma with Al electrode. (b) Gas pressure dependence of EUV intensity.

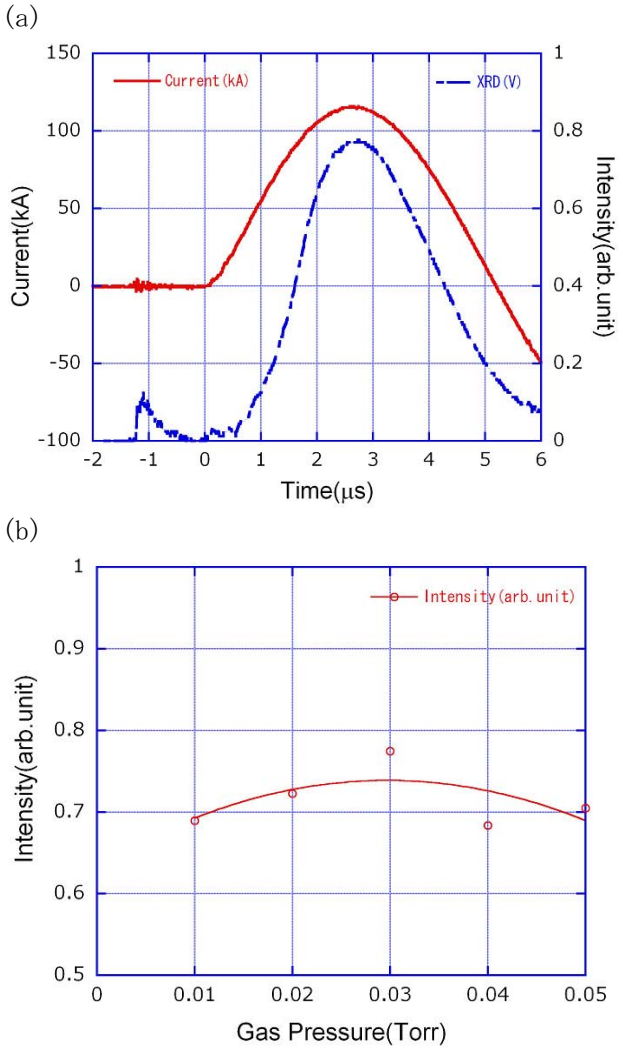

Fig. 4 (a) Discharge current and EUV signal of He z-pinch plasma with Sn electrode. (b) Gas pressure dependence of EUV intensity.

Next we made He discharge in order to utilize electrode materials for EUV radiation. Figure 3 (a) shows typical discharge current and EUV signal of He discharge with Al electrode. Both waveforms are similar to those of Ar discharge. As He plasma does not emit EUV line radiation, the EUV signal comes from Al ions. Figure 3 (b) shows a dependence of EUV intensity as a function of gas pressure. The EUV signal is almost constant with the pressure.

Figure 4 (a) shows discharge current and EUV signal of He discharge with Sn electrode. The current waveform is similar to the other discharges, but EUV intensity is much higher than them. The pressure dependence of EUV signal is almost constant.

In Fig. 5 pinch times of discharges with Al and Sn electrodes are compared. The pinch time of discharge with Sn electrode is clearly longer than that with Al electrode. The difference comes from the amount of contamination of electrode materials in the pinch medium, and the dynamics was changed.

IV. MHD Simulation

2-dimensional MHD simulation was carried out for better understanding of the development of plasma focus. The MHD code has been developed by Dr. V. Vikhrev in Kurchatov Institute.

Figure 6 shows evolution of plasma focus discharge with the experimental parameters. The 7.5 μF capacitor bank is charged up to 30 kV, and the chamber is filled with 5.0 Torr D_2 gas. The discharge is initiated on the surface of the insulator. The current sheet goes down to the right slowly. The velocity of the sheet is a little higher near the center conductor, and it becomes obvious at time 1.8 μs (Fig. 6 (a)). The balloon of current sheet develops near the center conductor, and it comes to the front surface of the conductor at time 2.2 μs (Fig. 6 (b)). And it reaches to the hole of the conductor at time 2.4 μs (Fig. 6 (c)). The radial motion is very rapid and finally the balloon contracts on the center axis at time 2.5 μs (Fig. 6 (d)). The simulation shows that the axial flow velocity is rather slow, but a ballooning occurs near the center conductor, and the radial motion of the balloon is rapid. The discharge current at the maximum pinch is 123 kA, which reproduces experimental results.

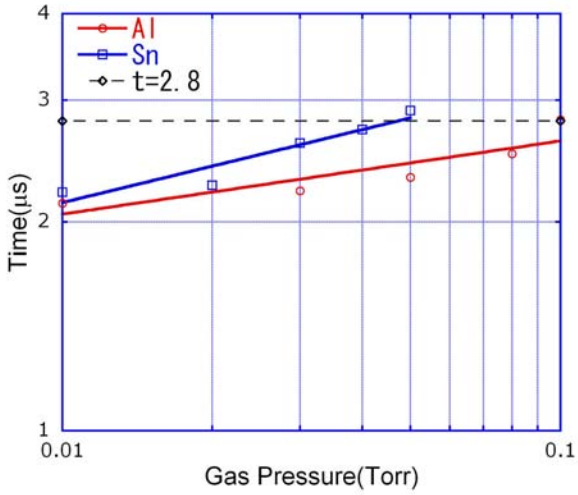

Fig. 5 Effect of electrode materials on the pinch time of z-pinch plasmas.

(a)

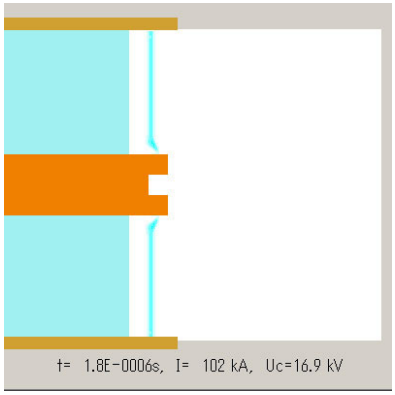

(b)

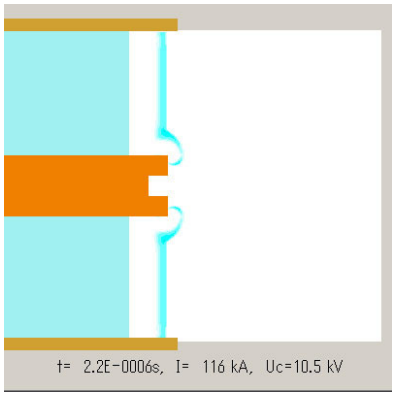

(c)

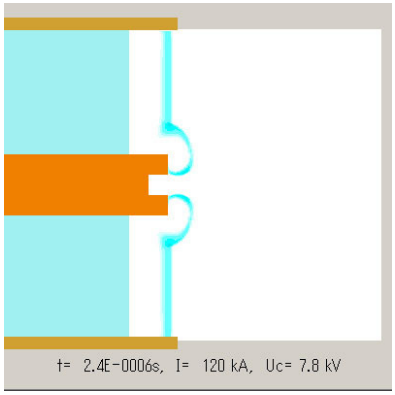

(d)

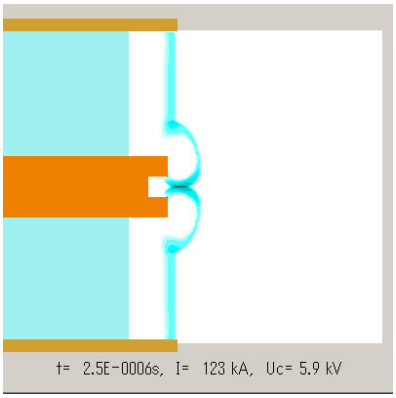

Fig. 6 MHD simulation of a plasma focus at (a) 1.8 μs, (b) 2.2 μs, (c) 2.4 μs and (d) 2.5 μs.

V. Summary and Discussion

A small plasma focus device was constructed for EUV radiation experiment. The maximum current and the quarter period are almost the same as the values expected from circuit parameters. This means that the change of plasma inductance due to dynamic pinch is small compared to the circuit inductance, and the efficiency of energy transfer is small.

In every discharge, the period of EUV radiation is comparable to the current pulse. This indicates that the plasma temperature is low, and the radiation comes from bulk plasma. Pinch is not so strong to produce hot plasma.

As shown in Fig. 5, the pinch time is different for each electrode materials. This means that the evaporated electrode materials are contaminated to the pinch medium. As the melting point of Sn is lower than Al, Sn is much easier to be evaporated for taking in the pinch plasma, and the use of Sn electrode was proved to be effective for producing Sn plasma.

MHD simulation of the focus development shows that only a small amount of the plasma near the center electrode moves rapidly to produce pinch plasma. The rest large amount of plasma does not contribute to the pinch plasma formation. This geometry of plasma focus needs to be improved for more efficient energy transfer.

References

[1] K. Takasugi, H. Suzuki, K. Morioka and T. Miyamoto: Jpn. J. Appl. Phys. **35**, 4051 (1996).

[2] F. Kobayashi and K. Takasugi: NIFS-PROC-54, 70 (2003).

A SKETCH ON PROBLEMS OF DISCHARGE PUMPED PLASMA EUV SOURCES

Majid MASNAVI, Mitsuo NAKAJIMA, Tohru KAWAMURA,
Eiki HOTTA, and Kazuhiko HORIOKA

Department of Energy Sciences, Interdisciplinary Graduate School of Science and Engineering, Tokyo Institute of Technology, 4259 Nagatsuta, Midori-ku, Yokohama 226 - 8502, Japan

This paper presents a brief review on the some rigid requirements of source for the extreme-ultraviolet lithography (EUVL) system. In addition, the conversion efficiency of xenon plasma in the pulsed power generator-based Z discharge plasmas is studied using an analytical snow-plow model coupled to the circuit equations and a zero-dimensional collisional radiative model. As an example and in connection with fast plasma heating in capillary-discharged plasma EUV source, the transient ionization effect on the plasma conversion efficiency of $4d^8 - 4d^7 5p$ transitions ($\lambda \sim 13.5$ nm, i.e., in-band transitions) of xenon has been theoretically investigated using one-dimensional, two-temperatures magnetohydrodynamic (MHD) model which includes a time-dependent xenon ionization model. Results indicate that for high volume manufacturing (HVM) EUVL system, the required in-band power is beyond of xenon gas at the current experimental conditions using a single discharge system.

Keywords: extreme-ultraviolet lithography, EUV source, conversion efficiency, Z discharge, capillary discharge, MHD model, ionization dynamics

BACKGROUND

Pulsed power generator-based Z discharge plasmas have proved to be an effective source of soft x-ray radiation. In particular, in the past few years capillary-discharged plasmas became reliable table top light sources in the soft x-ray and extreme ultraviolet (EUV) spectrum range. They opened up the way for a laboratory operation of a variety of applications such as the generation of intense coherent soft x-ray radiation, [1] laser wakefield accelerators, [2] or extreme ultraviolet lithography (EUVL). [3] The latter is of great commercial interest because it is the extension of today's optical lithography towards shorter wavelength. Currently, the work focused on three ionic systems (xenon, [4] tin, [5] lithium [6]) using laser-produced plasmas and discharge-produced pinch plasmas, [7–18] in which are believed to produce sufficient flux in the EUV region. Unfortunately, each elements have some critical problems, in point of view of industrial applications in the EUVL system such as low conversion efficiency, fast evaporation to the tube wall, or high debris production. Some of the industrial requirements and critical issues related to the source are listed in Table. 1. In fact, some of the requirements listed in Table. 1 depend on the companies, for instance, the Etendue for Canon's requirement is ~ 1 mm^{2}sr. In addition, these are few requirements which are interested in the present article. Figure 1 shows a cartoon of source position and requirement power at the source and intermediate focus. The requirement power at the source is calculated based on the average value of the Etendue range. The Etendue is the measure of light gathering power which depends on the source size and numerical aperture (*NA*), for instance, in the case of the spherical source, it is expressed as Etendue = $(\pi/2 \times$ Plasma Diameter $\times NA)^2$. Therefore, the Etendue limits the source size, as shown approximately in Fig. 1.

Table 1 Some industrial requirements and critical issues

EUV power (2% bandwidth)	80-120 W
Repetition frequency	>6000 Hz
Integrated energy stability	+/-0.3%
Etendue of source output	(1-3.3) mm^{2}sr
Source power and lifetime including condenser optics	
Debris mitigation	
Heat removal from discharge tube	< 30 kW

We are interested to carry out the present work by our interest in the possible use of pulsed-power plasma

author's e-mail: majid@es.titech.ac.jp

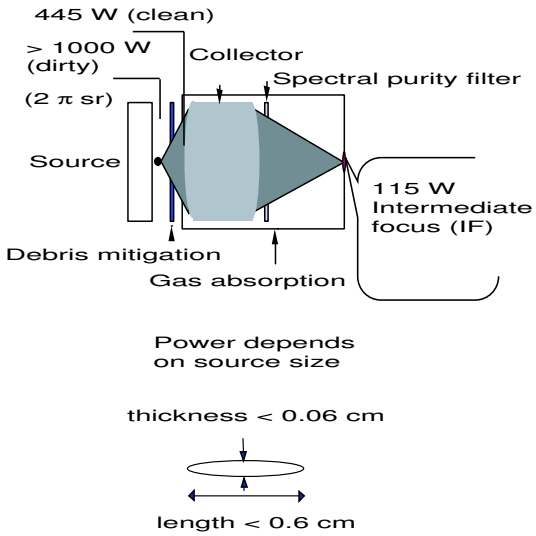

Fig. 1 A cartoon of source position and power requirements at the source and intermediate focus. The plasma source size is approximately based on the Etendue range.

Table 2 Capillary discharge source

Some of the advantages
Direct and efficient electric discharge EUV production
Simple and compact
Scalable to multi-kHz operation
Stabilized against neck-type instabilities
Etendue well-matched to α and β-tools
Some of the challenges
Capillary erosion and required replacement
Debris mitigation
EUV power (xenon), big issue (tin): debris, supply and remove tin

sources of the capillary-discharged Z pinch type in light source experiments. In fact, with regards to the process of EUV radiation, all axially symmetrical discharges can be subdivided in two unequal groups of stabilized and non-stabilized against neck (sausage) type instabilities: 1) capillary-discharged (wall stabilized discharges), and 2) Z discharges (Z pinches, plasma focus, gas embedded Z pinches, etc.), respectively. Table 2 shows some of the characteristics of capillary-discharged EUV source. A comparison of different discharge-produced pinch plasmas could be found in literature, for instance see refs. 19 and 20.

DISCUSSION AND CONCLUSIONS

Although xenon as a working gas has advantages compared with other ionic systems, for instance, owing to the low debris production due to it's inert characteristics at the room temperature, unfortunately, it's conversion efficiency (CE) to EUV in-band radiation (namely, within 2% bandwidth centered at wavelength of $\sim$ 13.42 nm [21]) is small (perhaps the best result is $\sim$ 0.16% sr^{-1} in Z discharge [5]) since a huge driving power is required to achieve practical exposure intensities at an intermediate focus ($\sim$ 115 W). On the other hand, the failure in the heat removal from a discharge bore tube [22] at the high power level ($>$ 30 kW) dictates us further investigations toward optimization of the CE of discharge-produced plasmas. The CE should depends on the conversion of stored electrical energy of pulsed-power generator to the internal plasma energy (i.e., the coupling efficiency of generator (CEG)), and then to in-band radiation of xenon (namely, the plasma conversion efficiency (PCE) or the intrinsic CE of plasma). [10, 23, 24] Theoretical results revealed that in the discharge-pumped xenon plasma, the transitions responsible for in-band radiation are mostly in ten-times-ionized xenon (Xe XI). [9]

(A) The snow-plow model coupled to the circuit (RLC) equations: The CEG

It is clear that the CEG depends on the design of pulsed-power generator (such as the inductance and the resistance) and initial parameters of the plasma load. For instance, the calculation results using RLC circuit equations coupled to zero-dimensional dynamic model (a simplified snowplow model [25]) for Z discharge [26, 27] revealed that the optimum regime of energy coupling to the plasma strongly depends matching between circuit and plasma, namely, on the mass, tube radius, and inductance. Generally, the Z pinch radial kinetic energy (namely, $K \sim \psi IV\tau_{\rm imp}$ where ψ is the efficiency of the converting delivered electrical energy into implosion kinetic energy which depends on the design of generator, I and V are the current and voltage at the insulator, and $\tau_{\rm imp}$ is the implosion time or the pinching time, i.e., the time of maximum compression) of implosion per unit of Z pinch mass (M) should be optimized to produce maximum radiation. This relation shows an optimization can be done for a lower V and longer $\tau_{\rm imp}$ (or longer rise time of plasma current ($\tau_{\rm r}$), if we assume that $\tau_{\rm imp} \sim \tau_{\rm r}$), if cylindrical gas symmetry in implosion phase could be controlled. However, the K/M can also be roughly scales as

$$K/M \propto v_{\rm imp}^2 \propto (R_c/\tau_{\rm imp})^2 \propto (R_c/\tau_{\rm r})^2 \qquad (1)$$

where $v_{\rm imp}$ is the implosion velocity and R_c is the cap-

illary radius (initial radius of plasma). This scale reveals that for a given pulsed-power device (constant current), for a longer τ_r (τ_{imp}), the capillary radius must be increases to get the same optimum of K/M. Furthermore, an optimum value of K/M is required to avoid overheating a small amount of xenon gas (high temperature of the imploding plasma is generally not desirable, since this results in a shorter ionization time of Xe XI charge state, rapid plasma expansion, low density, and less effective stagnation) or insufficiently heating (i.e., long ionization times of the lower charge states than Xe XI at the pinching phase) a large amount of gas.

Figure 2(a) shows a typical results of the normalized plasma radius (namely, $R = r/R_c$) and current ($C = I/I_0$) calculated using the snow-plow model coupled to the RLC circuit equations for two different conditions, namely, R_A (R_B) and C_A (R_B) against the normalized time (i.e., $\tau = t/t_c$), respectively. Here, $t_c = \sqrt{L_o C_0}$ where L_0 is the fixed stray inductance of the circuit, C_0 is the capacitance of the capacitor bank, and I_0 is the maximum of the current. To calculate the coupling efficiency of the generator to the internal plasma energy (i.e., the CEG), we follow the methods described in refs. 26 and 27. The equations are written using two scales of $\beta = (\mu l/2\pi)/L_0$ where l is the plasma length, and μ is the permeability of free space. Other scale is $\alpha = t_c/t_p$ where $t_p = \sqrt{4\pi^2\rho_0 R_c^4/\mu I_0^2}$ is the pinching time and ρ_0 is the initial density. The coupling efficiency is defined based on the plasma enthalpy at the minimum plasm radius (i.e., the maximum compression) to the energy initially stored in C_0. [26, 27] α is a scaling parameter which shows the characteristic capacitor discharge time to the characteristic pinch time. β shows the characteristic pinch inductance to the external inductance. Figure 2(b) shows that for fixed β value, the α parameter which includes mass, current, and capillary radius must be selected to make maximize the CEG. In other words, results based on kinetic energy and energy balance theory revealed that the optimum pinching condition for sinusoidal-like current is at some point after maximum where current is $\sim$ (20-30)% less. [26–28]

(B) Zero-dimensional collisional radiative model: The PCE

The problem of calculating kinetic factors that affect the PCE falls into two parts: the ionization dynamics, which determines the fractional abundance of Xe XI charge state and the excited state kinetics, which

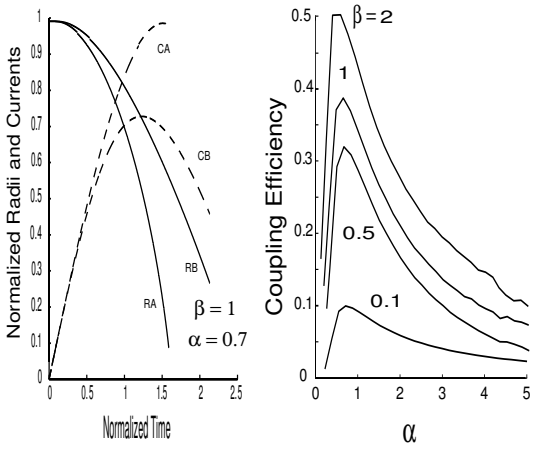

Fig. 2 (a) The normalized plasma radii and currents as function of normalized time. (b) The coupling efficiency of energy against α and for different β = 0.1, 0.5, 1, and 2 values.

determines the excited states populations of the Xe XI stage and the in-band radiation.

In plasmas created by fast capillary discharge, ionization dynamics are extremely important due to the very fast timescales of changing hydrodynamical plasma parameters at the pinching time (i.e., at the maximum compression of plasma), and ionization state distributions are considered to be far from their steady-state values. The transient effects become of increasing importance if the time scales for atomic processes are large in comparison to the time scales for the change of the plasma parameters. For example, if the plasma suffers a fast heating process such as shock wave heating (i.e., $S_i \leq (N_e t_h)^{-1}$, where N_e is the electron density, S_i is the total ionization rate coefficient, and t_h is the heating time), or in the case of fast cooling (i.e., $T_r \leq (N_e t_c)^{-1}$, where T_r is the total recombination rate coefficient, and t_c is the cooling time) the ionization state distributions, and consequently, the average ionic charge state, lag behind the electron temperature due to the relaxation effect of different charge states, in particular in the low electron density regime relevant to the fast capillary-discharged EUV source.

The dominant ionic charge state in relation to electron temperature is shown in Fig. 3, for different values of the $N_e t$ parameter where t is the time. The solid line ($N_e t = 3 \times 10^{11}$ cm^{-3} s) almost corresponds to the result of the collisional radiative equilibrium (CRE) model. We note that the solid line presented in Fig. 3 is consistent with the previous calculation

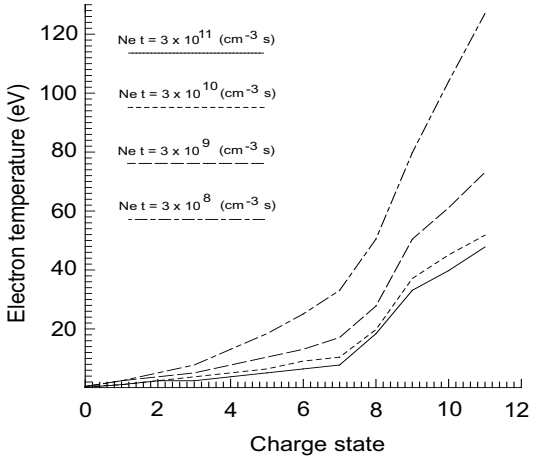

Fig. 3 Dominant ionic charge state for different values of $N_e t$ $(\mathrm{cm}^{-3}\ \mathrm{s})$ against the electron temperature; $N_e t = 3\times10^{11}$ (solid), $N_e t = 3\times10^{10}$ (dotted-line), $N_e t = 3\times10^{9}$ (dashed-line), and $N_e t = 3\times10^{8}$ (dot-dashed line).

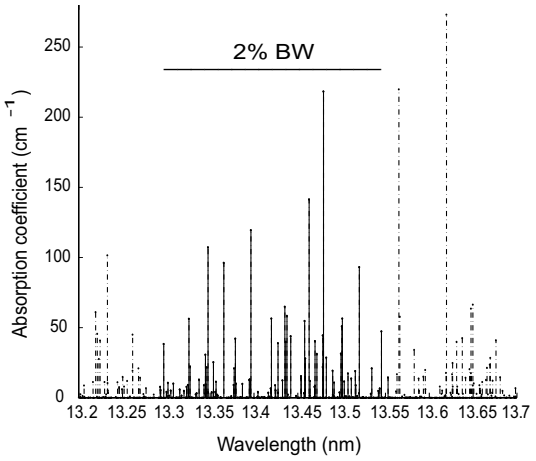

Fig. 4 Calculated spectrum of absorption coefficient at the line center of the Xe XI state versus wavelength for the region of 13.2 to 13.7 nm at $N_e \sim 10^{19}$ cm^{-3} and $T_e \sim 40$ eV.

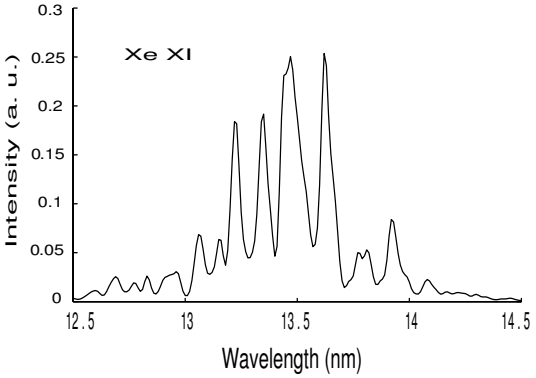

Fig. 5 The spectrum of Xe XI charge state with assumption of 0.02 nm broadening of the transition lines.

using the CRE model, [29, 30] which gives the temperature range of the maximum Xe XI ionization state $[\Delta T_e(\mathrm{Xe\ XI})]$ of $35 < \Delta T_e(\mathrm{Xe\ XI}) < 40$ eV. Here T_e is the electron temperature. It should keep in mind that, the steady-state ionization model (i.e., solid line in Fig. 3), does not depend on the ionization dynamics, namely, ionizing plasma history.

Figure 4 shows our calculated spectrum for the absorption coefficient at the line center of Xe XI against the important wavelength region from 13.2 to 13.7 nm at $N_e \sim 10^{19}$ cm^{-3} and $T_e \sim 40$ eV using the the necessary atomic data taken from the HULLAC atomic code package.

In Fig. 5, we show as an example a typical spectrum of Xe XI with assumption of 0.02 nm broadening of the transition lines. Using collisional radiative model and with comparison of theoretical and experimental spectrum, it is possible to understand more about the plasma parameters evolution in Z discharge type sources.

Figure 6 shows a contour plot of the PCE (in the unit of % sr^{-1} within a 2% bandwidth (BW), where 2% BW is calculated for the ±0.135 nm bandwidth centered at the wavelength of 13.42 nm [21]) as calculated using the CRE ionization model. To calculate the PCE at 2% BW, we have evaluated the level populations and optical depths based on the HULLAC data. To take into account the radiation transport, a homogenous plasma cylinder for the pinch plasma with dimensions of (a) 0.03 cm and (b) 0.04 cm diameter and 0.1 cm length has been assumed. Maximum of the PCE is achieved for $10^{18} < N_e < 10^{19}$ cm^{-3}. In pinch-type discharge-produced plasmas, the emission duration depends on the characteristic timescales of the changing plasma parameters, and also the ionization and recombination times of the given ionization state at pinching time. Generally, in the rapidly ionizing regime, the emission duration is approximately of the order of ionization time. However to estimate the PCE in Fig. 6, a typical value of the emission duration is estimated on the basis of inertial confinement time to be $\Delta t \sim 7.2\times10^{-7}\left(d/\mathrm{cm}\right)\sqrt{2Z_a}\left(T_i/\mathrm{eV}\right)^{-1/2}$, where d is the plasma diameter, T_i is the ion temperature, and Z_a is the atomic number. Note that it is assumed $T_e = T_i$. A comparison of Fig. 6(a) and 6(b) indicates that the larger plasma radius (in fact inside of the Etendue

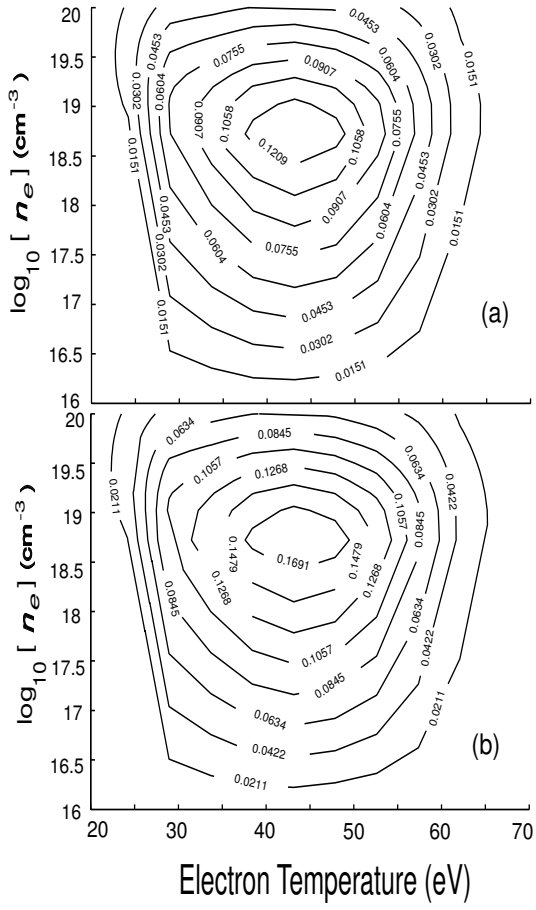

Fig. 6 Contour plot of the PCE (in unit of % sr^{-1} within 2% BW) in electron density-temperature space (a) the plasma radius is 0.015 cm and (b) the plasma radius is 0.02 cm. The calculation is based on the steady-state CRM (i.e., solid line in Fig. 3.).

limits) increases the PCE owing to the longer lifetime of the plasma and saturation of resonance lines due to the higher opacity.

(C) Ionization dynamics and one-dimensional MHD model

In fast capillary discharges, the plasma temperature at pinching time increases rapidly due to the thermalization through a shock implosion that is considered as a dominant heating process. [31, 32] The plasma thermalization time (τ_{th}) can be estimated by the time taken for a reflected shock wave to pass through the collapsing plasma shell that approximately is given by; $\tau_{th} \sim d/(v+w)$. Here, d is the plasma thickness, v is the shock velocity, and w is the velocity of reflected shock wave. For example, for shock velocity of $v \sim w \sim 5\times10^6$ cm/s (in fact, the reflected wave is always slower than primary one), and plasma thickness of $d \sim 0.02$ cm, the thermalization time is estimated to be order of 2 ns. Since the relaxation time of different ground states of xenon are greater than the timescale for change of the temperature and density at the pinching time, we coupled the MHD model to the quasi-steady-state based CR model. Hence, in order to evaluate the nonequilibrium effects on the PCE of Xe XI ion, the time evolutions of all the ground states are traced during the calculation of hydrodynamical plasma parameters using the one-dimensional, two-temperatures MHD model with cylindrical geometry in which is solved in the Lagrangian reference frame. [33]

A plot of the radius-time trajectories of the Lagrangian cells and the driving current is shown in Fig. 7(a). When the plasma is compressed by the azimuthal magnetic field generated by the induced current in the skin layer as shown in Fig. 7(a), it is also heated and finally producing a high density and temperature at the time of maximum compression called pinch. The time evolutions of the ion density (N_i), T_e, T_i, and average ionic charge state ($\bar{Z}$) against radius for times before pinching time (implosion phase) and after pinch (expansion phase) are shown, respectively, in Figs. 7(b), 7(c), 7(d), and 7(e). In addition, Fig. 7(f) shows the time evolutions of N_e and T_e on the capillary axis. An inspection of Fig. 7 reveals that the plasma temperature at pinching time increases rapidly, in other words, the maximal radiation in capillary-discharged EUV source corresponds to the moment of pinch formation. At the pinch, the plasma thermal energy exceeds the magnetic energy containing the plasma temporarily. As a result, the plasma expands as shown in Fig. 7(g) and in doing so reduces the temperature and becomes less dense. The population density of Xe XI charge state (Nz), $\bar{Z}$, and total integrated PCE (~ 0.14 % sr^{-1}) on the lifetimes of Xe XI stage is shown in Fig. 7(h). It should be noted that, to estimate opacity effect, we calculated optical depths and escape probabilities of each Lagrangian cells based on their local parameters, for instance, photon on the axis experiences absorption of each of the Lagrangian cells before escaping from the plasma. Comparing Fig. 7(a) and 7(g) shows that the expansion time is $\sim$ 14 ns which has agreement with the time-scale characteristic of the Bennett equilibrium, i.e., the mean Alfvén transit time ($\bar{\tau}_A = a/\bar{V}_A$ where a is the plasma radius, $\bar{V}_A$ (m/s) = $(1/4)\sqrt{\mu_0/\pi M_i N I}$ is the mean Alfvén ve-

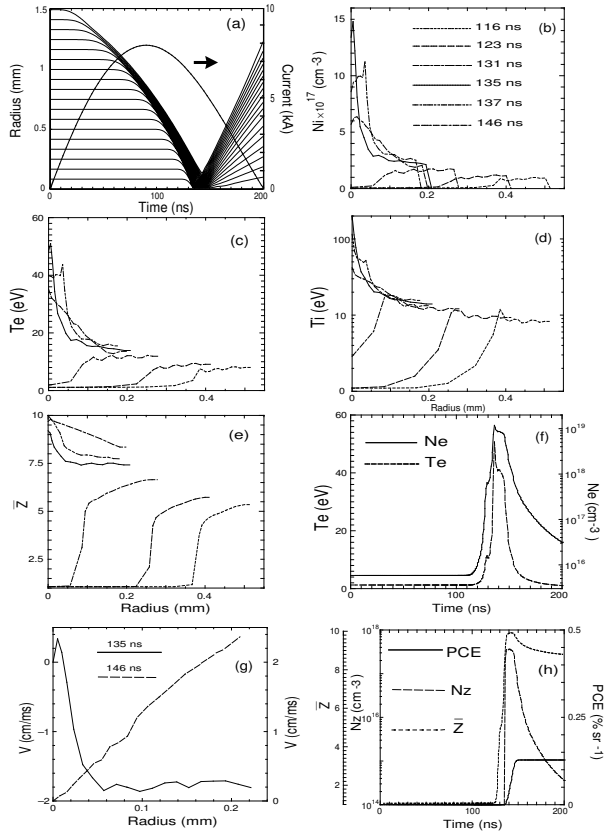

Fig. 7 (a) A plot of the radius-time trajectories of the Lagrangian cells and the driving current. (b) The time evolution of N_i against plasma radius. (c), (d), and (e) The corresponding time evolution of the T_e and T_i, and $\bar{Z}$ respectively. (f) Time evolutions of N_e and T_e on the axis. (g) Velocity of plasma versus radius at different times of 135 ns, and 148 ns. (h) Time evolutions of $\bar{Z}$, and N_Z on the axis, and the total integrated PCE. Note that the total PCE integrated on the lifetime of the Xe XI charge state.

locity, I is the plasma current, M_i is the ion mass, and $N = \int 2\pi n(r) r dr$ is the line density of ion).

If the external parameters (e.g., current pulse, capillary radius, gas pressure) are controlled in a suitable way, it is possible to enhance the conversion efficiency of discharge-pumped plasma EUV sources. For instance, the calculation results for different initial parameters reveal that the plasma efficiency of xenon to in-band radiation up to $\sim$ 1.5 % in 2π is possible with optimum selection of plasma parameters. On the other hand, the coupling efficiency of input energy from generator (it should keep in mind that, based on the simple results of the RLC circuit equation coupled to snow-plow model) to the plasma up to (40-50)% is realistic. Therefore, the total CE $\sim$ 0.75 in 2π. With assumption of 30 (70) kW input power, the output is 225 (525) W at the source. For HVM EUVL system ($>$ 1000 W), the required power is beyond of xenon gas at the current experimental conditions.

The detail of simulation results for different set of initial parameters and ions, in particular, new concept to overcome the CE limitation in discharged-pumped plasma EUV sources will be reported as future works.

ACKNOWLEDGMENTS

One of the authors (M. M.) wishes to express his gratitude for valuable discussion and the atomic data supporting received from Prof. Makoto Shiho and Dr. Akira Sasaki from the Japan Atomic Energy Research Institute. This work is partly supported by NEDO (New Energy and Industrial Technology Development Organization) and EUVA (Extreme Ultraviolet Lithography System Development Association) of Japan.

REFERENCES

[1] J. J. Rocca, Rev. Sci. Instrum. **70**, 3799 (1999).
[2] T. Hosokai, M. Kando, H. Dewa, H. Kotaki, S. Kondo, N. Hasegawa, K. Nakajima, and K. Horioka , Opt. Lett. **25**, 10 (2000).
[3] W. T. Silfvast, IEEE J. Quantum Electron. **35**, 700 (1999).
[4] M. A. Klosner and W. T. Silfvast, Opt. Lett. **23**, 1609 (1998).
[5] U. Stamm, J. Phys. D **37**, 3244 (2004).
[6] M. A. Klosner, W. T. Silfvast, and J. J. Rocca, Opt. Lett. **22**, 34 (1997).
[7] F. Gilleron, M. Poirier, T. Blenski, M. Schmidt, and T. Ceccotti, J. Appl. Phys. **94**, 2086 (2003).
[8] S. Churilov, Y. N. Joshi, and J. Reader, Opt. Lett. **28**, 1478 (2003).
[9] A. Sasaki, K. Nishihara, M. Murakami, F. Koike, T. Kagawa, T. Nishikawa, K. Fujima, T. Kawamura, and H. Furukawa, Appl. Phys. Lett. **85**, 5857 (2004).
[10] T. Krucken, K. Bergmann, L. Juschkin, and R. Lebert, J. Phys. D **37**, 3213 (2004) .
[11] A. Hassanein, V. Sizyuk, V. Tolkach, V. Morozov, T. Sizyuk, B. J. Rice, and V. Bakshi, in *Emerging Lithographic Technologies VIII*, edited by R. Scott Mackay, Proc. SPIE **5374**, 413 (2004).
[12] K. Bergmann, G. Schriever, O. Rosier, M. Muller, W. Neff, and R. Lebert, Appl. Opt. **38**, 5413 (1999).
[13] M. McGeoch, Appl. Opt. **37**, 1651 (1998).
[14] V. M. Borisov, A. V. Eltsov, A. S. Ivanov, Y. B. Kiryukhin, O. B. Khristoforov, V. A. Mishchenko, A. V. Prokofiev, A. Y. Vinokhodov, and V. A. Vodchits, J. Phys. D **37**, 3254 (2004).
[15] E. R. Kieft, K. Garloff, J. J. A. M. van der Mullen, and V. Banine, Phys. Rev. E **71**, 036402 (2005).

[16] N. Bowering, M. Martins, W. N. Partlo, and V. Fomenkov, J. Appl. Phys. **95**, 16 (2004).
[17] G. Schriever, K. Bergmann, and R. Lebert, J. Appl. Phys. **83**, 4566 (1998).
[18] A. Endo, IEEE J. Select. Topics Quantum Electron. **10**, 1298 (2004).
[19] W. Neff, K. Bergmann, O. Kosier, R. Lebert and L. Juschkin, Contrib. Plasma Phys. **41**, 589 (2001).
[20] E. Hotta, J. Plasma Fusion Res. **79**, 245 (2003).
[21] D. Attwood, *SOFT X-RAYS AND EXTREME ULTRAVIOLET RADIATION: Principles and Applications* (Cambridge, New York, 1999), Chap. 10, p. 395.
[22] N. R. Fornaciari, J. J. Chang, D. R. Folk *et al.*, in *Emerging Lithographic Technologies IV*, edited by E. A. Dobisz, Proc. SPIE **3997**, 120 (2000).
[23] M. Masnavi, M. Nakajima and K. Horioka, J. Plasma Fusion Res. **79**, 1188 (2003).
[24] M. Masnavi, M. Nakajima, A. Sasaki, E. Hotta, and K. Horioka, Jpn. J. Appl. Phys. **43**, 8285 (2004).
[25] N. A. Krall and A. W. Trivelpiece, *Principles of Plasma Physics* (McGraw-Hill, New York, 1973), Chap. 3, p. 125.
[26] J. Katzenstein, J. Appl. Phys. **52**, 676 (1981).
[27] S. Lee, J. Phys. D **16**, 2463 (1983).
[28] D. D. Ryutov, M. S. Derzon, and M. K. Matzen, Rev. Mod. Phys. **72**, 167 (2000).
[29] J. Blackburn, P. K. Carroll, J. Castello and G. O'Sullivan, J. Opt. Soc. Am. **73**, 1325 (1983).
[30] A. Sasaki, K. Nishihara, F. Koike, T. Kagawa, T. Nishikawa, K. Fujima, T. Kawamura, and H. Furukawa, IEEE J. Select. Topics Quantum Electron. **10**, 1307 (2004).
[31] T. Hosokai, M. Nakajima, T. Aoki, M. Ogawa, and K. Horioka, Jpn. J. Appl. Phys. **36**, 2327 (1997).
[32] A. Ben-Kish, M. Shuker, R. A. Nemirovsky, A. Ron, and J. L. Schwob, Phys. Rev. Lett. **87**, 015002 (2001).
[33] See, for example, K. T. Lee, S. H. Kim, D. Kim, and T. N. Lee, Phys. Plasmas **3**, 1340 (1996), and references therein.

MODIFICATION OF Z-PINCH PLASMAS WITH AN AXIAL MAGNETIC FIELDS

Yoshihiro Kondo[†], Akihiro Kimura[†], Shinichi Akiyoshi[†], Takao Namihira[††], Takashi Sakugawa[†], Sunao Katsuki[†], and Hidenori Akiyama[††]

[†] *Graduate School of Science and Technology, Kumamoto University*
39-1, Kurokami 2-chome, Kumamoto 860-8555, Japan
[††] *Dept. Electrical and Computer Engineering, Kumamoto University,*
39-1, Kurokami 2-chome, Kumamoto 860-8555, Japan

Abstract: This paper describes the effect of an axial magnetic field (B_z) on plasma pinch dynamics and on the extreme ultraviolet (EUV) emission property of a compact Z-pinch device for EUV sources. The Z-pinch xenon plasma was driven by a pulse current with an amplitude of 27 kA and duration of 150 ns in an alumina tube with a diameter of 5 mm. A quasi-static magnetic field of up to 360 gauss is applied to the plasma. The EUV emission was evaluated for spectra, spatial distribution of the emission, and light energy at 13.5 nm with 2% bandwidth. A time-resolved interferogram provides the electron line density and pinch dynamics of the plasma. When a magnetic field of 160 gauss was applied to the plasma, the emission energy was approximately double that without the magnetic field. The spectroscopic measurement shows that the EUV spectrum drastically varies with magnetic field strength. The time-resolved interferogram indicates that the axial magnetic field contributes by making the plasma compression smoothly and by sustaining certain plasma conditions longer. From these experimental results, it was concluded that applying an axial magnetic field can be an effective method to improve EUV emission..

Keywords : Z-pinch, axial magnetic field, EUV, spectrum shift, time-resolved interferogram, electron density profile

1. INTRODUCTION

Presently, the extreme ultraviolet (EUV) emission of xenon, tin or lithium ions are intensively being investigated for its use in future 32 nm or less rule photolithography process [1]. The "usable" in-band EUV power (13.5 nm 2%BW) required for the practical lithography tool is 115 W, which corresponds to the net output power at the source, is more than 500 W. Discharge produced plasmas (DPP) are presently the most powerful EUV source. In DPP EUV sources, with its highly repetitive operation in the range of 5 kHz, a huge electrical power of tens of kW is dissipated in the discharge chamber of which volume is in the range of a few cm^3. The power density at the inner surface facing to the plasma amounts to tens of kW/cm^2. The thermal load at the chamber causes problems, which degrade the lifetime of the components including electrodes, insulator wall as well as the light condenser optics. Most of the problems in DPP sources attribute the thermal load

to the components. In order to reduce the thermal load, it is important to minimize the energy input to the discharge and to improve the conversion efficiency (CE) from the discharge to in-band EUV energy, in addition to the components cooling. The experimentally demonstrated CE of the tin discharges EUV source is at most 2% so far [2,3]. The optimization of the plasma temperature and density for the 13.5 nm emission is very important to improve the CE unless new target materials and their combination for larger CE are found.

The generation process of the high energy density plasmas in DPP scheme is relatively flexible compared to the laser produced plasma (LPP) scheme EUV sources, and dependent on the current waveforms, target gas pressure, electrode geometry and initial ionization state of the target gas [4,5]. In addition, applying an axial magnetic field to the plasma is well known technique to suppress plasma instabilities during the compression [6], and used in several experiments of high energy density plasmas, such as Z-pinch X-ray sources [7] and capillary DUV lasers. The suppression of the plasma instabilities and the change in the emission spectra by applying an axial magnetic field were experimentally demonstrated [8]. However, there is no experiment that investigates its effect on practical-scale Z-pinch plasmas. We have developed a 15 J Z-pinch device for EUV light source to seek for the possibility to improve the conversion efficiency from discharge energy to 13.5 nm emission by using an axial magnetic field. In this paper, an effect of the axial magnetic field on the EUV emission from Z-pinch plasmas is discussed on the plasma behavior observed by using a time-resolved interferogram in addition to the in-band EUV emission energy and the EUV spectra.

2. EFFECT OF AXIAL MAGNETIC FIELDS

In a conventional Z-pinch scheme, an annular plasma, which is produced by a surface discharge at a cylindrical insulator wall for example, is compressed by magnetic pressure due to the current flowing through the plasma, I_z. In the pinch phase, strong compression and heating of the plasma occurs due to kinetic energy in the radial direction, a shock wave driven by the current sheet, and Joule heating. Therefore, temperature and density rapidly rise together, and high energy density plasmas, or so-called hotspot, are generated. High energy photons are emitted from the highly ionized ions in the high energy density plasmas. The emission spectrum varies with the energy density of the plasma. According to the calculation for radiation equilibrium, the optimum electron temperature and density for 13.5 nm emission from xenon plasmas are 30 ~ 40 eV and 10^{18} ~ 10^{19} cm^{-3}, respectively.

When an axial magnetic field is applied to an annular plasma as shown in Fig. 1, the pinch process changes. The external magnetic field flux cannot traverse the plasma sheet because the plasma shrinks rapidly enough to sustain eddy current in the plasma sheet. In the case of a gas uniformly distributed in the discharge chamber, the flux is gathered by the shrinking plasma together with the particles inside the annular plasma, which leads to an increase in the magnetic field strength inside the plasma. When the plasma shrinks to radius r, the magnetic flux density inside the plasma, B, is given by;

$$B = \frac{\eta B_0 r_0^2}{r^2}, \qquad (1)$$

where B_0, r_0 and η are the initial flux density of the external field, initial plasma radius, and leakage of the magnetic flux during compression ($0<\eta<1$), respectively. In the fast compression, η = 1 can be assumed. Therefore, the increasing magnetic pressure inside the plasma opposes the compression force driven by the plasma current. This phenomenon weakens the plasma compression and lowers the electron temperature and density in the plasma, which

leads to a shift in the emission spectrum toward a longer wavelength. We can make use of this effect to control the energy density of the pinched plasmas. Plasmas for which the energy density is most suitable for a specific wavelength, especially for 13.5 nm, are possible by adjusting the external axial magnetic field. The weakened compression allows for long sustainment of the high energy density plasma, which results in longer duration of emission of a specific wavelength. This would improve the conversion efficiency from the discharge for emission of the specific wavelength. There are some other practical benefits associated with the weakened compression achieved by using the axial magnetic field. Plasma instabilities can be suppressed, which leads to suppression of high energy ions in addition to the long plasma stagnation. Also the axial magnetic field is expected to result in effective heating of the plasma due to the Larmor motion of electrons.

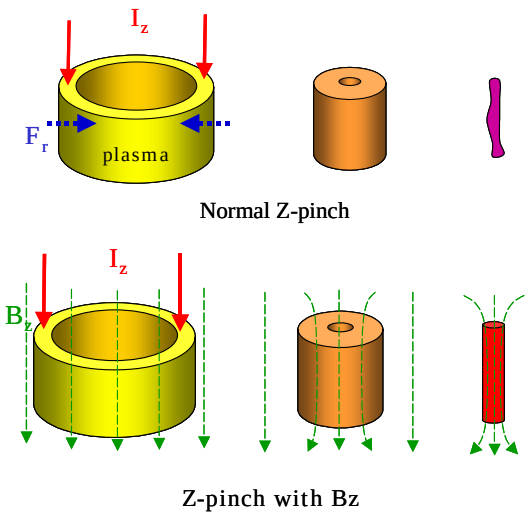

Figure 1 Effect of an external magnetic field on the pinch process of Z-pinch system.

3. EXPERIMENTSL SETUP

Figure 2 shows the cutting illustration of the main part of the z-pinch device, which consists of a 42 nF capacitor bank, a toroidal ferromagnetic core, and a z-pinch discharge tube. They are sandwiched with two circular metal plates. One of the metal plates is directly bolted on the vacuum chamber evacuated to 10^{-3} torr. The other is provided with negative high voltages. The z-pinch discharge tube, which consists of a hollow copper-tungsten alloy cathode, a stainless steel ring anode and a rounded alumina ceramic tube with the minimum diameter of 5 mm and the length of 10 mm, is located in the center of the coaxial structure. A flow rate of xenon gas fed into the discharge tube is fixed to be 50 cc/min. The discharge chamber can be optically accessed thorough two windows installed both side of the chamber.

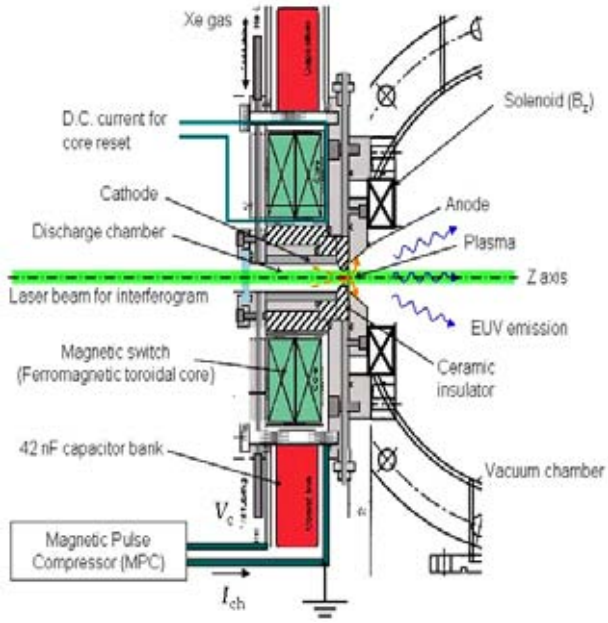

Figure 2 Cutting view of the Z-pinch device for the EUV source.

FINEMET^{TM} FT-1H (Hitachi Metals) was chosen as the material for the magnetic switch of the main circuit because of its high saturation field. The 42 nF capacitor bank is rapidly charged up to the voltage of 27 kV by a magnetic pulse compressor (MPC). The energy efficiency of the MPC exceeds 90%. The voltage and the energy per pulse delivered to the capacitor bank are 27 kV and 15 J, respectively. This circuit delivers the current with amplitude of 34 kA and pulse duration of

110 ns to a short circuit load. The magnetic switch prevents the reverse current, so that the current ends at a half period of the sinusoidal waveform. An air-core solenoid coil generating the axial magnetic field in the discharge chamber is fixed on the anode. The coil is driven by an independent power supply of and synchronized with the main discharge.

The maximum magnetic field strength generated on a discharge tube is 500 gauss. The charging voltage of the capacitor was measured with voltage divider (EP100K Pulse Electronic Engineering) and the discharge current is detected by a pick-up coil. EUV emission is evaluated with respect to an in-band EUV energy, EUV spectrum and source size. A transmission diffraction grating spectrometer (TGS) is used to observe EUV emission spectra of Z-pinch plasmas. Since a grating lattice (1000 lines/mm) is fixed on a 50 μm diameter pinhole, the spectrometer works also as a one dimensional pinhole camera in the perpendicular direction of the diffraction, which corresponds to the Z axis of the discharge. Wavelength and spatial resolutions of the spectrograph are 0.3 nm and 200 μm, respectively. The 1st order diffraction light is visualized by a micro channel plate (MCP) with a phosphor screen. Obtained spectra are calibrated by several sharp line spectra of oxygen ions in the CO_2 discharges. The in-band EUV energy is monitored by the EMON (Jenoptic Microtechnik), which basically consists of a calibrated silicon photodiode, two silicon/molybdenum multilayer mirrors and a zirconium filter. In addition, a time-resolved Mach-Zehnder laser interferogram is employed to observe the behavior of the Z-pinch plasmas. The second harmonic light of Nd-YAG laser (Surelite II, Contimuum) passes through the discharge tube along Z-axis of the system, and then meets the reference beam at the cubic half mirror. The interferogram was recorded by a CCD camera.

4. RESULTS AND DISCUSSION

4-1. In-band EUV energy with Bz

The figure3 shows the time-integrated in-band EUV energy (13.5 nm, 2% band- width), which is detected by EMON, as a function of the external axial magnetic field strength. The output EUV energy depends on the external magnetic field strength. When the B_Z = 170 gauss is applied, the EUV energy gains more than factor of 2 compared to that without the axial magnetic field. The B_Z = 40 gauss is large enough to gain 100% of the emission energy. The energy gain tends to decrease with increasing the magnetic field more than 190 gauss. The magnetic fields more than 255 gauss do not contribute to gain the EUV energy.

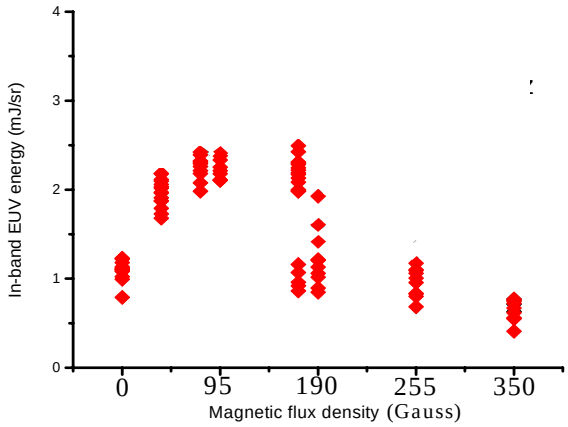

Fig. 3 Time-integrated in-band EUV energy (13.5 nm, 2% band- width), which is detected by EMON, as a function of the external axial magnetic field strength

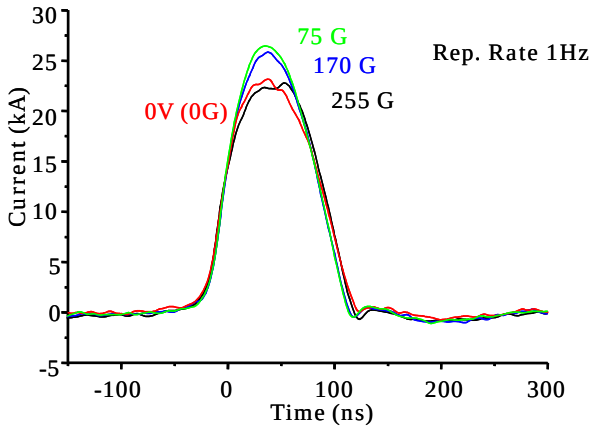

Fig. 4 Plasma current waveforms for different external magnetic field.

4-2. The discharge current with Bz

Figure4 shows the plasma current waveforms for different strengths of the external magnetic field. In the case no magnetic field is applied, the plasma current is suppressed at 22 kA because of the increase in the discharge inductance and resistance due to the strong compression. The average impedance defined by $Z_{av} = V_0/I_p$ is 1.23 Ω, where the impedance of the short circuit load is 0.90 Ω. When the pinch is released the current slightly is increased. When the magnetic field of 75 gauss is applied to the plasma, the current reaches 27 kA that is 90 % of that for short circuit load. This increase in the plasma current implies the compression should be weakened. When the larger magnetic field more than 170 gauss is applied to the plasma, on the contrary, the plasma current tends to decrease and the pulse duration increase with increasing the magnetic field strength. The pinched plasma is spatially stabilized by the strong axial magnetic field, which leads to the increase in its impedance. This is because the length of the pinched plasma along Z-axis becomes larger even though the plasma swells out.

4-3. EUV spectrum

Figure 5 shows the emission spectra in the EUV region of the Z-pinch plasma with different axial magnetic field strength of 0, 75, 170 and 255 gauss. Each spectrum is averaged over 100 shots. There are three major bands in this spectrum region, 11, 13.5 and 15 nm.

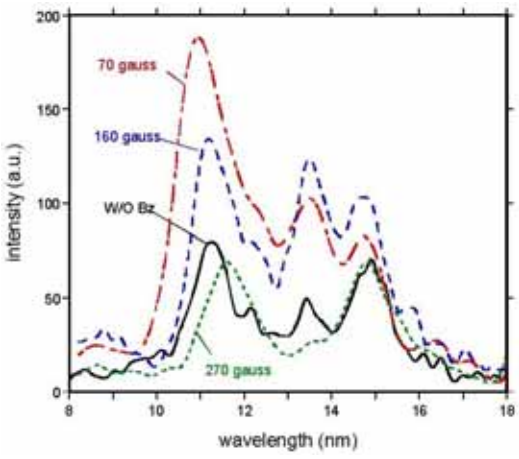

Fig. 5 Bz dependence of EUV energy Spectrum.

At first, at B_Z = 75 gauss, a line around 11 nm becomes very strong, and other peaks also become larger. When B_Z is increased to 170 gauss, the 11 nm band is reduced, and the 13.5 and 15 nm bands become more intense in contrast. At B_Z = 255 gauss, the intensity of the whole lines in this spectrum range are reduced. Especially, the 13.5 nm band almost disappears. In addition, 11 nm band appears to shift to longer wavelength side. In this condition, B_Z of 170 gauss is the best strength with respect to the output of 13.5 nm emission.

4-4. Behavior of Z-pinch plasma with Bz Figures 6 shows equi-density contour plots of the history of the radial profiles of the electron density integrated along the Z axis, called the line density, during the pinch. This is composed of several time-resolved line density profiles at different times. The reproducibility of each shot is sufficient to explain the plasma dynamics. Fig. 6 (a) and (b) are for the cases of B_z = 0 and 160 gauss, respectively. The outer most electron density contour and the interval between contours are 0.5×10^{17} cm^{-2}. Also, the shading is proportional to the electron line density.

According to Fig. 8(a), an annular plasma was initially formed near the insulator wall of the discharge chamber, and then the plasma moves toward the center. Strong compression occurs around t = 100 ns and the high density plasma stagnates at the center for tens of ns' in the case of B_z = 0. Subsequently the line density decays exponentially with a time constant of approximately 300 ns. When a magnetic field is applied to the plasma, the core plasma at the compression becomes thicker and the density gradient at the outskirt becomes smaller. the electron density rises relatively slower when the magnetic field is applied, and the rise rate becomes even smaller for the

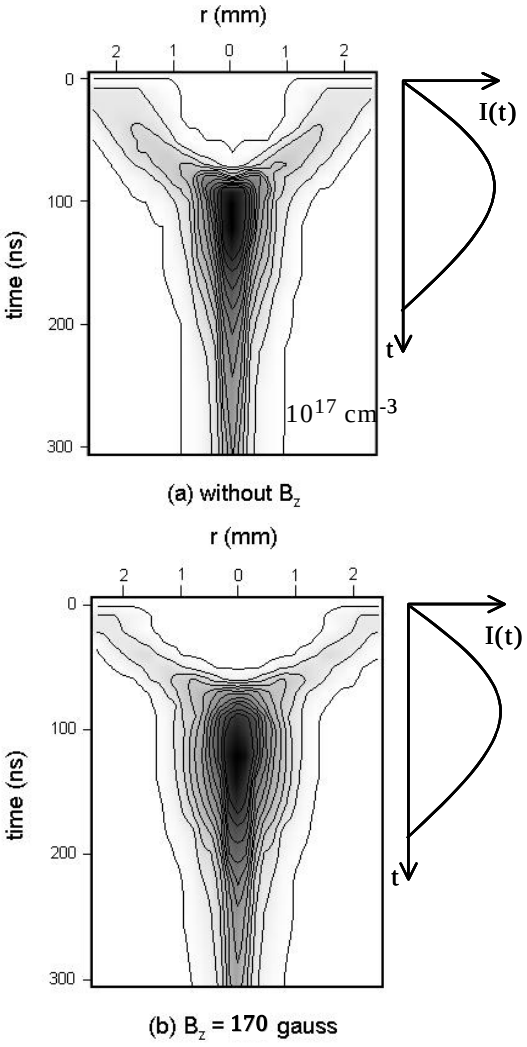

Fig. 6 Temporal development of electron density radial distribution for cases with and without the external magnetic field.

larger magnetic field, while the duration of high density is sustained longer..

5. SUMMARY

An external axial magnetic field was introduced for the purpose of controlling Z pinch plasmas, and its effects were investigated with respect to EUV emission energy, spectrum, and plasma dynamics. An axial magnetic field with the appropriate strength can double the EUV emission energy. In addition, the dominant emission bands shift towards longer wavelengths with increasing magnetic field strength. The time-resolved interference measurement shows that the behavior of the plasma varies with the axial magnetic field strength, which suggests a change in the energy density of plasma during the pinch phase. These experimental results lead to the conclusion that applying the axial magnetic field is an effective method of optimizing pinched plasmas for emission of a specific wavelength.

6. REFERENCES

[1] V. Banine, J.P. Benschop, M. Leenders, R. Moors, "Relationship between EUV lithographic system," Proc. SPIE 3997, 126-135 (2000)

[2] Pankert, The 3rd EUVL Symposium, Miyazaki, Japan, Nov. 1~4, 2004, SoP05 (unpublished)

[3] Stamm, The 3rd EUVL Symposium, Miyazaki, Japan, Nov. 1~4, 2004, SoP05 (unpublished)

[4] K. Bergman, G. Schriever, O. Rosier, M. Mueller,W.Neff,R.Lebert, "Highly repetitive extreme ultraviolet radiation source based on a gas-discharge plasma, Appl. Opt., 38, 5413-5417 (1999)

[5] W.N. Partlo, I.V. Fomenkov, R. Oliver, D.L. Bir x, "Development of an EUV (13.5 nm) light source employing a dense plasma focus in lithium vapor," Proc. SPIE 3997, 136-156 (2000)

[6] M.A. Liberman, J.S. De Groot, A. Toor, R. B. Spielman, "Physics of High-Density Z-Pinch Plasmas", Springer-Verlag (1998)

[7] T. Igusa, K. Takasugi, T. Miyamoto, "Control of radial motion of a gas-puff Z-pinch plasma by an axial magnetic field," NIFS PROC Series, Vol. 39, pp.70-79 (1998)

[8] A. Kimura, S. Katsuki, et al, "Modification of Z-pinch plasma using an External Axial Magnetic Field," Poster at the 3rd EUVL Symposium, Miyazaki, 2004, SoP06 (unpublished)

Development of gas jet type Z-pinch extreme ultraviolet light source for next generation lithography

Inho Song, Yusuke Honma, Kazuhiro Iwata, S.R. Mohanty, Masato Watanabe,
Toru Kawamura, Akitoshi Okino, *Koichi Yasuoka, Kazuhiko Horioka and Eiki Hotta

Department of Energy Sciences, Tokyo Institute of Technology,
Nagatsuta 4259, Midori-ku, Yokohama 226-8502, Japan
**Department of Electrical and Electronic Engineering, Tokyo Institute of Technology*
O-okayama, Meguro-ku, Tokyo 152-8552, Japan

ABSTRACT

A new gas jet Z-pinch source of 13.5 nm radiation, which has the characteristics of a gas jet type electrodes configuration and the scheme for radial extraction of extreme ultraviolet (EUV) light, has been developed. The gas jet type Z-pinch discharge head has two nozzles and two diffusers. The EUV beam is collected from the side of pinch plasma, generated in between the inner nozzle and corresponding diffuser, at the radial direction. The design feature of the gas jet type Z-pinch source accommodates the cylindrical annular shape helium (He) gas curtain that is produced by the outer nozzle. The estimated dimension of pinch plasma is to be FWHM diameter of 0.07 mm and length of 0.34 mm, and FW $1/e^2$ diameter of 0.15 mm and length of 1.2 mm. The EUV output in 2 % bandwidth at 13.5 nm is 0.78 mJ/sr/pulse.

Keywords: EUV light source, double gas jet, Z-pinch, radial collection, debris mitigation

1. Introduction

Cheaper, faster and smaller has been the long-standing mantra of the semiconductor industries. Therefore, in order to move with the pace of the motto, the semiconductor manufactures have to look for the new optical lithography tool for high volume manufacturing (HVM) of the next generation chips. Undoubtedly, the lithography at extreme ultraviolet (EUV) wavelength is a front-runner for the next generation chip-manufacturing tool. The EUV light source, the most critical component of the EUV lithography systems, plays a decisive role for early implementation of this tool in commercial scale production of chips at the 45 nm technology and beyond that [1]. Two major techniques based on discharge produced plasma (DPP) and laser produced plasma (LPP) are currently under intense investigations and these are still to compete for fitting into the EUV lithography scanner. The DPP sources using Xe appear to be capable of efficiency in the range of 0.6 % in 2 % bandwidth at 13.5 nm into 2π sr relative to the energy dissipated in the plasma [2-5]. The electrical input power requirement is, therefore, approximately 100 kW in order to generate 100 W of clean light at the intermediate focus (IF) of EUV scanner, taking into account the optical requirements that are expressed by the system etendue and cleanliness of the whole imaging system.

The EUV emission from the source based on DPP is incoherent and more or less isotropic in full solid angle. Due to constraint in the electrodes shape and the proximity of light emitting plasma to the electrodes, the DPP sources normally emit usable light into the forward direction. The light from these sources emerges out in a solid angle typically smaller than 2π sr. In this case, the grazing incidence reflectors can ideally be positioned in the free space in front of the light emitting plasma to collect EUV beam and then focus to the IF. On the contrary, in case of the LPP EUV sources, the laser and the injection apparatus are located at relatively large distances from the pinch plasma and, hence, the light can be collected in a solid angle equals to 4π sr. The collector mirror for the LPP sources is nearly at normal incidence to the source and the mirror surrounds to a large extent the nearly isotropically radiating LPP EUV source [6]. Because of the small and high brightness EUV plasma in case of LPP, its

collector optics may be designed to collect radiation emitted into a solid angle of up to 5 sr. On the other hand, in case of DPP plasmas, the current collector designs support only a 1.8 sr collection angle [7]. Nevertheless the DPP light sources have the advantages of efficiency, compactness and low cost. In order to apply the DPP light source to EUV lithography further development in collection angle is needed for improving HVM power. Another challenge of DPP EUV light source is the debris-free. The debris consisting of high energetic ions, neutrals and electrons from the plasma and the electrode materials lead to sputtering effects on the surface of the collector optics. Usually, a region of high-speed gas flow, named gas curtain are currently under development in many laboratories to slow down or stop the highly energetic particles debris. The gas curtain thickness must be of the order of a few centimeters in order to have a minimal absorption of EUV light and the gas type must have a high cross section for scattering of debris particles. Nevertheless, the gas curtain debris shielding arrangement is not easy to design and to install when adapted to a large solid angle electrode in DPP source [8].

The aforesaid challenges of designing a debris free EUV source having wider collection angles prompt us to propose and develop a new DPP source, named as gas jet type Z-pinch that address both the issues simultaneously. The developed gas jet Z-pinch source has a provision for extraction of EUV light in radial direction with respect to pinch axis so that it has a larger collecting solid angle than the general DPP sources and it may use the normal incidence reflector collector mirror like LPP system. In practice, the debris of DPP sources generally emerges out in a cone in forward direction and, therefore, the radial extraction of EUV light must be an interesting methodology to have a clean EUV light. Also, helium gas jet for gas curtain suppresses the debris and confines Xe in the Z-axis by limiting the expansion. Our approach promises a solid angle closer to that for LPP sources and a simple gas curtain; at the same time, it retains the characteristics of low cost and high efficiency of DPP sources. In this article, we address the early stage results of our investigation based on our innovative gas jet type Z-pinch EUV source.

2. The gas jet Z-pinch

The new gas jet type Z-pinch source has two nozzles and two diffusers. The inner nozzle (cathode), a device that accelerates gas flow, is responsible for Xe gas jet formation in between inner nozzle and corresponding diffuser. The diffuser (anode), a device that decelerates the gas flow, controls the vacuum inside the chamber for reducing the EUV absorption. The outer nozzle produces annular cylindrical He gas jet, which acts as a gas curtain. He gas curtain is parallel to Xe gas flow and, therefore, it helps the confinement of Xe. The source design assures that the entire EUV emission path is covered by the gas curtain. The EUV light is collected from the side of pinch plasma at the radial direction in order to improve the collection efficiency. Xe gas jet is positioned centrally between the cathode and anode via the action of inner nozzle.

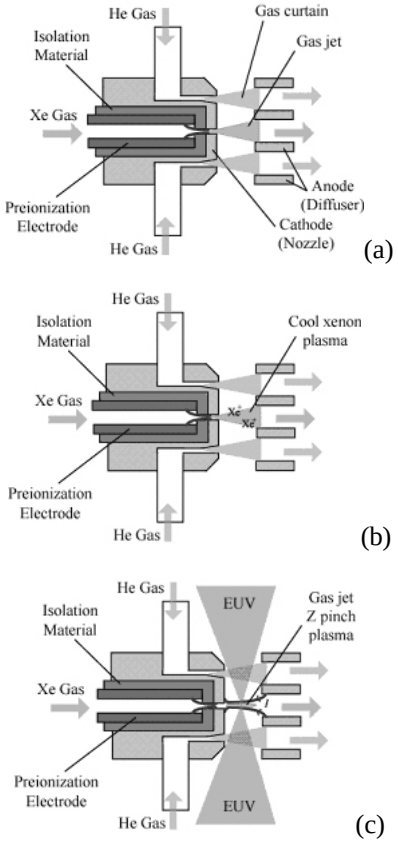

Fig. 1. Schematic of gas jet Z-pinch source showing (a) Xe and He gas jet flow; (b) ejection of weekly ionized Xe plasma and (c) pinch formation along with EUV generation.

The axis of both the gas jet is aligned to the axis of device (Z-axis) as shown in Fig. 1(a). The preionization of the working Xe gas is spatially separated from the main discharge region and a high voltage pulse is applied between preionization electrode and cathode, which are separated by a

ceramic insulator. The free electrons ionize the ambient Xe gas forming a low-density cold plasma, which comes out from the preionization region due to continuous flow of Xe gas. Thus, Xe ions stream together with neutral Xe atoms accelerates towards anode as shown in Fig. 1(b) and their flow dynamics is very complex that mainly depends upon pressures and nozzle's dimension. After a short while of preionization discharge, a pulsed high current is delivered from a pulsed power supply to ignite the Xe jet that appears in between the electrodes. The high current forms the main plasma and the self generated azimuthal magnetic field owing to the high current compress the main plasma to form a hot and high density pinch plasma column as shown in Fig. 1(c). This high-temperature plasma mainly radiates at around 13.5 nm in full solid angle. Many parameters such as separation between the electrodes and Xe gas flow rate control the EUV intensity and dimension of the EUV emitting plasma volume. The interesting feature of this configuration is that there is an ample scope of extracting clean EUV radiation in radial direction with respect to Z-axis

3. Experimental setup

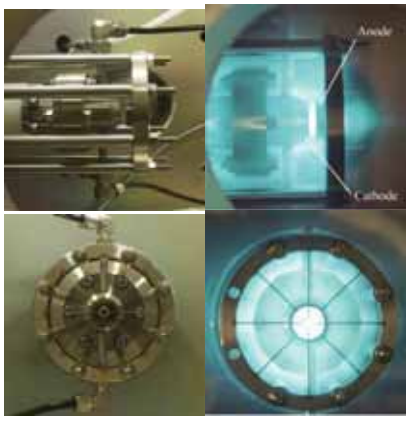

Fig. 2. Photos of gas jet type Z-pinch discharge head and discharges taken by digital camera.

Photos of the gas jet type Z-pinch source and discharge is shown in Fig. 2. Figure 2 shows the photos of gas jet type Z-pinch discharge head, which consists of cathode electrode (inner nozzle for Xe gas jet and outer nozzle for He gas curtain) and anode (diffusers). The electrodes of the source were made of stainless steel and the their dimension were typically chosen so as to suit the load current as well as to fit inside the detection chamber. The diameter of inner nozzle was 2 mm and cylindrical type opening, which had 0.2 mm width, was used as outer nozzle for He gas jet. Diameter of inner diffuser for anode was 6 mm and maximum and minimum diameters of outer diffuser were 20 mm and 24 mm, respectively. The flow rate of Xe gas in the gas jet type Z-pinch head was varied by changing Xe gas supplying pressure in between 5 Torr to 17 Torr so that the pressure inside the detection chamber was maintained below several mTorr. The preionization plasma was first created in the Xe gas jet by applying 6 kV pulse in between anode and cathode and, subsequently, the main plasma was formed by delivering a 9.5 kA current pulse having 320 ns pulse width and 160 ns risetime to the preionized plasma. The 9.5 kA current pulse was generated by the SI thyristor switched pulse power supply having stored energy of 15 J (9 kV charging voltage).

Several diagnostics were employed for studying the dynamics of the plasma, determining the size and energy of EUV plasma and inspecting visible spectra of plasma source. To look into the plasma dynamics between the electrodes, the framing photographs in visible region were taken by using a high-speed image converter camera (IMACON 468, 10 ns time resolution). In order to measure the time evolution of EUV photon output, an EUV photodiode (IRD, AXUV-100) coupled with Zr/C filter (200/50 nm) was employed. An EUV mini calorimeter consisting of a Zr filter, a Mo/Si multi-layer mirror and a photodiode, was also employed. The EUV mini calorimeter was calibrated by E-Mon (JOMT and AIXUV) [9] and was mainly used for the measurements of absolute in-band EUV energy and angular distribution of the emitted EUV radiation. The spectral emission of the source in the visible region was analyzed by employing a multi-channel spectroscope (Ocean Optics, HR2000) having maximum resolution of the order of 0.027 nm. The EUV pinhole camera that consists of 50 μm diameter pinhole, Zr filter (150 nm thickness) and X-ray CCD camera (Andor Technology Ltd. DO434) was employed at 90° from Z-axis for measuring the dimensions and stability of the EUV plasma. The Zr filter has a transparency of about 13 % to EUV light with a wavelength between roughly 12 and 18 nm, but it blocks over 99 % of any vacuum ultraviolet light emitted by the source at larger wavelengths. The X-ray CCD camera has 55 % quantum efficiency for soft to medium X-ray detection. The distance from the pinhole to the X-ray CCD was fixed at 369 mm and the distance from the source to the pinhole was

119 mm resulting in a magnification factor of 3.1.

4. Results and discussions

4.1 Plasma dynamics at different Xe gas supplying pressure

Keeping input stored energy at 15 J, the dynamics of the plasma inside the gas jet type Z-pinch was studied at radial position with the aide of high-speed framing camera in visible region by varying the Xe gas supplying pressure. A typical set of time-resolved high-speed camera photographs together with the main discharge current recorded at 10 Torr Xe flow rate is illustrated in Fig. 3. The photographs captured before the main discharge current visibly indicates the evidence of feeble preionized plasma that are generated as a consequence of the preionization current. The evidence of pinch plasma is prominent in the framing photo taken at a time around 80 ns. In fact, the pinch plasma occurs just before the maximum of discharge current pulse. The plasma is enough heated to emits copious amount of higher ionization state of Xe ions as evident from photodiode output. An intense EUV photon signal appears after about 60 ns of the initiation of discharge and it reaches its peak value during the pinch of plasma. The pinching action may last for few tens of nanoseconds and the plasma, after the pinch, expands in the radial direction thereby increasing the volume large luminous plasma in between electrodes.

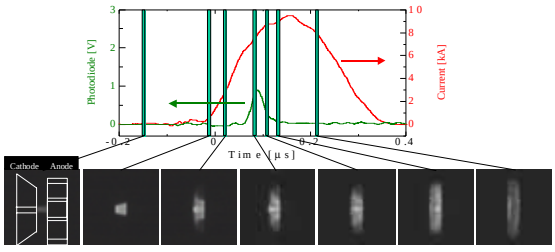

Fig. 3. Time-resolved framing photographs at charging voltage: 9 kV and Xe gas supplying: 10 Torr.

On further increase in the flow rate (17 Torr), the signal of EUV photodiode could not distinguished from the noise because of very low EUV output. Yet the framing photograph obtained after 300 ns of the start of main current exhibits some signature of pinch plasma as shown in Fig. 4. The delayed pinching action and the low output of EUV can be attributed to the initial condition of gas density. It may be noted that the higher Xe gas supplying pressure increases the initial mass condition that takes part in pinching action resulting a very slow pinching process. The plasma may not be enough heated to generate high EUV yield due to slow pinching action. However, the gas dynamical expansion from the nozzle, which is not only causes the density to drop but also moves the plasma out of focal volume, limits the heating of main plasma.

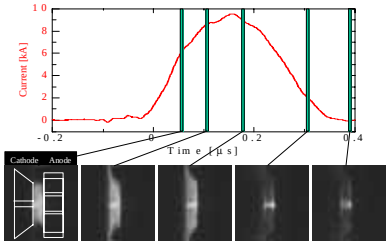

Fig. 4. Time-resolved framing photographs at charging voltage: 9 kV and Xe gas supplying: 17 Torr.

4.2 EUV pinhole images at different input energy and pressure

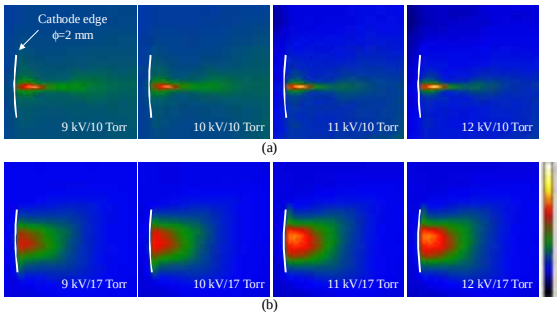

Fig. 5. EUV pinhole images for 10 pulses averaged at different input energy: (a) Xe gas supplying: 10 Torr and (b) Xe gas supplying: 17 Torr.

EUV pinhole images were recorded at 90° with respect to electrodes axis with an EUV pinhole camera for various input energies (15 J to 27 J) and Xe gas supplying pressures. Figure 6 shows the EUV images recorded at the typical experimental conditions as inscribed in those images. In the case of 10 Torr Xe gas supplying pressure, the EUV plasma images, shown in Fig. 5(a), are found to be extremely narrow cylindrical shape, which are fairly symmetrical with respect to the axis. However, a look at the images recorded at 17 Torr, shown in Fig. 5(b), indicates that the shape of the EUV plasma is blunted shape and the EVU radiating plasma is located at the upstream inside the cathode nozzle. The set of images shown in Fig. 5(a) is indicative of strong contraction

of main plasma into a narrow region whereas the set of images shown in Fig. 5(b) do not show any evidence as a point source. These results are in complementary to the evidences explained in preceding section. To investigate whether the input energy has any influence on the EUV intensity, measurements were made with four different input energies such as 15 J, 18.5 J, 22.4 J and 26.6 J by varying the charging voltages. The effect of input energy on EUV intensity is easily seen in those images shown in Fig. 6 and it is noticed that the intensity increases linearly with the increase of input energy.

4.3 Positional and energy stability

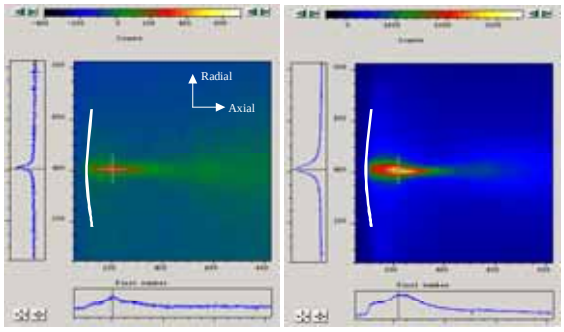

(a) (b)

Fig. 6. EUV pinhole images for (a) single pulse and (b) 20 pulses at 9 kV charging voltage and 10 Torr Xe gas supplying pressure.

In practice, the performance of an EUV light source for lithography depends upon their positional as well as energy stability. Therefore, these factors are estimated for our gas jet type Z-pinch source by superimposing images obtained for 20 discharges taken at 9 kV charging voltage and 10 Torr Xe gas supplying pressure. These results are shown in Fig. 6. The lineout of the single discharge image gives that the radial length of the source in the measure of FWHM and FW $1/e^2$ are about 0.07 and 0.15 mm, respectively. On the contrary, the axial length of the source in terms of FWHM and FW $1/e^2$ are about 0.34 and 1.2 mm, respectively. For the 20 discharges image, the radial FWHM and FW $1/e^2$ length of the source are of the order of 0.16 and 0.66 mm and the axial FWHM and FW $1/e^2$ length are of the order of 0.96 and 3.0 mm. The average image of 20 discharges demonstrates that the plasma size appears to be 2.5 times larger than in the single discharge image due to the fluctuations in both the size and positional stability. An unstable source would lead to a bigger integrated image size and thus undesired for coupling into EUV lithography system. Furthermore we have estimated of the EUV energy stability by integrating the intensity of EUV pinhole images for 20 discharges and the results show 5 % intensity fluctuation in our case. International SEMATECH requires that pulse-to-pulse positional stability must be below 10 % of the source size and energy stability is ± 0.3 % [10]. The characteristics of pinch plasma depend on several operating parameters such as the input energy, the discharge current rising time, the repetition frequency and the Xe gas supplying pressure and especially the dimensions and the shape of nozzle in gas jet type Z-pinch. Further investigations are needed to determine the position stability and intensity fluctuation under typical exposure conditions.

4.4 Spectra result in visible range

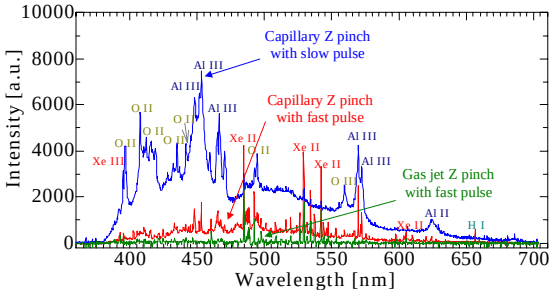

Fig. 7. Visible spectra results of capillary discharge and gas jet type Z-pinch at the same input energy.

As mentioned earlier, the main interest in developing this gas jet type Z-pinch EUV source is to reduce the debris substantially by innovative configuration. It is, therefore, interesting to study the spectral emission in visible region at first to have an idea about impurities emerging out of the source in radial direction. At 15 J input energy and 10 Torr Xe gas supplying pressure the visible spectrum is recorded at 90° with respect to electrode axis and shown in Fig. 7. The spectrum is superimposed with another spectra obtained in our work based on capillary discharge EUV plasma source for comparison of debris generation in both schemes. The detail of the capillary discharge work is communicated in Ref. 11. It appears from the Fig. 7 that the capillary discharge generates much impurity lines in visible range than that of gas jet type Z-pinch. The observed impurity lines of different ionization states of O and Al in capillary discharge come mostly

from the alumina capillary wall. No significant impurity contribution from the electrode materials is marked in the gas jet type Z-pinch discharge. The impurity lines together with Xe lines of lower ionization state affect the spectral purity of a EUV lithography source. The impurity line of EUV source is one of the factors, which influences the lifetime of optics mirror. Reference 12 discusses the spectral purity requirements for EUV source parameters to be installed in EUV lithography high volume production tools. The visible spectrum establishes that our gas jet type Z-pinch source radiates very clean EUV light with minor contamination in low ionization state of Xe and the prospects of radial extraction of EUV light seems to be fruitful.

4.5 Absolute in-band EUV measurement

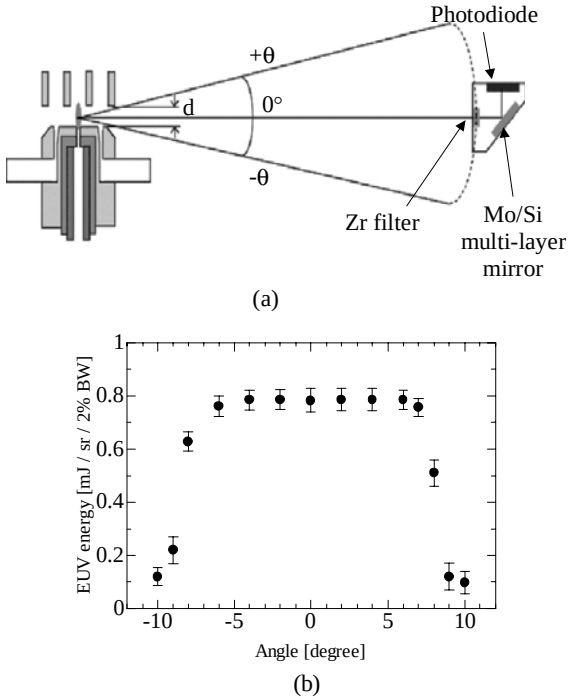

Fig. 8. A schematic view of the EUV mini calorimeter setup (a) and angular distribution of in-band EUV radiation observed at 9 kV, 10 Torr Xe gas supplying pressure.

As discussed earlier, the power requirement at IF of EUV lithography tool is still have a great challenge for source developmental work. So, in order to check the capability of our gas jet type Z-pinch source, the EUV power in absolute numbers is determined with the help of an absolutely calibrated EUV mini calorimeter. The schematic view of the mini calorimeter setup is shown in Fig. 8(a) and the measured angular distribution of in-band EUV radiation at 9 kV charging voltage and 10 Torr Xe gas supplying pressure is illustrated in Fig. 8(b). The EUV output in 2 % bandwidth at 13.5 nm is 0.78 mJ/sr/pulse, which is much lower value than as observed in other schemes. The available observation angle (± 8 degree) may lead to partial obscuration of the source and thus by dropping the output power. In spite of the low output energy, we believe that increasing the discharge current and improving the present nozzle design can achieve the high EUV yield.

5. Summary

In order to permit large solid collection angle and avoid the presence of debris in DPP EUV light source for lithography, it seems to be a good idea to collect EUV from the side of pinch plasma at radial direction. The concept of radial extraction of clean EUV light was successfully demonstrated by our new gas jet type Z-pinch discharge. The results of high-speed camera shows that the characteristics of gas jet type Z-pinch plasma has strong dependence on Xe gas supplying pressure. At 10 Torr Xe gas supplying pressure, the EUV plasma is extremely narrow cylindrical structure with 0.07 mm FWHM diameter and 0.34 mm FWHM length. No significant impurity spectra in visible range are marked in gas jet type Z-pinch discharge. Protection of condenser optics is probably easier in a gas jet type Z-pinch source by using cylindrical annular He gas nozzle. The characteristics attained with gas jet type Z-pinch source such as a small pinch plasma, large solid angle and an opportunity to reduce the effects of debris make such source the subject of our great interest.

We continue to study the emission under various conditions of gas pressure, discharge current, gap distance and different nozzle/diffuser dimensions for the characterization of the EUV emission properties of gas jet type Z-pinch and evaluation of the debris.

6. Acknowledgement

This work is partly supported by New Energy and Industrial Technology Development Organization (NEDO). S.R. Mohanty is indebted to JSPS for the financial support to work in Tokyo Tech. and he is also thankful to Director, Centre of Plasma Physics, Assam, India for granting leave to avail JSPS fellowship.

References

[1] V. Banine and R. Moors, Proceedings of SPIE, Vol.4343 (2001), pp.203-214.

[2] R. Lebert, K. Bergmann, L. Juschkin, O. Roiser and W. Neff, Proceedings of SPIE, Vol.4343 (2001), pp.215-225.

[3] I.V. Fomenkov, R.M. Ness, I.R. Oliver, S.T. Melnychuk, O.V. Khodykin, N.R. Bowering, C.L. Rettig and J.R. Hoffman, Proceedings of SPIE, Vol.5037 (2003), pp.807-821.

[4] Y. Teramoto, H. Sato, K. Bessho, T. Shirai, D. Yamatani, T. Takemura, T. Yokota, K.C. Paul, K. Kabuki, K. Miyauchi, M. Ikeuchi, K. Okubo, K. Hotta, M. Yoshioka and K. Toyota, Proceedings of SPIE, Vol.5374 (2004), pp.935-978.

[5] V.M. Borisov, A.V. Eltsov, A.S. Ivanov, Y.B. Kiryukhin, O.B. Khristoforov, V.A. Mishchenko, A.V. Prokofiev, A.Y. Vinokhodov and V.A. Vodchits, J. Phys. D: Appl. Phys., Vol.37 (2004), pp.3254-3265.

[6] P. Marczuk and W. Egle, Proceedings of SPIE, Vol.5533 (2004), pp. 145-156.

[7] U. Stamm, J. Phys. D: Appl. Phys., Vol.37 (2004), pp.3244-3253.

[8] E.V. Lopez, B.E. Jurczyk, M.A. Jaworski, M.J. Neumann and D.N. Ruzic, Microelectronic Engineering, Vol. 77, Issue 2 (2005) pp.95-102.

[9] T. Missalla, M.C. Schurmann, R. Lebert, C. Wies, L. Juschkin, R.M. Klein, F. Scholze, G. Ulm, A. Egbert, B. Tkachenko and B.N. Chichkov, Proc. SPIE, Vol.5374 (2004), pp.979-990.

[10] Joint specification ASML, Canon, Nikon, presented at the 3rd International EUVL Symposium, 2004, Miyazaki.

[11] I.H. Song, K. Iwata, Y. Honma, M. Masnavi, M. Watanabe, A. Okino, K. Yasuoka, K. Horioka, K.C. Ko and E. Hotta, Third International EUVL symposium.

[12] U. Stamm, I. Ahmad, V.M. Borisov, F. Flohrer, K. Gabel, S. Gotze, A.S. Ivanov, O.B. Khristoforov, D. Klopfel, P. Kohler, J. Kleinschmidt, V. Korobotchko, J. Ringling, G. Schriever and A.Y. Vinokhodov, Proceedings of SPIE, Vol.5037 (2003), pp.119-129.

HIGH-POWER EUV SOURCE FOR LITHOGRAPHY USING TIN TARGET

H. Horita[†], H. Imamura[††], H. Fukumoto[†], C.H. Zhang[†], T. Namihira[††], T. Sakugawa[†††], S. Katsuki[†], and H. Akiyama[††]

[†] *Graduate School of Science and Technology, Kumamoto University*
39-1, Kurokami 2-chome, Kumamoto 860-8555, Japan
[††] *Dept. Electrical and Computer Engineering, Kumamoto University,*
39-1, Kurokami 2-chome, Kumamoto 860-8555, Japan
[†††] *Cooperative Research Center, Kumamoto University*
Tahara 2081-7, Mashiki-machi,Kamimashiki-gun, Kumamoto 861-2202, Japan

Abstract: Xenon Z-pinch discharge sources are being developed for extreme ultraviolet (EUV) light for next generation lithography. However, the current sources generate in-band (2%), 2π EUV emission with conversion efficiency (CE) of <1%. Here we report progress in the development of a Z-pinch EUV source using a tin target, which was found to have significant potential for high conversion efficiency with wavelength of 13.5 nm. Xenon was used as the background gas, the experiments show that the magnitude of the EUV emission depended on not only the distance between the plasma and the rod surface, but also the pulse repetition rate of the discharge. Pinhole imaging, an EUV spectrograph and an in-band EUV energy monitor were used to characterize the EUV emission from the Z-pinch discharge.

Keywords: EUV sources, z-pinch, xenon emissions, tin plasma.

1. INTRODUCTION

Extreme Ultraviolet (EUV) radiation is becoming the semiconductor industry choice for next-generation lithography (NGL)[3]. Among the major source concepts, laser-produced plasma and gas discharge sources are most prominent contenders. However, the gas discharge plasma source has drawn much attention in last decade due to its simplicity and cost-effectiveness. The present xenon Z-pinch discharge sources generate in-band (2%), 2π EUV emission with conversion efficiency (CE) of <1%. Tin targets were found to have significant potential for high conversion efficiency (CE) with wavelength of 13.5 nm. Theoretical calculations [1] show that predominantly 4d-4f transitions in a number of adjacent ion stages (S_n^{8+}-S_n^{13+}) produce unresolved transition arrays (UTAs) [2] that are localized in this spectral area.

In this paper, we report the progress on z-pinch EUV source with tin target. Tin vapor including atoms and ions is produced by the ablation of the solid tin rod (diameter of 6 mm), which is due to the energy flux from the plasma. Xenon or helium is used as a background gas. The EUV emission depends on the distance between the plasma and the rod surface (~ 10s mm) and on the pulse repetition rate of the discharge (< 200 Hz). The z-pinch plasma is driven by the pulsed current with amplitude of 30 kA and duration of 110 ns. The EUV emission from z-pinch discharge is characterized with pinhole imaging, EUV spectrograph and in-band EUV energy monitor.

2. EXPERIMENTAL SETUP

A schematic of the Z-Pinch EUV sources is shown in Figure 1. Xenon gas is used as EUV emitter, which is continuously flowing through the discharge tube (diameter 3 mm and length of 5 mm). The capacitor

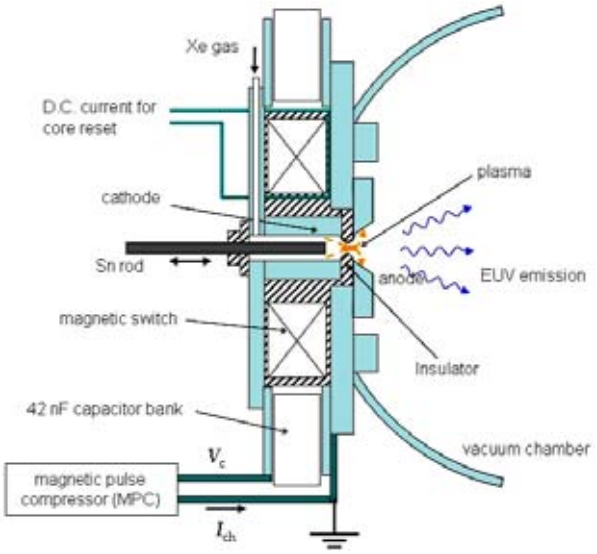

Fig. 1 Schematic of the Z-Pinch EUV source

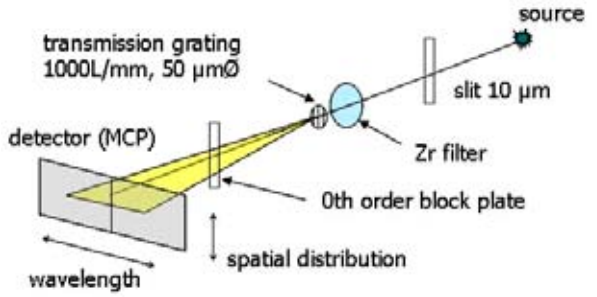

Fig. 2 Transmission grating spectrometer

banks, having a capacitance of 42 nF, were positioned symmetrically on the axis of Z-pinch discharges to provide electrical energy up to a charging voltage of maximum 35 kV. A tin rod with a 6 mm in diameter is fixed on the high voltage flange and its tip is faced to the plasma. The position of the tin rod tip can be moved continuously.

The EUV radiation from the Z-Pinch plasma was characterized by measurement for the temporal behavior of the EUV intensity and the pinhole images. We have optimized the Z-Pinch design parameters as well as the electrical parameters of the pulsed power excitation circuit (high voltage, capacitance and inductance to achieve the required source characteristics at high conversion efficiency. It is worth mentioning that the maximum EUV radiation is the most sensitive to the xenon flow rate and the discharge current. The EUV energy monitor E-Mon is used to measure pulsed EUV-energies from high power EUV-sources at central wavelength of 13.5 nm with a bandwidth of 2%. The energy monitor consists of a Zr filter, two Si/Mo multilayer mirrors and a calibrated photodiode. The principle of operation is filtering out the in-band range from the broad band spectrum of an EUV-source. The radiation is detected in a well-defined solid angle that is determined by an aperture and its distance from the source along the beam path. Figure 2 shows the structure of an EUV spectrometer, which also works as a pinhole camera. The spectrometer consists of a slit (10 µm), a Zr filter, a transmission grating, a micro channel plate (MCP) image intensifier, and a commercial-type digital camera. Wavelength and spatial resolutions are 0.3 nm and 90 µm, respectively.

3. RESULTS AND DISCUSSION

Experiments were performed with discharge peak value current of 30 kA, and a rise time in the range of about 110 ns. Figure 3 shows a typical discharge current signal and the corresponding EUV emission of a single discharge. About 45 ns after the ignition of the discharge the pinching of the plasma is indicated by the dip in the current signal, which is due to an increase of the inductance of the contracting plasma column. Experiments show that EUV emission strongly depends upon discharge current (amplitude, duration), filling gas pressure as well as charging voltage.

Time-integrated emission spectra of Z-pinch discharge system were recorded by employing EUV spectrometer at one end-on position. Figure 4 shows EUV spectra and

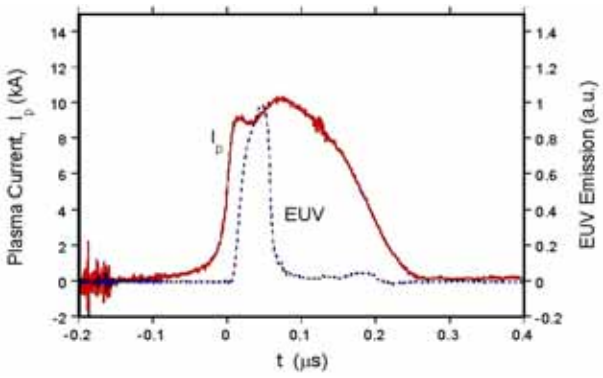

Fig. 3 A typical discharge current and EUV emission indicated by the photodiode

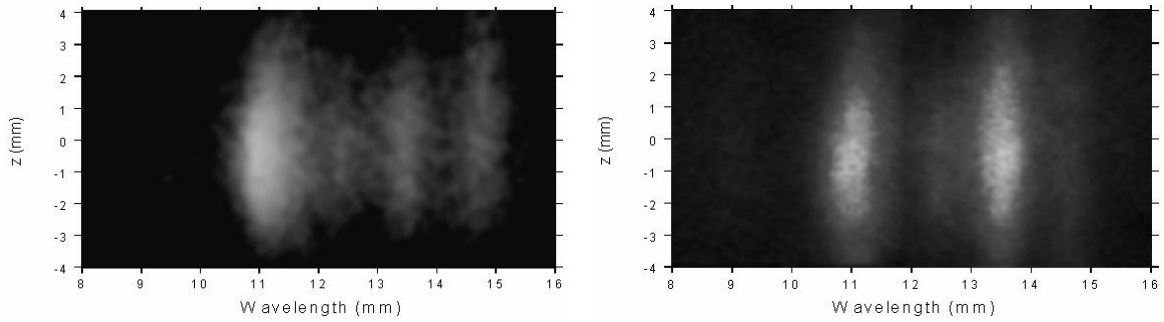

(a) (b)

Fig. 4 EUV spectra: Transmission Grating Spectroscopy (Δλ=0.3 nm)
(a) xenon (40 cc/min), (b) xenon (40 cc/min.) + tin rod placed at 15 mm from the plasma.

corresponding source sizes obtained by the transmission grating spectroscopy (Δλ=0.3 nm). Figures 5 and 6 show the EUV spectra and spatial distribution of EUV emission along Z-axis, respectively, derived from Fig. 4. We can clearly notice two or three broad band peaks within the 8-16 nm range. The most distinguished broad band peaks are centered at 11, 13.5 and 15 nm, each having a bandwidth of approximately 1-1.5 nm. These broad band peaks are attributed to the various ionization states of xenon (Xe^{11+}, Xe^{10+} and Xe^{9+}) and tin vapor. In the Figure 5, the spectrum in the case of xenon gas has only a very low photon flux at 13.5 nm in comparison to 11 nm. On the other hand, in the case of xenon + tin, although the spectrum still has a large photon flux at 11 nm, 13.5 nm emission is comparable to the 11 nm emission. The fact implies that the tin vapor is mixed in the plasmas and highly ionized together with xenon ions. As for the spatial distribution of the emission, the source size in the case of xenon + tin tends to be large. The tin might change the xenon flow and the electric field distribution.

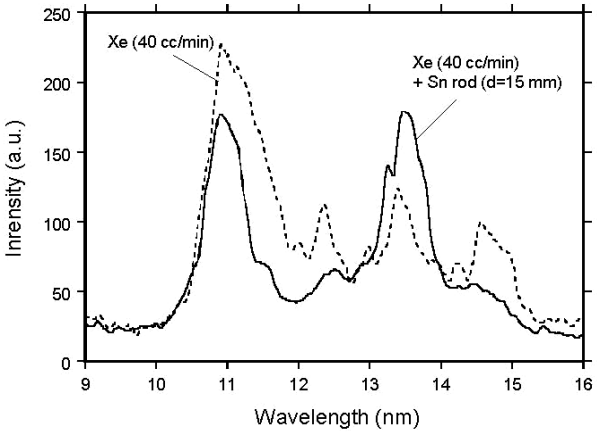

Fig. 5 EUV spectra for xenon

Figure 7 show the in-band EUV energy as a function of discharge repletion rate, for both cases with

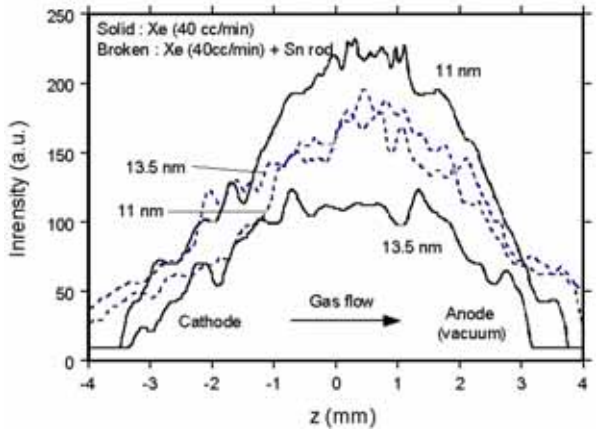

Fig. 6 Spatial distribution of the EUV emission along Z-axis. The position Z=0 indicates the center of electrode system.

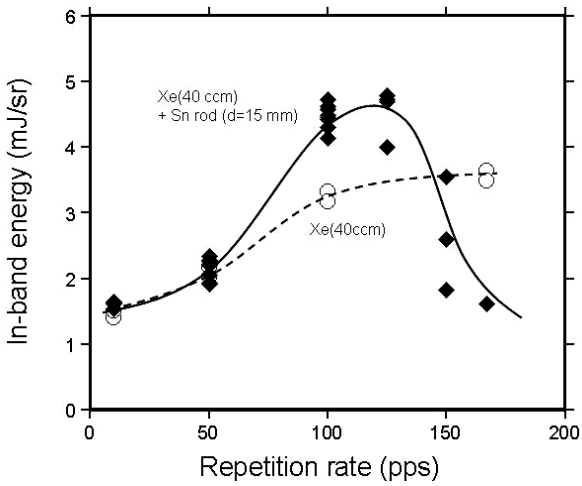

Fig. 7 In-band EUV energy per shot as a function of the discharge repetition rate.

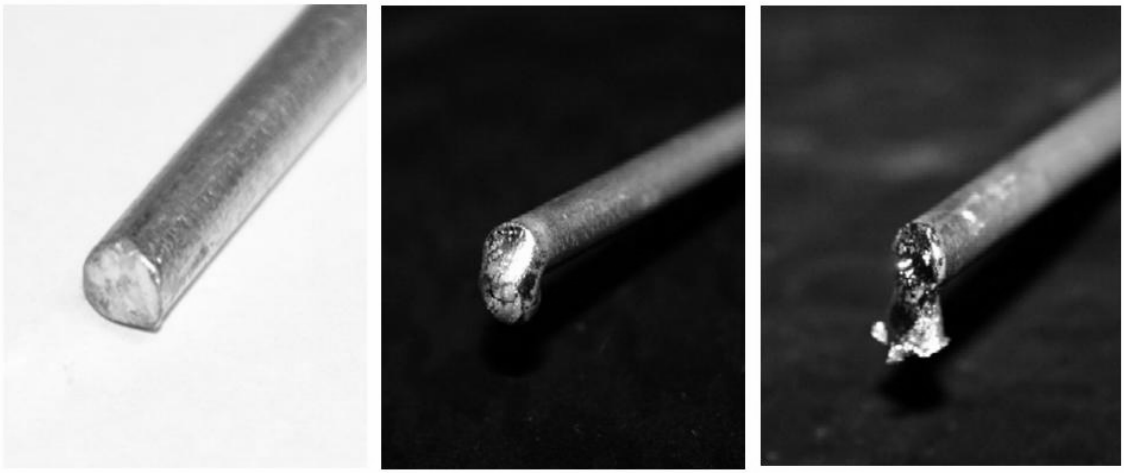

(a) fresh surface (b) 100 Hz (c) 167 Hz

Fig. 8 Tin rod surface before (a) and after 100,000 discharges for different repetition rate of the operation. Distance between the rod tip and the plasma is 15 mm.

and without the tin rod. With the repletion rate less than 50 Hz, in-band energy is the same between two cases. Also their spectra are quite similar to each other. The operation with 100 Hz, emission characteristic has dramatically changed. Even in the case of xenon, the EUV energy is increased with increasing the discharge repetition rare in our device. Furthermore, about 30 % of in-band energy is gained by using the tin rod. However, with the operation at 150 Hz, reproducibility of the emission energy is worse, and the energy is quite small at 167 Hz. It is deduced that the discharge repetition rate should be one of the factors to determine the temperature of the tin rod surface. The distance between the rod surface and the plasma is one another factor for the surface temperature. From the experiments with Tin rod with various distances, we found that the intensity of 13.5 nm emission strongly depends upon the distance. As one decrease the distance the intensity of the spectrum increase. The experimental result suggests that temperature control at the tin rod surface should be important for this technology. Figure 8 shows the photographs of the tin rod surface before and after 100,000 discharges for different frequencies. At the repetition rate of 100 Hz, which is the optimum condition for EUV emission energy, the surface seems to be molten and shape has been changed. At 167 Hz, apart of the rod is drooped down to the cathode wall. This might cause the discharge unsymmetrical to Z-azis.

The EUV energy monitor E-MON has been utilized to estimate the radiated energy at 13.5 nm having a bandwidth of 2%. It is estimated that our source emits 1.5-4.9 mJ/sr per pulse at 13.5 nm when input electrical energy is around 8 J. Typical in-band (13.5 nm) energy radiated by the only xenon filled Z-pinch is around 0.15 mJ/sr/shot for 2.5 J input energy, and the conversion efficiency is 0.4%. At present, 0.5% in-band (13.5 nm) conversion efficiency is achieved. The improved in-band conversion efficiency, in present set-up with tin target plus xenon as background gas, is due to tin vapor contributing to EUV emission.

4. CONCLUSION

The experimental results presented in this paper have shown the conversion efficiency from electrical energy to energy radiated at 13.5 nm was improved with tin target plus xenon as background gas in comparing with xenon gas only. The spectra exhibits tin target produced intense flux of photons at 13.5 nm. Tin vapor, including both atoms and ions, is produced by the ablation of a solid tin rod (6 mm diameter) by the energy flux from the plasma. The magnitude of the EUV emission depends on the distance between the plasma and the rod surface (~ tens of mm) and on the pulse repetition rate of the discharge (< 200 Hz). Further optimization potential is given by a better matching of

the current pulse to the pinch plasma load thus achieving better plasma conditions for radiating in the spectral range of interest.

5. REFERENCES

[1] Gerard O'Sullivan, EUVL Source Workshop, Antwerp 2003; available at *www.sematech.org*.

[2] Winnie Svendsen and Gerard O'Sullivan, Statistics and characteristics of xuv transition arrays from laser-produced plasmas of the elements tin through iodine, *Phys. Rev.* A 50, 3710, 1994.

[3] W. T. Silfvast, Intense EUV incoherent plasma sources for EUV lithography and other applications, *IEEE Journal of Quantum Electronics*, Vol. 35, pp. 700-708, May 1999

[4] E.R. Kieft, J. van der Mullen and G.M.W. Kroesen, Time-resolved pinhole camera imaging and extreme ultraviolet spectrometry on a hollow cathode discharge in xenon, *Physical Review E*, 68, 056403, 2003

[5] S. Katsuki, A. Kimura, A. Hongo, T. Sakugawa and H. Akiyama, Z-pinch EUV source driven by 100 ns current pulses, *Proc. Of the 2nd EUVL Symposium*, Antwerp, Belgium, 2003

[6] R. Lebert, K. Bergmann, G. Schriever and W. Neff, A gas discharged based radition source for EUV-lithography, *Microelectronic Enginering*, Vol. 46, pp. 449-452, 1999

[7] Masnavi Majid, Nakajima Mitsuo and Horioka Kazuhiko, Influence of nonequilibrium ionization process on the efficiency of a plasma discharge xenon source, *J. Plasma Fusion res.* Vol. 79, No. 11, pp. 1138-1192, 2003

[8] S.R. Mohanty, E. Robert, R. Dussart, R. Viladrosa, J.-M. Pouvesle, C. Fleurier, C. Cachoncinlle, A novel fast capillary discharge system emitting intense EUV radiation possible source for EUV lithography, *Microelectronic Enginering*, Vol. 65, pp. 47-59, 2003

EUV Emission from Sn Z-Pinch Plasma

Y. Yamaguchi and K. Takasugi

College of Science and Technology, Nihon University
1-8-14 Kanda-surugadai, Chiyoda-ku, Tokyo 101-8308, JAPAN

Sn z-pinch discharge was carried out for EUV emission experiment. The emission from Sn ion at the wavelength 13.5 nm was observed. The use of gold mirror was proved to be effective for the protection of the grating. The pinch time, the pinch current and the intensity of EUV emission increased with the delay time of discharge from gas-puff up to 0.35 ms.

Keywords: z-pinch, EUV, Sn, spectroscopy, gold mirror

I. Introduction

Z-pinch is an efficient system for generating high temperature and high density plasma.[1] Strong radiation from visible light to soft x-ray region comes out of z-pinch plasma. Hot spots are generated on the axis of the pinch column, and x-ray spectroscopy shows that the electron temperature of those spots is nearly 1 keV.[2]

Recently, EUV light source at the wavelength of 13.5 nm is strongly demanded for the next generation semiconductor lithography. The development of the light source using Xe or Sn has been undergoing. In the gas-puff z-pinch experiment EUV radiation from electrode material has been observed,[3] and this implies possibility for new source of radiation. In this experiment we have examined the possibility of producing metal plasma by the choice of electrode materials.

As we have experience on Ar gas-puff z-pinch, the EUV emission from highly ionized Ar ions can be used for calibration of EUV spectroscopy. We have also tried a gold mirror for protecting the grating.

II. Experimental Setup

Schematic diagram of the SHOTGUN z-pinch device is shown in Fig. 1. The storage section consists of 24 μF fast capacitor bank which is charged up to 25 kV (7.5 kJ). Plasma opening switch (POS) section has been installed for discharge current control experiment. Due to this section, the peak current is limited to about 200 kA. Pressurized gas is injected through a hollow nozzle mounted on the anode. The plenum pressure is 0.5 MPa in the experiment. The cathode has many holes in order to prevent stagnation of gas. The spacing between the electrodes is 30 mm. The anode is made of Sn in order to utilize electrode metal for EUV emission.

Rogowski coils are used for the measurement of discharge currents. The anode coil measures the input current from the power supply, and the cathode coil measures the current that flows between the electrodes.

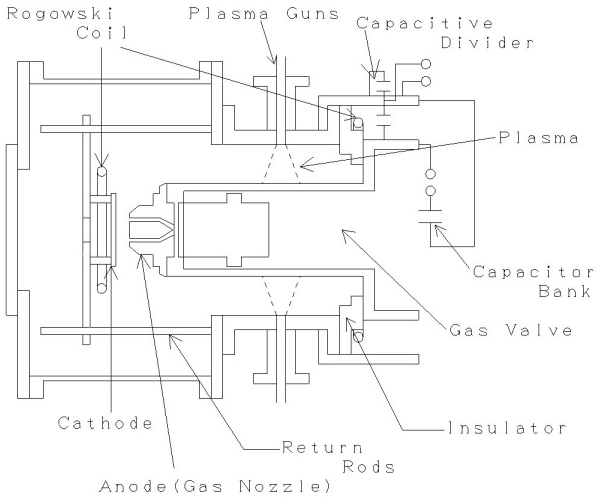

Fig. 1 Schematic diagram of the SHOTGUN z-pinch device. The POS section is attached for discharge current control experiment.

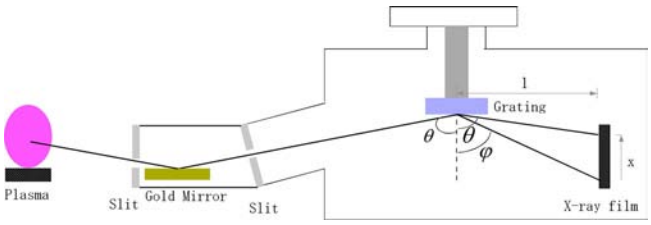

Fig. 2 Schematic diagram of the grazing incidence spectrograph. A gold mirror is installed for the protection of the grating.

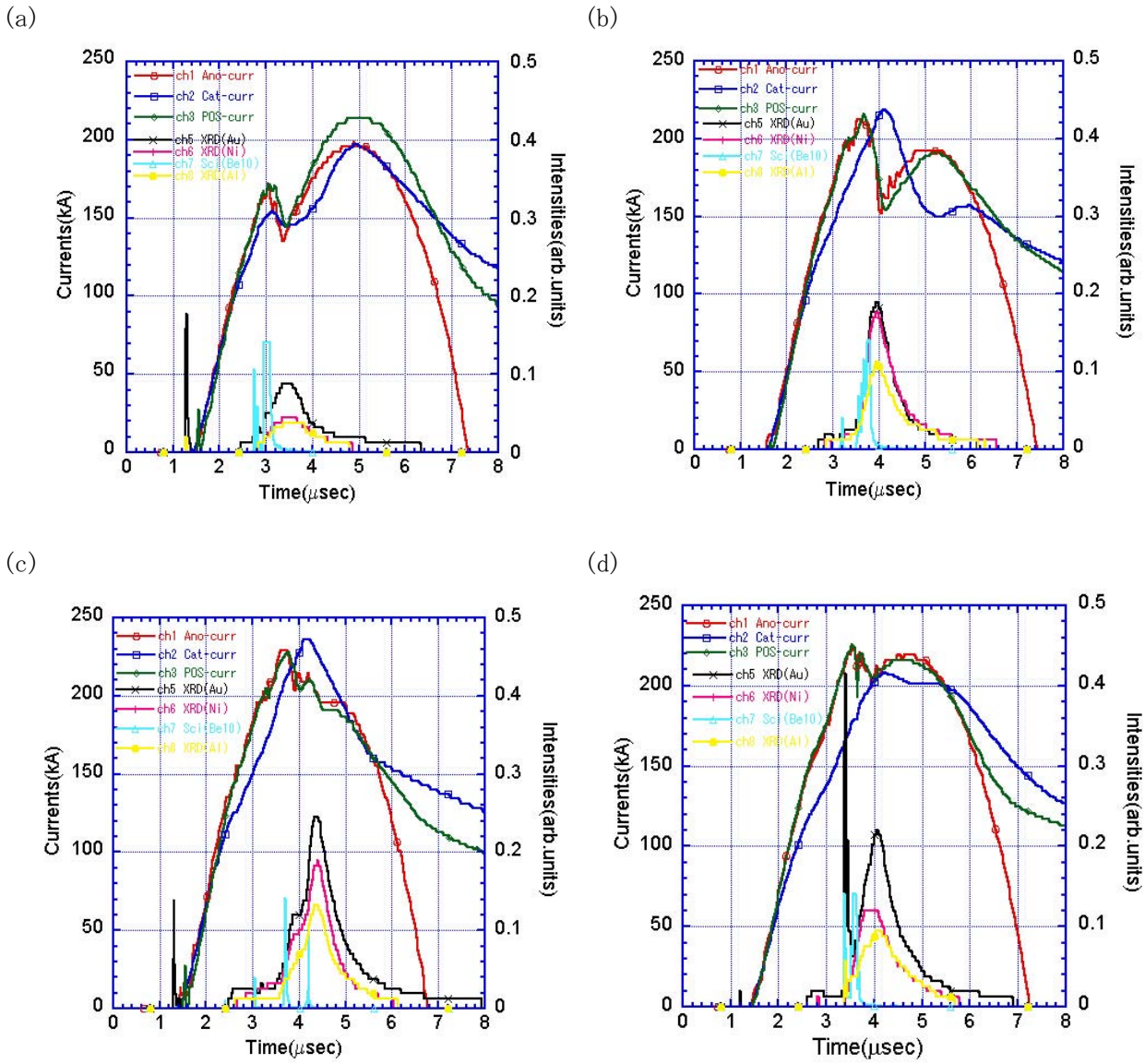

Fig. 3 Current waveforms, EUV and soft x-ray signals of the z-pinch plasma at (a) τ_d = 0.25 ms , (b) τ_d = 0.3 ms, (c) τ_d = 0.35 ms and (d) τ_d = 0.38 ms.

A scintillation probe is used to detect time dependent signal of soft x-ray emitted from the plasma. The probe is filtered by a 10 μm Be window, and it is sensitive to x-ray whose energy is above 1 keV. The EUV light emitted from the plasma is detected by an x-ray diode (XRD) with Al photocathode. The sensitive range of XRD is spreading from UV to soft x-ray (1 – 100 nm). The XRD signal mainly shows L-shell and M-shell radiations of Ar ions.

A glazing incidence spectrometer is used for the measurement of EUV light. The grating has the groove density 1200 lines/mm, and it is coated by Au. The spectrometer is designed at the incident angle θ = 87°. The distance between the grating and the film is 235 mm. Kodak BioMax-MS film is used for recording EUV spectra. Since there is no filter between the plasma and the grating, a gold mirror is attached for protecting the grating from sputtering. (Fig. 2) The available range of EUV light in the spectrometer is 4 - 20 nm.

III. Discharge Characteristics

Delay time of discharge from gas-puff is an important parameter of the gas-puff z-pinch. Gas pressure between the electrodes increases monotonically with the delay time. Figure 3 shows discharge current waveforms, XRD and scintillation probe signals. (a) At the delay time τ_d = 0.25 ms maximum pinch occurs at time 3.4 μs. A dip is formed in the current waveform, and XRD signal is observed.

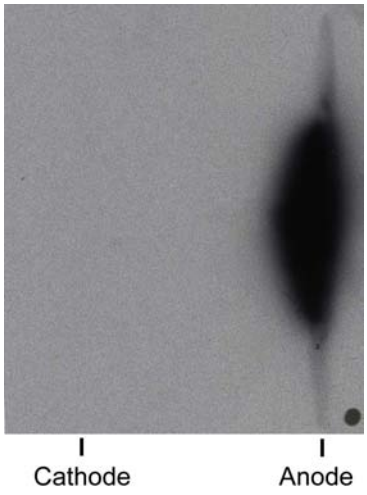

Fig. 4 Soft x-ray pinhole photograph of the z-pinch plasma. Intense soft x-ray is emitted from the surface of anode.

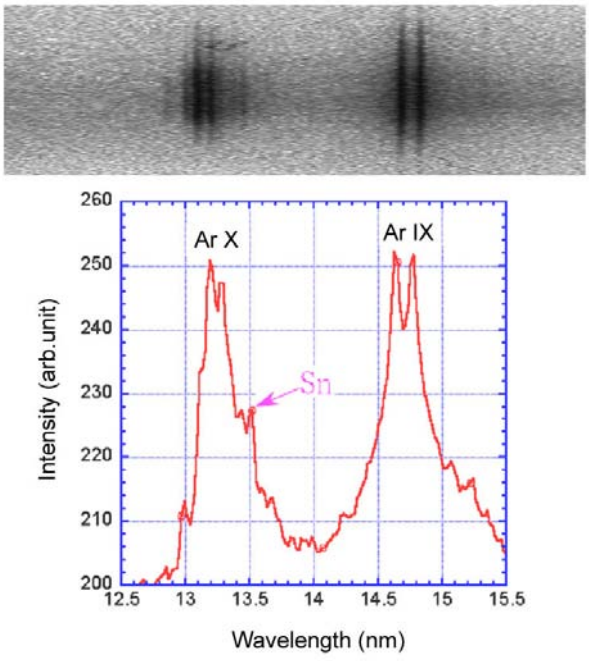

Fig. 5 EUV spectrum of He z-pinch plasma with Sn electrode. The spectrum is superposed on the Ar z-pinch spectra.

Soft x-ray signal is not coincident with the pinch. Soft x-ray pulses are detected prior to the pinch. (b) At τ_d = 0.3 ms the pinch occurs at time 4.0 μs. The maximum plasma current is about 200 kA. The cathode current is a little different from the anode current. The difference indicates some leakage of discharge current. (c) At τ_d = 0.35 ms the pinch occurs at time 4.4 μs, but the current dip is not clear. The XRD signal is most intense at this delay time. (d) The signal becomes a little small at τ_d = 0.38 ms. The difference in the currents becomes large.

IV. Soft X-Ray and EUV Radiation

A soft x-ray pinhole photograph of typical z-pinch discharges is shown in Fig. 4. Intense soft x-ray is emitted from the surface of anode. The soft x-ray is thought to be L-shell radiation of Sn ions. The soft x-ray is emitted in the burst before maximum pinch.

EUV spectra of Sn z-pinch plasma were measured by a grazing incidence spectrometer. As we have experience on the spectroscopy of Ar gas-puff z-pinch, Ar discharge was used for wavelength calibration of EUV spectroscopy. Figure 5 shows the Sn spectrum superposed on the Ar z-pinch spectra. Intense lines at 4.33 – 4.50 nm are Ar X, and lines at 4.87 – 4.92 nm are Ar IX. The observation is third order reflection of the grating. The weak line observed at 13.5 nm is the emission from Sn ions.

Figure 6 shows the spectrogram of He z-pinch plasma with Sn electrode. The data is exposed over 15 shots. The Sn spectrum at 13.5 nm is observed.

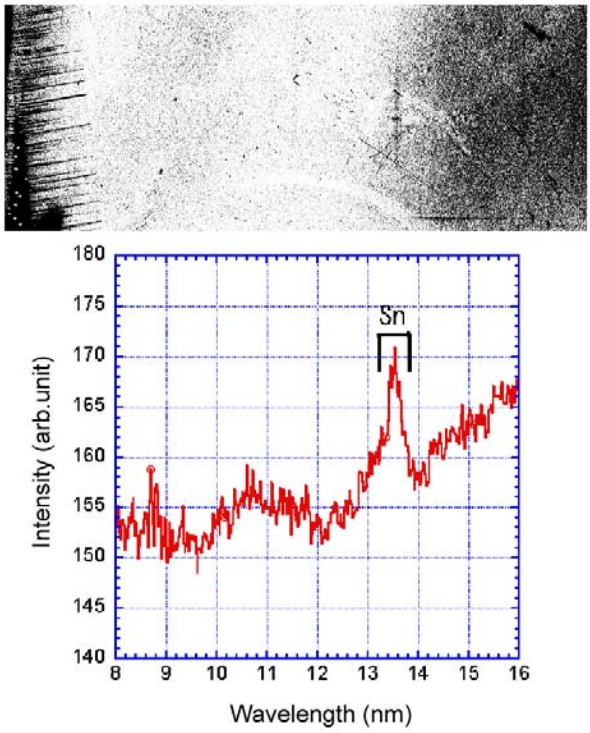

Fig. 6 EUV spectrum of He z-pinch plasma with Sn electrode.

V. Summary and Discussion

Sn z-pinch experiment has been conducted using He gas-puff z-pinch with Sn electrode. The use of gold mirror for grazing incidence spectroscopy was proved to be effective for the protection of the grating. Sn vapor and Sn ions are generated on the surface of anode, and EUV emission at the wavelength of 13.5 nm was observed.

As is common to the gas-puff z-pinch, pinch time and pinch current increased with the delay time τ_d up to 0.35 ms. Input energy of contracting z-pinch is roughly proportional to square of the current. This mechanism helps increasing in the intensity of EUV radiation.

References

[1] K. Takasugi, H. Suzuki, K. Morioka and T. Miyamoto: Jpn. J. Appl. Phys. **35**, 4051 (1996).

[2] K. Takasugi and H. Akiyama: Jpn. J. Appl. Phys. **43**, 6376 (2004).

[3] F. Kobayashi and K. Takasugi: NIFS-PROC-54, 70 (2003).

Performance of soft x-ray laser pumped by capillary discharge

Yusuke Sakai, Yuji Kakuya, Yifan Xiao, Hiroaki Taniguchi, Yasushi Hayashi, *Hamid Ghomi,
Masato Watanabe, Akitoshi Okino, Kazuhiko Horioka, and Eiki Hotta

Department of Energy Sciences, Tokyo Institute of Technology, Nagatsuta, Midori-ku, Yokohama 226-8502, Japan.
*Laser Research Institute, Shahid Beheshti University, Evin, 19839 Tehran, Islamic Republic of Iran

Abstract

We report the output characteristics of capillary discharge single-pass 46.9 nm Ne-like Ar soft-X-ray laser generated by a capillary z-pinch discharge. The coherence properties of the laser have shown to be improved with the increase of the length of laser amplifier from 20 up to 35 cm. The high degree of the spatial coherence of the laser beam produced by 35 cm long capillary is demonstrated by the results obtained in a classical Young's double-slit experiments. We found that the coherence length of the laser is 50 μm. For the 20 cm-long capillary, the diameter of a laser beam is in a range from 3.2 to 4.0 mm, which is corresponding to a range of divergence from 2.2 to 2.8 mrad. Finally, we introduce two spikes on X-ray diode (XRD) signal observed in a single shot.

KEYWORDS: capillary discharge, Z-pinch, soft X-ray laser, spatial coherence, coherence length, beam spot size, beam divergence.

1. Introduction

A laser has some excellent properties such as monochromaticity, high intensity, and coherency. These characteristics have made the laser more attractive than an ordinary light. For a soft X-ray laser, especially, its short wavelength enables material manipulations at molecular level. This has attracted great research interests in producing soft X-ray sources, because the above-mentioned properties have been urgently expected by some pioneering scientific application, such as biotechnology, X-ray holography, X-ray microscopy, and the diagnostics of dense plasma [1,2,3,4]. However, the excitation power for such soft X-ray lasing follows a 4.5 power rule of the lasing frequency. Producing an intense laser of shorter wavelength will therefore require a device of extremely large scale such as synchrotrons, which usually leads to high cost.

A novel table-top soft X-ray source, which is using Z-pinch plasma produced by capillary discharge, has been proposed. It is capable of generating high output laser, repeatable in operation and, most importantly, compact in size and low in cost. The process in generation of Ne-like Ar soft X-ray laser is as follows. Once discharge current pulse of ~30 kA is applied to the capillary filled with preionized argon gas, a plasma column is formed with an electron temperature of 60-80 eV and an electron density of $0.2\text{-}2\times10^{19}$ cm^{-3} due to the Z-pinch compression, which results in the generation of the population inversion for the 3p-3s transition that is required for the Ne-like Ar lasing. In 1995, Rocca *et al* demonstrated the lasing of Ne-like Ar soft-X-ray laser (3p-3s transition, wavelength is 46.9 nm) by the above-mentioned method, using a capillary with inner diameter of 3-4 mm and argon gas pressure of 6-100 Pa [5]. A spike in XRD output signal similar to Rocca's has been observed and reported in our previous works [6,7], which has been proven as Ne-like Ar lasing (J=0-1, μ=46.9 nm) by spectroscopy [8]. In this paper, we have evaluated the characteristics of the Ne-like Ar soft-X-ray laser, such as spatial coherence and divergence. We found that the coherence of the laser were improved by increasing the length of capillary discharge plasma from 20 up to 35 cm. High degree of spatial coherence of the laser beam produced by 35 cm long capillary has been demonstrated. A convenient measuring method for the divergence of the laser beam has been proposed. And we found two spikes on XRD signal in a single shot using a 35 cm-long capillary.

2. Experiment setup

The device used in this experiment is schematically shown in Fig. 1. We used a capillary with an inner diameter of 3 mm and a length of 200 mm or 350 mm, which is made of Al_2O_3 ceramics to reduce the degree of ablation from the inner wall.

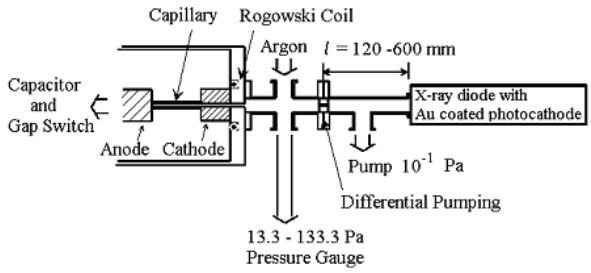

Fig. 1. Schematic diagram of the experimental apparatus

The discharge system is driven by a pulsed power supply as shown in Fig. 2, which consists of a 3-stage Marx generator, a 2:28 step-up transformer and a pulse-forming line (PFL) made of a water capacitor. The impedance of the PFL is 5.5Ω. The gas in a capillary is predischarged by a current of ~20 A, which is provided by a separate circuit. The maximum output voltage of the Marx generator is 60 kV, which subsequently yields a

PFL output voltage of 430 kV. With this power supply system, it is able to obtain a discharge current pulse up to 32 kA. In this experiment, the system is operated at 1 pulse per minute. The time evolution of laser output power is detected by an X-ray diode (XRD). The XRD used is schematically shown in Fig. 3. The photocathode is made of gold, which enables a sensitive detection of X-ray from 10 to 100 eV [9]. In order to reduce the noise from the background radiation and the reabsorption of laser light by the neutral argon gas between the end of capillary and the XRD, a pinhole of 1 mm in diameter is located at a distance of 15 mm from the end of the capillary and the section between them is differentially pumped. The distance between the pinhole and the XRD is adjustable in order to obtain a qualitive indication of the directivity of the laser. A negative bias voltage of 800 V is applied to the photocathode of the XRD with respect to its mesh anode, and they are separated by a distance of 2 mm. When a laser spot has an diameter of 2 mm, the output of XRD is estimated to saturate at a current of 0.45 A, which corresponds to an output voltage of 22.5 V.

3. Experimental results

3.1 Beam divergence

As shown in Fig. 3, an aperture of 4 mm in diameter has been adapted in front of the mesh anode to eliminate the background radiation. The XRD is located at a distance of 72 cm from the end of the capillary. A bellows is adapted at the upstream end of the drift tube, which enables adjustment of the location of the XRD without breaking vacuum. Two series of the experiments have been conducted to measure the beam size of the SXR laser by changing the location of the XRD horizontally (x direction) and vertically (y direction), where the center of the beam is set initially in the vicinity of the origin of coordinates. Fig.4 (a) shows the XRD output measured by changing the location of the XRD horizontally. The laser signal is observed in a range from –4.0 to 4.0 mm, which corresponds to a range of 8.0 mm and is relatively symmetrical with respect to the center of the beam axis. This indicates that the beam spot has a diameter of 4.0 mm, since the aperture radius of 2 mm has to be subtracted from both sides. Fig.4 (b) shows the plots of the results measured by changing the position of the XRD vertically. It is seen that the axial symmetry in vertical direction becomes worse than that in horizontal direction. The laser signal is observed in a range of 7.2 mm from –3.2 to 4.0 mm, which corresponds to a beam size of 3.2 mm. This result indicates that the cross section of the beam is not circular and its diameter varies from 4.0 to 3.2 mm. The range of the beam diameter obtained above corresponds to a range of beam divergence from 2.2 to 2.8 mrad. However, we cannot obtain the beam diameter from the full width at half maximum of the beam intensity because it is not possible to obtain the radial distribution of laser intensity. Efforts will be made in the future to reduce the diameter of the aperture or use a slit for deducing the laser beam diameter.

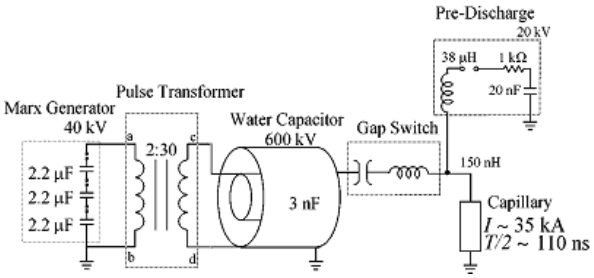

Fig. 2. The power supply system

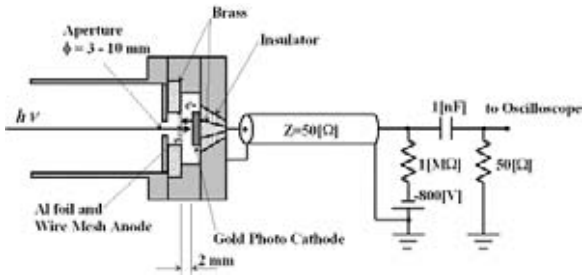

Fig. 3. Schematic diagram of the X-ray diode

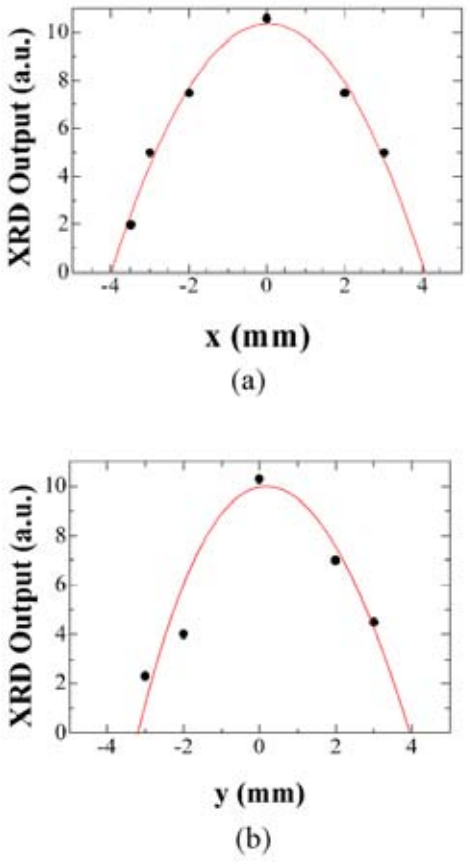

Fig.4. XRD output measured by changing the position of XRD horizontally (a) and vertically (b).

3.2 Spatial coherence

Schematic diagram of classical Young's double slit experiment using a tungsten wire is shown in Fig.5. In this experiment, we have used a cylindrical thin tungsten wire with a diameter of 50 μm or 100 μm. Double-slit interference fringe pattern of the laser was detected by an X-ray CCD camera having 1024×1024 pixels and 13 μm pixel size. We used also an Al filter with a thickness of 0.8 μm to reduce the intensity of laser and cut off the background radiation. Distance between the double-slit and the X-ray CCD is 580 mm or 1070 mm as shown in Fig.5. From Fig.6 (a) and (b) it is shown that the coherence of the laser is improved with increasing the length of lasing medium from 20 cm up to 35 cm. This indicates that the aspect ratio of the plasma column has been increased and only the central part of the laser, which has a good spatial coherence without being refracted by electron density antiguiding, can reach the wire double-slit[10,11].

Comparing interference fringe pattern of Fig.6 and 7, we can see that the contrast of interference fringes becomes more distinct with increasing distance between the double-slit and the screen, from 580 mm to 1070 mm because the intervals of interference fringes are larger. From the interference fringes shown in Fig.7 (a) and (b), which are obtained by using a wire with a diameter of 50 μm and 100 μm, respectively, we have confirmed that the wavelength of the laser is 46 ± 0.9 nm and 46 ± 1.2 nm. The result is in good agreement with the wavelength of Ne-like Ar soft-X-ray laser (3p-3s transition, 46.9 nm). And the coherence length[12] of the laser is obtained to be 50 μm.

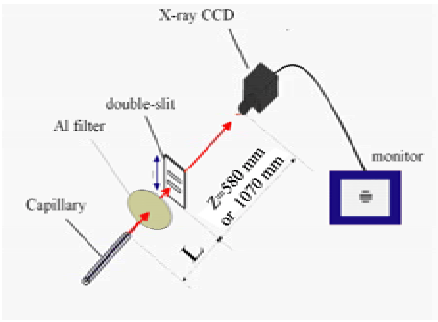

Fig.5 Schematic diagram of Young`s double slit experiment using tungsten wire.

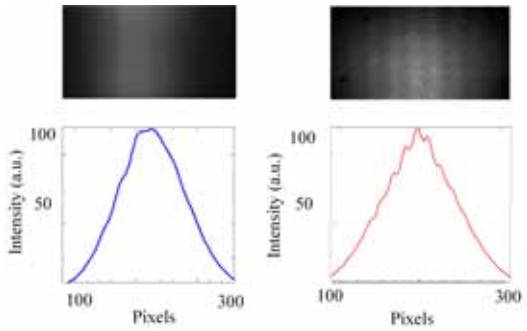

Fig.6 Interference fringes observed with a wire double-slit (wire diameter = 50 μm) using (a): 20cm or (b): 35 cm-long capillary. Distance between double-slit and X-ray CCD camera is 580 mm.

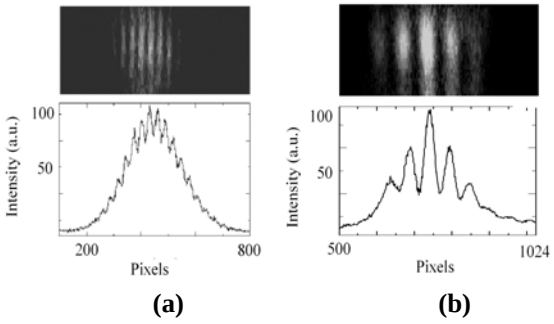

Fig.7. Interference fringes obtained by a wire double-slit ((a): wire diameter = 50 μm, (b): wire diameter = 100 μm) using a 35 cm-long capillary. Distance between double-slit and X-ray CCD camera is 1070 mm.

3.3 Two spike of XRD

Using a capillary with a length of 35 cm, we sometimes observe two spikes of XRD signals as shown in Fig.8. The second spike is observed about 5 ns later than the first one. According to the report by the group of Czech researchers, there is a possibility to obtain a Be-like Ar 2p-2s transition (λ is 42.6 nm) by recombination excitation. To evaluate the second spike, spectroscopic measurement is needed.

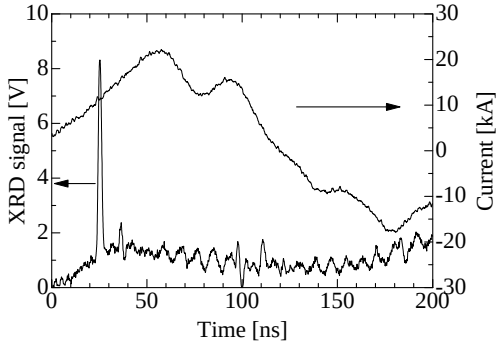

(a) One spike

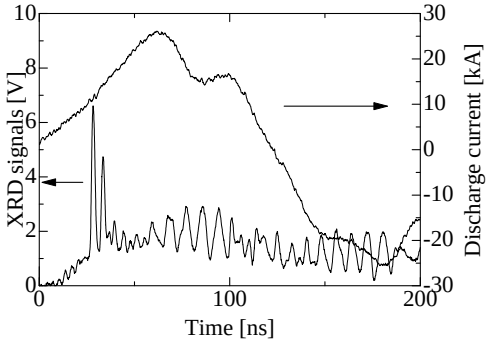

(b) Two spikes

Fig.8 XRD signal from discharge in a 350 mm-long ceramics capillary. (a) : One spike in XRD signal. (b) : Two spikes of XRD signal.

4. Conclusion

We report the output characteristics of capillary discharge single-pass 46.9 nm Ne-like Ar soft-X-ray laser. For the 20 cm-long capillary, divergence of laser beam is measured to be 2.2 to 2.8 mrad. By Young's double slit experiment using a cylindrical tungsten wire, we confirmed that the wavelength of soft-X-ray laser is 46.9 nm. Coherence of the laser has been improved with increasing the length of laser medium from 20 cm up to 35 cm and the coherence length of the laser is found to be 50 μm. Finally we observed two spikes of X-ray diode (XRD) signal in a single shot, which indicates the possibility of lasing by recombination excitation.

Reference

[1] R. C. Elton: "X-ray Laser", Academic Press Inc., USA (1990)

[2] J. E. Trebes, S. B. Brown, D. L. Matthews, D. G. Nilson, G. F. Stone, D. A. Whelan, "First Demonstration of X-ray Holography Using an X-ray Laser", Science, Vol.238, p.517 (1987)

[3] L. B. Da Silva, J. E. Trebes, S. Mrowka, T. W. Barbee, J. Brase, J. A. Koch, R. A. London, B. J. MacGowan, D. L. Matthews, D. Minyard, G. Stone, T. Yorkey, E. Anderson, D. T. Attwood, D. Kern, "Demonstration of x-ray microscopy with an x-ray laser operating near the carbon K edge", Opt. Lett., Vol. 17, p.754 (1992)

[4] L. B. Da Silva, T. W. Barbee, R. Cauble Jr., P. Celliers, D. Ciarlo, S. Libby, R. A. London, C. Matthews, S. Mrowka, J. C. Moreno, D. Ress, J. E. Trebes, A. S. Wan, and F. Webwe, "Electron Density Measurements of High Density Plasmas Using Soft X-Ray Laser Interferometry", Phys. Rev. Lett., Vol. 74, pp.3991-3994 (1995)

[5] J. J. Rocca, V. Shlyaptsev, F. G. Tomasel, O. D. Cortazar, D. Hartshorn and J. L. A. Chilla,: "Demonstration of a Discharge Pumped Table-Top Soft X-ray Laser", Phys. Rev. Lett.,Vol.73, pp.2192-2195 (1994)

[6] G. Niimi, Y. Hayashi, A. Okino, M. Watanabe, and E. Hotta, "Development of Soft X-Ray Laser Using Capillary Discharge", J. Plasma & Fusion Res., Vol.77, No.12, pp.1239-1248 (2001) (in Japanese)

[7] G. Niimi, Y. Hayashi, N. Sakamoto, M. Nakajima, A. Okino, M. Watanabe, K. Horioka, and E. Hotta,"Development and Characterization of a Low Current Capillary Discharge for X-ray Laser Studies", IEEE Trans. Plasma Sci., Vol.30, pp.616-621 (2001)

[8] Y. Hayashi, Y. Xiao, N. Sakamoto, H. Miyahara, G. Niimi, M. Watanabe, A. Okino, K. Horioka, and E. Hotta, "Performances of Ne-like Ar Soft X-ray Laser using Capillary Z-Pinch Discharge", Jpn. J. Appl. Phys., Vol.42, pp.5285-5289 (2001)

[9] R. B. Cairns and J. A. R. Samson, "Metal Photocathodes as Secondary Standards for Absolute Intensity Measurements in the Vacuum Ultraviolet", J. OPT. SOC. AME., Vol.56, pp.1568-1573 (1966)

[10] Y. Liu, M. Seminario, F. G. Tomasel, C. Chang, J. J. Rocca, D. T. Attwood, "Achievement of essentially full spatial coherence in a high-average-power soft-x-ray laser", Physical Review A. Atomic, Molecular, and Optical Physics, Vol.63, No.3, pp.33802 (2001)

[11] Richard A. London, Moshe Strauss, and Mordecai D. Rosen, "Modal analysis of x-ray laser coherence", Phys. Rev. Lett., Vol.65, pp.563–566 (1990)

[12] M. Born and E. Wolf, "Principles of Optics", 7th ed., Cambridge University Press, Cambridge (1999)

Rail Gap Switch Using Porous Metal as Electrode with UV Irradiation

Seizo FURUYA, Tatsuya NODA, Saburo TAKANO and Juichi IRISAWA
Department of Electrical Engineering, Nagaoka University of Technology,
1603-1 Kamitomioka, Nagaoka, Niigata 940-2188, Japan

For multichannel gap switches, the shorter the formative and statistical time lags of each gap, the larger the number of arc channels. As we examined the breakdown characteristics of a sphere/plane gap using a mirror-finished brass plate and a porous metal as plane electrodes, we confirmed that formative and statistical time lags decrease when porous metals are used as a discharge electrode, so we expect that the number of arc channels increases when porous metal is used as one of the electrodes of a rail gap. We have already confirmed that the number of arc channels increases in the case of a gap length of 1 mm when porous metal is used as an electrode. In this report we describe the effect of UV irradiation on the rail gap using a porous metal as electrode.

KEYWORDS: rail gap switch, arc channel, porous metal, ferrite sharpener, UV irradiation

1. Introduction

As for multichannel gap switches, the shorter the formative and statistical time lags of each gap, the larger the number of arc channels. As we examined the breakdown characteristics of a sphere/plane gap using a mirror-finished brass plate and a porous metal as plane electrodes, we confirmed that the formative and statistical time lags decrease when porous metals are used as a discharge electrode[1)], so the number of arc channels of a self-breakdown-type rail gap with a porous metal is expected to increase. Then we compared the results of the rail gap using a mirror-finished brass plate and a porous metal as one of the electrodes of the rail gap[2)]. In the case of a gap length of 1 mm, the number of arc channels increases when porous metal is used as a lower electrode instead of a mirror-finished plate. In this report we describe the effect of UV irradiation on the rail gap using a porous metal as electrode.

2. Experimental Setup

Figures 1(a) and 1(b) show a cylinder/mirror-finished plate gap and a cylinder/porous metal gap, respectively. The upper electrode is a brass cylinder of 18 mm in diameter and the lower electrode is a brass plate of 5 mm in thickness. When the lower electrode was a porous metal, it was placed on the brass plate shown in Fig. 1(b). The active length of the rail gap was 200 mm. The lower electrode was grounded and positive or negative voltage pulses were applied to the upper electrode. The experiments were carried out in air at 1 atm. Figure 2 shows the surface micrograph of the porous metal we used. The porous metal was made of copper and its average pore diameter was 600 μm. Its size was 210 mm long, 40 mm wide and 2 mm thick. It was manufactured by Mitsubishi Materials Corp. UV light source (Hamamatsu Photonics L937-02) was set parallel to the rail gap, as shown in Fig. 3. The distance between the source and the gap was 100 mm.

The rectangular voltage pulses applied to the gap were generated by a 100-cm-long coaxial-type ferrite

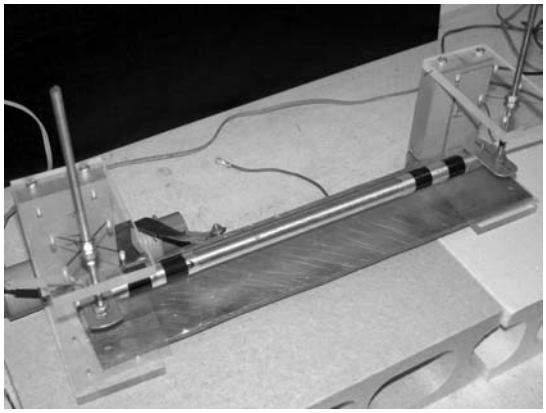

(a) cylinder/mirror-finished plate

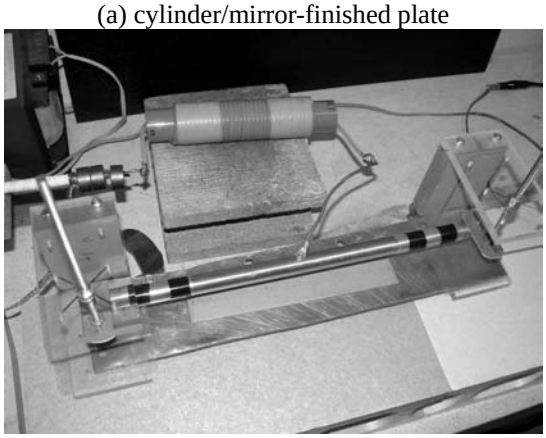

(b) cylinder/porous metal

Fig. 1 Geometry of gap

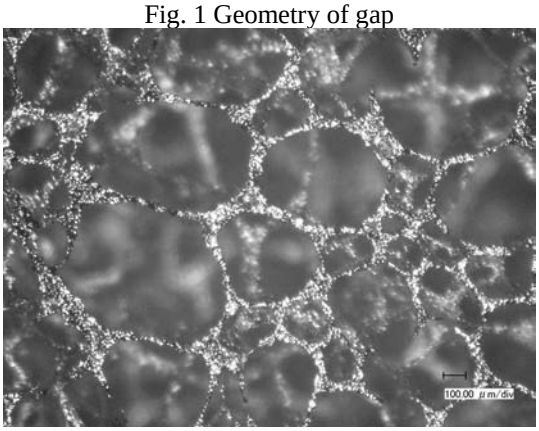

Fig. 2. Surface micrograph of porous metal used

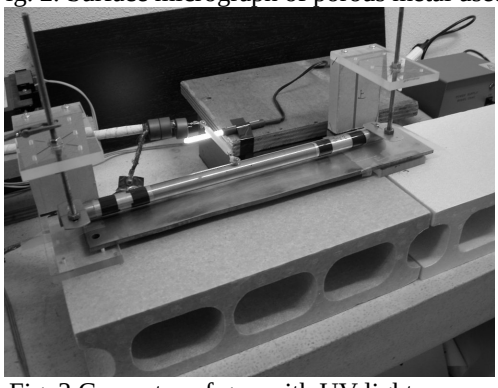

Fig. 3 Geometry of gap with UV light source

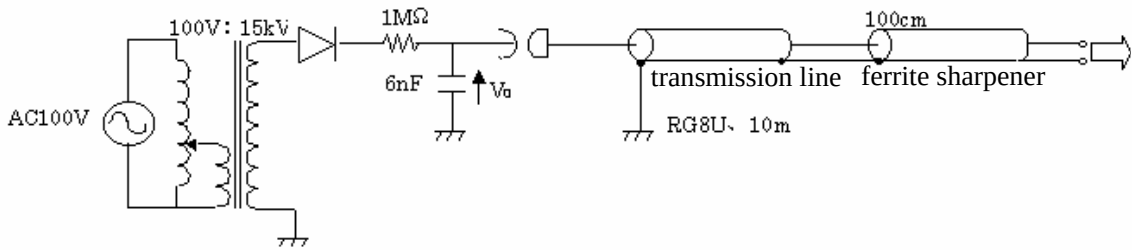

Fig. 4 Electrical circuit to generate pulses applied to gap

sharpener[3,4]. Figure 4 shows the electrical circuit used to generate pulses. The input voltage pulse which has a slow rise time is steepened at the end of the sharpener due to its nonlinear effect. Figures 5(a)-5(c) show the voltage waveforms of the open-ended ferrite sharpener applied to the rail gap. Figure 5(a) shows the waveform when the charging voltage of the capacitor V_0 is +10 kV, Fig. 5(b) +15 kV and Fig. 5(c) +20 kV. The voltages become approximately twofold V_0. Voltages were measured using a Tektronix high-voltage probe (P6015A) and a Hewlett-Packard digital oscilloscope (HP54542A).

The number of arc channels was evaluated by open-shutter photographs of a digital camera. Under each condition 10 shots were performed.

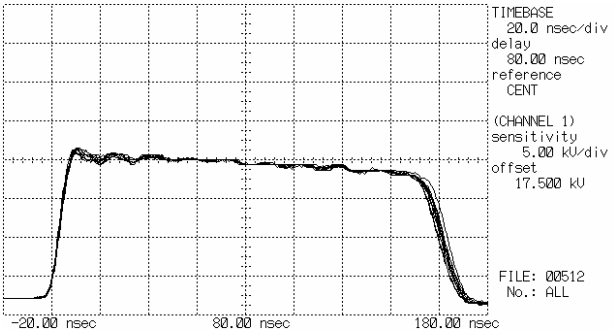

(a) V_0 is +10 kV

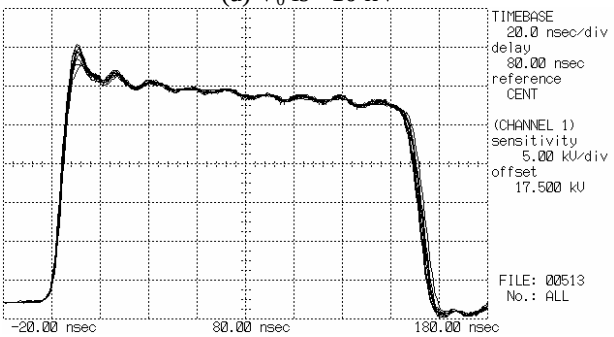

(b) +15 kV

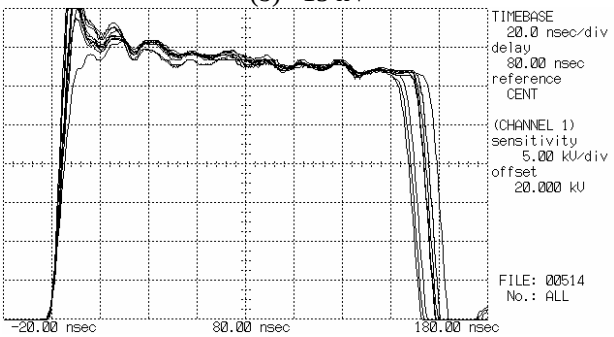

(c) +20 kV

Fig. 5 Voltage waveforms of open-ended sharpener

3. Experimental Results and Discussion

Figure 6(a) shows an example of a discharge photograph with UV irradiation. The lower electrode is porous metal and the charging voltage of the capacitor V_0 is +20 kV. The gap length of the rail gap is 1 mm. As shown in the figure, 3 arc channels were generated. Figure 6(b) shows another example of a discharge photograph with UV irradiation. The lower electrode is a mirror-finished plate and V_0 is +20 kV. The gap length of the rail gap is 5 mm. In this case, 1 arc channel was generated.

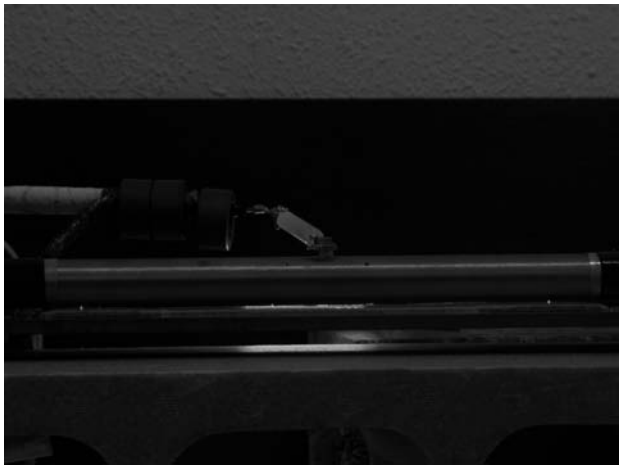
(a) porous metal, +20 kV, 1 mm

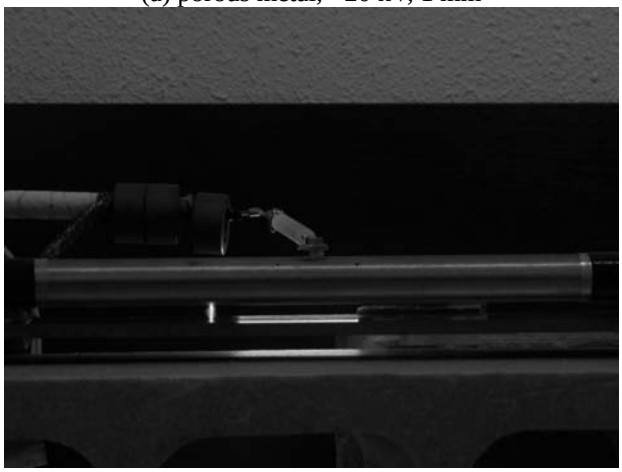
(b) mirror-finished, +20 kV, 5 mm

Fig. 6 Discharge photographs with UV irradiation

Figures 7(a)-7(d) show voltage waveforms with breakdown. The left in each figure shows the waveform without UV irradiation and the right with UV irradiation. Ten shots are superimposed in each figure as 10 shots were performed under each experimental condition. In

the case of a gap length of 1 mm, shown in Figs. 7(a) and 7(b), the breakdown voltage with UV irradiation is smaller than that without UV irradiation. In the case of 5 mm, shown in Figs. 7(c) and 7(d), as for the breakdown voltage and the jitter of breakdown time, a significant difference is not apparent.

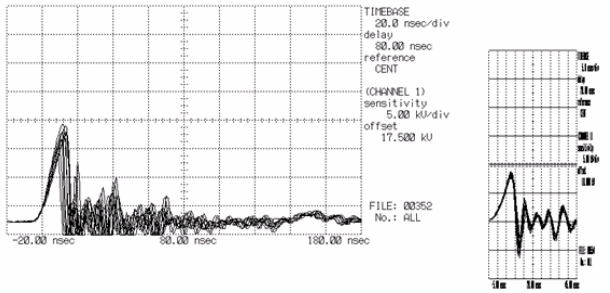

(a) mirror-finished, +10 kV, 1 mm

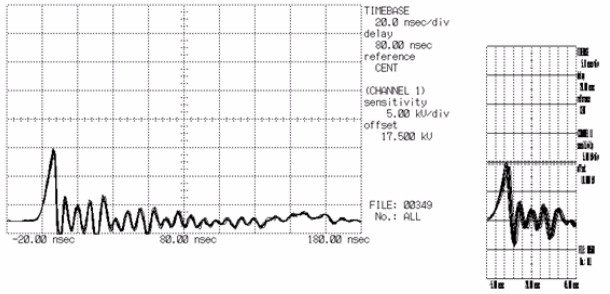

(b) porous metal, +10 kV, 1 mm

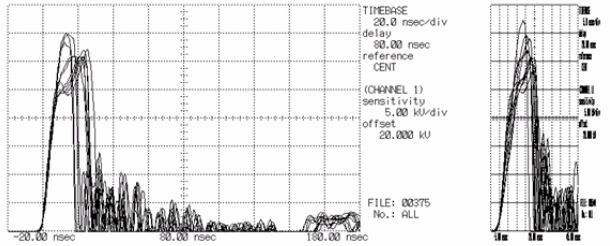

(c) mirror-finished, +20 kV, 5 mm

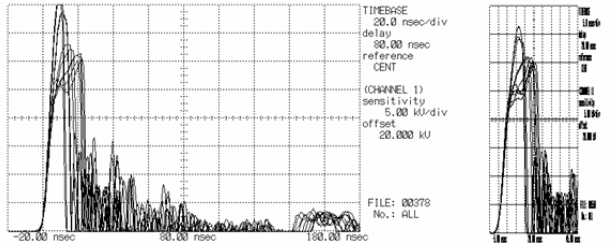

(d) porous metal, +20 kV, 5 mm

Fig. 7 Voltage waveforms with breakdown

Figures 8(a)-8(f) show the number of arc channels when V_0 is changed. In the case of a short gap length, the number of arc channels with UV irradiation increases when the lower electrodes are both a porous metal and mirror-finished plate. In the case of a long gap length, the effect of UV irradiation is small. As for the increase rate of the number of arc channels, a significant difference between the results of the mirror-finished plate and those of the porous metal was not observed.

4. Conclusion

We examined the effect of UV irradiation on the rail gap using a porous metal as electrode. As a result, we obtained the following results.

(1) As for the jitter of breakdown time, a significant difference between the results with and without UV irradiation is not apparent. However, in the case of a short gap length, the breakdown voltage with UV irradiation is smaller than that without UV irradiation.

(2) In the case of a short gap length, the number of arc channels with UV irradiation increases when the lower electrodes are both a porous metal and mirror-finished plate. In the case of a long gap length, the effect of UV irradiation is small.

(3) As for the increase rate of the number of arc channels, a significant difference between the results of the mirror-finished plate and those of the porous metal was not observed.

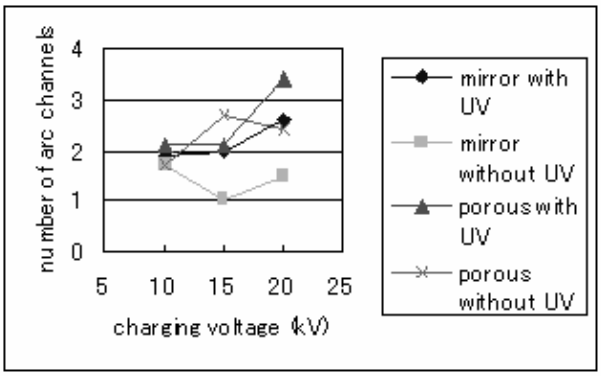

(a) positive, 1mm

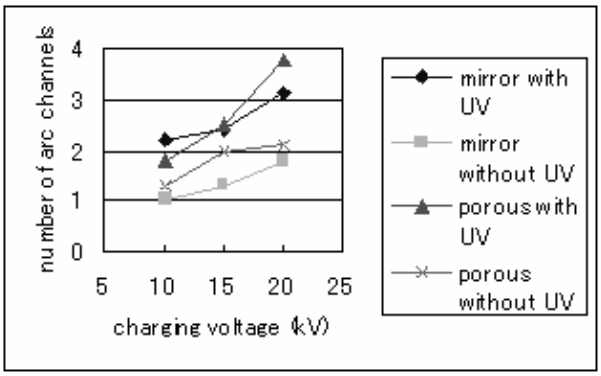

(b) negative, 1mm

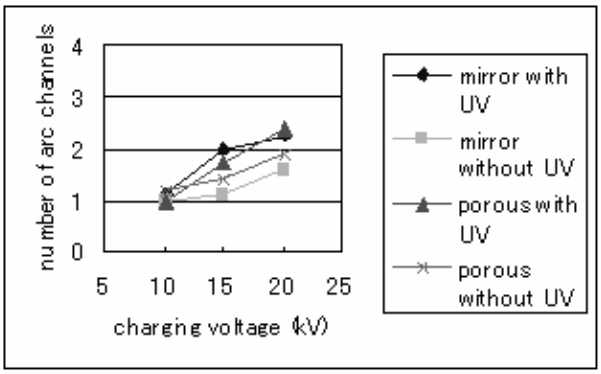

(c) positive, 3mm

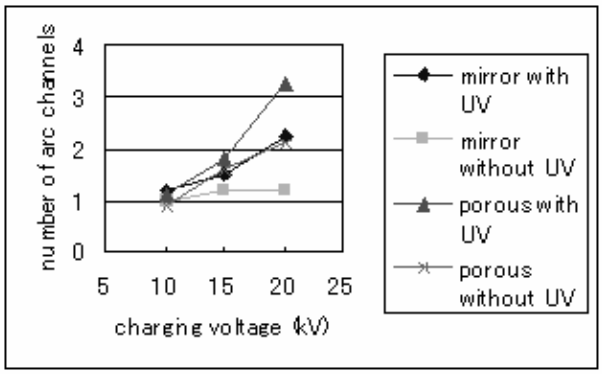

(d) negative, 3mm

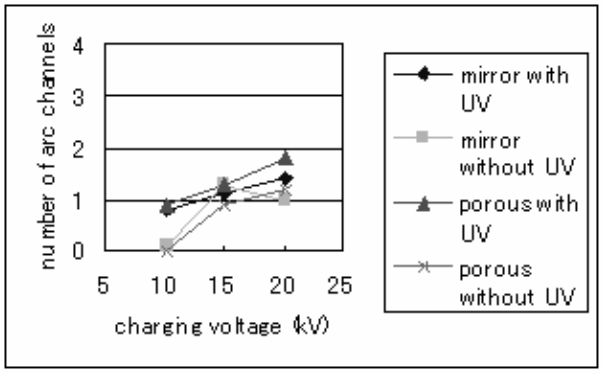

(e) positive, 5mm

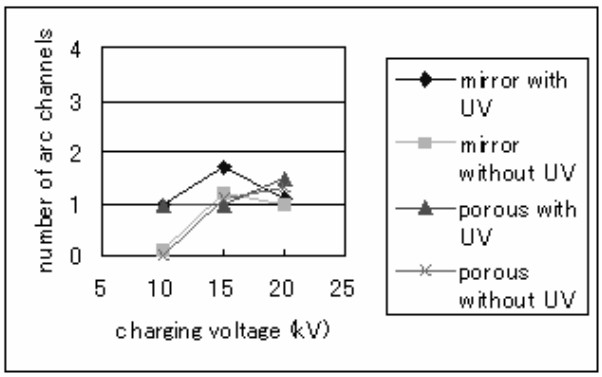

(f) negative, 5mm

Fig. 8 The number of arc channels

References

1) Seizo FURUYA, Saburo TAKANO and Juichi IRISAWA: Breakdown Characteristics of Porous Metals, Jpn. J. Appl. Phys. 43 (2004) 1602
2) Seizo FURUYA, Hiroaki TANAKA, Saburo TAKANO and Juichi IRISAWA: Rail Gap Switch Using Porous Metal as Electrode, Jpn. J. Appl. Phys. 44 (2005) 1422
3) Seizo FURUYA, Haruo MATSUMOTO, Hitoshi FUKUDA, Takao OHBOSHI, Saburo TAKANO and Juichi IRISAWA: Simulation of Nonlinear Coaxial Line Using Ferrite Beads, Jpn. J. Appl. Phys. 41 (2002) 6536
4) Seizo FURUYA, Katsuaki TACHI, Saburo TAKANO and Juichi IRISAWA: Surge Impedance of Nonlinear Coaxial Line Using Ferrite Beads, Jpn. J. Appl. Phys. 43 (2004) 1131

Development of Pulsed Power Generator using Semiconductor Opening Switches

Tomoyuki Yokoo, Hirokazu Honma, Weihua Jiang, and Kiyoshi Yatsui
Extreme Energy-Density Research Institute, Nagaoka University of Technology.
Nagaoka, Niigata 940-2188, Japan

Abstruct

A compact repetitive pulsed power generator with semiconductor opening switch (SOS) has been developed. The generator has been designed to acheve the peak output voltage of over 10 kV with maximum repetition rate of 1 kHz. A pulse compression circuit with a saturabe transformer and an insulated-gate bipolar transistor (IGBT) are employed to operate the SOS. This paper reports the circuit design and its operating characteristics.

Keywords: pulsed power technology, semiconductor opening switch, inductive energy storage

1. Introduction

Pulsed power technology has been widely applied for various fields such as discharge-pumped excimer laser, flue gas treatment, sterilization, and so on.

In typical pulsed power generators, capacitive energy storages and solid-state switches such as power semiconductor devices and saturable magnetic cores are employed to operate at high repetition rate. However, due to the energy transfer time from capacitor to the load depend on time constant RC, this type of generators have difficulty in obtaining shorter output pulse durations on a high impedance load.

The pulsed power generator with inductive energy storage can be realized to output shorter voltage pulse due to the energy transfer time from the inductor to the load depend on time constant L/R. In addition, peak output voltage increases and its rise time decreases if the current interruption time is shortened. Therefore, it is considered that this type of generator is more suitable for discharged load.

In this paper, the development of a compact repetitive pulsed power generator with inductive energy storage and its characteristics are described. The generator employs a semiconductor opening switch (SOS) to obtain a shorter pulse duration and high repetition rate with the inductive energy storage scheme. A pulse compression circuit with saturable transformer and a semiconductor switch (IGBT) are used to operate the SOS.

2. Semiconductor opening switch

An SOS diode[(1)-(2)] is a specially designed semiconductor diode for using as opening switch, which has a semiconductor p^+-p-n-n^+ structure and is fabricated to obtain a super hard reverse recovery under the large reverse current conditions. The SOS diode conducts reverse current during a certain specific time due to the residual carrier in the structure of semiconductor. The residual carriers are provided by the forward current flows through the SOS diode.

When the reverse current flows through the SOS diode, uncompensated holes arises in the p region of structure, due to the drawing of residual carriers. As a result, the voltage across the SOS rapidly increases and the reverse current through the SOS is switched to the load which is connected in parallel. This phenomenon is called SOS-effect.

The SOS-60-4 is employed in the present systems. Its assembly consists of 80 diodes connected in series to achieve a maximum reverse voltage of 60 kV. Fig. 1 shows the photograph of SOS-60-4. Its specifications are listed in Table1. Regardless of the small dimension, the SOS-60-4 is able to conduct large current (up to 4 kV) and is able to interrupt it in very short time (less than 15 ns). Due to the diode recovery time is less than 1 μs, the repetition rate at continuous operation can be as high as 1 kHz and is only limited by the thermal loss at the switching. As seen in Fig. 1, the SOS-60-4 has copper heat sinks to enhance the heat releases from the diodes.

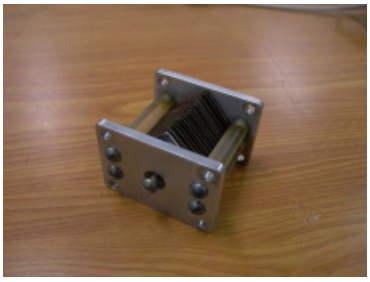

Fig. 1 Photograph of SOS-60-4.

Table 1 Specifications of the SOS-60-4 diode.

Maximum peak reverse voltage	60 kV
Maximum forward pumping current	1 kA
Maximum reverse (cutoff) current	4 kA
Forward pumping time	150-400 ns
Reverse pumping time	40-100 ns
Current interruption time	5-15 ns
Dimension	65×62×44 mm
Mass	~0.2 kg

3. Experimental setup

Our target is to develop a repetitive pulsed power generator for applications to flue-gas treatment. The basic requirements to the generator at output are shown in Table 2. To achieve these output parameters, we have developed a circuit design as shown in Fig. 2. The parameters of the forward current, the reverse current (I_F and I_R as shown in Fig. 2.) and the inductance of the transmission line determine as shown in Table 3

Table 2 Output parameters of generator.

Peak output voltage	≥10 kV
Voltage pulse width	≤100 ns
Repetition rate	1 kHz

Table 3 Circuit parameters.

Transmission line	Current pulse width	Peak current	Total inductance
$C_0 \rightarrow C_1$ (I_0)	1 ms	200 mA	1 H
$C_1 \rightarrow C_2$ (I_F)	1 μs	15 A	4.8 μH
$C_2 \rightarrow C_2$ (I_R)	200 ns	140 A	3.4 μH

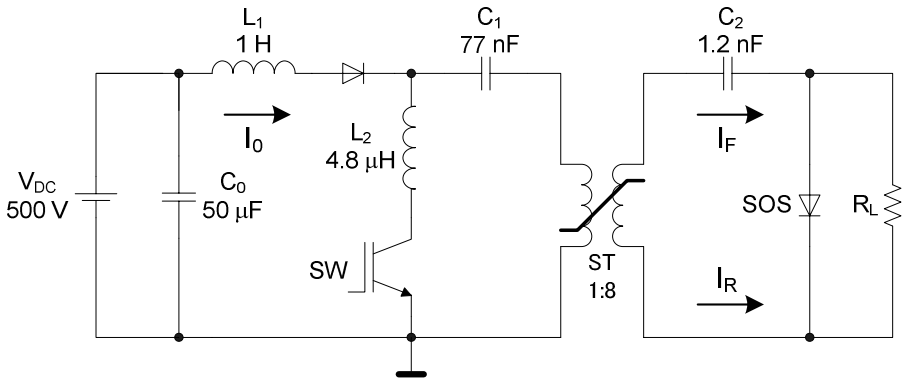

Fig. 2 Circuit diagram.

It is considered that a relatively high cutoff current can be obtained if the reverse current pulse width is shorter than forward current. Therefore, the magnetic pulse compression circuit with a saturable transformer is employed to present systems.

Saturable transformer ST is used to increase the voltage and to isolate the secondary winding from the primary when the charging of C_2 is finished. IGBT is use as an initial switch SW.

A capacitor C_0 is charged by DC power supply. Due to resonance between C_0 and C_1, the C_1 charging voltage is two times higher than the voltage of DC power supply. When the charging of C_1 is finished, it discharges with the triggering of SW. During the discharging of C_1, the ST is unstauration state. Therefore, the electrical energy from capacitor C_1 is transferred via C_1-L_2-ST and C_2 is charged by a resonant current and the voltage is amplified by the ST. The secondary winding current that charges capacitor C_2 flows in forward direction of SOS and injects carriers. When the voltage of C_2 reaches the peak, ST saturates. The C_2 discharging current pulse is compressed, which flows through the SOS as a reverse current. At the same time, the energy from C_2 is transferred to inductance of ST. Finally, due to SOS effect, reverse current is interrupted and then a sharp high voltage pulse switch causes inductive energy arises in the load.

As a inductor of saturable transformer ST, toroidal type magnetic core is used with the winding ratio of 1:8. The saturation period of the specific magnetic core is estimated by the following equation.

$$V_{ST2} \cdot t = n_{ST2} \Delta B S \cdots\cdots\cdots\cdots\cdots\cdots\cdots\cdots \quad (1)$$

where V_{ST2}, t, n_{ST2}, ΔB and S are the voltage across the secondary windings, the period until saturation, the number of secondary windings, the saturation magnetic flux and the cross-section of magnetic core, respectively.

The saturated secondary inductance L_{S-ST2} is estimated by following equation.

$$L_{S-ST2} = \frac{\mu_0}{2\pi} \ln\left(\frac{b}{a}\right) \cdot l \cdot {n_{ST2}}^2 \cdots\cdots\cdots\cdots\cdots\cdots\cdots\cdots (2)$$

where μ_0, a, b and l are space permeability, the inner diameter, the outer diameter and the thickness of the core. The ST has a common reset circuit for allowing full-magnetic flux variation. The reset circuit has a bias

coil of approximately 20 μH to separate it from the generator. The parameters of magnetic core are shown in Table 3.

Table 3. Parameters of saturation transformer ST

Charging voltage V_{ST2}	8 kV
Inner diameter a	0.0763 m
Outer diameter b	0.1013 m
Sickness l	0.0125 m
Cross section S	0.00016 m^2
Number of winding n_{ST2}	16 Turn
Saturation magnetic flux ΔB	1.7 T
$V \cdot t$	0.004 Vs
Saturation time t	1.08 μs
Saturated inductance L_{S-ST2}	217 nH

4. Experimental result

The voltage and current were measured by high voltage probe (Iwatsu Test Instruments corp. HV-P30) and current transformer (Pearson Electronics, LTD. Model 110) respectively. All measured signals were recorded by a digital oscilloscope (Lecroy Corp. WR6030). Due to the relatively low output power of the DC power supply, the test was carried out with burst mode operation (20 shots burst and 2 sec rest period).

Figure 3 shows (a) the capacitor C_1 voltage and (b) secondary winding current waveforms of shorted load. During 1 μs, the peak forward current of 15 A flows in forward direction of SOS, while the capacitor C_2 is charged to approximately 7 kV. The reverse direction current reaches 140 A in 100 ns. The inductance of the circuit C_2-ST-SOS was calculated to be 3.4 μH from Fig. 3(b)

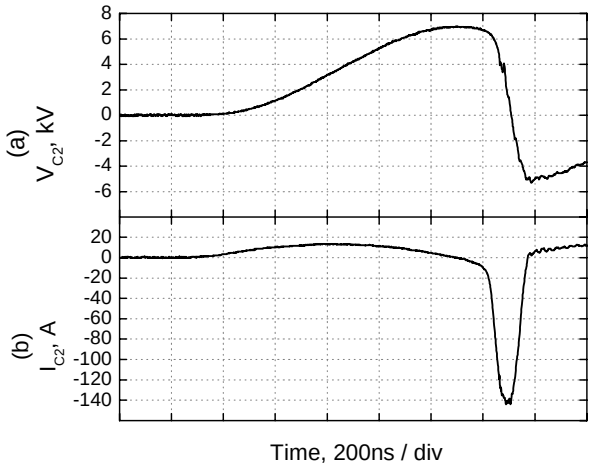

Fig. 3 Wavefirms of (a) capacitor C_2 Voltage and (b) secondary winding current of shorted load

Figure 4 shows (a) the voltage waveform of 200 Ω and (b) the current waveform of SOS. The reverse current reaches 130 A in approximately 100 ns, and then interrupted.This results in voltage with amplitude of 12 kV across the load with pulse width of 100 ns.

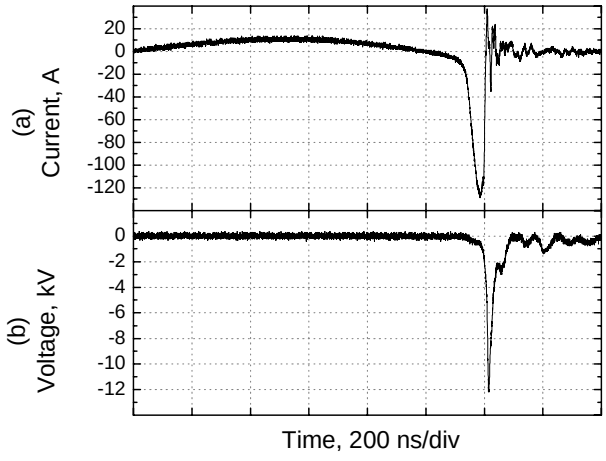

Fig. 4 Wave forms of (a) SOS current and (b) voltage of resistive load of 200 Ω

Figure 5 shows (a) the voltage and current waveforms of the resistive load and (b) output power and total output energy. The load current reaches 40 A.

Output power and total energy were calculated to be 380 kW and 10 mJ respectively.

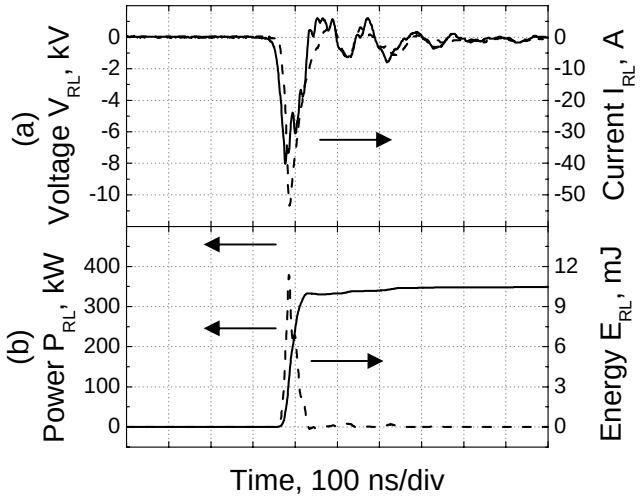

Fig. 5 Waveforms of (a) voltage and current of resistive load of 200 Ω and (b) output power and energy

Shown in Fig. 6 is dependence of the peak output voltage and the total output energy on the load resistance. It is clearly seen that the output voltage is increased if the load resistance is increased, but the output energy decreases correspondingly.

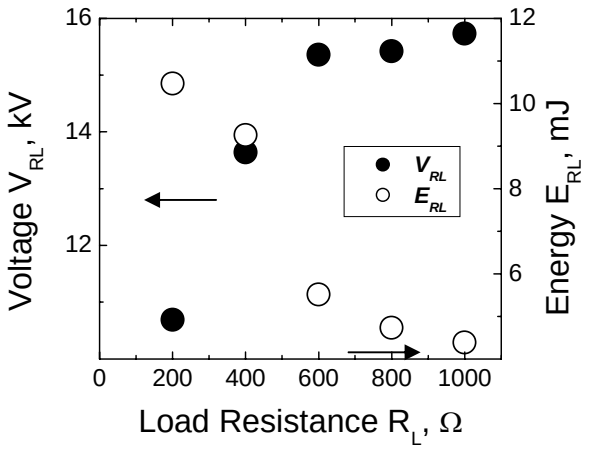

Fig 6. Dependence of the peak output voltage and the total output energy on the load resistance.

Figure 7 shows the dependence of the energy transfer efficiency on the load resistance. The energy transfer efficiency is calculated by following equation

$$\eta = \frac{E_{RL}}{E_{C1}} \times 100 \quad (\%) \cdots\cdots\cdots\cdots\cdots\cdots \quad (3)$$

where, E_{RL} and E_{C1} are the total output energy and the capacitor C_1 stored energy respectively. It is clearly that the energy efficiency from the stored energy in the initial capacitor to the load decreases as the load resistance is increased. In this experiments, the maximum energy efficiency of 27 % is obtained on the resistive load of 200 Ω. It is necessary to optimize the circuit parameters to improve the energy efficiency.

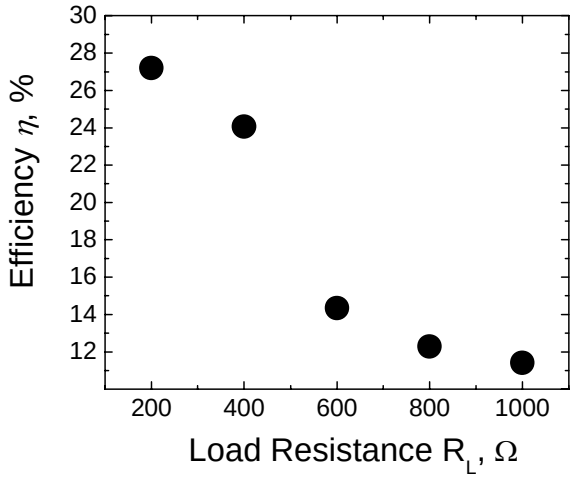

Fig.7 Dependence of the energy transfer efficiency on the load resistance.

Figure 8 shows the voltage waveform of capacitor C_1 when the generator is operated at the repetition rate of 1 kHz The reason to use the C_1 charging voltage waveform to confirm the repetitive operation is that the output pulse is too narrow to be seen in the

time scales of Figs. 8　From this result, it is seen that the generator can operate at 1 kHz in burst mode.

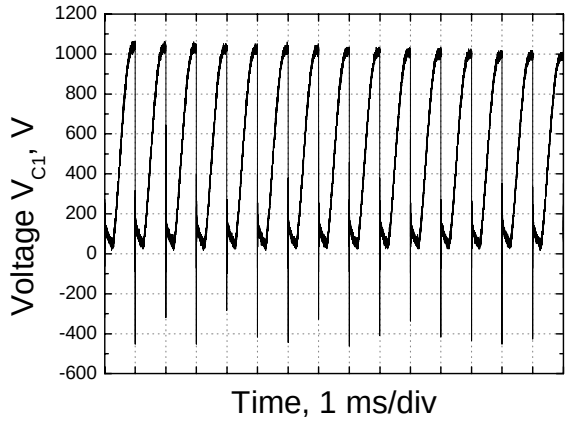

Fig. 8. Waveforms of capacitor C_1 voltage.

5. Conclusion

A compact repetitive pulsed power generator with inductive energy storage has been successfully developed. The design and tests of the generator was carried out, and the following results were obtained.

1) Peak output voltage of ~12 kV on a resistive load of 200 Ω with pulse width of 100 ns were obtained.
2) Load voltage increases and the output energy decreases with incleasing load resistance. The maximum energy transfer efficiency in this experiment is 27%
3) The generator can be operated at the repetitionrate of 1kHz in the burst mode.

References

1) S. N. Rukin, “High-Power Nanosecond Pulse Generator on Semiconductor Opening Switches (Review)”, Instrum and Experimental Techniques Vol. 42, No. 4, pp. 439-467. (1999)
2) W. Jiang, K. Yatsui, K. Takayama, M. Akemoto, E. Nakamura, N. Shimizu, A Tokuchi, S. Rukin, V. Tarasenko and A. Panchenko, “Compact Solid-State Switched Pulsed Power Generator and Its Applications” Proc. of the IEEE. Vol. 92, No. 7, pp. 1180-1196. (2004)

Breaking of Ice using Pulsed Power

Satoshi Ihara and Chobei Yamabe
Department of Electrical and Electronic Engineering,
Faculty of Science and Engineering, Saga University,
1 Honjo-machi Saga 840-8502, Japan
e-mail : iharas@cc.saga-u.ac.jp

ABSTRACT

The breaking of ice using shock waves produced by a pulsed power generator is suggested as a new method for navigation of icebreakers in order to realize the safe and quick navigation in icebound sea. The shock wave can be produced by applying the voltage between the electrodes contacted to an ice sample. The ice breaking by the pulsed power was demonstrated in the tap water experimentally. During the experiments the ice sample was artificially made from pure water. In the salt water with salinity of 3.5 %, the ice sample was not broken according to the results obtained using the cylindrical electrode with flat tip. Using the conical electrode with the sharp-pointed tip, above ice sample was broken. The shockwave caused by the ionized region formed at the tip of conical electrode, and the localized intense stress at crack seem to be the important mechanisms of ice breaking in the salt water.

Keywords : pulsed power, shock wave, ice, icebreaker, icebound sea

1. Introduction

Recently, the development of navigation system for icebreakers on icebound sea has been important for the advancement of the natural resources production. For example, in 1999 in the Northern Sakhalin in the Sea of Okhotsk, the commercial production of crude oil and gas started. At present, production during the winter season is not carried out. Year-round production, including the winter season, during which the Sea of Okhotsk is covered by the sea ice, is planned to start from 2004.[1-3)]

To make possible the navigation in icebound sea, an icebreaker crushes the sea ice using the force generated by the ship's mass. As the ship advances into an unbroken ice field, crushing of ice begins to occur at the point of contact. A specially shaped hull made of high-strength material is required for the design of the icebreaker. Furthermore, in the regions, where the thick ice sheets exist, a navigation time is prolonged because continuous crushing is difficult or even impossible. If the worst comes to the worst, it is possible that the navigation is impossible. Realizing a new method of icebreaking to decrease the disadvantage points above is beneficial to the marine transport and shipbuilding.

In this research, the icebreaking using pulsed power is proposed as a new method for the operation of icebreakers in the icebound sea.[4)] The ice is broken by shock wave produced by the pulsed power. The reasons for using pulsed power are as follows:

(1) The degree of damage to the hull can be significantly decreased.

(2) The continuous breaking can be realized because the pulsed power generator can be operated

repetitively.

The overview of the icebreaking process using the pulsed power is shown in Fig. 1. The pulsed power generator is loaded on the ship, and the electrodes connected to the generator are guided to the ice surface from the bow using an insulated rod with several joints.

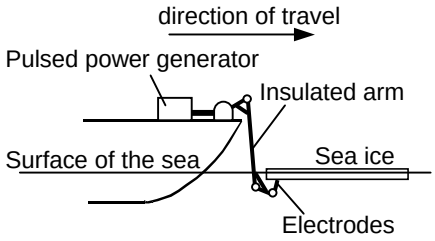

Fig. 1 Overview of the icebreaking process using pulsed power.

The fundamental researches on the destruction of solid materials using the pulsed power were carried out for the development of the new drilling and demolition technologies.[5, 6] On the works described in Ref. 6, the Marx generator was employed as an energy source, and granite was used as a sample of solid material. The rod electrodes were contacted to surface of sample, which was immersed in water. Although the destruction of solid materials such as rocks using the pulsed power was tested in detail until now, there was a lack of the experimental results for breaking of ice. Thus, the demonstration of the breaking of ice and the obtaining of the fundamental data were necessary.

The final purposes of this research are to evaluate the efficiency of ice breaking by pulsed power, and to discuss the usefulness of this method. In order to do that, the demonstration of ice breaking and the discussion of the breaking mechanisms are needed. In this research experiments on breaking of ice are carried out using the pulsed power generator and an ice sample. In these experiments ice samples were made from pure water, placed into a plastic vessel, which was filled with water or salt water. Also the shape of electrode was tested. In this paper, experimental results and mechanisms of breaking are described and discussed.

2. Experimental Apparatus and Method

Figure 2 shows a schematic diagram of the experimental apparatus.[4] A Marx generator, with six capacitors with a capacitance of 0.2 μF, was used as a pulsed power generator. The capacitors of the generator were charged to a negative high voltage, and triggered by an external signal to a gap switch. The circuit parameters R_s, circuit inductance including L_s were estimated to be approximately 20 Ω and 1.5 μF, respectively, assuming that C_s was 33 μF. The ice sample was placed into a plastic vessel, which was filled with water. At first the tap water was used. On the next step salt water with salinity of 3.5% was used to simulate the actual condition. Ice samples were made from pure water. The electrodes were made of a dielectric material (Polyethylene) and metal (copper).

Figure 3 shows setup of the electrode system and the dimensions of the electrodes.[4] The tips of electrodes contacted the surface of the ice sample. In this experiments, two kinds of shapes of electrodes, cylindrical and conical (shown in Fig. 4), were tested to investigate the electrode shape effects, especially in the case of using salt

water.

In the experiments the voltage between the electrodes was measured using a high-voltage probe (EP-50K: Pulse Electric Engineering Co., Ltd.), and the current was measured using a current probe (Model 110A: Pearson Electronics, INC). The digital oscilloscope (DS4374: IWATSU) was used to observe the waveforms.

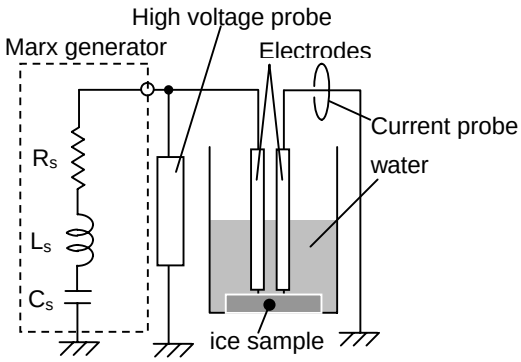

Fig. 2 Equivalent circuit and configuration of apparatus.

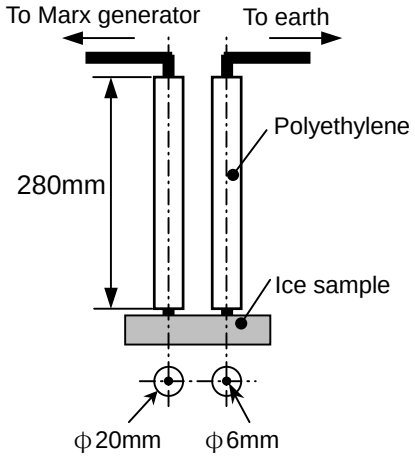

Fig.3 Configuration and dimensions of electrodes.

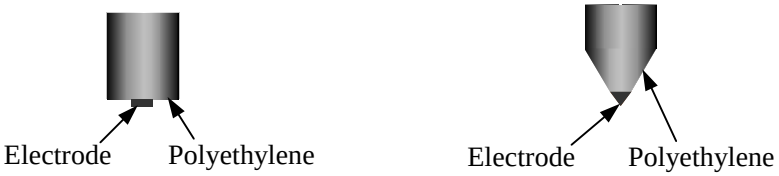

(a) Cylindrical electrodes. (b) Conical electrodes

Fig. 4 Cylindrical (a) and conical (b) electrodes.

3. Experimental Results and Discussions

3.1 Results in the case of using Tap Water[4)]

The experiments in the case of using the tap water were carried out. In this experiments, the cylindrical electrodes were used, and dimensions of ice sample were 95×82×28 mm (thickness of 28 mm). The experimental results were shown in Ref. 4. At t=0 a voltage of 50 kV was applied to the electrodes, and after 30 μs the discharge current started to rise. The photograph of discharge between the electrodes was taken. It was confirmed from this photograph that the discharge occurred on the surface between the electrodes. The photographs of the ice sample after applying the voltage, which were presented in Ref. 4, clearly showed that the ice sheet was broken by the discharge.

The power was calculated from the current and voltage waveforms, and the energy was calculated from the integral of the power. The inductance of the discharge region was neglected. It can be seen that the values of the maximum power and energy were 40 MW and 33 J, respectively. At that time the charging energy of the power

supply, which was calculated from the measured voltage just before the discharge started, was 36 J. Therefore almost all charging energy was consumed by the discharge between the electrodes, the discharge led to the breaking of the ice.

The *V-I* characteristics obtained from voltage and current waveforms had two regions, which had negative and positive slopes (refer to Ref. 4). The negative slope denoted the formation of the arc discharge, and the positive slope denoted the decrease in the discharge current during a time constant for the parameters of the electric circuit including the discharge region. The resistance evaluated from positive slope in the *V-I* characteristic was approximately 9 Ω at a current less than 1 kA.

3.2 Results in the case of using Salt Water

In practice, the sea ice exists in a seawater or water with higher conductibility than the tap water. Thus, the experiments using the salt water with the salinity of 3.5 % were carried out in order to simulate the real conditions. The voltage and current waveforms in the case of the salt water are shown in Fig. 5(a), where the cylindrical electrodes were used. In above case icebreaking was not confirmed. Also the discharge emission could be observed only at the tip of electrodes. The total charging energy of pulsed power generator was 60 J. On the other hand, using the conical electrodes the ice sample was successfully broken, with the same total charging energy. Fig. 5(b) shows the voltage and current waveforms in the case of conical electrodes. In this case also the discharge emission could be observed only at the tip of electrodes. Although the voltage waveforms were decreased in a certain time constant after the peak value in both cases, the clear difference was indicated in the current waveforms. The higher peak current was observed in the case of the conical electrodes than the cylindrical electrodes.

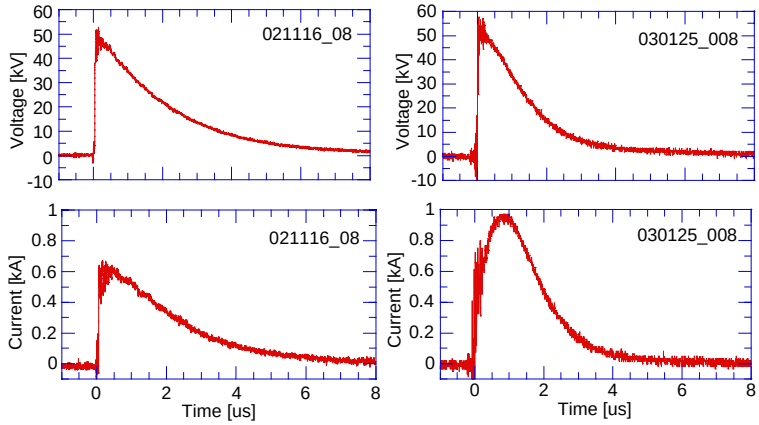

(a) Cylindrical electrodes (b) Conical electrodes

Fig. 5 Voltage and current waveforms in cases of (a)cylindrical and (b)conical electrodes.

Fig. 6 shows the waveform of the discharge power calculated from the voltage and current waveforms presented in Fig. 5. The peak value of discharge power increased from 25 MW to 40 MW by changing the electrode shape from the cylindrical to the conical one. From the experimental results it was found that the conical electrode with sharp-pointed tip was effective for the breaking of ice.

Figure 7 shows the *V-I* characteristics obtained from Figs. 5(a) and (b). It can be seen from this figure that in

the case of cylindrical electrode *V-I* characteristics had almost constant positive slope, what indicated that the current observed here was caused by the ions contained in the salt water. The resistance evaluated from this positive slope in Fig. 7 was approximately 63 Ω . In the other words, this current could be regarded as a leakage current because it did not contribute to the breaking of ice sample. Such a leakage current was consumed as a joule loss. In the case of the conical electrode the negative slope region was observed at voltage of 50 kV to 40 kV, and then the positive slope region appeared at less then 30 kV. The resistance evaluated from this positive slope was approximately 30 Ω .

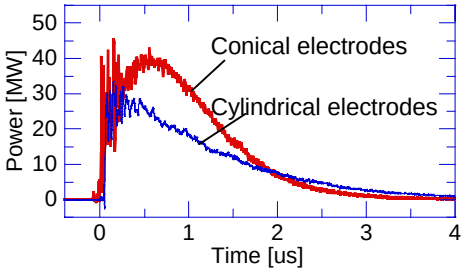

Fig. 6 Discharge power waveforms in cases of cylindrical and conical electrodes.

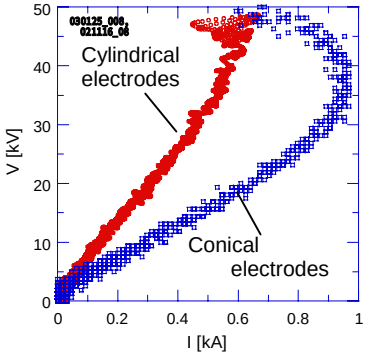

Fig. 7 *V-I* characteristics in cases of cylindrical and conical electrodes.

4. Discussions

In the tap water, formation of arc discharge between the electrodes was observed clearly, and the ice sample was broken, where the cylindrical electrodes were used. The negative slope region in *V-I* characteristic (shown in Fig. 7 of Ref. 4) indicates the formation of arc discharge. From these results, main phenomena for the discharge and icebreaking in the tap water was presumed as follows,

(1) By applying voltage across the electrodes the arc discharge starts to be formed at the surface of ice sample. This step corresponds to the negative slope region in *V-I* characteristics.

(2) Starting of arc discharge forms the shockwave.

(3) Local intense stress occurs in the cracks inside the ice during propagation of the shockwave, and then it is resulted in the break of the ice.

Using the conical electrodes the sharp-pointed tip of the electrode got into the ice sample, and the icebreaking was realized in the salt water, while in case of cylindrical it did not take place. The main effects of using the conical electrode were as follows:

(1) The energy loss by leakage current decreased because the tip of electrode got into the ice sample.

(2) The region with intense electric field was formed inside the ice.

Taking account of above effects, the following phenomena were supposed mechanisms for the icebreaking.

(1) Ionized regions are formed by the high electric field at the tip of the conical electrode. This step corresponds to the negative slope region in *V-I* characteristic shown in Fig. 7.

(2) The shockwave is induced by forming of ionized regions.

(3) Local intense stress occurs in the cracks inside the ice during propagation of shockwave, and then it is resulted in the break of the ice.

The difference of above phenomena between the cases of tap water and salt water is caused by resistivity of water. In the case of salt water no arc discharge path was observed between the electrodes because of leakage current caused by low resistivity of salt water. It suggests that the shockwave with enough pressure for icebreaking can be not generated in the case of salt water and cylindrical electrodes. Using the conical electrodes, the leakage current was decreased and ionized region was formed inside the ice sample. The formation of ionized region results in the formation of negative slope region in *V-I* characteristic. The peak value of discharge power increases rather then in the case of cylindrical electrodes. It seems that the ionized region promotes the formation of the shockwave with high pressure and realizes the icebreaking. In the medium with low resistivity, the following things are important for icebreaking.

(1) To decrease leakage current flow through the medium.

(2) To make a source of shockwave inside ice sample, for example using electrode with sharp-pointed tip.

Fulfilling above conditions causes that the peak value of the discharge power increases, and the formation of shockwave is promoted. In Fig. 6 the higher peak power, obtained in the case of conical electrode, is caused by the above conditions. In our results, threshold value of the discharge power for icebreaking was unknown. In order to evaluate the threshold value, the experiments in which the charging energy is changed, are necessary.

Figs. 8(a) and (b) shows the photographs before and after the discharge. Presented sample with the thickness of 40 mm was not broken during the first discharge. It could be seen from this photograph that the cracks were formed around the electrodes. This sample was broken after the third shot at the same charging energy of the capacitor. Fig. 9 shows the sample broken by the discharge. It was possible that the discharge power was slightly changed at every shot, while the charging energy of pulsed power generator was constant. In almost all cases the sample was broken along the line through the point of the electrodes contact, as shown in Fig. 9. It seemed from the observations shown in Figs. 8 and 9 that the cracks were formed by the discharge, and then these cracks induced the break of the ice sample. Also the observations confirmed the breaking mechanisms described above.

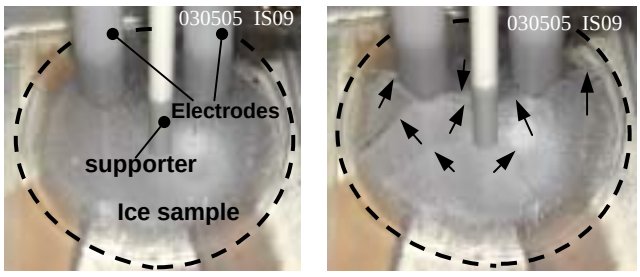

(a) Before discharge (b) After discharge

Fig. 8 Photographs before and after the discharge .

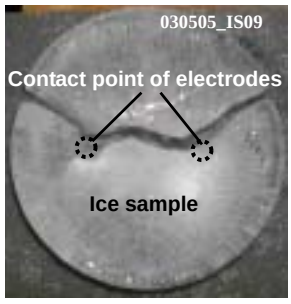

Fig. 9 Ice sample broken by discharge.

According to Ref. 6 it was found that on the destruction of granite with large number of voids, a partial discharge affected the energy efficiency of destruction. It is a localized discharge occurring at which the insulators

with different dielectric constant are located. Generally, ice also has many small voids containing air. Therefore for the breaking of ice, although the partial discharge was not detected directly, it was possible that the partial discharge inside the void was one of the important mechanisms of breaking of the ice sample

In our experiment, all the ice samples were made in the same freezer and under the same conditions. Therefore each experimental data obtained here could be compared relatively. In the future works, the experiments taking account of the property of ice, and the experiments using the natural sea ice are planed.

5. Conclusions

In this research, the icebreaking using the pulsed power was proposed as a new method for operation of the icebreakers in icebound sea. In this research breaking of the ice sample artificially made from pure water by pulsed power was demonstrated in the tap water experimentally. In order to simulate actual condition, the ice sample in the salt water with salinity of 3.5 % was tested. From the results using the cylindrical electrode with flat tip, the ice sample was not broken. Using the conical electrode with sharp-pointed tip, the ice sample was successfully broken. It was found from the results that the conical shape is effective for icebreaking in medium with low resistivity. It seemed that the shockwave caused by ionized region at tip of conical electrode, and the localized intense stress at crack were important mechanisms of the ice breaking in the salt water.

The experiments taking account of the various properties of ice, and the experiments using the natural sea ice are necessary to be carried out as the next works in order to evaluate the efficiency of breaking.

Acknowledgement

The authors would like to thank Dr. S. Uto from the National Maritime Research Institute and Dr. S. Ushio from the National Institute of Polar Research, for providing information for this research.

References

1) K. Izumiya, A. Konno and S. Sakai: Proc. 17th Int. Symp. Okhotsk Sea & Sea Ice, 2002 (Okhotsk sea & cold ocean research association, Mombetsu, Hokkaido, 2002) p. 267.

2) A. Konno and K. Izumiya: Proc. 17th Int. Symp. Okhotsk Sea & Sea Ice, 2002 (Okhotsk sea & cold ocean research association, Mombetsu, Hokkaido, 2002) p. 275.

3) K. Ogiwara, N. Otsuka, K. Kanaami, S. Takahashi, K. Maida and H. Saeki: Proc. 17th Int. Symp. Okhotsk Sea & Sea Ice, 2002 (Okhotsk sea & cold ocean research association, Mombetsu, Hokkaido, 2002) p. 290.

4) S. Ihara and C. Yamabe: Jpn. J. Appl. Phys. Vol. 42 (2003) pp. L 489-490

5) I. V. Lisitsyn, H. Inoue, I. Nishizawa, S. Katsuki and H. Akiyama: Journal of Applied Physics, Vol. 84, No. 11, pp.6262-6267, 1998.

6) I. V. Lisitsyn, H. Inoue, S. Katsuki and H. Akiyama: IEEE Trans. Dielectrics and Electrical Insulation, Vol. 6, No. 1, pp. 105-108, 1999.

7) Schwarz, J. and Week, W. F.: J. Glaciol., Vol. 19, pp. 499-530, 1977

8) Frankenstein, G. and Garner, R. : J. Glaciol., Vol. 6, pp. 943-944, 1967

Development of Bipolar-pulse Accelerator for Intense Pulsed Ion Beam Acceleration

T. Tomita, K. Masugata, Y. Shimizu, Y. Fujioka, I. Kitamura
H. Tanoue*, K. Arai*

Toyama University, 3190 Gofuku, Toyama 930-8555, Japan
*National Institute of Advanced Industry Science and Technology,
1-1-1, Umezono, Tsukuba-shi, Ibaraki 305 -8568, JAPAN

ABSTRACT

To improve the purity of an intense pulsed ion beams a new type of pulsed ion beam accelerator named "bipolar pulse accelerator (BPA)" was proposed. To confirm the principle of the accelerator a prototype of the experimental system was developed. The system utilizes B_θ type magnetically insulated acceleration gap and operated with single polar negative pulse. A coaxial gas puff plasma gun was used as an ion source, which was placed inside of the grounded anode. Source plasma (nitrogen) of current density ≈ 25 A/cm^2, duration ≈ 1.5 μs was injected into the acceleration gap by the plasma gun. The ions are successfully accelerated from the grounded anode to the drift tube by applying negative pulse of voltage 240 kV, duration 100 ns to the drift tube. Pulsed ion beam of current density ≈ 90 A/cm^2, duration ≈ 50 ns was obtained at 40 mm downstream from the anode surface. Ion species and energy of the beam was evaluated by TPS and found that the beam consists of N^+ and N^{2+} of energy 300-150 keV. To evaluate the irradiation effect of the ion beam to solid material, amorphous silicon thin film of thickness ≈ 500 nm was used as the target, which was deposited on the glass substrate. The film was found to be poly-crystallized after four shot of irradiation. For the bipolar pulse experiment bipolar pulse generator has been developed.

Keyword: intense pulsed ion beam, bipolar pulse, plasma gun, nitrogen ion beam

1. Introduction

Intense pulsed ion beams (PIB) of carbon, nitrogen or aluminum, have a wide area of applications including nuclear fusion, materials science, etc. For example, PIB is expected to be applied to a "pulsed ion beam implantation" to semiconductor since doping process and annealing process is expected simultaneously. The PIB is also expected to be use in a crystallization process of semiconductor thin films or surface modification process of metallic materials.

PIB can easily be generated in a conventional pulsed power ion diode using flashboard ion source [1]. However, since many kinds of ions are produced in the same time in the flashboard ion source, the purity of the beam is usually very poor. For example, in a point pinch ion diode we found that produced PIB contains much kind of ions including protons, multiply ionized carbons, and organic ions [2]. Hence an application of the PIB has been extremely limited.

To improve the purity a new type of pulsed power ion beam accelerator named "bipolar pulse accelerator (BPA)" was proposed [3-5]. As the first step of the development of the BPA, a prototype of the experimental system of the accelerator was constructed to confirm the principle. By using the system the acceleration of ion beam was successfully confirmed [6,7]. In addition, the accelerated beam was used to irradiate amorphous silicon thin films to evaluate the irradiation effects of PIB. In the paper the results of the experiments are described.

2. Bipolar Pulse Accelerator

Figure 1 shows the concept of the bipolar pulse accelerator [3]. A conventional PIB diode is also shown

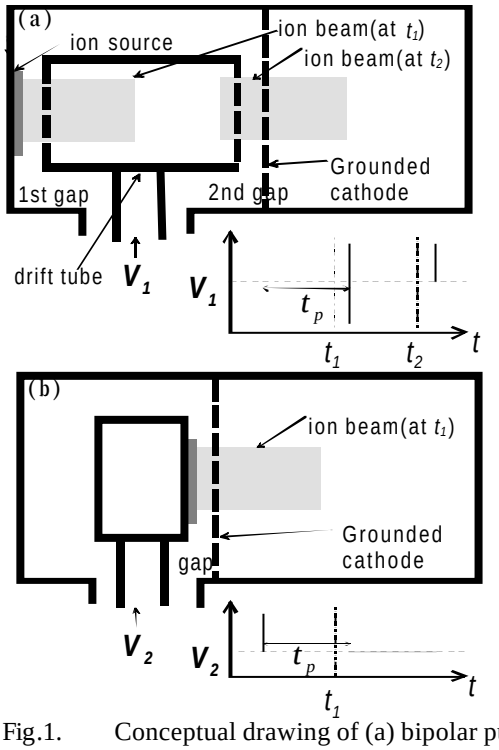

Fig.1. Conceptual drawing of (a) bipolar pulse accelerator and (b) conventional pulsed ion beam accelerator.

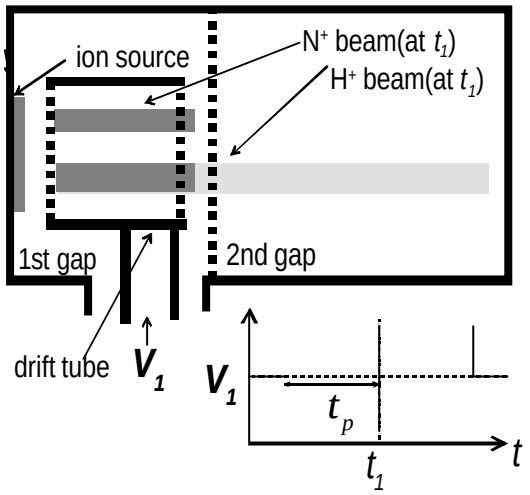

Fig.2. Principle of the improvement of the purity of the ion beam.

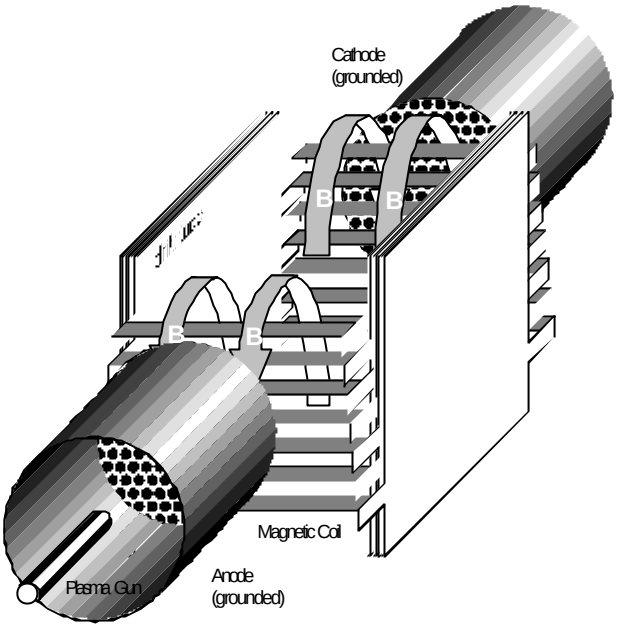

Fig.3. Conceptual drawing of B_y type magnetically insulated gap of the bipolar pulse accelerator.

for comparison. As shown in Fig.1 (a), proposed ion accelerator consists of a grounded ion source, a drift tube and a grounded cathode. In the diode, bipolar pulse (V_1) is applied to the drift tube. At first the negative voltage pulse of duration t_p is applied to the drift tube and ions on the grounded ion source are accelerated toward the drift tube. If t_p is adjusted to the time of flight delay of the ions to pass the drift tube, the pulse is reversed and the positive voltage of duration t_p is applied to the drift tube when top of the ion beam reaches the 2nd gap. As a result the ions are again accelerated in the 2nd gap toward the grounded cathode.

As seen in Fig.1 (b), in the conventional PIB diode, ion source is placed on the anode where high voltage pulse is applied, while in the proposed ion diode, ion source is on the grounded anode. This seems to be favorable for the active ion sources where ion source is powered by an external power supply.

Here, considering the acceleration of ions in the case that ion source contains N^+ and impurity ions of H^+ in the proposed diode (see Fig. 2). In the case, ions of N^+ and H^+ are accelerated in the 1st gap toward the drift tube when negative voltage is applied. In Fig. 2, N^+ and H^+ beams are schematically described and as seen in the figure, due to the deference of the velocity the length of H^+ beam is much longer than that of N^+. Here assuming that the length of the drift tube is designed to be same as the beam length of N^+ of duration t_p at acceleration voltage V_p. It is, for example calculated to be 15.7 cm when V_p = 500 kV, t_p = 60 ns. When N^+ beam of length 15.7 cm is in the drift tube ($t = t_1$) the voltage is reversed and positive voltage is applied to the drift tube, which accelerate N^+ beam in the 2nd gap. In contrast, since length of H^+ beam at V_p = 500 kV, t_p = 60 ns is 58.7 cm, 73 % of the beam is out of the drift tube at t_1 and it is not accelerated in the 2nd gap. Hence 73 % of H^+ beam is removed in the accelerator [4].

Figure 3 shows the conceptual design of the BPA. The accelerator consists of a grounded anode, drift tube and a grounded cathode. To produce insulating magnetic fields in both acceleration gaps, a magnetic field coil of grating structure is used to produce uniform magnetic field in vertical direction (y-direction).

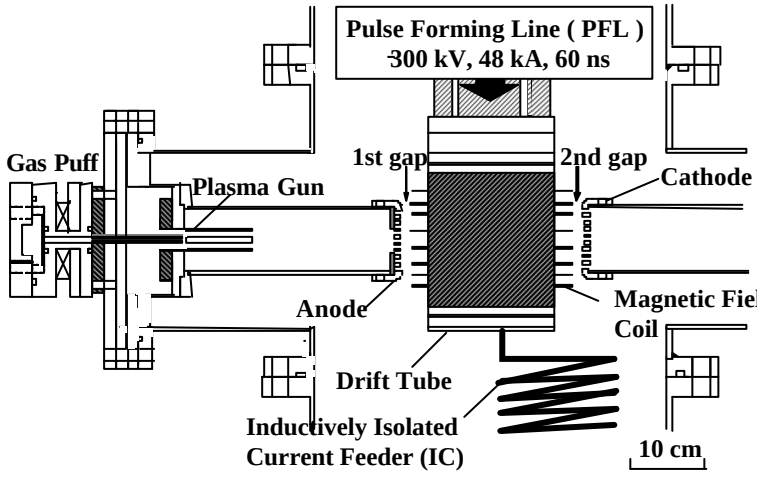

Fig.4. Cross-sectional view of the experimental system.

3. Accelerator Experiment

Figure 4 shows the cross-sectional view of the experimental system. The system consists of a grounded anode (copper), a drift tube (stainless steel) and a magnetically insulated acceleration gap (MIG). The drift tube is connected to a high voltage terminal of a high voltage pulsed power generator. A Blumlein type pulse forming line (PFL) was used [8], which generate an output pulse of -300 kV, 48 kA, 60 ns. By applying negative pulse to the drift tube, ions on the anode are accelerated toward the drift tube. The magnetic coil of the MIG is installed on the rectangular drift tube where acceleration voltage is applied and produces

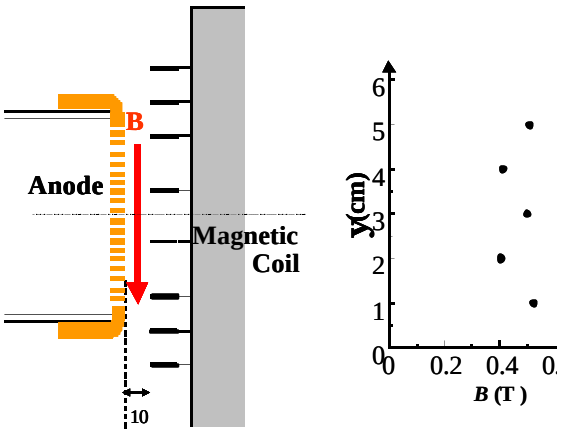

Fig.5. Magnetic field (B_y) distribution in the acceleration gap when charging voltage of the bank is 4.0 kV.

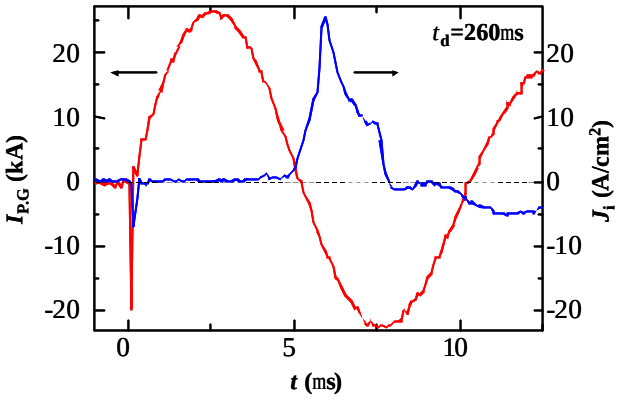

Fig.7. Typical waveforms of the discharge current of the plasma gun ($I_{P.G}$) and the ion current density (J_i). J_i was measured by BIC placed at 130 mm downstream from the top of the plasma gun.

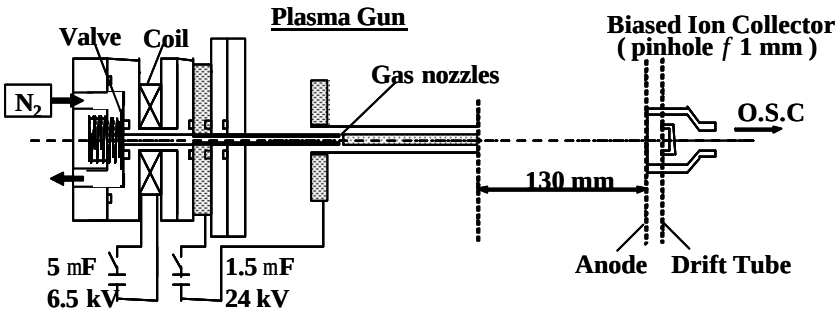

Fig.6. Cross-sectional view of the gas puff plasma gun.

magnetic field of vertical direction (y-direction). To obtain higher transmission efficiency of the ion beam, right and left sides of the coil (facing the anode or cathode) consist of 8 blades each and have a grating structure. Each of the blades (10 mm^W x 118 mm^L x 1 mm^T) is connected in series and constructs an 8-turn coil. Since high voltage pulse is applied to the drift tube, pulsed current produced by the capacitor bank (500 μF, 5 kV) is applied to the coil through an inductively isolated current feeder (IC). The IC is a helically winded coaxial cable and the outer conductor of the IC is connecting the grounded vacuum chamber and the drift tube with inductance of 12.4 μH.

The anode and the cathode are brass electrode of diameter 78 mm, thickness 5 mm. The electrodes are uniformly drilled with apertures of diameter 4 mm, giving beam transmission efficiency of 58 %. To produce anode plasma (source plasma of the ion beam) gas puff plasma gun was used, which was placed inside the anode.

Figure 5 shows the magnetic filed distribution in the gap. As seen in the figure uniform B_y field of strength 0.4 - 0.5 T is produced in the acceleration gap of $d_{A\text{-}K}$ = 10 mm.

Figure 6 shows the detail of the gas puff plasma gun used in the experiment. The plasma gun consists of a high-speed gas puff valve and a coaxial plasma gun. The gas puff valve consists of a nylon vessel, an aluminum valve and a drive coil and the vessel is pre-filled with N_2 gas. By applying pulse current to the drive coil, the magnetic stress produced by the pulsed magnetic field presses the aluminum valve to open the valve. As the results, filled gas in the vessel expands with a supersonic velocity and reaches the gas nozzles on the inner electrode of the plasma gun.

The plasma gun has a pair of coaxial brass electrodes, i.e. an inner electrode of outer diameter 6 mm, length 65 mm, and an outer electrode of inner diameter 16 mm. Since it takes about a hundred μs to open the valve and several tens μs for N_2 gas to reach the gas nozzle of the plasma gun, the capacitor bank of the plasma gun is discharged with a delay time of t_d around 230-320 μs. To apply pulsed current to the gas puff coil and the plasma gun, capacitor banks of 5 μF and 1.5 μF were used, respectively. Each capacitor was usually charged to 6.5 kV, and 24 kV, respectively.

Figure 7 shows the waveforms of the discharge current of the plasma gun ($I_{P.G}$) and the ion current density (J_i) obtained by a biased ion collector (BIC) when t_d = 260 μs. As seen in the figure $I_{P.G}$ rises in 2.5 μs and have a peak value of 27 kA. The peak value of J_i = 25 A/cm^2 was obtained at 130 mm downstream from the plasma gun on the axis at t = 7 μs after the rise of $I_{P.G}$.

Figure 8 shows the dependence of J_i on t_d evaluated. As seen in the figure J_i rises at $t_d \approx$ 230 μs and have a peak around 290 μs, and after that decreased. The results suggest that it takes 230 μs after the election of gas puff coil for the gas to reach the nozzles.

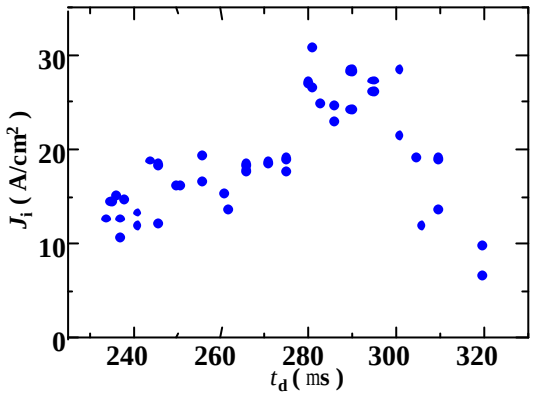

Fig.8. The dependence of the ion current density J_i on the delay time of the discharge current rise from the rise of gas puff current t_d.

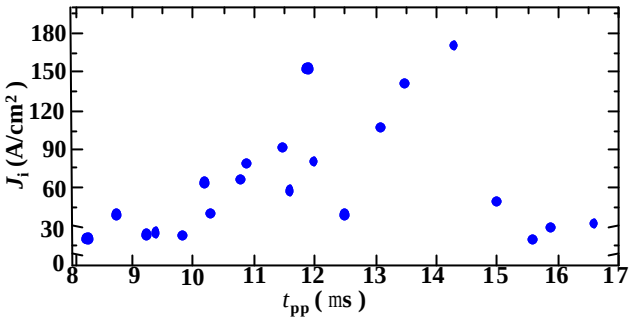

Fig.11. Dependence of the peak values of ion current density (J_i) on the delay time (t_{pp})

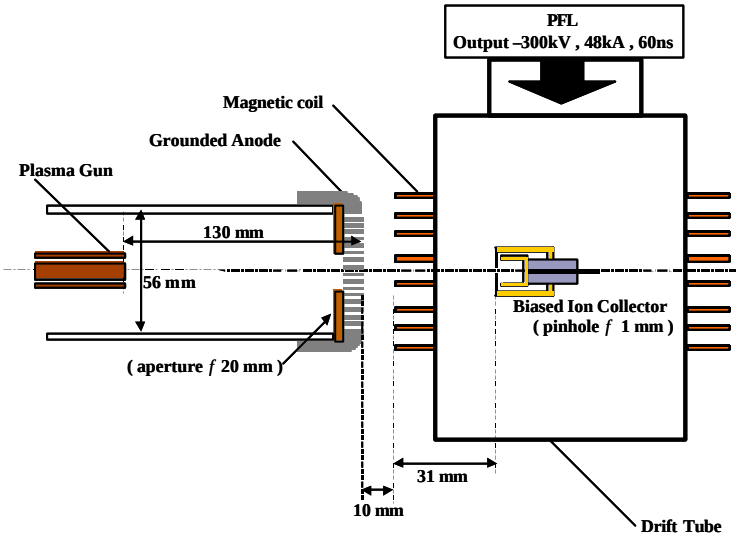

Fig.9. Experimental setup of beam acceleration experiment.

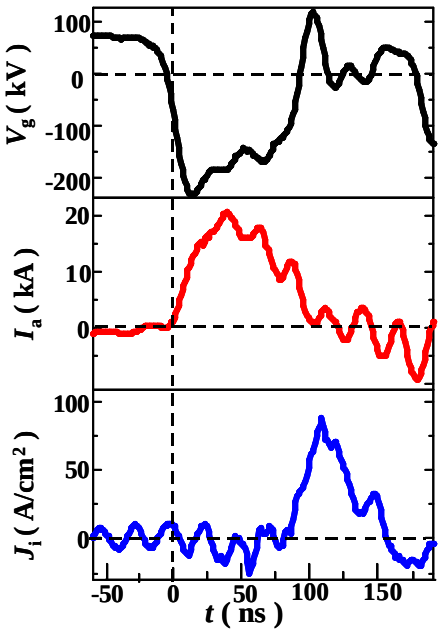

Fig.10. Typical waveforms of gap voltage (V_g), anode current (I_a) and ion current density observed at 40 mm downstream from the anode surface (J_i).

4. Experimental Results

To confirm the acceleration of ions in the 1st gap negative pulse was applied to the drift tube. Figure 9 shows the set-up of beam acceleration experiment to measure the accelerated ion beam. To limit the beam diameter and enhance the beam current density on the axis, aperture plate of aperture diameter 20 mm is installed inside the anode. BIC was installed inside the drift tube to observe the ion current density (J_i). Since high voltage pulse is applied to the drift tube, inductively isolated coaxial cable of same structure as IC was used to transport the BIC signal. The system was operated at 80 % of the full charge condition of the PFL. Insulating magnetic field of 0.3 - 0.4 T was applied to the acceleration gap of gap length $d_{A\text{-}K}$ = 10 mm. The plasma gun was operated at the condition of $t_d \approx 290$ μs in advance to the PFL operation and the PFL was fired at t_{pp} = 9-20 μs after the rise of the $I_{P,G}$ to apply negative high voltage pulse to the drift tube.

Figure 10 shows typical waveforms of the output voltage (V_g), the anode current (I_a) and the ion current density (J_i). They were obtained at the condition of t_{pp} = 12.5 μs. Here, I_a was measured at the root of the anode and it is considered to be equivalent to the current flowing across the 1st gap. J_i was measured at 40 mm downstream from the anode surface. As seen in the figure, V_g rises at t = -5 ns and peak voltage of -230 kV was obtained. I_a rises with V_g and has a peak of 20 kA whereas J_i rises at t = 80 ns and have a peak of 27 A/cm^2.

Figure 11 shows the dependence of the peakvalue of J_i on the delay time (t_{pp}) for the fixed condition of t_d, the insulating magnetic field and the charging voltage of the PFL. As seen in the figure J_i increases monotonically with increasing t_{pp}. This seems to be due to that quantity of the plasma on the anode or in the 1st gap increases with increasing t_{pp}. Due to the increase of output current of the PFL with t_{pp}, V_g decreases with increasing t_{pp}.

Figure 12 shows the beam pattern obtained on the thermo sensitive paper. The paper was placed at 41 mm

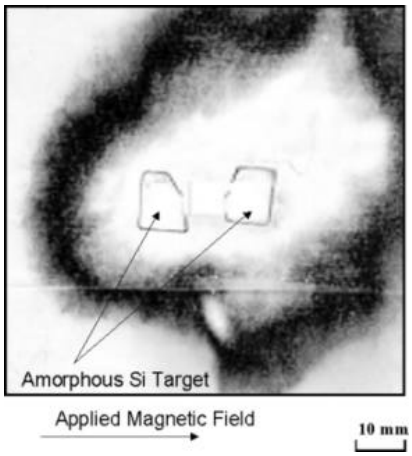

Fig.12. Beam pattern obtained on a thermo sensitive paper. The paper was placed at 41 mm downstream from the anode surface.

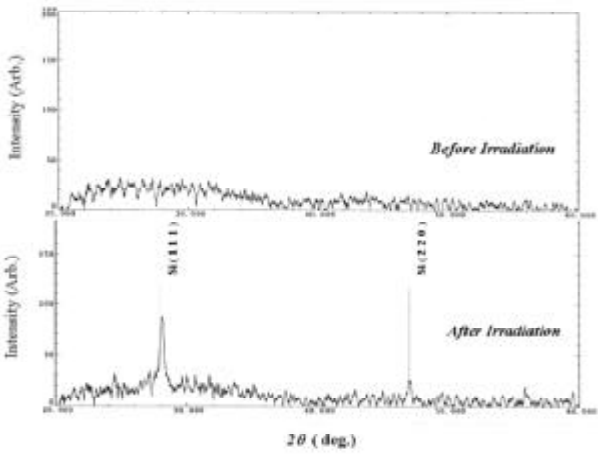

Fig.14. X-ray diffraction pattern of the amorphous silicon thin films before and after the ion beam irradiation.

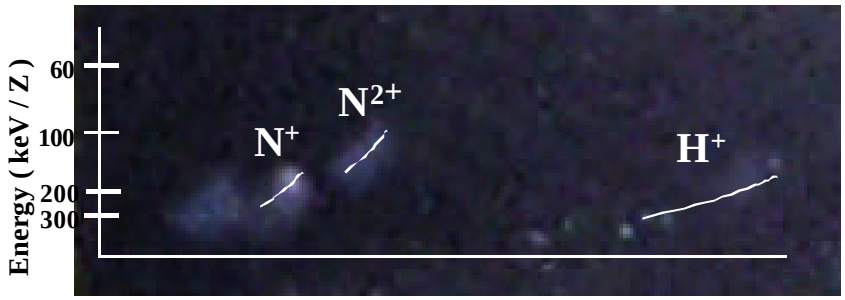

Fig.13. Ion track pattern obtained by the Thomson parabola spectrometer.

downstream from the anode surface and 4 shots of ion beams were fired to enhance the contrast of the pattern. As seen in the figure, round black pattern is observed with white central part around the beam axis. The white part is due to the ablation of the surface of the paper, hence indicating the strong irradiation of the beam. The size of the white part has an elliptic shape of long axis 60 mm short axis 45 mm. The size is much larger than the size of the plasma-limiting aperture of diameter 20 mm installed inside the anode. Which suggest that the size of source plasma expands in the acceleration gap after passing the aperture.

To evaluate the species and the energy spectrum of the ion beam Thomson parabola spectrometer was used. Figure 13 shows the example of the track pattern recorded on the ion track detecting plate of CR-39. Here, deflecting magnetic field and electric field are applied in vertical direction; hence ions are deflected in vertical direction and horizontal direction by the electric field and the magnetic field, respectively. In the figure, singly and doubly ionized nitrogen ions of energy 300-150 keV are observed with impurity of hydrogen and heavy ions.

5. Beam irradiation Experiment

To evaluate the annealing effect of the pulsed ion beam to the materials, amorphous silicon thin films was used as a targets. The films have a thickness of 500 nm and fabricated on the glass substrate. Two targets was placed at 41 mm downstream from the anode and attached on the thermo sensitive paper as shown in Fig. 12. Here, the amorphous thin film placed at right-hand side was removed after the irradiation due to that beam intensity was too strong and cause surface ablation. Hence only the target placed at left-hand side was evaluated. Figure 14 shows the X-ray diffraction pattern of the target. As seen in the figure no diffraction peak is observed in the target before the irradiation. In contrast clearer peaks of Si (111) and Si (220) were observed on the target after the irradiation. The results clearly indicate that the target of amorphous silicon thin film was poly-crystallized by the irradiation.

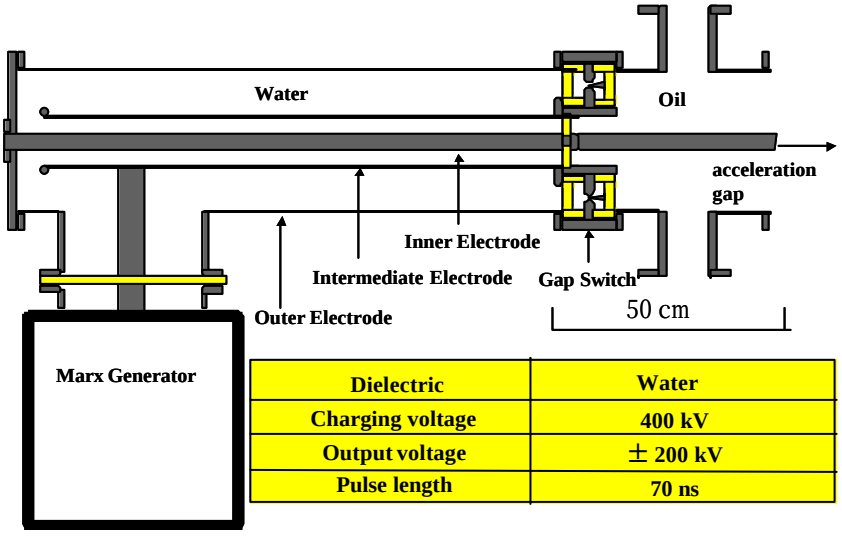

Dielectric	Water
Charging voltage	400 kV
Output voltage	± 200 kV
Pulse length	70 ns

Fig. 15. Cross-sectional vies of the Bipolar pulse generator.

6. Development of Bipolar Pulse generator

For the bipolar pulse experiment, we are developing a bipolar pulse generator. The cross-sectional view of the pulse line is shown in Fig. Б. The line is the double coaxial type [3] and has an enhanced trigger type rail gap switch on the end of the line between the intermediate conductor and the outer conductor. The expected switching inductance is 10 nH [9]. The designed output pulse is (-200 kV, 7 Ω, 70 ns) + (+200 kV, 7 Ω, 70 ns). The line was constructed and new we are evaluating the electrical characteristics.

7. Conclusion

To confirm the principle of the bipolar accelerator a prototype of the experimental system was developed. The system utilizes B_y type magnetically insulated acceleration gap and operated with single polar negative pulse. A coaxial gas puff plasma gun was used as an ion source, placed in the grounded anode. Source plasma (nitrogen) of current density ≈ 25 A/cm^2, duration ≈ 1.5 μs was injected into the acceleration gap. The ions are successfully accelerated from the grounded anode to the drift tube by applying negative pulse of voltage 240 kV, duration 100 ns to the drift tube. Pulsed ion beam of current density ≈ 90 A/cm^2, duration ≈ 50 ns was obtained at 40 mm downstream from the anode surface. Ion species and energy of the beam was evaluated by TPS and found that the beam consists of N^+ and N^{2+} of energy 300-150 keV. To evaluate the irradiation effect of the ion beam to solid material, amorphous silicon thin film of thickness ≈ 500 nm was used as the target, which was deposited on the glass substrate. The film was found to be poly-crystallized after four shot of irradiation. For the bipolar pulse experiment bipolar pulse generator of designed output pulse is (-200 kV, 7 Ω, 70 ns) + (+200 kV, 7 Ω, 70 ns) has been developed.

Acknowledgement

This work was partly supported by the Research Foundation for the Electro Technology of Chubu.

References

1) E. Chishiro, A. Matsuyama, K. Masugata and K. Yatsui, "Dependence of characteristics of Br-type magnetically insulated diode on configuration of insulation magnetic field", Jpn. J. Appl. Phys., **35**(4A), pp.2350-2355 (1996).
2) K. Masugata, H. Okuda, K. Yatsui and T. Tazima, J. Appl. Phys. **80** pp. 4813-4818, 1996
3) K. Masugata, "High current pulsed ion beam accelerators using bi-directional pulses" Nuclear Instrum. & Methods in Phys. Res., **A 411**, pp.205-209, (1998)
4) K. Masugata, K. Kinbara, T. Atsumura, Y. Kawahara, T. Takao, I. Kitamura, and T. Takahashi, *Proc. 12th Symp. on High Current Electronics (1st Int'l Congress on Radiation Physics, High Current Electronics, and Modification of Materials, Tomsk, Russia, 24-29 September 2000), ed. by G. Mesyats, B. Kovalchuk, and G. Remnev,* pp.111- 114 (2000)
5) K. Masugata, I. Kitamura, T. Takahashi, Y. Tanaka, H. Tanoue, K. Arai, *Proc. 28th IEEE Int'l Conf. on Plasma Science and 13th IEEE Int'l Pulsed Power Conf., Las Vegas, Nevada, June 17-22 2001, ed. by R. Reinovsky and M. Newton,* pp. 1366-1369 (2001).
6) K. Masugata, Y. Shimizu, Y. Fujioka, I. Kitamura, H. Tanoue, K. Arai "Development of Bipolar-pulse Accelerator for Intense Pulsed Ion Beam Acceleration", Nuclear Instruments & Methods in Physics Research, Section **A , 535/3** pp. 614-621 (2004)
7) Y. Fujioka, C. Mitsui, I. Kitamura, T. Takahashi, K. Masugata, H. Tanoue, K. Arai, Development of Bipolar Pulse Accelerator for Intense Pulsed Ion Beam Acceleration, Research Report, **NIFS-PROC-54** (National Institute for Fusion Science, Nagoya, Japan, Workshop on Physics and Applications of Micro and Fast Z-Pinch Plasmas, Dec. 5-6, 2002) pp.38-44 (2003)
8) K. Masugata, S. Tsuchida, H. Saitou, K. Yatsui, K. Shibata and M. Shigeta, "Fast charging Blumlein pulse forming line" Laser and Particle Beams **15**(2) pp.249-258 (1997)
9) K. Masugata, H. Tsuchida, H. Saitou, and K. Yatsui, "Studies and performance of decreased rail gap switch inductance by enhancing multi-channeling via gas mixture", IEEE Trans. on Plasma Science, **25**(1) pp.97-99 (1997).

Formation of Strongly Coupled Plasma Using Pulse-Power Discharges in Water

Toru Sasaki,* Mitsuo Nakajima, Tohru Kawamura, and Kazuhiko Horioka
Department of Energy Sciences, Tokyo Institute of Technology,
Nagatsuta 4259, Midori-ku, Yokohama, 226-8502, Japan

Dense plasmas are produced using exploding wire discharges in water. The exploding plasma is tamped and stablized by the surrounding water. From a comparison of them with exploding wire discharges in air, the point of wire evaporation is assured. The evolutions of plasma radius, conductivity, and a shock wave accompanied with the explosion, are measured. These measurements are compared with theoretical estimations based on a simplified model and MHD simulation. The results show that, at 2μsec from start of discharge, the coupling parameter of them are 2-3 and the electrical conductivities are almost 10 times larger than the ones obtained with Spitzer's model.

Keywords: strongly coupled plasma, equation of state, conductivity, pulse-power discharge, wire explosion

I. INTRODUCTION

Properties of dense plasma are of interest concerning the interiors of the giant planets, white dwarfs and the hydrodynamics of fuel pellet of inertial confinement fusion(ICF) [1–5]. To optimize the fuel pellet dynamics of heavy-ion-beam ICF, ion beam stopping power, pressure and thermal transport in the dense plasma sholud be accurately predicted especially at the tamper surface of direct fusion or in the X-ray converter of indirect fusion pellet. The stopping power and transport coefficients of strongly coupled plasma are investigated on a theoretical basis using distribution function[6–8] or Moleculer Dynamics (MD)[9] simulation. If the data base of these parameters are wrong, the gain of fuel pellet is difficult to optimize. The reason why this is that the fuel pellet is irradiated with finite number of beams. The allowable level of nonuniformity should be intrinsically decided by that of the energy deposition profile of the target. We need to know the initial pressure profile and transport coefficients for making a high gain pellet. In a labratory experiment, the warm and dense plasma is not stationary. Therefore, the fast energy input is required to make the dense plasma state[10–15].

The dense and/or low temperature plasma is correlated by Coulomb force and characterized by the Coulomb coupling parameter Γ for the ions and the degeneracy parameter θ for the electrons. Here, Γ is a measure of the Coulomb interaction and is defined as the ratio of average Coulomb interaction energy to average kinetic energy

$$\Gamma = \frac{Z^2 e^2}{4\pi\epsilon_0 a k_B T}, \tag{1}$$

where $a = (3/4\pi n_i)^{1/3}$ is the ion-sphere radius, Z is the average ionization state, k_B is the Boltzman's constant, n_i is the ion density, and T is the plasma temperature. The degeneracy parameter used as a measure of the level of degeneracy of electron is

$$\theta = \frac{k_B T}{E_F} = \frac{2 m_e k_B T}{\hbar^2 \left(3\pi^2 n_e\right)^{2/3}}, \tag{2}$$

where E_F is the Fermi energy, n_e is the electron density and m_e is the mass of electron.

The plasma in strongly coupled state is produced by wire explosion driven by a fast pulse generator. A density-temperature diagram with a possible parameter regime of the exploding wire plasma is shown Fig. 1. In this study, we concentrate our efforts on the behavior of strongly coupled plasma, both experimentally and numerically. In contrast to previous experiment, our study is intended to make a semi-empirical scaling of the equation of state and transport coefficients.

II. EXPERIMENTAL SETUP

A schematic diagram of the experimental arrangement is shown in Fig. 2 [14, 15]. The capacitor bank; C consists of cylindrically arranged $8 \times 0.4\mu$F low inductance

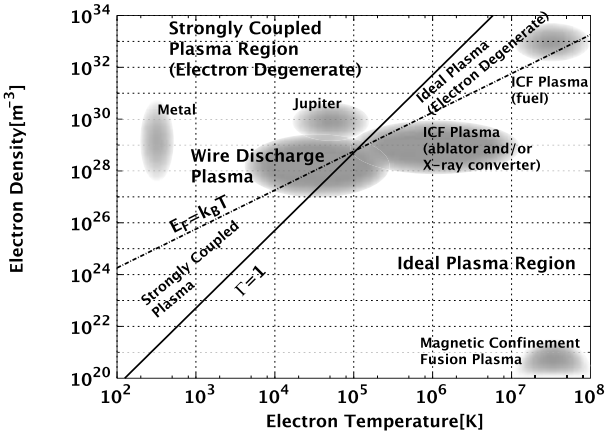

FIG. 1: Expected parameter regime of wire explosion plasma and some typical parameters on density-temperature diagram.

*Electronic address: sasaki@es.titech.ac.jp

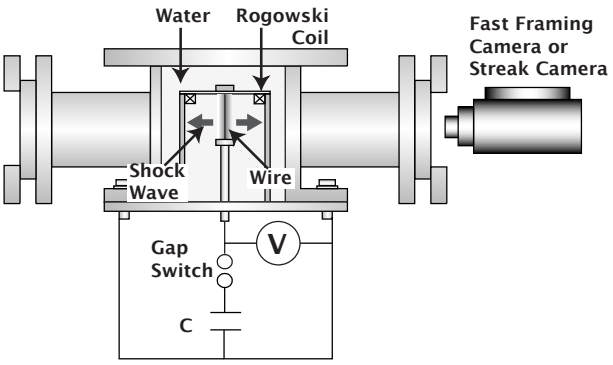

FIG. 2: Schematic diagram of experimental arrangement for exploding wire in water.

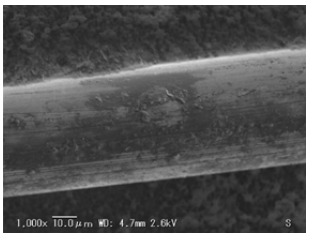

FIG. 3: Enlarged photograph of 50μm wire.

capacitors. The wire specimens are copper, aluminium and tungsten. The capacitor bank was charged to at least 10 kV to ensure vaporization of the wire, and it is switched by a low-inductance spark gap switch. Figure 2 shows the positions of the Rogowski coil and the voltage detector. These detectors directly measured the current and voltage of the wire plasma. The test chamber was filled with water, and the expanding plasma was tamped at high density by the surrounding water. We measure the plasma evolution using an image convertor camera (HADLAND PHOTONICS : Imacon 468) mounted with a discontiguous microscopic lens (QUESTAR : QM100). Shock surface-time diagrams of the exploding wire were obtained a shadowgraph method using a streak-camera(Hamamatsu : c2830) and a LD Laser(532nm, CW 250mW:LDC-2500:SUWTECH).

The experimentaly obtained voltage waveform is composed of resistive and inductive parts. The stray inductance of system of the discharge device was estimated to be $L = 105$nH from the short circuit waveforms of the current and voltage. Thus, the effective resistance $R(t)$ was evaluated using the next equation;

$$R(t) = \frac{V(t) - LdI/dt}{I(t)}, \tag{3}$$

and leading to the conductivity of the wire $\sigma(t)$ via

$$\sigma(t) = \frac{l}{\pi r_p^2(t) R(t)}, \tag{4}$$

l being the length of the wire and/or plasma, and $r_p(t)$ its radius. The effect of self-magnetic field on the resistance

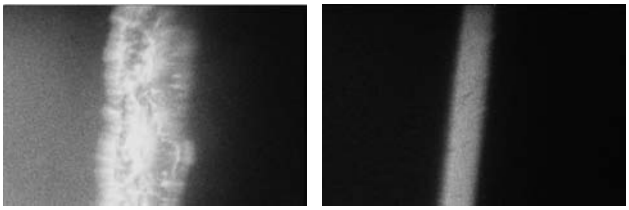

(a) (b)

FIG. 4: Framing photographs of Al plasma; (a) in air and (b) in water, taken with an image converter camera with gate time 10 ns, at 240 ns after beginning of discharge.

are negligible because the electron collision frequency is much higher than the electron cyclotron frequency. In this experiments, the wire length is selected to be 18 mm. The diameter of wire is selected to be 100 μm, considering the skin depth δ given by

$$\delta = \frac{1}{\sqrt{\pi\sigma\mu f}}, \tag{5}$$

where μ is the permeability and f is frequency of the electro-magnetic wave. For all wires employed in this experiment, the skin depth was larger than the diameter of the wires.

III. RESULTS AND DISCUSSIONS

A. Vaporization timing and comparison of plasma evolution in air and in water using Al-wire

Figure 4 shows a comparison of wire discharges in water and in air. As shown, the surrounding water is effctive in tamping and stabilizing the plasma. These results show a benefical effect of water for making a dense and uniform plasma column. The other reason of stabilizting effect is the initial condition of wire(Fig. 3). As shown, it had little nonuniformity on surface. The evaporation time of Al is predicted to be about 200ns by the image.

Typical voltage and current waveform of the Al-wire discharge in water and in air are shown Fig. 5. The current waveforms have two peaks both in air and in water. The first peak of the current waveforms can be correlated to the phase transition of evapolation. The first peak of voltage in water delays compared with that in air. Figure 6 shows evolutions of the resistance of wire/plasma in water and in air using the same wire. The diameter of wire/plasma is almost constant while solid - liquid phase. Therefore, the resistance of wire/plasma is coincidentally evolved unitl the liquid-vapor phase transition. The resistans curves in Fig. 6 are indicating the liquid-vapor phase transition at about 200 ns. Thus, the evolution of input energy and required energy for evaporation are

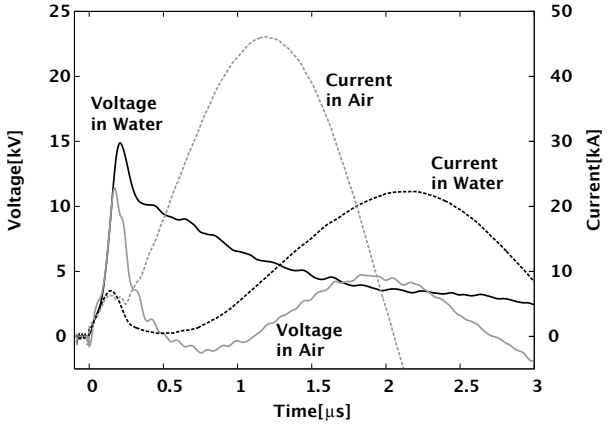

FIG. 5: Typical wave form of Al wire discharges in air and in water

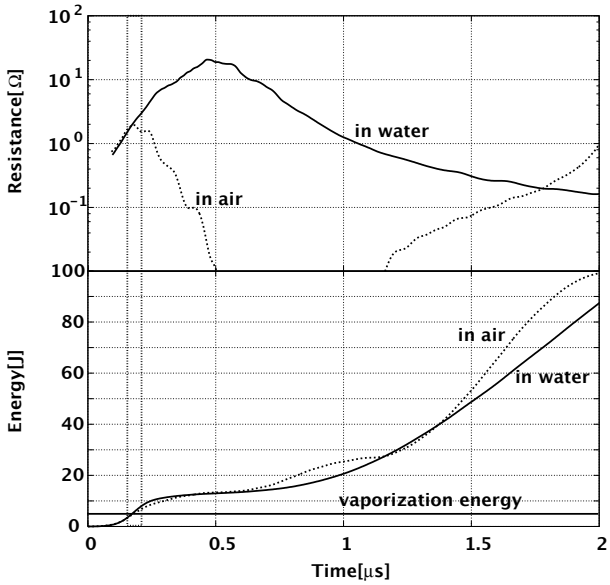

FIG. 6: Evolution of resistans and input energy in air and in water

shown in Fig. 6. The required energy for evaporation of Al-wire is estimated to be 5.1 J. A comparison of evolving registance and energy deposition also indicates the liquid-vapor phase transition at about 200ns. Similar results are also obtained for the other wire materials. After about 200 ns, the energy input to Al-wire is ceased for a while, due to increase of the resistivity. Probably because the expansion wave of in the Al-wire plasma arrives at the axis, which cool down the plasma.

B. Evaluation of wire plasma

All of framing images of the fast framing camera showed symmetric cylindrical expansion of the plasmas. The evolution of plasma surface is shown in Fig. 7. The

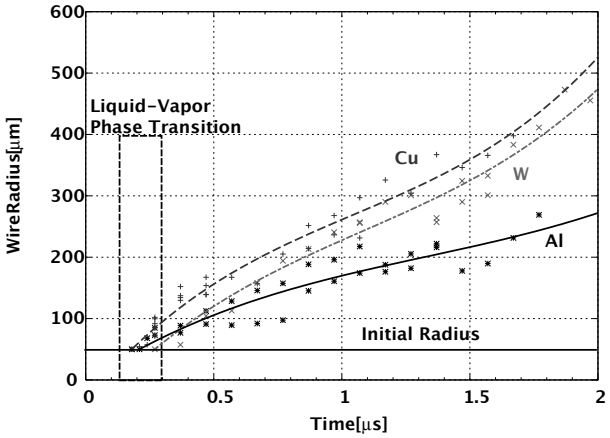

FIG. 7: Evolution of plasma surface taken from images of converter camera.

evaporation time of Cu-wire was about 200ns, and W-wire was about 300ns. The results are consistent with the one shown in Fig. 6. In case of exploding plasma with strongly tamped mode, the velocity of wire surface is affected by the initial density. Therefor, Cu and W wires have almost the same velocity profile.

A streak shadowgraph of the Cu-wire explosion is shown in Fig. 8. It indicates that the Cu-wire evolved accompanied with a cylindrical symmetric shock wave. The shock velocity in water was estimated to be 3×10^3 m/s and corresponding Mach number was about 2. Evolutions of shock surface are shown in Fig. 8(b). In case of instantaneous line explosion, a self-similar solution predicts the shock evolution as,[16]

$$R(t) = \xi_0 \left(\frac{E}{\rho}\right)^{1/4} t^{1/2}, \tag{6}$$

where ξ_0 is normarized length, E is the energy of unit length, ρ is the density, t is the time. Equation 6 shows that the cylindrical shock radius evolves depending on $t^{1/2}$. However, we can see from Fig. 8(b) the experimental results are independent of this scaling and this means the shock behavior is affected by the history of plasma pressure.

The evolution of energy and the region of liquid-vapor phase transition are shown in Fig. 9 for Al,Cu and W wires. The Cu-wire can receive the fastest energy input. The result shows that initial resistance of wire also affect the evolution of wire plasma.

The particle number density is predicted from the evolution of contact surface. Assuming a homogeneous expansion, the number density of the plasma is obtained from

$$n(t) = n_0 \left(\frac{r_0}{r_p(t)}\right)^2 \tag{7}$$

where $r_p(t)$ is wire/plamsa radius, r_0 is the initial wire radius and n_0 is the initial particle number density. The

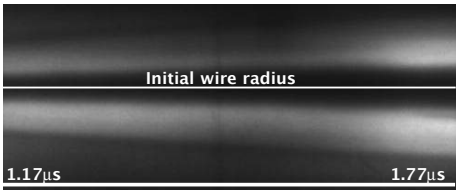

(a)

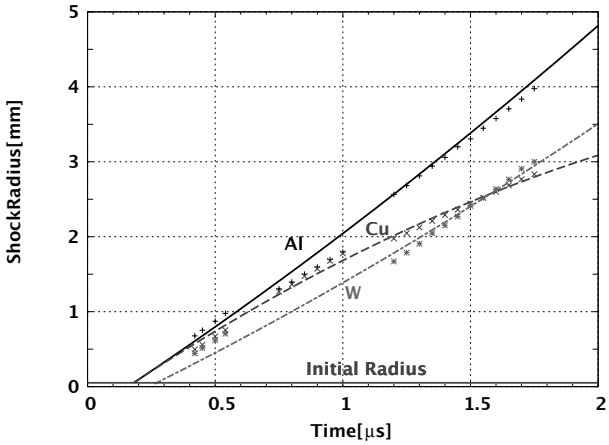

(b)

FIG. 8: (a)Streak image of Cu-wire plasma and shock surface from 1.17μs to 1.77μs. (b)Evolution of shock surface.

particle number density of all materials is estimated to be over $10^{21}1/\mathrm{cm}^3$ until 2μs.

Assuming LTE(Local Thermodynamic Equiblium), the temperature of wire/plasma is given by the next equation;

$$E_{input} = \left(e(\rho, T) \ + \frac{p}{\rho} \right) m_{wire}, \tag{8}$$

where E_{input} is the input energy, $e(\rho, T)$ is the internal energy of unit mass, p is the pressure, ρ is the density, m_{wire} is the mass of wire. The ideal EOS approximation leads to,

$$E_{input} = \frac{3}{2} (1 + Z) \, k_B T N_0, \tag{9}$$

where N_0 is total particle number. The average ion charge Z is estimated using the Thomas-Fermi ionization state model of More[17], and eq. (9). Using the simplified assumption mentioned above, the temperature is estimated to be about 5 $\sim$ 10 eV, and the average ionization is predictied to be 2.5 $\sim$ 3 at 2 μs.

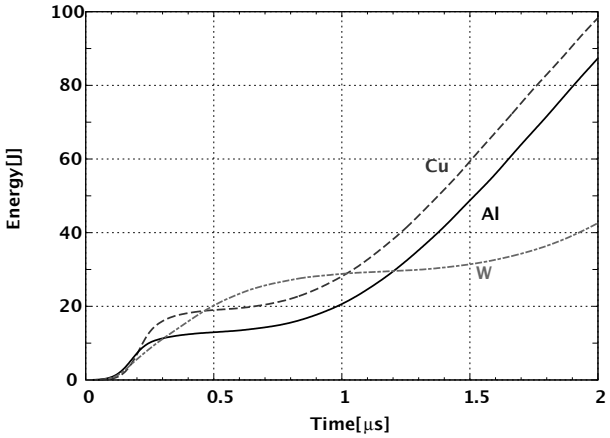

FIG. 9: Evolution of input energy for Cu, Al and W-wire discharges.

C. Conductivity and coupling parameter

The curves of wire/plasma conductivity are obtained from the evolution of radius and resistance shown in Fig. 7 and eq. (4), which is shown in Fig. 10 for Al, Cu and W wires. The wire plasma evolved with phase transition from solid, liquid, and to vapor then dense plasma. After the first phase transition, the conductivity of Cu and Al have minimum values at 500 ns, W at 1μs. The region is supposed to be dominanted by dense low temperature vapor. After this phase, conductivity of all of wires gradually increases according to the plasma evolution.

The Sptizer's conductivity[18, 19] is used as a comparison with the strongly coupled plasmas. The Spitzer's conductivity σ_{sp} is

$$\sigma_{sp} = 2.63 \times 10^{-2} \gamma \frac{T_e^{3/2}}{Z \ln \Lambda}, \tag{10}$$

where T_e is the electron temperature, $\ln \Lambda$ is the Coulomb logarithm, γ is the coefficient depending on the average ionization Z. The Coulomb logarithm $\ln \Lambda$, depends on the temperature and the density, which includes a degeneracy factor modeled by Lampe [20–22]. Figure 10 shows the predicted conductivity using the electron temperature T_e and the average ionization Z. As shown, observed conductivities are 10 times the Spiter's conductivity.

The evolution of coupling parameter is shown in Fig. 11. The coupling parameter Γ depends on the average ion charge, temperature and density. The estimated coupling parameter is $\Gamma \sim 2$ for Al-wire, $\Gamma \sim 2.5$ for Cu-wire and $\Gamma \sim 3$ for W-wire.

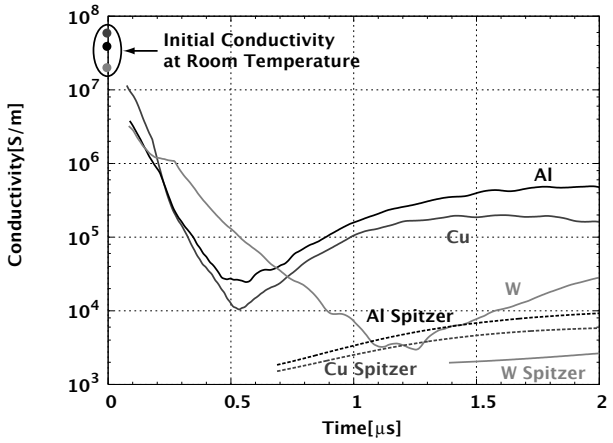

FIG. 10: Evolutions of conductivity for Cu, Al and W-wire, and comparison of those experimental conductivities with the Spiter's one.

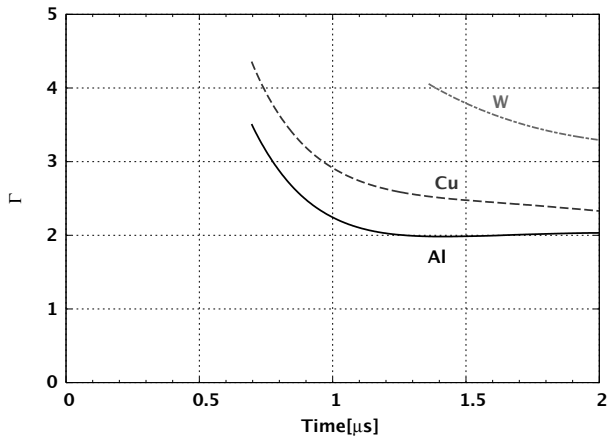

FIG. 11: Evolutions of coupling parameter.

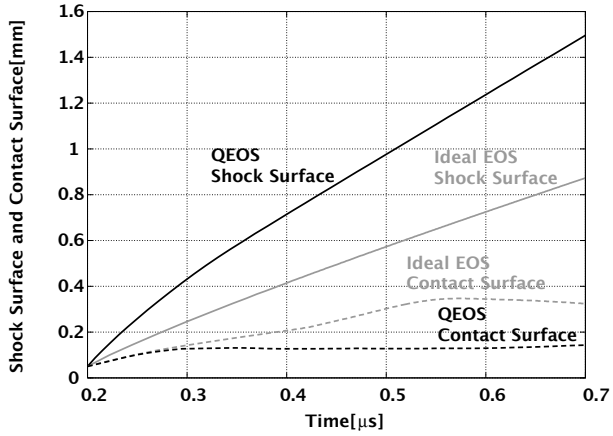

FIG. 12: The evolution of shock surface and contact surface driven by the hydrodynamics based on ideal EOS and QEOS

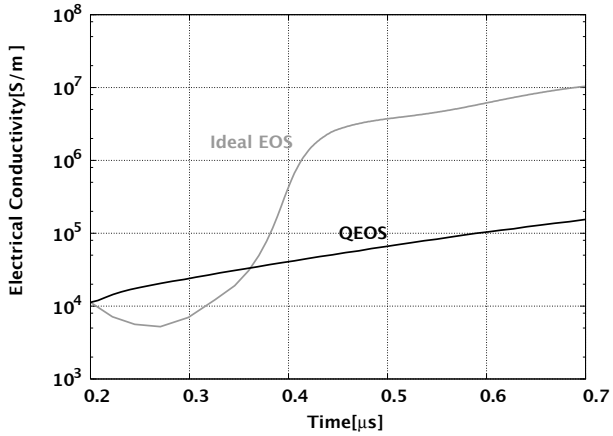

FIG. 13: The evolution of electrical conductivity based on ideal EOS and QEOS

IV. SIMULATION MODEL AND RESULTS

A. Simulation model

In our study, we intended to make a semi-empirical scaling of the equation of state (EOS) and transport coefficients in strongly coupled plasma. To describe the hydrodynamics generated by a pulsed electro-magnetic energy applied to a wire, an 1D-MHD model was used. The set of equations of the model consists of the law of conservation of mass, momentum, and energy together with Maxwell's equations. We calculate the hydrodynamics of wire plasma using the RCIP-CUP method[23–26]. To solve the hydrodynamics, the ideal EOS or QEOS[27] is used. The first step to understand the evolution of strongly coupled plasma is to make a comparison of the hydrodynamic evolutions based on the ideal EOS and QEOS. In this calculation, the transport coefficients are introduced from Spiter's model. For the undefined parameter of Coulomb logarithm, Lampe's degeneracy factor is used [20–22].

The initial condition of simulation is set in a cylindrical coodinate and 50μm wire radius is assumed. The other region is filled with water. The initial temperature is assumed to be 3000 K for Al-wire evolution, considering the vaporization temperature at 2690 K of Al. The voltage is derived from the experimental result.

B. Comparison of results based on ideal EOS and QEOS

The evolution of shock surface and contact surface using these EOS models are shown in Fig. 12. We can see that the shock velocity depends on EOS models and, the shock velocity using QEOS is to be about 3×10^3m/s. The result using QEOS could give us a better prediction of the experimental results. However, both results could not predict the behavior of contact surface, probably because of incorrect transport coefficients.

These results using the ideal EOS and QEOS are com-

pared, and both results show the density profile is uniform. This result is supporting the estimation of the wire plasma density from experimentally observed diameter of plasma column. Both results also show that the current density has uniformed profile.

Evolutions of electorical conductivity derived from the numerical simulations using both EOS are shown in Fig. 13. We can also see that the results strongly depend on EOS models.

V. CONCLUSIONS

In this paper we have shown the time evolution of electrical conductivity, density, shock wave and input energy accompanied by Al, Cu and W-wire explosion using pulse power discharges. We have compared the plasma evoluations in air and in water. Experimental results have shown that the surrounding water is effctive in tamping and also in stabilizing the plasma. From the comparison, we could determin the timing of evaporation. Using a simplified model, we have predicted the temperature and effective charge as a function of input energy. The predicted temperature and effective charge indicate the formation of the low temperature and high density plasma. The coupling parameter Γ is estimated to be 2 for Al-wire, 2.5 for Cu-wire and 3 for W-wire at 2μs from the start of the discharge. In this parameter regine, the experimentally obtained conductivities are 10 times larger than the ones based on Spizer's formula.

We have discussed effects of EOS and transport coeffients on the magnetohydrodynamics using numerical simulations. Results show that both the behavior of plasma evolution and the shock wave evolution in surrounding water are strongly depending on these factors.

The results shown here are the first step to make a semi-empirical scaling of EOS and transport coefficients in strongly coupled plasmas.

We are planning to evaluate the pressure history from the shock wave trace in water, and also directly estimate the temperature using a time-resolved spectroscopy. These measurements together with the MHD simulation based on them should enable us the semi-empirical scaling of the strongly coupled plasma.

[1] N. R. COUNCIL, *Frontiers in High Eneregy Density Physics* (NATIONAL ACADEMIES, 2003).
[2] A. I. Ogoyski, T. Someya, T. Sasaki, and S. Kawata, Physics Letters A **315**, 372 (2003).
[3] T. Someya, A. I. Ogoyski, S. Kawata, and T. Sasaki, Phys. Rev. ST AB **7**, 044701 (2004).
[4] J. Lindl, Phys. Plasma **2**, 3933 (1995).
[5] K. A. Long and N. A. Tahir, Phys. Lett. **91A**, 451 (1982).
[6] Y. T. Lee and R. M. More, Phys. Fluids **27**, 1273 (1984).
[7] S. Kuhlbrodt and R. Redmer, Phys. Rev. E **62**, 7191 (2000).
[8] S. Ichimaru, H. Iyetomi, and S. Tanaka, Phys. Rep. **149**, 91 (1987).
[9] G. Zwicknagel, C. Toepffer, and P.-G. Reinhard, Physics Reports **309**, 117 (1999).
[10] S. Saleem, J. Haun, and H. J. Kunze, Phys. Rev. E **64**, 056403 (2001).
[11] I. Krisch and H. J. Kunze, Phys. Rev. E **58**, 6557 (1998).
[12] H. Yoneda, H. Morikami, K. ichi Ueda, and R. M. More, Phys. Rev. Lett. **91**, 075004 (2003).
[13] H. Morikami, H. Yoneda, K. ichi Ueda, and R. M. More, Phys. Rev. E **70**, 035401 (2004).
[14] T. Mizoguchi, T. Kikuchi, M. Nakajima, and K. Horioka, NIFS-PROC-54 (2004).
[15] K. Horioka, M. Nakajima, T. Sasaki, and T. Mizoguchi, Procidings 15th International Conference High Power Particle Beams (2004).
[16] Y. B. Zeldovich and Y. P. Raizer, *Physics of Shock Waves and High-Temperature Hydrodynamic Phenomena* (ACDADEMIC PRESS New York and London., 1966).
[17] R. M. More, *Atomic Physics in Inretial Confinement Fusion Part I & Part II* (UCRL-84991, 1981).
[18] J. Lyman Spitzer and R. Härm, Phys. Rev. **89**, 977 (1953).
[19] R. S. Cohen, J. L. Spitzer, and P. M. Routly, Phys. Rev. **80**, 230 (1953).
[20] M. Lampe, Phys. Rev. **170**, 170 (1968).
[21] M. Lampe, Phys. Rev. **174**, 276 (1968).
[22] H. Brysk, P. M. Campbell, and P. Hammerling, Plasma Phys. **17**, 473 (1975).
[23] H. Takewaki, A. Nishiguchi, and T. Yabe, J. Comput. Phys. **61**, 261 (1985).
[24] F. Xiao, T. Yabe, G. Nizam, and T. Ito, Comput. Phys. Comm. **94**, 103 (1996).
[25] T. Yabe, Y. Ogata, K. Takizawa, T. Kawai, A. Segawa, and K. Sakurai, J. Comput. and App. Math. **149**, 267 (2001).
[26] S. Y. Yoon and T. Yabe, Comput. Phys. Comm. **119**, 149 (1999).
[27] R. M. More, K. H. Warren, D. A. Young, and G. B. Zimmerman, Phys. Fluids **31**, 75 (1988).

Characterization of pulsed discharge plasma underwater

T. Namihira, T. Yamaguchi, K. Yamamoto, S. Sakai, C. Yamada, J. Choi, T. Kiyan, T. Sakugawa, S. Katsuki and H. Akiyama

Department of Electrical and Computer Engineering, Kumamoto University, 2-39-1 Kurokami, Kumamoto 860-8555, Japan

Abstract

Recently, pulsed discharge plasma produced underwater has been an attractive method to treat wasted water. It is well known that pulsed discharge in water has some physical effects, such as an intense electric field at a tip of discharge plasma, an ultra violet radiation, a chemically radical formation and shockwave generation, for cleaning water. However, the physical characteristics of the pulsed discharge plasma induced underwater are still unclear. For the optimization of the water treatment system utilizing pulsed discharge in water, it is essential to have knowledge about the plasma feature generated by electrical discharge underwater.

In this paper, the temperature of and the electron density in the discharge plasma underwater are described. The magnetic pulse compressor (MPC) was developed and was used to cause the electrical breakdown in water. The developed MPC is all-solid state and is, therefore, maintenance-free generator. Two kind of spectroscopic measurements called as the line-pair method and the Stark broadening carried out for define the temperature of and the electron density in plasma produced underwater. According to experimental results, the temperature of and electron density in the discharge plasma between point-plane electrodes immersed in water are determined 15,000 K and $10^{18}/cm^3$, respectively.

Keywords: Pulsed discharge, electron temperature, electron density

I. INTRODUCTION

In last decade, the pulsed power technology has been developed quickly and can cause the electrical discharge breakdown in liquid medium, such as water and dielectric oil. The discharge in liquid follows some physical phenomena, such as an intense electric field at a tip of discharge column, a radical formation in discharge channel, an ultra violet radiation from discharge and a shockwave generation on boundary between plasma and liquid medium. These phenomena are very attractive for treatments of polluted water and aquatic harmful bacteria and are, however, still lack of knowledge. To realize variety of industrial, medical and environmental application, it is considerable interest in the understanding of electrical breakdown in liquid medium for the optimization of the application systems.

Analysis of optical emission induced by a pulsed discharge underwater was available to define the temperature (T_P) of and the electron density (N_e) in discharge plasma. In this work, the line-pair method and the Stark broadening of H_α spectral were utilized to compute the T_P and N_e, respectively.

II. EXPERIMENTAL SET-UP AND CALUCULATION THEORY

A.Pulsed power generator and discharge electrode

Fig. 1 shows the electrical circuit of the magnetic pulse compressor (MPC) used in this paper. The maximum charged energy into C_0 is 40 J/pulse. Firstly the dc power supply charged C_0 up to setting voltage and then the gate-turn-off thyristor (GTO) turned on. After switching GTO, the saturable inductor SL_0 saturated and main discharge current from C_0 flowed in primary circuit. At that time, the stored energy into C_0 forwarded into C_1 through the pulse transformer PT_1 (4:24). After the energy transportation from C_0 to C_1, the saturable inductor SL_1 saturated and then the discharge current from C_1 flowed in secondary circuit. At the same time, the stored energy into C_1 forwarded to load via the pulse transformer PT_2 (1:5). Finally, the positive pulse voltage was generated at the secondary circuit of PT_2. All magnetic core in the MPC were made by the FINEMET^{TM} (FT-3H, Hitachi Metals, Japan). The MPC has no mechanical and discharge switches and was constructed using all-solid state devices. In the experiments, C_0 was charged up to 2.0, 2.8 and 3.6 kV.

The needle to plane geometry electrode which was immersed into tap water (Conductivity: 25 mS/m) was used as the discharge electrode in this experiment. The radius of curvature at the needle tip was 30 μm. The distance between the tip of needle electrode and plane electrode was fixed at 100 mm. In the experiment, the applied voltage to and the discharge current through the needle to plane electrodes were measured using the voltage divider (EP-100K, Pulse Electronic Engineering

Co., Japan) and the current monitor (Model 110A, Pearson Electronics, Japan), respectively. The Oscilloscope (HP54542A, Hewlett-Packard, USA) recorded the signal from the measurement devices.

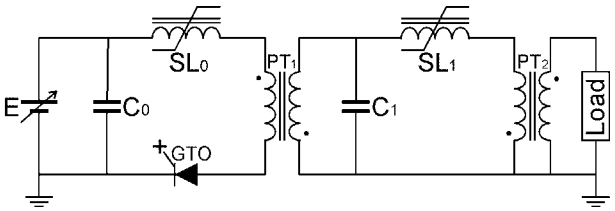

Fig. 1 Equivalent circuit of MPC used in the paper.

B.Calculations of plasma temperature and electron density

Optical emission spectroscopy is a suitable diagnostic to obtain physical information about discharge plasma, such as composition, temperature and electron density. In this paper, the temperature of and the electron density in the discharge plasma produced underwater were calculated by two kinds of spectroscopic measurements. One is the line-pair method for the calculation of the plasma temperature. Another one is based on the Stark broadening of H_α line which has interaction with the electron density.

The temperature of discharge plasma induced in water was given by the following equation [1],

$$\ln(\frac{I\lambda}{Ag_u}) = -\frac{1}{kT}E_u + C \qquad (1)$$

where I, λ, A, g_u, k, T, E_u and C are with emission intensity, its wavelength in nm, its transition probability in 10^8/s, its statistical weight, Boltzmann's constant in eV/K, plasma temperature in K, upper energy level in eV and constant. In this work, four emission lines from copper as anode needle were observed and were used for the calculation of plasma temperature with the Boltzmann's plot. The values of λ, A, g_u and E_u for copper emissions were in Ref. 1.

On the other hand, the electron density was calculated by following equation [2],

$$N_e = 8.02\times10^{12}\times[\frac{\Delta\lambda_{H_\alpha StarkFWHM}}{\alpha_{H_\alpha StarkFWHM}}]^{\frac{3}{2}} \qquad (2)$$

where N_e, $\Delta\lambda_{H\alpha StarkFWHM}$ and $\alpha_{H\alpha StarkFWHM}$ are with electron density in cm^{-3}, full width at half maximum (FWHM) of H_α spectral broadened by the Stark effect in nm and the Stark constant which was given in Ref. 3. Fig. 2 shows the dependence of N_e on $\Delta\lambda_{H\alpha StarkFWHM}$ for different plasma temperature. It is obvious from Fig. 2 that the plasma temperature in the range of 5,000 to 40,000 K has no significant influence on $\alpha_{H\alpha StarkFWHM}$.

Fig. 3 shows the typical integrated photograph of discharge plasma produced in water. In all spectroscopy measurements, a dotted circle in Fig. 3 indicates the region of anode needle tip utilized to sample the discharge emission. The optical multi-channel analyzer (Macs 320, Atago Bussan, Japan) monitored the emission coming out of the anode discharge region through the quartz optical fiber. The emission spectra were displayed by the personal computer.

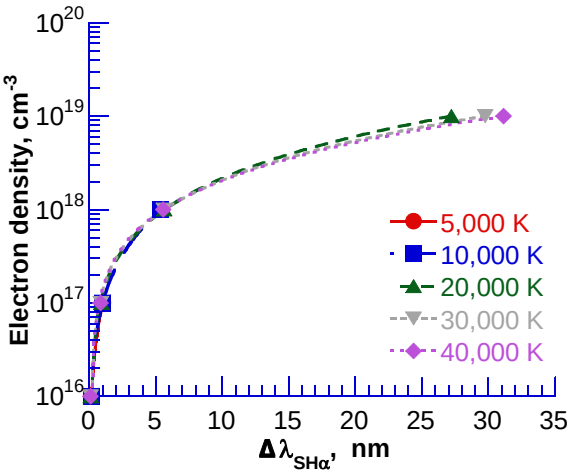

Fig. 2 Relationship between N_e and $\Delta\lambda_{H\alpha StarkFWHM}$.

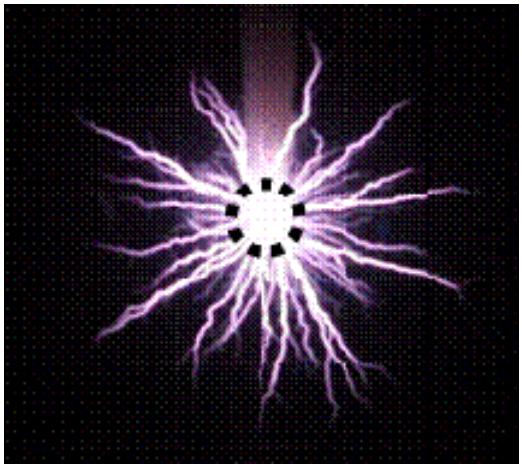

Fig. 3 Typical steel photograph of discharge induced underwater. Condition: V_{ch} into C_0 of MPC=3.6 kV.

III. RESULTS AND DISSCUSSIONS

A.apperances of pulsed discharge plasma underwater

The integrated-photographs of the pulsed discharge induced in water are shown in Fig. 3. It will be observed from Fig. 3 that the discharge spread in all directions for all applied voltages in the range of maximum voltage from 67 to 82 kV. The length of discharge plasma was almost same for different applied voltages to the needle electrode. On the other hand, the number of discharge channels increased with increasing the applied voltage.

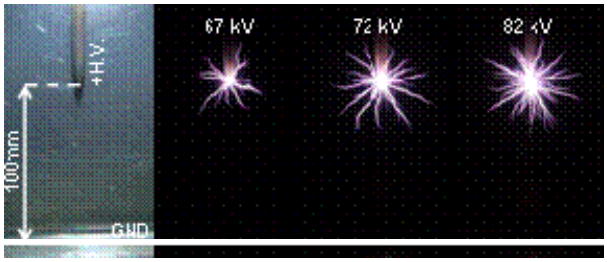

Fig. 3 Discharge appearance for different applied voltages

B.Temperature of pulsed discharge plasma underwater

Fig. 4 shows the typical time-integrated copper spectra of discharge emission in case of 82 kV of applied voltage to the needle electrode. In this experiment, the copper needle was utilized as the discharge electrode. It is confirmed from Fig. 4 that four copper spectra were emitted from discharge plasma locating around needle electrode. Fig. 5 shows the Boltzmann's plot calculated by the Eq. (1) and spectra in Fig. 4. From the inclination of the Fig. 5 (Boltzmann's plot), the plasma temperature was computed at 15,000 K. This temperature (=15,000 K) was also calculated in cases of 67 and 72 kV of applied voltage.

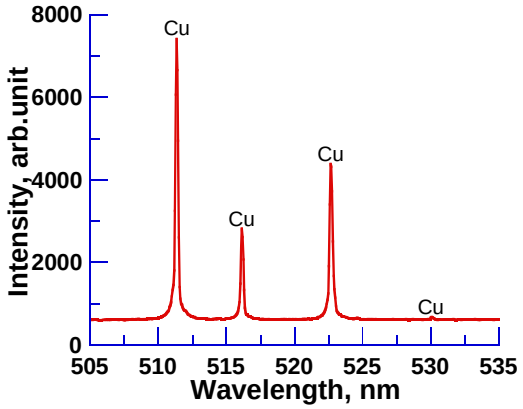

Fig. 4 Four copper spectra emitted from discharge plasma.

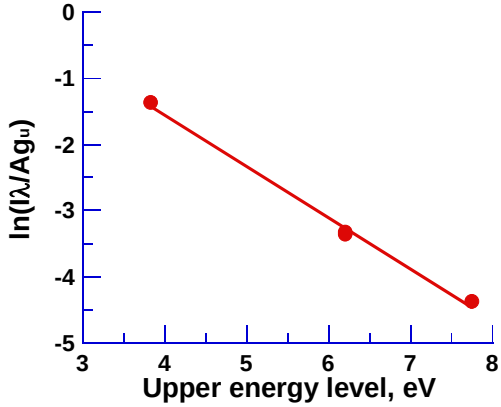

Fig. 5 Boltzmann's plot computed from Eq. (1) and Fig. 4.

C.Electron density in pulsed discharge plasma underwater

It should be noted that spectral broadening caused by the Doppler effect can be ignored when the plasma temperature is 15,000 K. For this plasma temperature, the Doppler broadening computed at less than 0.1 nm. The following equation was used in the calculation of the Doppler broadening [1].

$$\Delta\lambda_D = 2[\frac{2kT\ln 2}{Mc^2}]^{\frac{1}{2}}\lambda_O \qquad (3)$$

where $\Delta\lambda_D$, K, T, M, c and λ_0 are with broadening width caused by Doppler effect in nm, Boltzmann's constant in J/K, plasma temperature in K, radiator mass in kg/molecule, light speed in m/s and unshifted wavelength in nm, respectively.

Fig. 6 shows the typical spectral of H_α (=656.3 nm) broadened by Stark effect. To define the FWHM of broadened H_α spectral, the Lorentzian function was used to make the fitting curve to the spectral measured in experiment. The Lorentzian function is well known as a main function for Stark broadening and is expressed as follow.

$$I(\lambda) = \frac{A}{(\lambda_O - \lambda)^2 + (B/2)^2} + C \qquad (4)$$

where I, λ, λ_0, A, B and C are with emission intensity, wavelength in nm, center wavelength (656.3 nm for H_α) in nm, constant, constant corresponding to the FWHM and constant, respectively.

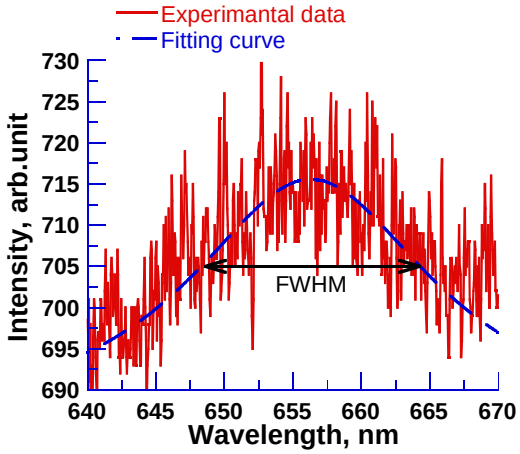

Fig. 6 Typical H_α spectral broadened by Stark effect

Fig. 7 shows the dependence of H_α spectral on time and the waveforms of the applied voltage to and the discharge current in the electrode. It was seen in Fig. 7 that the Stark broadening was smaller with time. This is because that the stored energy in C_1 of MPC decreased with time. Fig. 8 shows the time-dependence of electron density in the discharge plasma underwater and the waveforms of the applied voltage to and the discharge current in the needle to plane electrode. For all applied voltages, the

electron density in discharge plasma located around needle electrode exceeded 10^{18} /cm^3 during early discharge time (<4 μs) and then it decreased quickly with being lower voltage and smaller current.

IV. CONCLUSIONS

The magnetic pulse compressor was constructed as the maintenance-free generator for producing the discharge plasma in water. The temperature of and the electron density in the pulsed discharge plasma induced in water have been calculated by spectroscopic measurements. The following have been deduced.

1. The maintenance-free generator based on the magnetic pulse compressor circuit was utilized to produce the discharge underwater.
2. The temperature of the discharge plasma induced in water was calculated at 15,000 K.
3. The electron density of the discharge plasma underwater was estimated at above 10^{18} / cm^3 in the initial discharge phase.

V. REFERENCES

[1] T. Namihira, S. Tsukamoto, D. Wang, S. Katsuki, R. Hackam, K. Okamoto and H. Akiyama, "Production of nitric monoxide using pulsed discharges for a medical application", IEEE Transactions on Plasma Science, Vol.28, No.1, pp.109-114, 2000.

[2] J. Ashkenazy, R. Kipper and M. Caner "Spectroscopic measurements of electron density of capillary plasma based on stark broadening of hydrogen lines", Physical Review A, Vol.43, No.10, pp.5568-5574, 1991.

[3] H.R. Griem, "Spectral line broadening by plasma", Academic Press, New York and London, 1974.

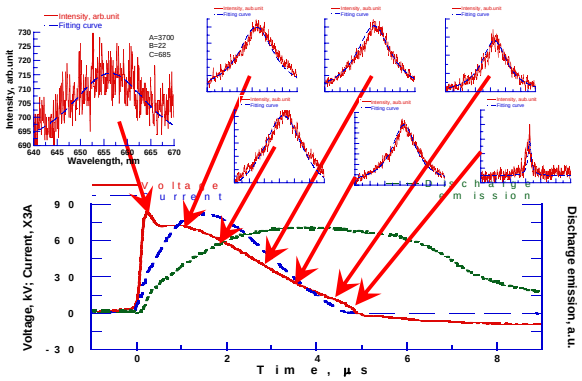

Fig. 7 Dependence of H_α spectral broadened by Stark effect.

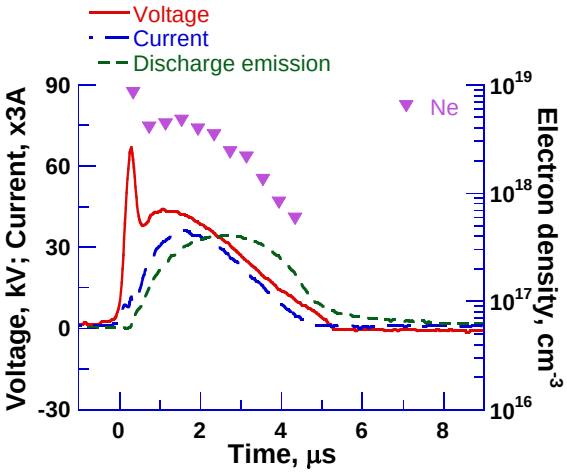

(a) Applied voltage of 67 kV

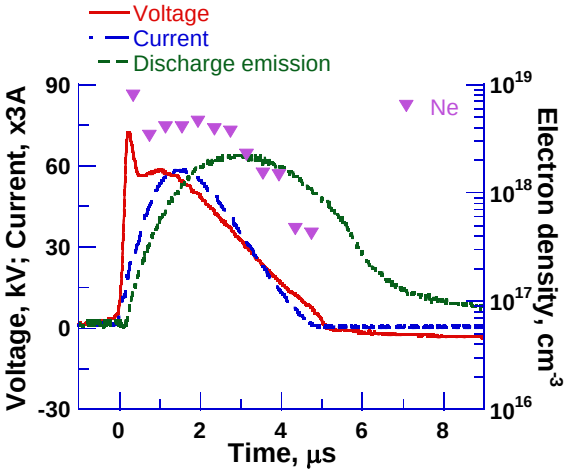

(b) Applied voltage of 72 kV

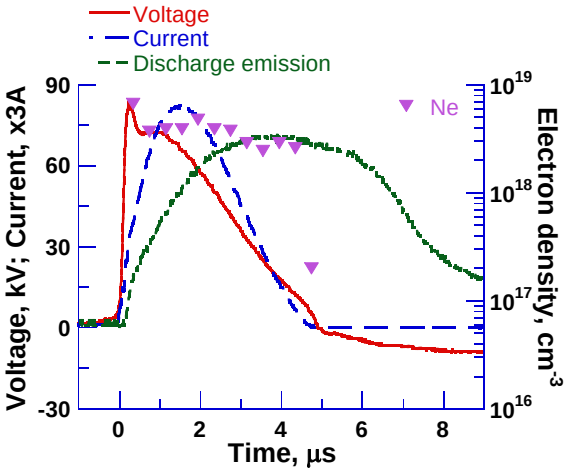

(c) Applied voltage of 82 kV

Fig. 8 Time-dependence of electron density for three applied voltages to the electrode.

Characteristics of Pulsed Discharge Plasmas in Supercritical Carbon dioxide*

T. Kiyan [aξ], T. Namihira[b], T. Sakugawa[c], S. Katsuki[b], H. Akiyama[b]

[a]*Graduate School of Science and Technology, Kumamoto University,*
[b]*Department of Electrical and Computer Engineering, Kumamoto University,*
[c]*Cooperative Research Center, Kumamoto University*

Abstract

In recent years, several studies about electrical discharge plasma in supercritical carbon dioxide (CO_2) have been carried out. One of the unique characteristics of supercritical fluid is a large density fluctuation near the critical point that can result in marked dramatic changes of thermal conductivity. Therefore, the electrical discharge plasma produced in supercritical fluid has unique features and reactions unlike those of normal plasma produced in gas phase. In our experiments, two types of large volume plasma, namely the pulsed streamer discharge and the pulsed arc discharge have been generated in a supercritical CO_2. It was found that the characteristic of the pulsed discharge plasma in supercritical CO_2 depends on the change of the CO_2 density near the critical region.

Keywords: Pulsed discharge, Arc discharge, Streamer discharge, Plasma, Supercritical carbon dioxide

I. INTRODUCTION

Recently, the supercritical fluid is greatly considered as the substitute of the organic solvent used in foodstuffs, medicine and also in chemical reaction technology due to its benign property to environment [1, 2]. Supercritical fluids have unique tunable properties like diffusivity, density, thermal conductivity and mass transfer rate, which can be adjusted continuously by changing temperature and /or pressure. Specially, in the chemical reaction field, supercritical fluid is effectively used to enhance the reaction rate with the control of reaction path such as prevention of the catalyst degradation evolving poisoning material, radical reaction and ion reaction at high temperature. In water medium and at atmospheric condition, discharge plasma was successfully produced and actively used to treat aquatic harmful living organisms, environmental contaminant and also for recycling of building construction materials [3, 4, 5, 6]. Discharge plasma in supercritical fluid has various active chemical effects those might be very interesting and peculiar which would indicate a new horizon to this field.

A large volume of pulsed discharge plasma was successfully produced in supercritical CO_2 at 8 MPa [7]. Specially, near the critical region of CO_2 (31.1℃ and 7.38 MPa), a large fluctuation of its density is observed that can results in some dramatic change of thermal conductivity. Supercritical carbon dioxide is considered as reaction medium because it is nontoxic, non corrosive, inflammable and not explosive. The objectives of our works are to study the potentiality of supercritical CO_2 as a unique medium for plasma formation as well as the characteristics of pulsed discharge plasma.

Fig. 1 shows a typical photographs of the arc discharge (thermal plasma) produced by our experimental apparatus at 0.1 to 8.0 MPa and at 60℃. For instance, the light emitted from discharge plasma directly indicates its chemical activity.

In supercritical CO_2, it is observed that the discharge plasma is much brighter than that in gas phase. It has been already reported that the micrometer-scale discharge plasma in supercritical CO_2 can be generated with very lower voltage than predicted by Paschen's law, but the mechanism for this phenomenon remains unclear [8].

Figure 1. Pressure dependency of arc discharge in CO_2

II. EXPERIMENTAL SETUP

Fig. 2 shows the schematic diagram of the supercritical plasma reactor (AKICO Co., Japan) provided an inspection window through which continuous monitoring is performed. Reactor vessel is made of stainless steel: SUS316 having compressive strength of 30 MPa and the total volume of reaction cell of 1,300 ml. Carbon dioxide was pumped with the syringe pump (THAR SE100X, ISCO Inc., USA) to the cell. The pump head was cooled at about 8℃ by flowing cooling liquid through cooler. A thermocouple and a backpressure regulator controlled the temperature and the pressure of the reaction cell. The experimental pressure was changed from 0.1 to 20 MPa

* The work is supported by the 21st century center of excellence (COE) program on pulsed power science.
ξ email: kyan@sci.kumamoto-u.ac.jp

by introducing carbon dioxide at constant experimental temperature. Fig. 3 shows the electrical circuit of a Blumlein type Pulse Forming Network (B-PFN) consists of 7 stages, which has a capacitor (1.7 nF) and an inductor (0.2 μH), and the pulse transformer (winding ratio 1:3).
A high voltage probe (EP100K, Pulse Electronic Engineering Co. Ltd., Japan) was used to measure the voltage. The current was measured by a current transformer (4997, Pearson Electronics, Inc., USA), which was connected to a digital oscilloscope. During experiment, B-PFN charging voltage was constant at 17.5 kV and 13 kV for the cases of pulsed arc discharge and streamer discharge, respectively, by using DC power source (PS/EW40R15, GLASSMAN HIGH VOLTAGE, INC., USA). The point to plane electrode was employed and the gap distance of electrode was fixed at 10mm.

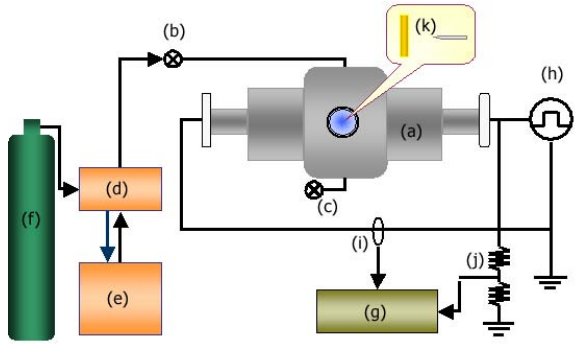

Figure 2. Schematic diagram of the experimental setup, and indices mean as follow; (a) SCF cell, (b) CO_2 inlet, (c) CO_2 outlet, (d) Syringe pump, (e) Cooling system, (f) CO_2 cylinder, (g) Digital oscilloscope, (h) B-PFN DC power source, (i) Current transformer, (j) High voltage probe, and (k) Point to plane electrode.

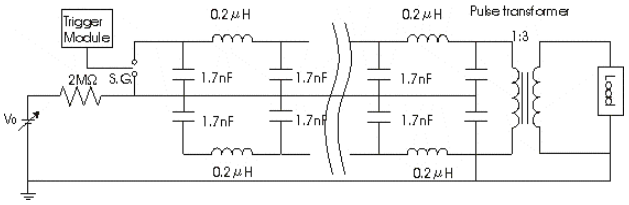

Figure 3. The schematic of Blumlein type pulse forming network and pulse transformer.

III. RESULT AND DISCUSSION

Two types of pulsed discharge plasma such as arc discharge plasma and streamer discharge plasma were produced in supercritical CO_2 by applying pulse voltage. The experimental conditions are shown in Table 1.

Table 1. Experimental conditions

Discharge type	Arc discharge		Streamer discharge
Charging voltage	17.5 kV		13 kV
Temperature	32.5℃	100℃	37℃
Pressure	From 0.1 to 20 MPa		From 0.1 to 10 MPa
Electrode gap	10 mm		10 mm
Pulsed width	260 ns		195 ns

A. Arc discharge

Fig. 4 shows the photograph of typical arc discharge plasma in supercritical CO_2. The electrode gap was 10mm, and was conducted using needle to plane simple electrode geometry. Fig. 5 shows the waveforms of the applied voltage and the discharge current in the needle to plane electrode.

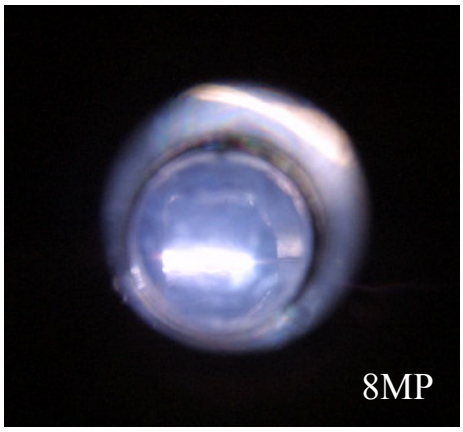

Figure 4. Photograph of typical arc discharge plasma in supercritical carbon dioxide at pressure of 8MPa.

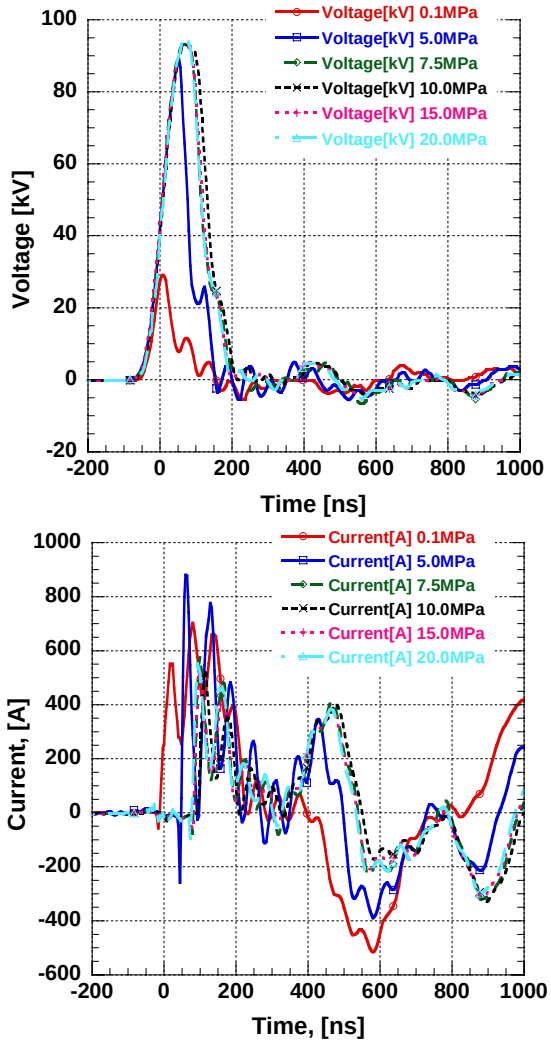

Figure 5. The typical waveforms of applied voltage and discharge current at different pressures in temperature of 32.5℃.

Fig. 6 shows the dependence of the peak voltage on the pressure in cell at temperature of 32.5℃ and 100℃.

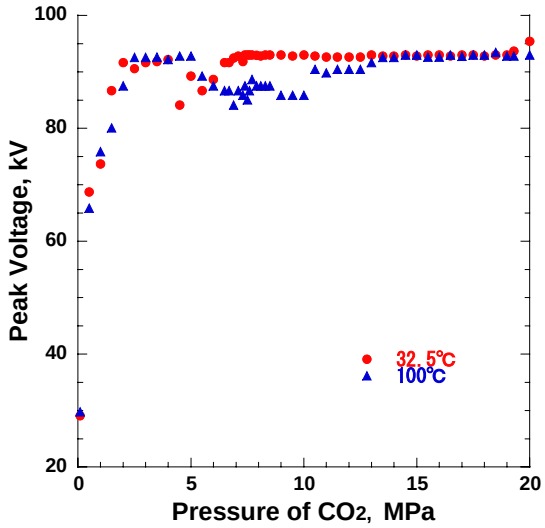

Figure 6. Characteristic of peak voltage at different pressures and temperatures.

Fig. 6 shows that the peak voltage is almost constant at the vicinity of 2 MPa followed rapidly increase, and decreases at the vicinity of 5-7 MPa. The peak voltage is almost again constant after around 10 MPa. This effect may be due to the output voltage of B-PFN did not reach at the design value and was saturated with about 90kV.

Ito and Terashima [8] reported that a rapid decrease of the breakdown voltage happens in the supercritical region using the electrode gap of the micrometer scale. Similar tendency was observed in our experiment but it was not so remarkable. In general, the clustering phenomenon [1, 2] may be considered to explain the competitive effect of the intermolecular interaction of the solvents (effect of the microscopic) and the swinging in the vicinity of a critical point (effect of the macroscopic) on breakdown. Because of the index that relates to fluctuation is the isothermal compressibility k_T and it is specifiable as follows:

$$k_T = -\frac{1}{V}\left(\frac{\partial^2 G}{\partial P^2}\right)_T = -\frac{1}{V}\left(\frac{\partial V}{\partial P}\right)_T,$$

where V, P and T show the volume of fluid, pressure and absolute temperature, respectively. G stands for Gibbs's free energy. The density fluctuation F_d is obtained from the relationship of that spatial fluctuation of the molecules number $\Delta N^2 = \langle N^2 \rangle - \langle N \rangle^2$, the isothermal compressibility k_T and Boltzmann's constant k_B [9]:

$$F_d = \frac{\langle (\Delta N)^2 \rangle}{\langle N \rangle} = \frac{\langle N \rangle k_T k_B T}{V}.$$

Therefore, from the equation of states, and density $\Delta\rho^2$, it is easily seen that the following relations hold:

$$\frac{\langle (\Delta\rho)^2 \rangle}{\langle \rho \rangle^2} = \frac{k_T k_B T}{V}$$

Figs. 7(a), 7(b) show the pressure dependency of "Time delay from the voltage impression to the dielectric breakdown: T_{Delay}" in the point-plane electrode set up in supercritical CO_2 on "Density of carbon dioxide: N_{CO2}".

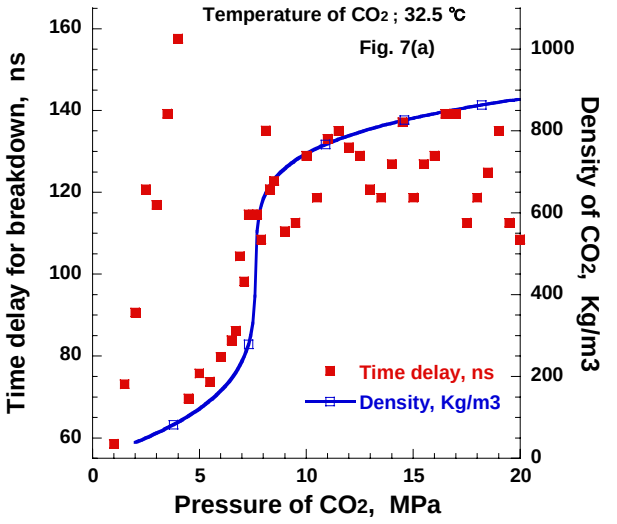

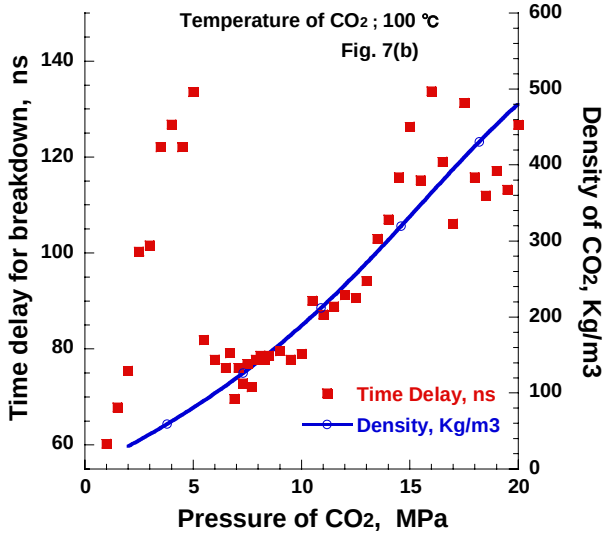

Figure 7. Characteristics of time delay for breakdown and of density of CO_2 at different pressure and at temperature of (a) 32.5℃ and (b) 100℃.

The T_{Delay} is defined as Full Width at Half Maximum (FWHM) of applied voltage. The solid lines in Fig. 7(a) and 7(b) indicate the variation of CO_2 density with pressure at 32.5℃and 100℃, respectively, is calculated from the equations of stats. It reveals that the time delay gradually increases near critical point where the large density fluctuation of CO_2 is usually observed this may be due to which a local channeling between the electron and cluster is formed.

B. Streamer discharge

For the production of streamer discharge, the charging voltage to the generator was controlled so as not to occur the arc discharge and applied voltage to the electrode was

13 kV of peak while the gap between the point and plane electrode was 10 mm. The temperature of reaction cell was kept at 37℃. Photographs of the streamer discharge were taken by using a digital single lens reflex camera (D30, Canon, Japan) through the inspection window of reaction cell. The operating conditions of the camera were the diaphragm F22, exposure time 3s (4 shots integrated) and ISO sensitivity 200. Under our experimental condition (0.1-10 MPa), the waveform of voltage during the production of streamer discharge was almost unchanged and the pulse width and the peak voltage were 195ns and 69kV, respectively.

Figure 8. Photograph of the streamer discharge plasma at pressure of 9.5MPa and at temperature of 37℃.

Fig. 8 shows the integration photograph of the pulsed streamer discharge at 9.5MPa. It was observed that the brightness and thickness of electrical discharge channels increase with the increase in pressure and the brightest one obtained at 9.5 MPa shown in Fig. 6 except at near critical pressure, 7.5 MPa. This effect may be because of the higher input energy at 9.5 MPa and other causes such as thermal conductivity.

IV. SUMMARY

We have produced discharges plasma (arc discharge, streamer discharge) both in gaseous carbon dioxide and in supercritical carbon dioxide. And we have investigated that the relation of time delay and the solvent density in supercritical carbon dioxide. Time delay of breakdown voltage and peak voltage were measured at 32.5℃ and 100℃ for arc discharge and at 37℃ for steamer discharge within the pressure ranges of 0.1 to 20 MPa.

It is concluded that from near critical conditions the time delay for breakdown voltage gradually increased with pressure, though there was fluctuation before critical pressure. A greater discrepancy of the time delay for breakdown was observed near this critical point due to the abrupt change of the density of CO_2. The brightest and thickest streamer discharge plasma was produced at 9.5 MPa. So we think the density of CO_2 is vital parameter for the plasma production in supercritical fluids.

V. REFERENCES

[1] Y. Arai, T. Sako and Y. Takebayashi (Eds.), Supercritical Fluids Molecular Interactions, Physical Properties, and New Applications, Springer, 2002.

[2] Mark A. McHugh and Val J. Krukonis, Supercritical Fluid Extraction: Principles and Practice, 2nd edition, Butterworth-Heinemann, 1993.

[3] S. Masuda, S. Hosokawa, X. Tu and Z. Wang, "Novel plasma chemical technologies - PPCP and SPCP for control of gaseous pollutants and air toxics," J. Electrostatics, vol. 34, no. 4, pp.415–438, 1995.

[4] R. Hackam and H. Akiyama, "Air pollution control by electrical discharges", IEEE Transactions on Dielectrics and Electrical Insulation, Vol. 7, No. 5, pp.654-683, 2000.

[5] T. Namihira, S. Tsukamoto, D. Wang, H. Hori, S. Katsuki, R. Hackam, H. Akiyama, M. Shimizu, and K. Yokoyama, "Influence of gas flow rate and reactor length on NO removal using pulsed power," IEEE Trans. Plasma Sci., vol. 29, pp.592-598, Aug. 2001.

[6] T. Obo, S. Kunitomo and K. Suda, "Inactivation of Chlorine-Resistant Microorganisms by a Pulsed Discharge in water", IEEJ Trans. FM, Vol. 124, No. 6, pp.471-476 (2003)

[7] H. Akiyama et al., 2nd Int'l Workshop on Microplasma, Hoboken, NJ, USA (2004)

[8] T. Ito and K. Terashima, Appl. Phys. Lett. 80, pp.2854-2856 (2002)

[9] H. E. Stanley, Introduction to Phase Transitions and Critical Phenomena Oxford University Press, Oxford, 1971

Electromagnetically Driven Radiative Shocks and Their Measurements

K. Kondo, M. Watanabe, M. Nakajima, T. Kawamura and K. Horioka
4259 Nagatsuta, Midori-ku, Yokohama, 226-8502, Japan
Department of Energy Sciences, Tokyo Institute of Technology

Experimental results on a generation of strong shocks in a compact pulse power device are reported. The characteristics of strong shocks are different from hydrodynamical shocks' because they depend on not only collisions but radiation processes. Radiative shocks are relevant to high energy density phenomena such as the explosions of supernovae. When initial pressure is lower than about 50 mtorr, an interesting structure is confirmed at the shock front, which might indicate a phenomenon proceeded by the radiative process.

Keywords: Radiative shocks, Pulse power, High energy density physics

I. INTRODUCTION

Strong shocks and related phenomena are universal in astrophysics, such as supernovae. The energy of shock is related to the neutrino luminosity[1] and agree with the observation on SN (SuperNova) 1987A. Especially, examining the structure of radiative shock is important to make clear the composition of elements vicinity of a supernova. If pressure, temperature and / or the other physical quantity of the supernova explosion are reproduced in a laboratory scale device, they can significantly contribute to astronomic observation and simulation of the stellar evolution.

It is well known that ordinary hydrodynamic shocks have a well-predictable discontinuous surface. However, characteristics of the radiative shocks are different from hydrodynamic Shocks'. The temperature behind shock is so high that radiative process dominates to form the shock structure. Temperature distribution is not discontinuous and has a precursor[2]. This precursor makes the X-ray emission of the shocked surrounding medium more complex[3].

Recently, using laser, the high energy density plasma is generated for astrophysics[3, 4]. The high energy density plasma is generated in laser irradiated target because it has characteristics of high intensity and directivity. Although laser can produce extremely high power, it is inefficient and too large equipment. In contrast with laser system, pulse power is more efficient and more compact. In this paper, experimental results on a generation of radiative shock in the pulse power is reported.

II. EXPERIMENTAL SETUP

It is the purpose of this study to generate strong shocks and investigate the radiative process in a laboratory scale pulse-power device. A plasma focus system is used for generating shocks. The concept of plasma focus is schematically shown in Fig.1. To make a strong and plain shock wave, cross section of the discharge area is gradually decreased with tapered electrodes and an acrylic guiding tube with constant cross section is located behind the electrodes. For generating strong shocks such as radiative shocks, it is necessary that contact surface, fixed current sheet, push the fluid. A thin Al foil is mounted on the insulator to play the role.

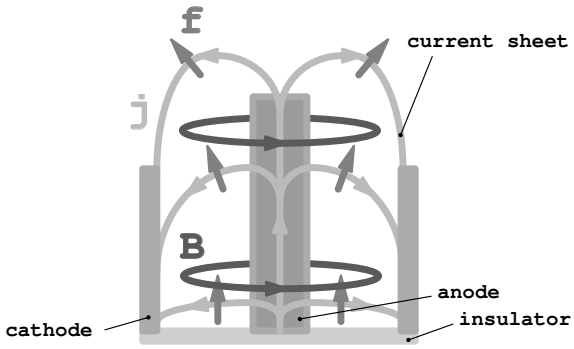

FIG. 1: Plasma focus system

The experimental setup of pulse power and its equivalent circuit are shown in Fig.2 and 3. 12 capacitors of 0.4 μF are arranged in a concentric pattern for reducing the inductance of the experimental setup. Charging Voltage is 20 kV and discharge current is measured by a Rogowski coil. Typical discharge current has LCR damped oscillation waveform, which is and shown in Fig.4. As shown, the peak discharge current is about 180 kA at 0.9 μs.

To change Mach number that indicate the strength of shock wave, initial pressure of gas is controlled by a rotary vacuum pump.

This configuration composed of the acrylic guiding tube is advantageous to measure the shock speed and enables us to make one-dimensional analysis. Shock speed is measured by a fast framing-streak camera through the acrylic tube.

III. EXPERIMENTAL RESULTS

The initial gas is air in this experiment. Initial pressure is measured by a pirani gage and a capacitance manometer. A typical experimental result is shown in Fig.5 at initial pressure of 300 mtorr. In the figure, 4 parts at 2100, 2300, 2500 and 2700 ns are framing images and the

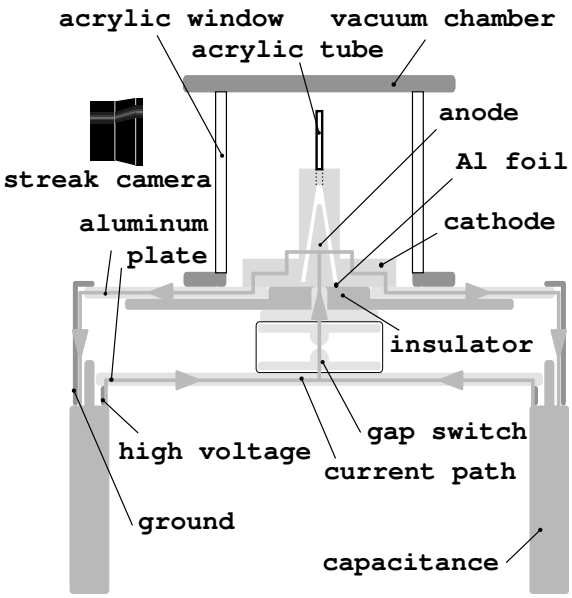

FIG. 2: A sketch of experimental setup

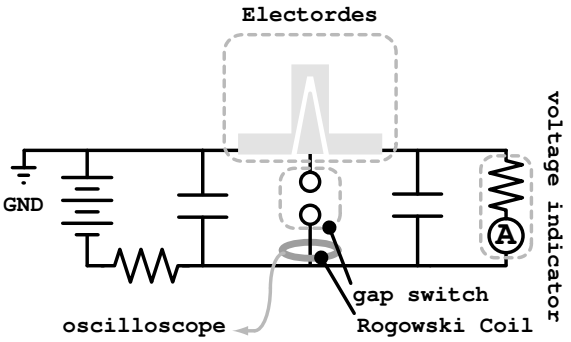

FIG. 3: Equivalent circuit of experimental arrangement

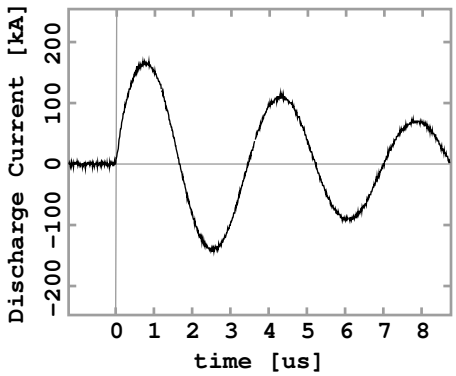

FIG. 4: Typical discharge current

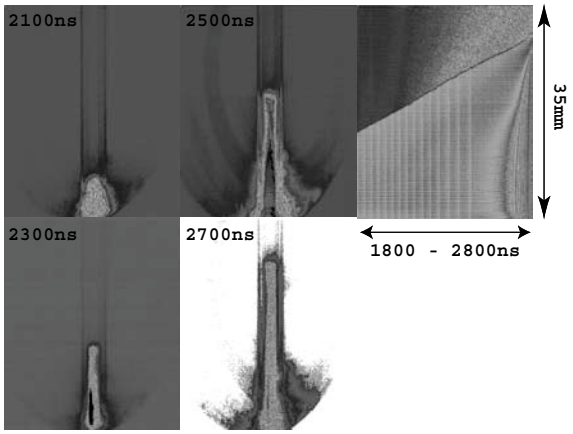

FIG. 5: An experimental result at initial pressure 300 mtorr

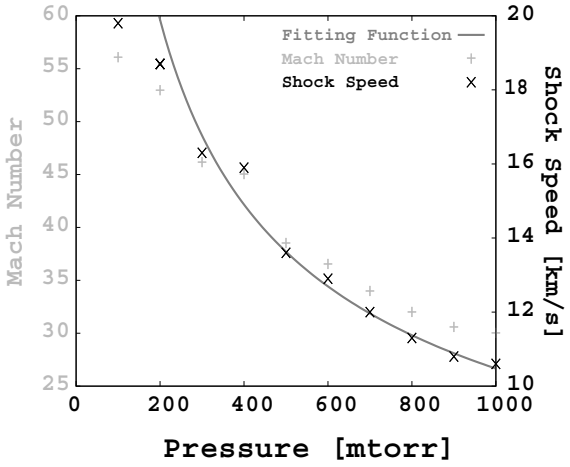

FIG. 6: Relation between initial pressure and shock speed

upper-right is the streak record of the discharge plasma through the guiding tube between 1800 and 2800 ns in Fig.5.

The shock speed is estimated to be about 16.2 km/s from the streak picture in Fig.5 at initial pressure 300 mtorr. The shock speed is evaluated as a function of initial pressure. A relation between the initial pressure and the shock speed is shown in Fig.6 in the range from 100 to 1000 mtorr. The Mach Number M is standardized by a sound velocity v_{N_2} of N_2 at room temperature, 300 K.

$$v_{N_2} = \sqrt{\frac{\partial p}{\partial \rho}\Big|_s} = \sqrt{\gamma RT} \approx 353[m/s] \tag{1}$$

$$M \equiv \frac{D}{v_{N_2}} \tag{2}$$

Where R is gas constant, D is the shock speed of experimental results. It is clear in Fig.6 that the lower the

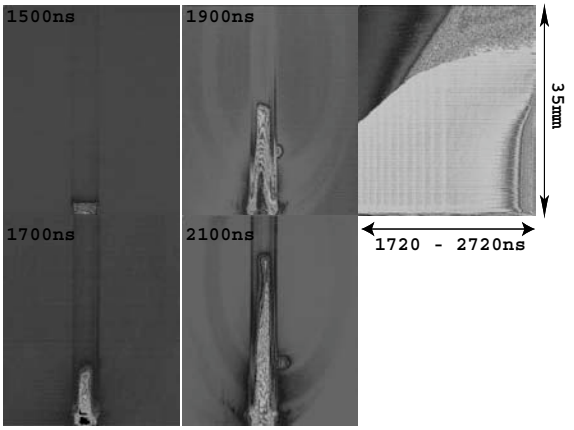

FIG. 7: An experimental result at initial pressure 50 mtorr

initial pressure is , the higher the shock speed is. The line is a fitting curve derived from the Rankine-Hugoniot relation. The Rankine-Hugoniot relation is

$$\frac{p_2}{p_1} = \frac{2\gamma}{\gamma+1}M^2 + \frac{1-\gamma}{\gamma+1} \approx \frac{2\gamma}{\gamma+1}M^2 \tag{3}$$

$$M \approx \sqrt{\frac{\gamma+1}{2\gamma}\frac{1}{p_2}}\frac{1}{\sqrt{p_1}} = \alpha\frac{1}{\sqrt{p_1}} \tag{4}$$

where, p_1 is the pressure in front of a shock surface, p_2 is the pressure behind the shock, γ is the specific heat ratio in air, $\gamma \approx \frac{7}{5}$, and α is a constant. The relation of Eq.4 by least-square fitting is shown with line in Fig.6. Here, α is evaluated to be 843.19. Using Eq.4, p_2 is estimated to be about 8.3×10^2 torr. Here, p_2 is the effective magnetic pressure, which is supposed to be dominated by the discharge current and the experimental set up. In this experiment, p_2 is assumed to be constant.

As shown in Fig.6, the experimental results can be fitted with the Rankine-Hugoniot relation appropriately between 200 and 1000 mtorr.

The experimental result obtained in lower than 100 mtorr is different from that in higher than 100 mtorr. The result obtained by the fast camera at initial pressure 50 mtorr is shown in Fig.7. In the figure, 4 parts at 1500, 1700, 1900 and 2100 ns are framing images and the upper-right is streak picture at between 1720 and 2720 ns.

We have to pay attention that the streak picture in Fig.7 can be divided into two parts. The shock speed is estimated to be about 24 km/s in the first part and 44 km/s in the second part. The shock speed in the first part, 24 km/s, corresponds to the scaling curve in Fig.6, but in the second part is different.

IV. DISCCUSION

The shock wave measured at pressure lower than 100 mtorr has an interesting structure. The shock wave can be classified by a criterion for shock speed D. The criterion[5, 6] for the radiative shock wave is derived from the Rankine-Hugoniot relations including radiation pressure and energy[7]. The Rankine-Hugoniot relations including radiation pressure and energy are

$$\rho_1 u_1 = \rho_2 u_2 \equiv \dot{m} \tag{5}$$

$$\dot{m}u_1 + P_{th1} + P_{rad1} = \dot{m}u_2 + P_{th2} + P_{rad2} \tag{6}$$

$$\begin{aligned}&\dot{m}\left(\frac{\gamma}{\gamma-1}\frac{P_{th1}}{\rho_1} + \frac{1}{2}u_1^2\right) + u_1(E_{rad1} + P_{rad1}) \\ &= \dot{m}\left(\frac{\gamma}{\gamma-1}\frac{P_{th2}}{\rho_2} + \frac{1}{2}u_2^2\right) + u_2(E_{rad2} + P_{rad2})\end{aligned} \tag{7}$$

where ρ, u, P, and E are, respectively, density, velocity, pressure and the energy density. The subscript 1, 2, "th" and "rad" refer to the upstream flow, downstream flow, thermal element and radiation element. In the equations above, the radiation flux is not taken into account since outside the transition zone there is no gradient. The criterion, which characterize a full radiative regime, yields

$$D \geq D_{rad} = \left(\frac{7^7 k^4}{72a}\frac{n_1}{\mu_1^3}\right)^{\frac{1}{6}} \tag{8}$$

where k, a, n_1 and μ_1 are, respectively, the Boltzmann constant, the first radiative constant, the particle density, and the particle mass in the upstream region in front of the shock surface. However, the criterion assumes that matter and radiation fulfill the local thermodynaical equilibrium condition[6]. When the observed shock speed is more than the critical value D_{rad}, it satisfy the condition that ratio between thermodynamical pressure P_{th} and radiative pressure P_{rad}, $P_{rad}/P_{th} \sim 1$ in the downstream region behind of shock surface.

The experimentally obtained D and the critical speed D_{rad} in between 50 and 1000 mtorr are shown in Table I.

This estimation indicates that the condition lower than 100 mtorr satisfies the criterion for the radiative shock wave. The experimental result at $p_1 = 50$ mtorr, in which the interesting structure is confirmed, might indicate that it was proceeded by a radiation process.

V. SUMMARY

In this paper, experimental results on a generation of raditative shock in a compact pulse power device is reported. Results show that the lower initial pressure is,

TABLE I:
Reraltion between The experimentally obtained D and the critical speed D_{rad} in a initial pressure.

Initial pressure [mtorr]	D [km/s]	D_{rad} [km/s]
1000	13.0	23.5
700	12.0	22.1
300	16.3	19.4
100	19.8	16.1
50	23.9	14.3

the higher shock speed is. Electromagnetically driven shocks with M $\sim$ 50 are observed.

In operating condition with initial pressure of less than 50 mtorr, an interesting structure was confimed. This result might indicate that it was proceeded by a radiaiton process.

However, when the initial pressure is 50 mtorr, mean free path in front of the shock wave is $\approx$ mm. In this condition, an anomalous factor may affect the structure and speed of the shock wave because the characteristic length of experimental setup is $\approx$ mm. D_{rad} must be decreased to sufficiently satisfy the criterion for radiative shock wave. As D_{rad} is inversely proportional to the particle mass, we are planning to change the working gas to a heavier gas such as Xe in the future experiments.

[1] H. A. Behte Astro. J. **490**, 765 (1997).
[2] Zel'dovich, Ya. B., & Raizer, Yu. P. 1966, New York : Academic, Physics of Shock Waves and High Temperature Hydrodynamic Phenomena (1966).
[3] J. C. Bozier *et al.* Asroph. J. Supp. **127**, 253 (2000).
[4] S. Bouquet *et al.* Phys. Rev. Lett. **92**, 225001 (2004).
[5] X. Fleury, Laser and Particle Beams **20**, 263-268 (2002).
[6] S. Bouquet *et al.* Asroph. J. Supp. **127**, 245 (2000).
[7] D. Mihalas, & B. W. Mihalas, New York : Oxford Univ. Press, Foundation of Radiation Hydrodynamics (1984).

Optimum Insulator Length in Mather- Type Plasma Focus Devices

H.R.Yousefi and K.Masugata

Faculty of Eng., Toyama Univ., Toyama, 930-8555 Japan

Abstract

It was studied plasma focus devices in order to identifying the design parameters and reasonable relationship among device characteristics. In this paper we have pointed out that the Mather-type plasma focus device operated in the optimum regimes has remarkably low effect on design parameters related to the insulator-electrode geometry. A quantitative parameter has been defined as the ratio of insulator sleeve length and radial distance between the electrodes, "$L_{ins}/b-a$".

1. Introduction

Plasma focus (PF) devices have proven to be an effective tools in the investigation of a variety of phenomena such as J×B acceleration of current sheath, pinch formation, neutron generation and the production of x-rays in high temperature, high-density plasma. The plasma focus is an excellent device for studying plasma dynamics and thermodynamic processes. It is also a rich source of soft x-rays and a variety of the plasma phenomena including nuclear fusion plasmas can be investigated [1]. A number of factors must come together to make the device work properly, which such as geometry of electrodes, geometry of insulator sleeve, type and pressure of filling gas, and the rate of discharge current rise (the steeper the better). The insulator that surrounds the first part of the inner electrode has an important role in the plasma focus dynamics. Since the anode length has reverse correlation with insulator length therefore when the insulator length is decreased or increased actually Anode length is change. Zakaullah etal (1989) indicated that the neutron yield is relatively low whenever the insulator sleeve length deviates from the optimum value. For optimum sleeve length, the sleeve surface appears symmetric and homogeneous all round, predicting an azimuthally symmetric current sheath which in turn leads to higher neutron yield [2]. The optimum insulator sleeve length also reduces the neutron flounce anisotropy. Zakaullah and et al [3] have reported that when the sleeve is too long, the increase inductance may cause the current sheath, to remain at the sleeve surface for longer period of time, and that when the sleeve is too short, the rapid current sheath development may cause spoke formation. As it is known that soft x-ray and neutron yield strongly depends on the curvature of current sheath and the curvature of current sheath has a correlation with the dimension of the device especially to insulator [4,5].similar investigations have been done in the neutron yield dependence on pressure of filling gas for different anode

length [6]. And they could show that optimum anode length can provide highest neutron yield. Since the filling pressure is strongly correlated with the electrode length therefore dependence of neutron yield on the filling pressure was studied by zakaullah etal (1995, 1998, and 1999).In this paper we present a comparative study of some Mather-type device in an optimum condition and introduce two new models. Actually with this model we can obtain insulator and anode length optimum limitation as approximately and then with adjustment the pressure we will reach to optimum condition of device.

2. Theoretical considerations

Much effort has been allocated to the finding of scaling laws for the neutron output with various input parameters, specially the input energy. Accordingly, it has been tried to identify a relationship between insulator length and the spacing between the anode and the cathode under an optimum condition during the pinch. Based on zakaullah et.al, s recent article on a PF device with different insulators and the investigation of neutron efficiency and optimum pressure, it can bee concluded that there is an optimum length for insulator sleeve. The optimum insulator sleeve length provides neutron yield over a wide pressure range of 2-10 mbar whereas for other lengths the pressure range of interest appears relatively narrow [2]. PF devices are generally operated with deuterium in the pressure range of 0.5-10 mbar but recently J .M. Koh etal [4] have reported that highest neutron yield can be produced under 20 mbar pressures. It was found that the insulator length strongly affects the filling pressure and hence the neutron yields. Generally the discharge tends to shorten its path with increasing pressure. Hence by increasing or decreasing the insulator length the pressure range of the gliding discharge is shifted toward lower or higher pressure values, respectively. If the insulator length becomes smaller than the radial distance between the electrodes we will not only have a discharge along the cylindrical insulator but also a discharge radial between the electrodes becomes visible [7]. Therefore, we introduce an optimum insulator sleeve length, (L_{opt}) in which, the optimum pressure corresponding to the maximum neutron yield, is increased with an increase in the insulator length up to L_{opt} with a sudden subsequent decrease. In the present study more than twenty PF devices with different energies have been examined and a limit for the design of insulator length has been arrived at (Table-1). The scaling parameter can be defined as $L_{ins}/b-a$ which takes up values from 1 to 1.8.Where b is the inner radius of the cathode, a is the outer radius of the anode and L_{ins} is the insulator length (Fig. 1). This quantity controls the discharge of the plasma in the gun tube and its constancy over a wide range of plasma focus devices. Since changing insulator length actually points to the curvature of the current sheath; we have tried to find a correlation between the curvature of the current sheath and the neutron yield. The current sheath curvature for different insulator lengths in a PF device has been plotted, and neutron yield for them compared through eq.(1).

$$Z(r) = -\frac{a}{2q}\left[x(x^2 - q^2)^{1/2} - (1-q^2)^{1/2} - q^2 \mathrm{Ln}\frac{x + (x^2 - q^2)^{1/2}}{1 + (1-q^2)^{1/2}} \right] \qquad (1) \qquad [8]$$

With x = r/a

$q = (\mu_0 I^2 / 8\pi^2 a^2 \rho_0 u^2)^{1/2}$ (2)

Where r is the distance from the axis, a the radius of the center electrode, ρ_0 the density of the undisturbed gas, I the current in the plasma sheath, and u the velocity of the sheath. It seems that for optimum insulator length in every plasma focus device in which current sheath is passed from point of r=b, there is the highest neutron yield. The optimum length has been determined by use of r=b in eq.(1) for different devices **,** it means that $Z(r=b) = L_{opt}$.

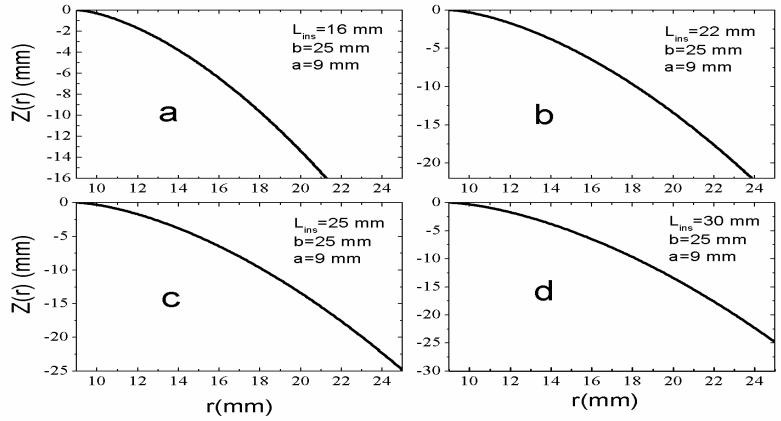

Fig.2 Current sheathe curvature for a device [2] with constant dimension and four different insulator lengths

Results and Discussion

In the first model, a dimensionless parameter "$L_{ins}/b-a$" was defined and found that a good focusing effect is usually obtained in plasma focus experiment when this parameter is in the limited range $(b-a) \leq L_{ins} \leq 1.8\,(b-a)$. This length can provide optimum pressure with the highest neutron or x-ray yield. Also found that when insulator length deviates from this range, neutron yield is decreased.

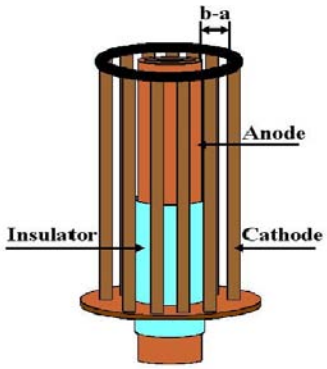

Fig. 1 Schematic of Plasma focus device

Table1: List of characteristics data for various Mather-Type PF devices

Mather-Type PF devices	W_0 (kJ)	V_0 (kV)	a (mm)	b (mm)	L_{ins}	$\frac{L_{ins}}{b-a}$	Min < L_{ins} < Max		L_{opt}	**F**
							Min	Max		
Reference (9)	?	20	10.5	25	25	1.7	14.5	26	19	> 1.6
Reference (10)	2.2	25	10.5	36	45	1.8	25.5	46	49	> 2.1
Reference (11)	1	22	8.5	25	25	1.5	16.5	29	27	> 1.8
Reference(12)	2.3	12	9	25	25	1.5	16	29	25	> 1.8
Reference(13)	2.2	25	10.5	40.5	45	1.5	30	54	65	> 2.2
PFII(14)	4.7	30	18	36	35	1.9	18	34	19	> 1.5
Reference(15)	7	25	17.5	40	26	1.1	22.5	40	28	> 1.6
Reference (16)	3.3	15	9.5	32	27	1.2	22.5	40	42	> 2
Reference(2)	2.3	12	9	25	16	1	16	29	25	> 1.8
Reference(2)	2.3	12	9	25	22	1.3	16	29	25	> 1.8
Reference(2)	2.3	12	9	25	30	1.8	16	29	25	> 1.8
Reference (17)	4.7	30	19	42	35	1.5	23	41	28	> 1.6
Reference(18)	700	25	48	76.5	45	1.5	28.5	51	22	> 1.3
KPF-1M(19)	40	25	25	50	30	1.2	25	45	27	> 1.5
Reference(20)	1.8	38	10	22.5	20	1.6	12	22.5	15	> 1.6
CPF-1M(21)	40	25	40	65	30	1.2	25	45	20	> 1.3
Reference(22)	200	20	50	100	63	1.2	50	90	53	> 1.5
Reference(23)	2.3	12	9	25	25	1.5	16	29	25	> 1.8
Reference(24)	2.3	12	9	28.8	25	1.2	20	36	35	> 2
DPF-40(25)	18	20	32	59	35	1.3	27	49	26	> 1.4
ICN-(26)	3.3	30	20	50	30	1	30	54	42	> 1.7

The curve of current sheath was plotted by use of eqs.1 (with q=1) for a device with constant dimension and four different insulator lengths. In accordance with Zakaullah,s[10] finding , the neutron yield in optimum condition were approximately 6×10^7, 1.7×10^8, 2×10^8, 8×10^7 for insulator lengths of 16, 22, 25, 30 respectively. These results indicate that the neutron yield for an insulator length of 25 mm is the highest. Figure (2) from (a) to (d) shows that with an increase in the insulator length, the tail of parabolic goes higher. Therefore, it can bee seen that whenever current sheath is passed from the point of r=b we will have the highest neutron yield. This result in good agreement with our insulator length's range (table-1, ref.10, 11), Also as shown in table (1), optimum insulator length for more devices is in good agreement with the range of defined range. When the insulator length deviates from the optimum value, the leakage current will be increased And the modification factor, as well as, the current sheath speed is decreased. Consequently transit time of plasma sheath to the end of anode will be bigger than the current rise time from the capacitor bank whereas this is contradictory to the most important pinch condition, in which The plasma axial transit time is equal to the quarter time period, and then it becomes the optimized condition for the DPF**.** Below the optimum insulator length, the axial transit time (t_a) is increased. Therefore, in order to synchronize t_a with the current rise time from the capacitor bank, one needs to decrease the pressure. Below the optimum pressure the number density of the deuterons accelerated in the axial direction is lower which results in a lower neutron yield. At lengths above the optimum, the axial transit time (t_a) is decreased and in order to synchronize t_a with the current rise time from the capacitor bank should be increase the pressure, At pressures above the optimum pressure the speed of the deuterons decreases during the post collapse phase as it has to pass through dense ambient which will result in less efficient beam–target interaction leading to low neutron yield.

Reference:

[1] M.Zakaullah and et al. Physica Scripta 53(1996)360.

[2]M.Zakaullah and etal.Physics.Letters A.**137**, 39 (1989)

[3] M.Zakaullah and et al.Plasma Source Sci.Techno.**4** (1995) 117-124

[4] J M Koh and etal Plasma Sources Sci. Technol. **14** (2005) 12–18

[5] 30th EPS Conference on Contr.Fusion and Plasma Phys., St.Petersburg, 7-11 July 2003 ECA Vol.**27A**, P-1.208

[6] Hyung-Jong Woo and etal.Plasma Phys.Control.Fusion 46(2004)1095-1104

[7]H.Bhuyan and et al.Meas.Sci.Technol.**14**, 1769 (2003).

[8] H.Krompholz.Phys.letters, **77A,** No.4 (1980)

[9]J.Fugeas nd .Vonpamel.J.Appl.Phys.**66** (3), 1080 (1989)

[10]R.k.Rout and etal. IEEE Trans.plasma Sci.**23**, 996 (1995)

[11]J.N.Feugeas.J.Appl.Phys.**66**(8), 467(1989)

[12]M.Zakaullah and et al. Plasma Source Sci. Technol. **7** (1998) 206-218

[13]A.Shyam and R.k.Rout.IEEE Trans.on plasma Sci, **25,** No.5, 1166 (1997)

[14]H.Kelly and A.Marquez.Plasma phys.control.fusion **38,** 1931 (1996)

[15] Mehrdad Kashani.Journal of the physical society of Japan. **72**, No.3, 526 (2003)

[16]S.Lee and etal. Am.J.Phys.**56** (1), 62 (1988)
[17]C.Moreno, H.Bruzzone.IEEE Trans.on plasma Sci., **28**, No.5, 1735 (2000)
[18]T.R.Yeh and et al. Experimental studies of the 700 kJ two-Gun plasma focus Devices
[19]F.N.Beg and et al. Applied physics letter. **80**, No.16, 3009 (2002)
[20]N.I.Ayzatsky and etal.ВОПРОСЫ АТОМНОЙ НАУКИ И ТЕХНИКИ .**39,** 141 (2001)
[21]H.Bruzzone and R.Vieytes.Plasma Phys.Control.Fusion **35**, 1745,(1993).
[22]M.Zakaulllah and et al. Plasma phys.control.fusion.**35**, 689 (1993).
[23]M.shafiq and et al. Plasma Source Sic.Technol.**12**, 199 (2003)
[24]Ming Fang Lu. Nuclear Instruments and Methods in Physics Research B **117,** 452 (1996)
[25]F.Castillo and et al. The Fuego NuevoII Dense Plasma Focus.
[26] A.Donges and et al.Physics letters.**76** A, No.5, 6. (1980).

SOFT X-RAY GENERATION WITH 120 kJ PLASMA FOCUS DEVICE

J. Mizuno, M. Sato and K. Shimoda

Department of Electronic Engineering, Gunma University,
1-5-1 Tenjin-cho, Kiryu, 376-8515, Japan

ABSTRACT

We newly constructed a 120 kJ plasma focus device. In a preliminary experiment, the discharge current reached at 670 kA by 3.7 microseconds from initiation of discharge current, and a clear dip is seen at the tops of it. Moreover generation of soft X-rays is verified by the PIN diode signal with the beryllium foil of which thickness was 20 micrometers.

Keywords: plasma focus, soft X-ray

1. Introduction

The plasma focus device is well known as an inexpensive and compact source of intense soft X-rays. It has been used for number of applications: soft X-ray microscopy[1)], soft X-ray lithography[2)], X-ray backlighting for high-density plasmas[3)]. Recently the plasma focus device has been also studied as a EUV light source[4)]. For the EUV light source, high repetition rates and less debris are important, but high intensity is required for the soft X-ray source. In order to obtain higher intensity of the soft X-ray source, control for the size and the geometry of soft X-ray sources generated in the focused phase is important. More easy way to obtain higher intensity of the soft X-ray source is increase of the plasma current in the focused phase. So we newly constructed a 120 kJ plasma focus device.

We had been performed the experiment with a small plasma focus device[5)]. There were two problems in this small plasma focus device. First problem was the weak intensity of the soft X-ray source. We tried measurement with a crystal spectrometer, but clear line images were not obtained. This fact suggests the weakness in the intensity of the soft X-ray source. Second problem was the shape of the soft X-ray source. It is well known that the geometries of soft X-ray sources are column shapes in the case of low Z gases, and are spot shapes (hot spot) in the case of high Z gases[3)]. In our experiment, images of soft X-ray sources were often column shapes in the case of argon gas (high Z gas). This fact might be caused by no optimization for working condition, but we simply consider that the current flowing into pinched plasma is relatively low. Therefore we constructed a new large plasma focus device.

In this paper details of the new plasma focus device and the results obtained by preliminary experiment are presented.

2. Experimental Setup

We newly constructed a 120 kJ plasma focus device. This device is consisted of a condenser bank, electrodes, a vacuum vessel and several cables. The photograph of this device is shown in Fig. 1. The condenser bank is composed from eight condensers, and box shape condensers are shown in left side of Fig. 1. The maximum voltage and the maximum stored energy of each condenser are 45 kV and 15 kJ, respectively. Total stored energy of this condenser bank is 120 kJ. Each condenser has a start switch and a crowbar switch, because these condensers were firstly made for power supply of magnetic confinement experiment at STP group in Institute of Plasma Physics at Nagoya University. The crowbar switches are not required in our experiment, but there are kept upon the condensers because replacement of those is so difficult.

The start switches are fired by using a three-stage triggering system shown in Fig. 2. First stage of it is a thyratron pulse generator of which output voltage is 16 kV. This output voltage fires the gap switch of second stage, and the output voltage of 28 kV is supplied to the gap switch of the third stage. Finally the pulsed voltages of 45 kV are supplied to the start switch attached to the condenser. Then the charges stored in

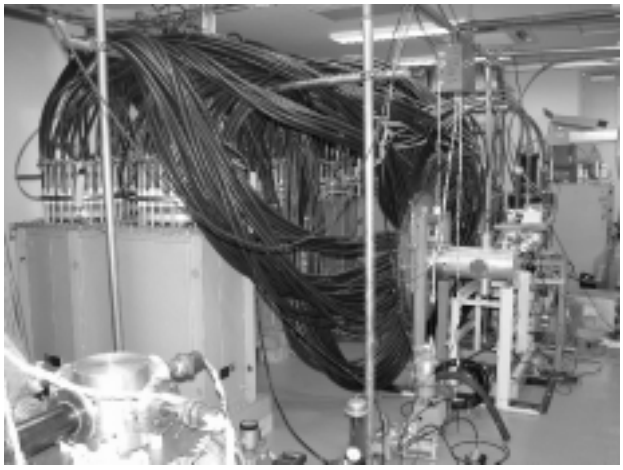

Fig. 1 The photograph of 120 kJ plasma focus device.

the condensers are transferred to the electrodes through the several cables. The cables are the RG-17A/U coaxial cables and there lengths are 4 m. Twenty-four cables are connected to each condenser, and the sum of the cables is 192. The all cables are connected to a collector plate. The collector plate is 0.95 m in diameter and is attached to the vacuum vessel. The vacuum vessel is cylindrical shape and is shown in right side of Fig. 1. The collector plate and the vacuum vessel are made of aluminum. The charges passing through the cables are collected and supplied to the electrodes.

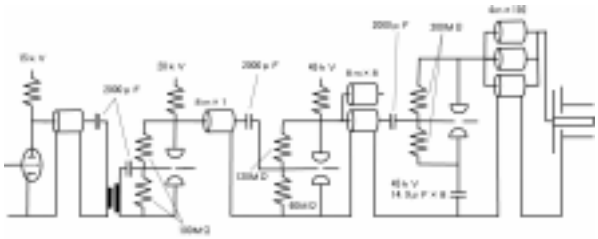

Fig. 2 Schematic drawing of the three-stage triggering system.

In the vacuum vessel, an inner and an outer electrode are placed. The outer electrode is constructed from 18-copper rods of which diameters are 10 mm; the geometry of the outer electrode is like a square cage. The inner electrodes are column shape, and outlooks of the electrodes are shown in Figs. 3. Figures 3 (a) and (b) show the electrodes for 120 kJ plasma focus device and that for the small plasma focus device, respectively. The outer diameter of the inner electrodes and the inner diameter of the outer electrodes are 50 and 100 mm, respectively. The lengths of the electrodes are different in Figs. 3 (a) and (b). The lengths of the electrodes are 380 mm in Fig. 3 (a), and are 2.45 times longer than those in Fig. 3 (b). The difference in the lengths of the electrodes is caused by the difference in capacitances of the condenser banks. The value of 2.45 is empirically determined by the ratio of the capacitances (119.2 μF／55.6 μF). Insulators are located between the inner and the outer electrode. The insulators are made of a Pyrex glass, and the outer diameters of those are 55 mm. The length of the insulator shown in Fig. 3 (a) is 75 mm, and is little longer than the value of 51 mm shown in Fig. 3 (b).

Figures 4 show the schematic drawings of the experimental setup and the four stages in plasma focus operation. In the 120 kJ plasma focus device, the four stages in plasma focus operation are same as those in the usual plasma focus devices; breakdown occurs on the surface of the insulator, the current sheet is generated and runs down, the current sheet radially collapsed and the focused plasma is finally generated on the axis of the diodes. The feature of our new device is long run down phase. This caused by the large capacitance of the condenser bank mentioned above. In the preliminary experiments reported here, the condenser bank was used with the charged voltage of 12 kV. Hydrogen gas was used as a working gas, and its pressure was 5 torrs.

In the experiments, a Rogowski coil was used to measure the discharge current, and two PIN diodes were used to detect the visible lights and soft X-rays generated from the pinched plasma. In front of one PIN diode, the beryllium foil of which thickness was 20 micrometers was set as a filter, and was used to detect the soft X-rays. In front of another PIN diode, the thin quartz glass of which thickness was 1.5 mm was attached. This quartz glass is able to pass through visible light and ultraviolet rays of which wavelengths are longer than 170 nm. Appearance of this signal suggests the pinched plasma moves into a small region around the diode axis.

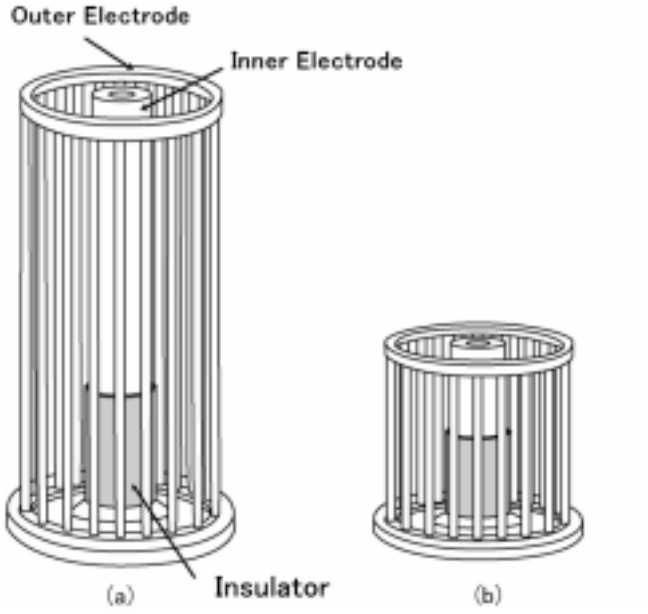

Fig. 3 Outlooks of the electrodes; 120 kJ plasma focus device (a), small plasma focus device (b).

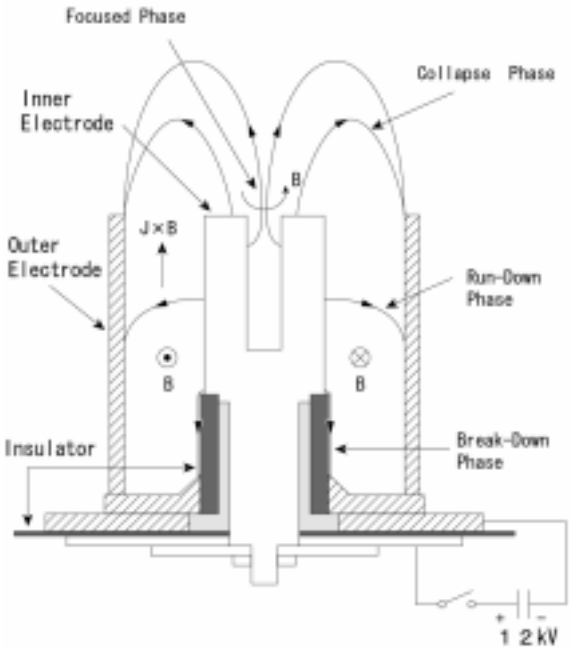

Fig. 4 The schematic drawings of the experimental setup and the four stages in plasma focus operation.

3. Experimental Results

The typical waveforms of a discharge current and the PIN diode signals are shown in Figs. 5. In upper figure of Figs. 5, the upper and the lower trace correspond to the discharge current and the PIN diode signal, respectively. In these figures the PIN diode signals obtained with the thin quartz glass are called by visible lights. In the shot shown in upper figure of Figs. 5, the discharge current reaches to about 670 kA by 3.7 microseconds from initiation of discharge current, and a clear dip is seen at the tops of it. From the signal called by visible light, pinching of the plasma is verified. In the shot shown in lower figure of Figs. 5, the maximum value of the discharge current is relatively low, but generation of soft X-rays is verified. The maximum value of the PIN diode signal is 25 V, and this value became high in comparison with that obtained by the small plasma focus device.

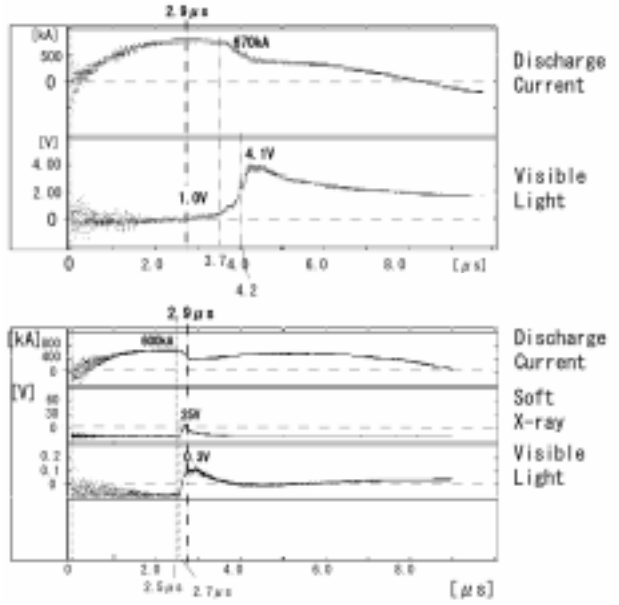

Fig. 5 The typical waveforms of a discharge current and the signals of the PIN diodes

4. Summary

We newly constructed a 120 kJ plasma focus device. In a preliminary experiment, the discharge current reached at 670 kA by 3.7 microseconds from initiation of discharge current, and a clear dip is seen at the tops of it. Moreover generation of soft X-rays is verified by the PIN diode signal with the beryllium foil of which thickness was 20 micrometers. The preliminary experiments were performed by the charged voltage of 12 kV. After maintenance of the condenser bank, we will try the experiment with higher charged voltage. Our goal in near future is to perform the experiment in which the discharge current exceeds 1 MA.

References

1) M. Howells, J. Kirz and D. Sayre, Sci. Am., **264** (1991) 42.
2) Y. Kato, I. Ochiai, Y. Watanabe and S. Murayama, J. Vac. Sci. Technol., **B6** (1988) 195.
3) F. Beg, I. Ross, A. Lorenz, J. Worley, A. Dangor and M. Haines, J. Appl. Phys., **88** (2000) 3225.
4) M. McGeoch, Appl. Opt. **37** (1998) 1651.
5) H. Itano, N. Iwami, K. Shimoda and M. Sato, NIFS-PROC-50 (2001) 131.

Generation of Intense Pulsed Heavy Ion Beam by a B_y Type Magnetically Insulated Ion Diode with Active Ion Source

M. Higashiyama, S. Takata, R. Tejima, J. Kawai, I. Kitamura, K. Masugata
Faculty of Eng., Toyama Univ., Toyama, 930-8555 Japan
H. Tanoue, and K. Arai
National Institute of Advanced Industry Science and Technology,
1-1-4, Tsukuba, Ibaraki, 305-8568 Japan

ABSTRACT

A new type of pulsed heavy ion beam diode was developed, where a new acceleration gap configuration is used with active ion source of gas puff plasma gun. With the plasma gun, nitrogen plasma was produced and injected into the acceleration gap of the diode. The ion diode was operated at diode voltage ≈ 200 kV, diode current ≈ 2.0 kA, pulse duration ≈ 150 ns. Ion beam of ion current density ≈ 13 A/cm^2 was obtained at 55 mm downstream from the anode. From Thomson parabola spectrometer measurement we found that N^+ and N^{2+} beam of energy 60-300 keV were accelerated with impurity of protons of energy 60-150 keV. The purity of the beam was estimated to be 87 %. By using spherical electrode for focusing ion beam ion current density was enhanced by a factor 2 and ion current density of 27 A/cm^2 was obtained. To generate metallic ions, vacuum arc plasma gun was developed and aluminum plasma of ion current density > 500 A/cm^2 was obtained with plasma drift velocity 2.5×10^4 m/s.

Keywords: Intense pulsed ion beam, Pulsed power ion diode, Plasma gun, Magnetically insulated ion diode

1. Introduction

Intense pulsed heavy ion beams (PHIB) such as carbon, nitrogen, or aluminum have a wide area of applications including nuclear fusion, materials science, etc. For example, by the irradiation of PHIB on to the material, very attractive effects are expected as shown in the followings;

1) Pulsed surface heating,
2) Production of high dense ablation plasma,
3) Production of strong pressure and shock wave,
4) Deposition of atoms.

Hence it is expected to be applied to surface treatment [1], thin films deposition [2], or an implantation process. Especially for the implantation process, PHIB is expected to be used as a new type of ion implantation technology since the ion implantation and surface heat treatment or surface annealing are completed in the same time [3-6].

Pulsed ion beams usually have been generated in pulsed power ion diodes with surface flashover ion sources. However, in the diodes producible ion species are limited. In addition the beams usually contains much quantity of impurity ions [7,8]. In the implantation process highly pure ion beam is required, hence conventional pulsed ion diode is not suitable for the process.

To produce pulsed heavy ion beam with acceptable purity a new type of pulsed ion beam source has been developed. In the ion souse B_y type magnetically insulated acceleration gap is used with active ion source of gas puff plasma gun [4,5]. In addition to produce metallic ions, vacuum arc plasma gun was developed[4]. In the paper preliminary results of the experiments are described.

2. Ion Diode Experiment

Figure 1 shows the schematic of the experimental system. The system consists of a high voltage pulsed power generator, a gas puff plasma gun, and a B_y type magnetically insulated ion acceleration gap (diode).

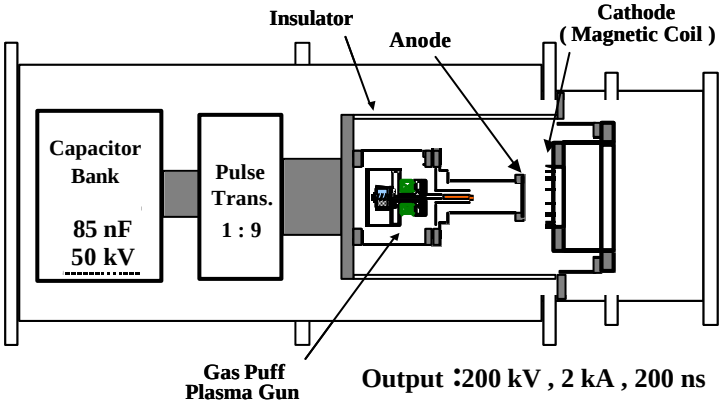

Fig.1. Schematic of the experimental system.

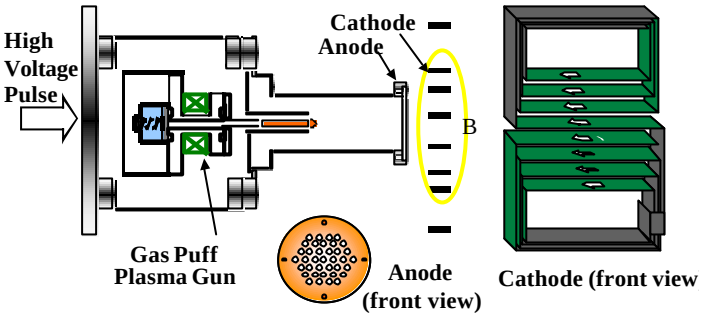

Fig. 2. Cross-sectional view of the B_y type magnetically

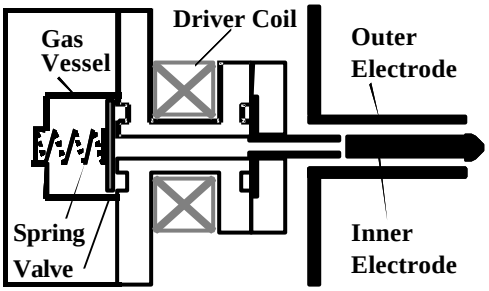

Fig. 3. Gross-sectional view of the gas puff plasma gun.

The pulsed power generator used in the experiment consists of a fast capacitor bank and a step up transformer. The capacitor bank of maximum charging voltage 50 kV produces high power pulse of duration ~150 ns (FWHM). The pulse is voltage magnified by the multi-turn step up transformer using magnetic cores of amorphous metal. The output parameter of the generator is 200 kV, 2 kA, 150 ns, which is applied to the anode of the diode.

The diode consists of a cylindrical anode of diameter 60 mm at the top, length 115 mm, and a cathode of grid structure. Inside the anode a gas puff plasma gun was installed to produce ion source plasma. In the experiment the gap length $d_{A\text{-}K}$ was adjusted to 10 mm and the vacuum chamber was evacuated to 5 x 10^{-3} Pa.

Figure 2 shows the detail of the diode. The top of the anode is a copper plate of diameter 60 mm. To introduce the source plasma to the acceleration gap, the copper plate is drilled with apertures of 5 mm in diameter in the central area of 40 mm in diameter. The cathode has a grid structure to pass through the accelerated ions. To produce a magnetic field in the acceleration gap to insulate electron flow, the cathode also acts as a multi-turn magnetic field coil. The coil is made of phosphor bronze strip of thickness 1 mm, width 10 mm and has an 8-character like shape. A capacitor bank of 250 μF, 5 kV is used to apply a pulse current of rise-time 50 μs to the coil. By applying a pulse current of 10 kA, uniform magnetic field of 0.8 T is produced in the gap.

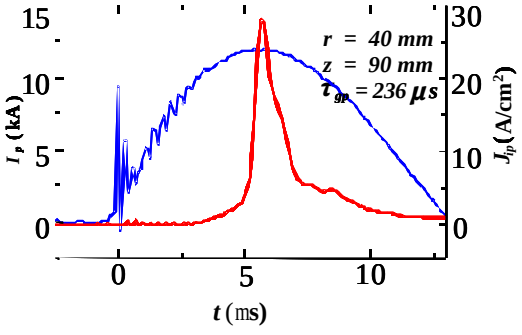

Fig. 4. Typical waveforms of discharge current (I_p) and ion current density (J_{ip}) of the plasma gun.

Figure 3 shows the cross-sectional view of the gas puff plasma gun. The plasma gun consists of a high-speed gas puff valve and a coaxial plasma gun. The gas puff valve consists of a nylon vessel, an aluminum valve and a driver coil. The vessel is pre-filled with 2 atm of N_2 gas. By applying pulse current to the driver coil, the magnetic pressure pushes the valve to open. After opening of the valve the gas expands and reaches to the gas nozzle on the inner electrode of the plasma gun.

The plasma gun has a pair of coaxial electrodes, i.e. an inner electrode of outer diameter 6 mm, length 80 mm, and an outer electrode of inner diameter 18 mm. Since it takes ≈ 150 μs to open the valve and several tens μs for N_2 gas to reach the gas nozzle on the inner electrode of the plasma gun, the capacitor bank of the plasma gun is discharged with a delay time of t_{gp} = 236 μs. Capacitor banks of 20 μF and 3.3 μF are used for the driver coil and the plasma gun, respectively. The capacitor banks were charged to 5.5 kV, and 17 kV, respectively. Since the plasma gun is placed inside the anode where high voltage pulse is applied, pulsed currents generated by the capacitor banks are fed through inductively isolated coaxial cables.

The ion current density of the plasma (J_{ip}) produced by the plasma gun was evaluated by a biased ion collector (BIC) placed at z = 90 mm downstream from the top of the plasma gun where the anode is placed in the acceleration experiment. Figure 4 shows typical waveforms of the discharge current (I_p) and J_{ip}. As seen in the figure I_p rises to 12 kA in 6 μs and J_{ip} of 28 A/cm^2 was obtained at 6 μs after the rise of. I_p Form the peak value and the pulse width of J_{ip} (28 A/cm^2, 1.1 μs (full width at half maximum)) and considering the geometric transparency factor of the anode plate the quantity of injected plasma is estimated to be 10^{14} ions/cm^2/shot.

3. Experimental results

In the acceleration experiment the pulse power system was fired at delay time of t_d after the rise of the discharge current of the plasma gun. Figure 5 shows typical waveforms of diode voltage (V_d) and diode current (I_d) when t_d = 12 μs. As seen in the figure V_d rises in 150 ns and has a peak of 220 kV. On the other

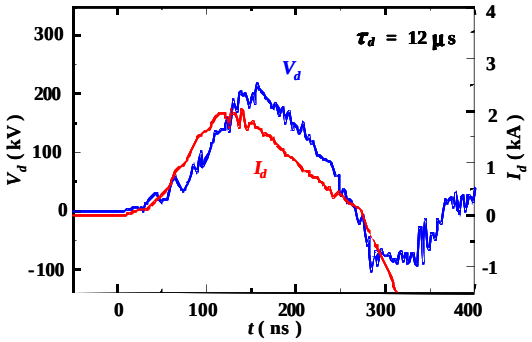

Fig. 5. Typical waveforms of diode voltage (V_d) and diode current (I_d).

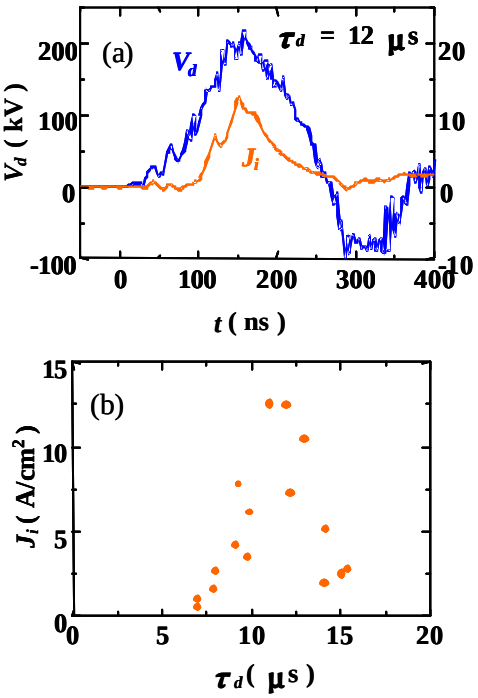

Fig. 6. (a) Typical waveform of ion current density (J_i) with V_d. (b) Dependence of J_i on t_d.

hand I_d rises with V_d and have a peak of 2.0 kA at t = 125 ns and after that decreases.

Figure 6 (a) shows the ion current density of the accelerated beam J_i measured by the BIC placed on the axis at z = 55 mm downstream from the surface of the anode. The waveform of V_d is shown as the reference. As seen in the figure J_i of 13 A/cm^2 is obtained at 130 ns after the rise of V_d. Considering the time of flight delay, the ions corresponding the peak of J_i seems to be accelerated before the peak of V_d. Figure 6 (b) shows the dependence of the peak values of J_i on t_d. As seen in the figure J_i rises at t_d = 6 μs and has a clear peak at t_d around 12 μs. The result suggests that when t_d < 12 μs J_i increases with t_d due to the increase of the quantity of injected plasma whereas when t_d > 12 μs the quantity of the plasma penetrated to the acceleration gap is too much and the diode impedance becomes too low to keep the acceleration voltage.

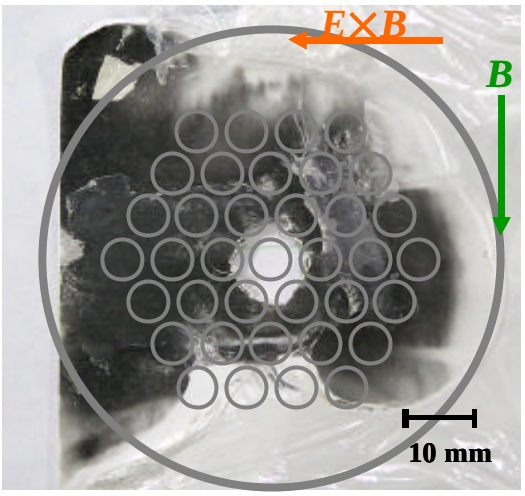

Fig. 7. Damage pattern of the ion beam recorded on the thermo-sensitive paper.

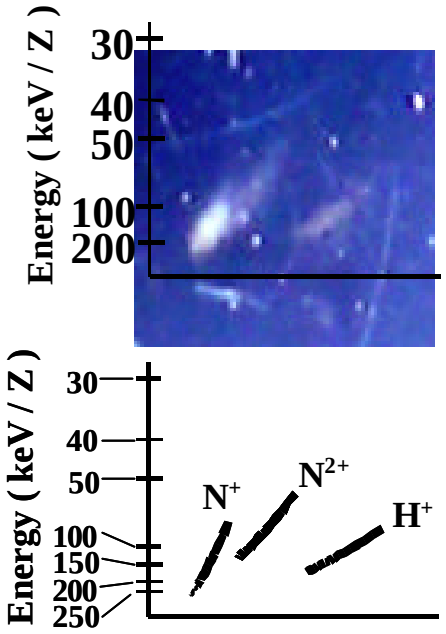

Fig. 8. The example of ion track pattern obtained by the Thomson parabola spectrometer. recorded on the thermo-sensitive paper.

Figure 7 shows the damage pattern of the ion beam recorded on the thermo-sensitive paper. Position of the anode is shown in the figure as the reference. As seen in the figure the beam tends to sift to the direction of $\boldsymbol{E}\times\boldsymbol{B}$ drift.

To evaluate the species and the energy spectrum of the ion beam Thomson parabola spectrometer [9] was used. Figure 8 shows the example of the track pattern recorded on the ion track detecting plate of CR-39. Here, deflecting magnetic field and electric field are applied in vertical direction; hence ions are deflected in vertical direction and horizontal direction by the electric field and the magnetic field, respectively. In the figure, singly and doubly ionized nitrogen ions are observed with impurity of hydrogen ions. Since each ion track on CR-39 is produced by an irradiation of

Table I. Energy and the number ratio of each ion species evaluated by TPS measurement.

Ion specie	N^+	N^{2+}	H^+
Energy (keV)	60-300	100-300	60-150

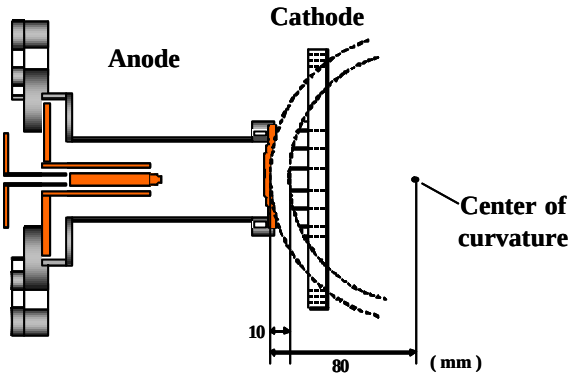

Fig. 9. Cross-sectional view of the focus type ion diode.

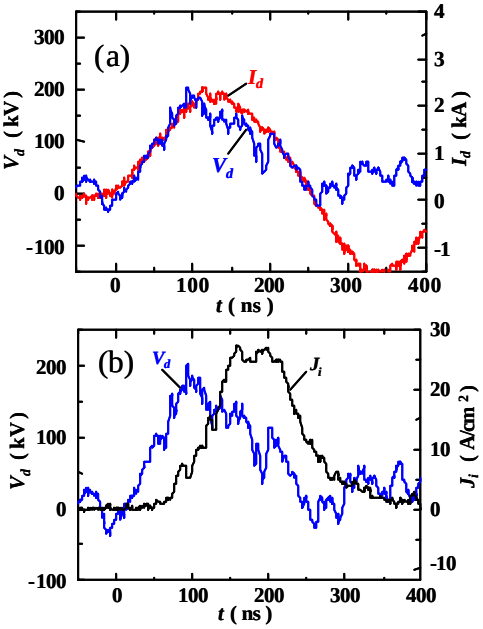

Fig. 10. Typical waveforms of (a)V_d and I_d, and (b) J_i.

single ion, we have evaluated the ion number ratio on each ion species by counting the track number. The energy range and the number ratio of each ion species evaluated from the track pattern are listed in table I. From the table we see that 13.5 % of impurity ions of protons are included in the beam, hence the purity of the beam is evaluated to be 86.5 %.

To enhance the ion current density focusing type ion diode was used. Figure 9 shows the cross-sectional view of the diode. The diode is basically same as the

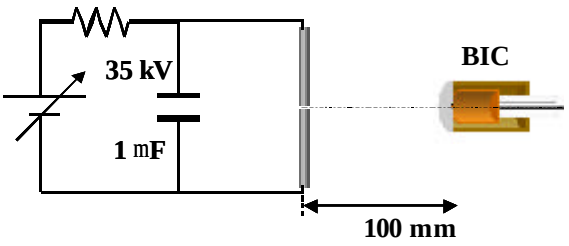

Fig. 11. Experimental setup of self-breakdown type vacuum discharge ion source.

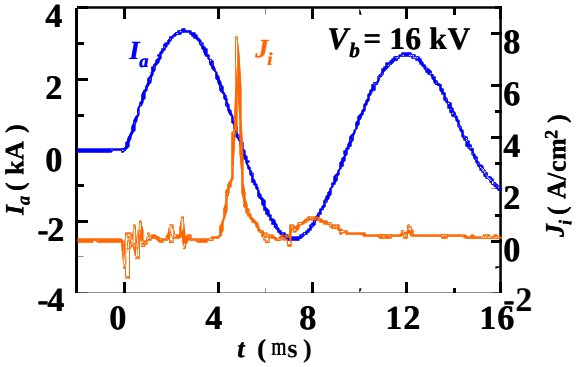

Fig. 12. Typical waveforms of discharge current (I_a) and ion current density (J_i).

diode shown in Fig.2 but the anode and the cathode are spherically shaped with radius of curvature of 80 mm and 70 mm, respectively. The gap length was adjusted to the same value as the diode shown in Fig. 2.

Figure 10 shows the typical waveforms of V_d, I_d and J_i of the diode obtained at t_d = 8.8 μs. Here, J_i was measured on the axis at z = 55. As seen in Fig. 10 (a), V_d rises in 100 ns and has a peak of 190 kV whereas I_d rises with V_d and have a peak of 2.2 kA at t = 120 ns. In Fig.10 (b), we see that J_i of 27 A/cm^2 is obtained at 170 ns after the rise of V_d. Considering the time of flight delay, the ions corresponding the peak of J_i seems to be accelerated around the peak of V_d. From the experiment we found that by using spherical electrode, J_i was enhanced by factor 2.

4. Development of vacuum discharge metallic ion source

Pulsed ion beams of metallic ions are attractive for materials processes, however they cannot be obtained yet. To develop an intense pulsed metallic ion source we are developing vacuum discharge ion source [10]. Figure 11 shows the experimental setup to evaluate the characteristics of vacuum discharge. In the experiment self-breakdown type capacitor bank of C=1μF, maximum charging voltage 35 kV was used. As the discharge electrode a pair of aluminum rod of diameter 6 mm was used, which was placed face to face with gap length 1 mm. To measure the ion current density BIC was placed at 100 mm apart from the gap. The experiment was done in the vacuum of 4×10^{-3} Pa.

Figure 12 shows the typical waveforms of

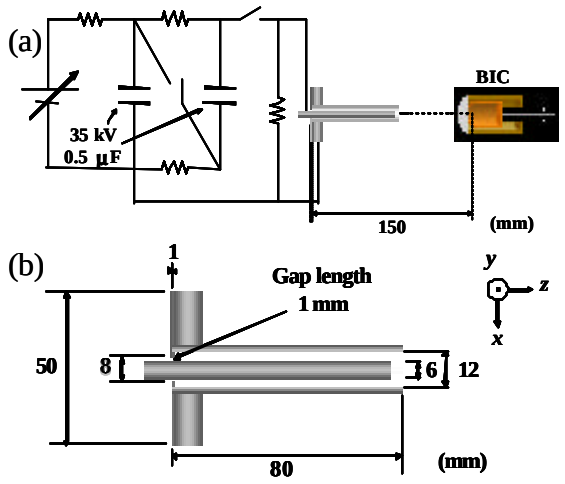

Fig. 13. (a) Experimental setup of synchronized type vacuum discharge ion source with (b) detail of the electrode..

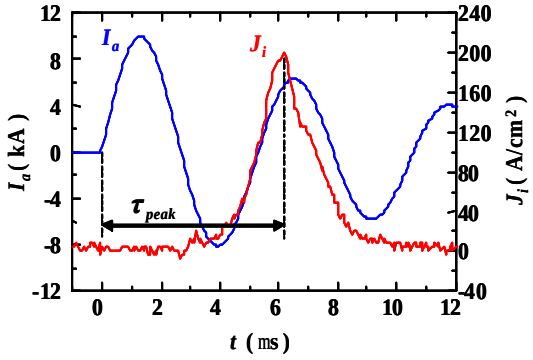

Fig. 14. Typical waveforms of I_a and J_i.

discharge current (I_a) and ion current density (J_i) at 29th shot after the exchange of the electrodes. At the shot the electrodes was self-broken at charging voltage V_b = 16 kV. As seen in the figure sinusoidal waveform of I_a of quarter cycle 2.5 μs, peak current 3.4 kA was observed. About 4.8 μs after the rise of I_a, J_i of 8 A/cm^2 was observed with pulse width 240 - 320 ns.

The V_b has a strong dependence on the shot number. In the first 7 shots V_b is around 10 kV. However, V_b gradually increases after 7th shot and reaches 30 kV around 25th shot. The V_b still increases and it exceeds the maximum charging voltage of 35 kV after 32nd shot.

To evaluate the drift velocity of the plasma by a time of flight method (TOF), two BIC's were placed at 112 and 206 mm downstream from the discharge gap, respectively. The TOF delay time between of two BIC signals was 2 μs, which gives the drift velocity of 4.7 $\times 10^4$ m/s. Assuming aluminum ions it corresponds to the ion energy of 311 eV.

To apply the ion source to the intense pulsed ion diode synchronized operation of the ion source is required. For the purpose, a Marx type capacitor bank was used, where two capacitors of 0.5 μF, 35 kV each

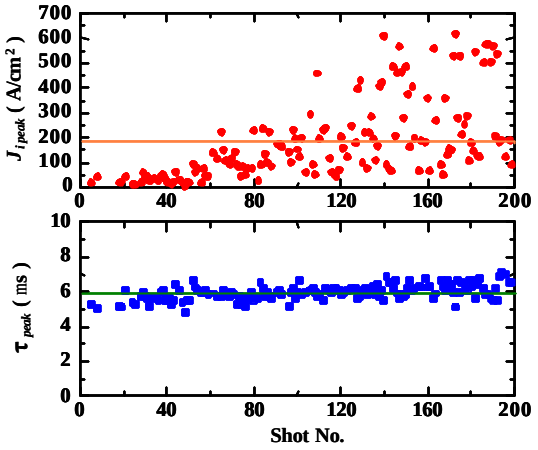

Fig. 15. Dependence of J_{ipeak} and t_{peak} on the shot No.

was used as shown in Fig. 13. A coaxial type configuration is used as the vacuum discharge electrodes in the experiment. The inner diameter of the outer electrode, the outer diameter of the inner electrode and the length are 12 mm, 8 mm, and 80 mm, respectively. On the root of outer electrode disc electrode is placed to reduce the gap length to 1 mm. The experiment was done at the total charging voltage of 60 kV.

Figure 14 shows the typical waveforms of I_a and J_i observed at 150 mm downstream from the top of the electrode. As seen in the figure sinusoidal waveform of I_a of quarter cycle 1.3 μs, peak current 10 kA was observed. About 6.2 μs after the rise of I_a, J_i of 200 A/cm^2 was observed with pulse width 2.1 μs.

Figure 15 shows the dependence of the peak value of J_i (J_{ipeak}) and the delay time of the peak of the J_i from the rise of the I_a(t_{peak}). As seen in the figure J_{ipeak} has a large scattering but tend to increases with shot No. Very large value of J_{ipeak} > 500 A/cm^2 was obtained at shot No. > 140. The average value of J_{ipeak} in the 200 shot is calculated to be 181 A/cm^2 whereas the standard deviation was evaluated to be 161 A/cm^2. t_{peak} is relatively stable and tend to increase gradually with shot. The average value of t_{peak} in 200 shot was around 6 μs. Form the average value of t_{peak} the drift velocity of the plasma was estimated to be 2.5$\times 10^4$ m/s.

5. Summary

To apply PHIB to materials processes purity of the beam is very important. For the purpose a new type of ion beam diode was developed. In the diode a new acceleration gap configuration is used with active ion source of pulsed plasma guns. Two types of plasma guns were developed to generate variety of ion beams, i.e. a gas puff plasma gun and a vacuum arc plasma gun. With the gas puff plasma gun, source plasma of nitrogen ions was produced. The current density of the plasma was evaluated to be ≈ 28 A/cm^2 at 90 mm downstream from the top of the plasma gun. The plasma was injected into the acceleration gap of the

diode and the ion diode was successfully operated at diode voltage ≈ 200 kV, diode current ≈ 2.0 kA, pulse duration ≈ 150 ns (FWHM). Ion beam of ion current density ≈ 13 A/cm^2 was obtained at 55 mm downstream from the anode. The energy and species of the beam was evaluated by a Thomson parabola spectrometer and found that N^+ and N^{2+} beam of energy 60-300 keV were accelerated with impurity of protons of energy 60-150 keV. The purity of the nitrogen beam was estimated to be 87 %. By using spherical electrode for focusing ion beam ion current density was enhanced by a factor 2 and ion current density of 27 A/cm^2 was obtained.

To generate metallic ions vacuum arc plasma gun was developed. The characteristics of the plasma gun were evaluated and source plasma of current density > 500 A/cm^2 was obtained with plasma drift velocity 2.5×10^4 m/s.

Acknowledgement

This work was partly supported by the Research Foundation for the Electro technology ob Chubu.

References

[1] H.A.Davis, et al., Matelials Chemistry and Physics **54**, pp.213-218 (1998)

[2] K. Yatsui, X. Kang, T. Sonegawa, T. Matsuoka, K. Masugata, Y. Shimotori, T. Satoh, S. Furuuchi, Y. Ohashi, T. Takeshita, and H. Yamamoto, Application of intense pulsed ion beam to materials science, Phys. Plasma **1**(5), pp.1730-1737 (1994).

[3] K. Masugata, Y. Shimizu, Y. Fujioka, I. Kitamura, H. Tanoue, K. Arai, Development of Bipolar-pulse Accelerator for Intense Pulsed Ion Beam Acceleration, Nuclear Instruments & Methods in Physics Research, Section A , 535/3 pp. 614-621 (2004)

[4] K. Masugata, R. Tejima, M. Higashiyama, J. Jawai, I. Kitamura, H. Tanoue, K. Arai, Generation of Intense Pulsed Heavy Ion Beam by a By Type Magnetically Insulated Ion Diode with Active Ion Source, Plasma Devices and Operations, 13(1) pp. 57-65 (2005)

[5] K. Masugata, K. Takao, M. Shiotani, T. Honda, R. Tejima, I. Kitamura, and T. Takahashi, Application of Intense Pulsed Ion Beam to Materials Processes, Proc. Int'l Power Modulator Conf., Hollywood, CA, USA, June 30-July3, 2002, pp. 552-555 (2002)

[6] K. Masugata, Y. Kawahara, C. Mitsui, I. Kitamura, T. Takahashi, Y. Tanaka, H. Tanoue, K. Arai, Development of Bipolar Accelerator for Pulsed Ion Beam Implantation, ibid, pp.334-337 (2002)

[7] E. Chishiro, A. Matsuyama, K. Masugata and K. Yatsui, Dependence of characteristics of Br-type magnetically insulated diode on configuration of insulation magnetic field, Jpn. J. Appl. Phys., **35**(4A), pp.2350-2355 (1996).

[8] K. Masugata, H. Okuda, K. Yatsui and T. Tazima, Diagnosis of high-brightness ion beams produced in point pinch diodes, J. Appl. Phys. **80**(9) pp. 4813-4818 (1996)

[9] K. Masugata, H. Okuda, K. Yatsui and T. Tazima, Evaluation of brightness of intense pulsed ion beam by a Thomson spectrometer, Laser and Particle Beams **15**(2), pp.325-338 (1997).

[10] I. Brown, Vacuum arc ion sources, Rev. Sci. Instrum. **65** (10), pp. 3061-3081 (1994)

Improvement of Proton Source Based on Cylindrical Inertial Electrostatic Confinement Fusion with Ion Source

Kunihito Yamauchi, Sonoe Ohura, Atsushi Tashiro, Masato Watanabe,
Akitoshi Okino, Toshiyuki Kohno, Eiki Hotta, and Morimasa Yuura*

Department of Energy Sciences, Tokyo Institute of Technology
4259 Nagatsuta, Midori-ku, Yokohama 226-8502, Japan

**Pulse Electronic Engineering Co.,Ltd.*
274 Futatsuzuka-michishita, Noda, Chiba 278-0016, Japan

ABSTRACT

Inertial Electrostatic Confinement Fusion (IECF) device is a compact fusion proton/neutron source with an extremely simple configuration, high controllability, and hence high safety. Therefore, it has been studied for practical use as a portable neutron/proton source for various applications such as landmine detection and medical positron emission tomography. However, some problems remain for the practical use, and the most critical one is the insufficiency of absolute neutron/proton yields. In this study, a new IECF device was designed and tested to obtain high neutron/proton yields. The key features of the new device are the cylindrical electrode configuration in consideration of better electrostatic confinement of ions and extraction of protons, and an integrated ion source that consists of sixteen ferrite magnets and biasing the grid anode. To investigate the performance characteristics of the device and the effect of the ion source, three kinds of experimental setup were used for comparison. At first, the device was operated with the basic setup. Then a cusp magnetic field was applied by using ferrite magnets, and the grid anode was negatively biased. As a result, it was confirmed that the ion source works effectively. At the same voltage and current, the obtained neutron production rate was about one order of magnitude higher than that of the conventional spherical IECF device. The maximum neutron production rate of 6.8×10^9 n/s was obtained at a pulsed discharge of –70 kV and 10 A with an anode bias voltage of –1.0 kV.

Keywords

Inertial Electrostatic Confinement, Fusion, Proton Source, Neutron Source, Positron Emission Tomography

1. Introduction

Inertial Electrostatic Confinement Fusion (IECF)[1] is a scheme to confine ions electrostatically with two concentric electrodes. Generated ions are accelerated toward the center with sufficient energy to cause fusion reactions, and recirculate inside the anode through a highly transparent grid cathode. Because of such a simple configuration of the device, IECF is practically expected as a portable neutron/proton source that is more safe and controllable.

As one of the IECF applications, medical positron emission tomography (PET) is most featured now. PET scanning is an advanced diagnosis with using nuclear medicine. It provides us the functional information inside our body and is used especially for detecting cancers or tumors. But the PET scanning system is very expensive because it must include a cyclotron, which is used for the production of the short-life positron emitters on demand, and this high initial cost of the system is the obstacle to popularize

the PET inspection. Thus the IECF proton source is expected to be replaced the cyclotron. However, some problems remain for the practical use, and the most critical one is the insufficiency of absolute proton yield. In this study, a new IECF device was designed and tested to obtain high proton yield, which is enough to produce the short-life PET nuclei.

2. Experimental Setup

The key features of the new device are the cylindrical electrode configuration in consideration of better electrostatic confinement of ions and extraction of protons, and an integrated ion source that consists of ferrite magnets and biasing the grid anode.

The schematic and the cross section of the cylindrical IECF device are shown in Figs. 1 and 2, respectively. The cylindrical vacuum chamber made of stainless steel is 393-mm dia. and 340-mm high. A cylindrical grid anode is 200-mm dia., 320-mm high, which consists of 32 stainless steel rods of ϕ1.2 mm, is placed at the center of the chamber. A cylindrical grid cathode is 40-mm dia., 380-mm high, which consists of 16 stainless steel rods of ϕ1.6 mm, is set inside the anode concentrically. The chamber is evacuated to 10^{-5} Torr with a turbomolecular pump, and then the pressure is controlled at 1–100 mTorr by feeding D_2 or H_2 gas through a control valve.

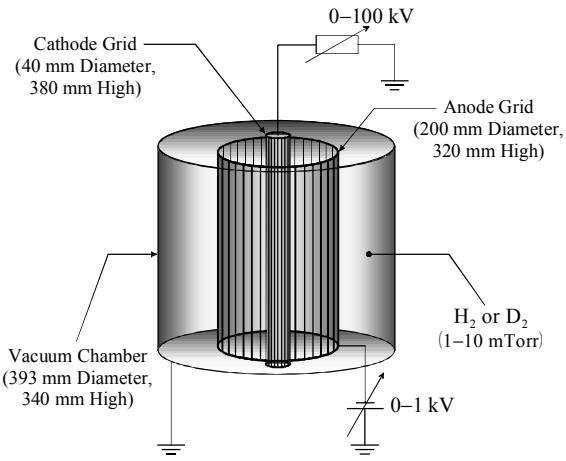

Fig. 1 Schematic of the cylindrical IECF device

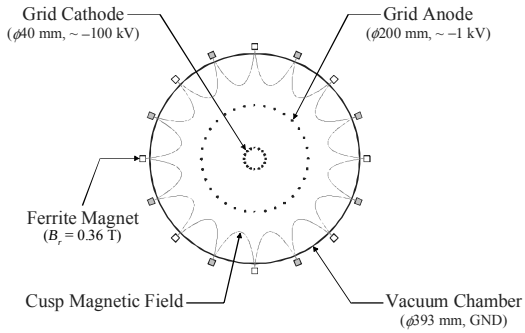

Fig. 2 Cross section of the cylindrical IECF device

A negative high voltage is applied to the cathode by a CVCC dc power supply of –100 kV, 60 mA or a pulse generator system of –100 kV, 10 A, 200 pps. The anode is negatively biased by another CVCC dc power supply and a few resistors of 20–100 kΩ connected in parallel. The cathode voltage and the anode bias voltage are conditioned independently.

To generate energetic ions efficiently, an ion source, which consists of 16 ferrite magnets and biasing the grid anode, is installed. The ferrite magnets are 11-mm square and 300-mm long, and have a residual magnetic flux density of 0.36 T. To form a cusp magnetic field near the chamber wall, the ferrite magnets are mounted around the chamber with alternating the magnetic polarities. Electrons accelerated toward the chamber wall are trapped in the cusp magnetic field and the path and life of electrons are elongated. As a result, the electrons ionize more deuterium molecules, and then these generated ions are extracted toward the center by the negatively biased anode. Thus the ions can obtain the almost full energy that corresponds to the cathode voltage. In this paper, to investigate the performance of the new IECF device and the effect of the ion source, three kinds of experimental setup were used for comparison.

3. Results and Discussions

3.1 Characteristics of basic IECF setup

At first, the cylindrical IECF device was operated with the basic setup. In this setup, ions are generated only by the glow discharge between the cathode and the grounded anode. Figure 3 shows a bottom-view photograph of star-mode discharge plasma. The formation of a converged plasma core at the center and the light emission like spokes are clearly observed with the shadow of the cathode end.

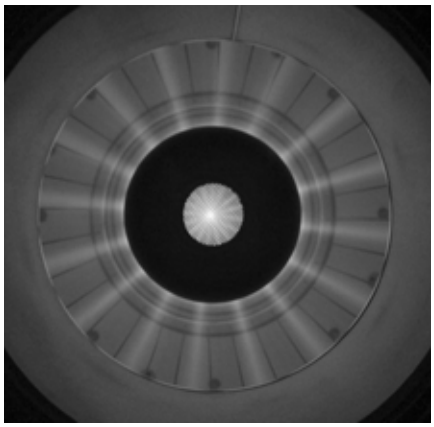

Fig. 3 Photograph of discharge plasma

The neutron production rate of the basic IECF setup in dc operation was measured. Figure 4 shows the relationship between the neutron production rate and the cathode current at constant cathode voltages. The neutron production rate is proportional to the cathode current. The neutron production tendency of the new cylindrical device is almost the same as that of conventional spherical ones. This implies that the beam-background fusion reaction is also dominant in cylindrical device as well as conventional spherical ones. The maximum neutron production rate of 2.1×10^6 n/s was obtained at a dc discharge of –60.0 kV and 10.0 mA.

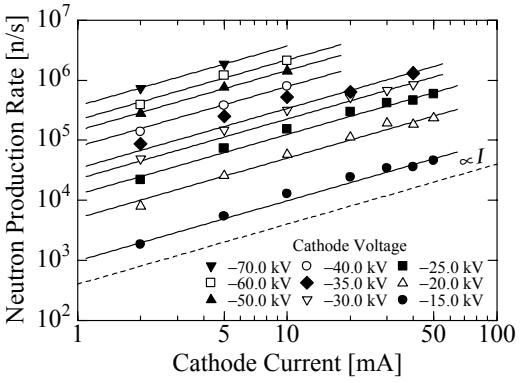

Fig. 4 Neutron production rate vs. cathode current at constant voltages (basic setup)

Figure 5 shows the comparison of neutron production rate between the basic setup and the conventional spherical one[2]. The new cylindrical device can generate 3–8 times higher neutron yield than the conventional spherical one. This increase may be caused by the better electrostatic confinement of ions, which results from the reduced influence of the feedthrough to the cathode. In case of the spherical device, it can not be avoided physically that the electric field is distorted by the existence of the feedthrough. Therefore, many recirculating ions are pulled to the feedthrough and then lost by colliding with it. However, in the cylindrical device, ions can recirculate without the collisional loss because the feedthrough does not affect essentially.

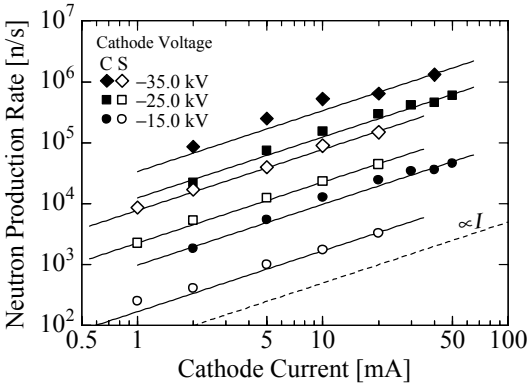

Fig. 5 Comparison of neutron production rate between the basic setup (C) and the conventional spherical device (S)

3.2 Effect of cusp magnetic field

A cusp magnetic field was applied to the basic IECF setup by using ferrite magnets in order to investigate its effect. In case of this setup, generated ions are extracted toward the center by the electric field leaked through the grounded grid anode.

Figure 6 shows the breakdown voltage of the cylindrical device. The breakdown voltage was reduced to a half with applying the cusp magnetic field. This indicates that the cusp magnetic field works effectively as an ion source.

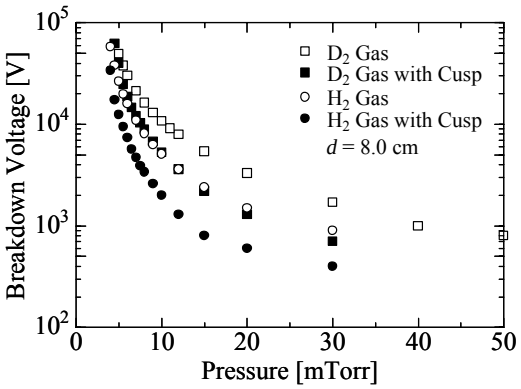

Fig. 6 Breakdown voltage vs. gas pressure

Figure 7 shows the comparison of neutron production rate between the setups with and without the cusp magnetic field. The neutron production rate was enhanced by a factor of about 1.5 with applying the cusp magnetic field. This also indicates that the cusp magnetic field works effectively as an ion source, and implies that the average energy of ions was increased. However, the neutron production tendency is almost the same as that of the basic setup without the cusp magnetic field and conventional spherical devices, hence the beam-background fusion reaction is also dominant.

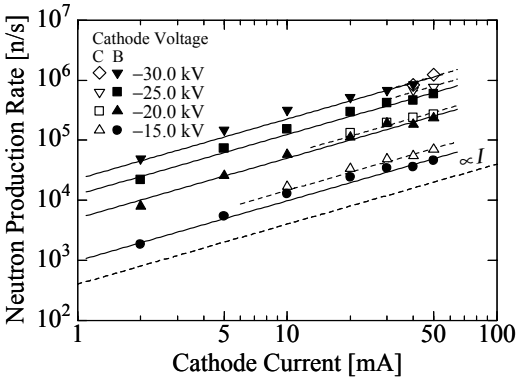

Fig. 7 Comparison of neutron production rate between the setups with and without the cusp magnetic field

3.3 Effect of biasing anode

From the previous experimental results, it was confirmed that the cusp magnetic field works effectively as an ion source. For more efficient extraction of ions generated in the cusp magnetic field, the grid anode was negatively biased by a few hundreds volts. To bias the anode, three shunt resistors of 20, 50, 100 kΩ and a dc power supply were used. Because the discharge current flows into the grid anode, the anode can be negatively biased in the case that only an anode resistor is used.

Figure 8 shows the relationship between the relative neutron production rate and the anode bias voltage at a cathode voltage of –15.0 kV. Here, the relative neutron production rate was normalized by the result of the grounded anode case. It is found that the neutron production rate increases and becomes saturated with the anode bias voltage. The saturation indicates that the biased anode works well and most of ions generated outside the anode are extracted. Figure 9 also shows the relationship between the relative neutron production rate and the relative anode bias voltage. In this figure, the anode bias voltage was also normalized by the cathode voltage, and the results at some cathode voltages are plotted together. This graph indicates that the neutron production rate is enhanced by a factor of about 1.4 with effectually biasing the anode. In addition, at the same voltage and current, the neutron

production rate obtained with this setup was about one order of magnitude higher than that of the conventional spherical IECF device.

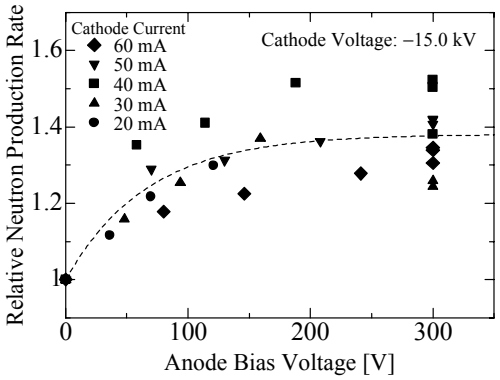

Fig. 8 Relative neutron production rate vs. anode bias voltage at a cathode voltage of −15.0 kV

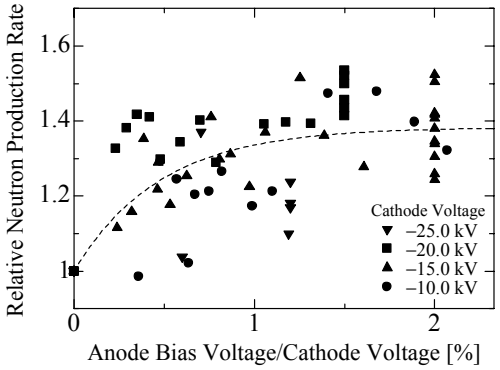

Fig. 9 Relative neutron production rate vs. relative anode bias voltage

3.4 Condition of stable dc operation

From the previous experimental results, it was confirmed that the neutron yield was effectively enhanced by using the cusp magnetic field and biasing the anode. However, there is a problem that a stable dc operation can hardly be obtained with enhancement of ion source effect. Figure 10 shows the experimental condition for stable dc discharge. In case of the basic IECF setup, the stable dc discharge can be obtained at almost all the region. But a periodic discharge occurs and the stable region shifts to higher current and lower voltage side with enhancement of ion source effect. The periodic discharge is caused by the CV/CC mode change of the dc power supply system because the CVCC control can not follow the rapid decrease of impedance as a result of the enhanced ion/electron multiplication effect in the discharge formation. For stable dc operation, three kinds of CVCC dc power supply were tried to use. But the periodic discharge was observed in all cases. To stabilize the dc discharge at a high voltage, a dc power supply system with larger current capacity and better load following capability is needed. However, these requirements do not matter to pulsed operation essentially. Therefore, the ion-source-assisted IECF is suitable for pulsed operation.

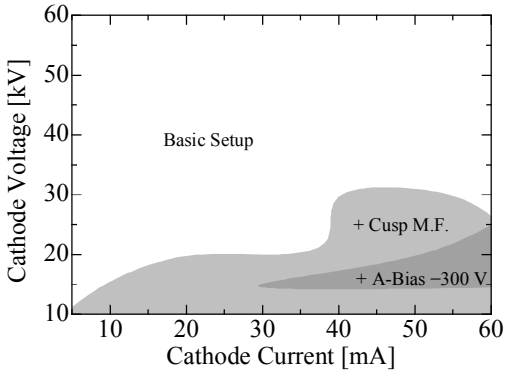

Fig. 10 Experimental condition of stable dc discharge

3.5 Pulsed operation

Pulsed operation was carried out in order to investigate the characteristics of the device in a high-voltage and high-current region. The pulse repetition rate and the pulse width were set at 4 Hz and 20 μs, respectively. Figure 11 shows the relationship between the neutron production rate and the pulse current. Here, the data of the anode bias voltage of −1.0 kV and the anode ground are plotted for comparison. In this pulsed high-current region, the neutron production rate is also proportional to the cathode current, which implies that beam-background fusion reaction is dominant. And the anode bias

voltage does not affect the neutron production tendency of the device. However, it is found that the biased anode is also effective in pulsed operation. The maximum neutron production rate of 6.8×10^9 n/s was obtained at a pulsed discharge of –70 kV and 10 A with an anode bias voltage of –1.0 kV.

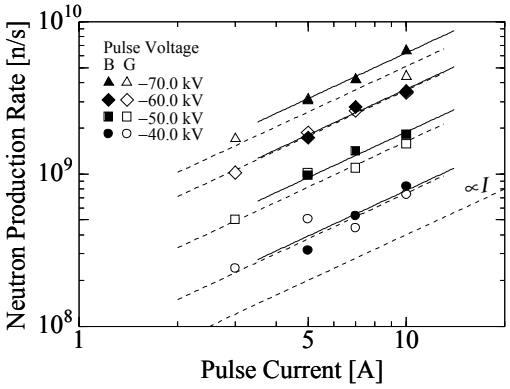

Fig. 11 Neutron production rate vs. pulse current (B: anode bias voltage of –1.0 kV, G: anode grounded)

4. Conclusions

A new cylindrical IECF device with an ion source was designed and tested. At first, the device was operated with the basic setup. As a result, it is found that the cylindrical device can generate several times higher neutron yield than conventional device. This increase may be caused by the better electrostatic confinement of ions that results from the cylindrical electrode configuration. The maximum neutron production rate of 2.1×10^6 n/s was obtained at a dc discharge of –60.0 kV and 10.0 mA.

Then a cusp magnetic field was applied by using ferrite magnets and the grid anode was negatively biased by a few hundreds volts. It was confirmed that the cusp magnetic field and the biased anode works effectively as an ion source. At the same voltage and current, the obtained neutron production rate was about one order of magnitude higher than that of the conventional spherical IECF device. However, there is a problem that a stable dc operation can hardly be obtained with enhancement of ion source effect.

In order to investigate the characteristics of the device in a high-voltage and high-current region, pulsed operation was carried out. It was also confirmed that the integrated ion source works effectively. The maximum neutron production rate of 6.8×10^9 n/s was obtained at a pulsed discharge of –70 kV and 10 A with an anode bias voltage of –1.0 kV. This result demonstrates that the cylindrical IECF device has potential applicable to a proton source for PET scanning system because the proton yield required to produce short-life PET isotopes is 10^9 n/s or higher.

References

[1] G. H. MILEY et al., “Inertial-Electrostatic Confinement Neutron/Proton Source”, *Proc. 3rd Int. Conf. on Dense Z-pinches*, AIP Press, pp.675–688 (1994).

[2] K. YAMAUCHI et al., “Neutron Production Characteristics and Emission Properties of Spherically Convergent Beam Fusion”, *Fusion Technol.*, **39**, 3, pp.1182–1187 (2001).

Effect of Ion Implantation on DLC Properties

Yoshihiro Oka[1], Michiharu Kirinuki[1], Tsuneo Suzuki[2], Mitsuyasu Yatsuzuka[1], Kiyoshi Yatsui[2]
[1]Graduate School of Engineering, University of Hyogo
[2]Extreme Energy-Density Research Institute, Nagaoka University of Technology

Abstract

Diamond-like carbon (DLC) films were prepared by a hybrid process of plasma-based ion implantation and deposition (PBIID) using hydrocarbon gas plasmas. It was found that the film stress, density, hydrogen content, and hardness were dependent on negative pulsed voltage for ion implantation. Ion implantation to substrate served to produce a graded interface of carbon component in the boundary region of DLC film and substrate. Ion implantation to DLC film reduced the residual stress to several MPa, enhancing the adhesive strength of DLC film. Furthermore, the adhesive strength of DLC film on SUS304 substrate was increased above the epoxy resin strength by implantation of mixed Si and C ions.

Keywords: diamond-like carbon, plasma-based ion implantation and deposition, residual stress, density, hydrogen content, hardness, carbon depth profile, adhesive strength

1. Introduction

Diamond-like carbon (DLC) has been studied by many researchers in recent years because DLC has excellent mechanical and tribological properties such as high hardness, strong wear resistance, low friction coefficient, and chemical inertness[1]. Typical preparation methods of DLC film are sputtering deposition, ion beam deposition, plasma CVD, and cathodic arc deposition. However, DLC films produced by these dry processes usually had the large compressive residual stress above 10 GPa[2-4] that often caused for poor adhesion, so that thick DLC films of more than a few μm in thickness were hard to produce on metal surfaces. Metallic interlayer[5], such as Si or Ti, and graded interface of carbon composition, produced by carbon implantation [6] were used to improve the adhesive strength of DLC film. Compressive residual stress was also found to be a strongly correlated with the ion energy during deposition and to be reduced by the ion impact[3] or ion implantation to the film[7,8]. Plasma-based ion implantation (PBII)[9, 10] technique is, which is able to implant ions with high energy above 10 keV into three-dimensional substrates, can be a promising surface treatment method for industrial applications. Authors have successfully prepared the thick DLC films of more than 10 μm in thickness on three-dimensional substrates using a hybrid processing system of PBII and deposition (PBIID)[11-13]. However, effects of ion implantation on properties and adhesive strength of DLC film have not been fully understood yet.

In this paper, we present effects of ion implantation on residual stress, density, hydrogen content, hardness, depth profile of carbon in a boundary region of DLC film and substrate, and adhesive strength of DLC film prepared by PBIID method using methane (CH_4), acetylene (C_2H_2), toluene ($C_6H_5CH_3$), and organic metal compound gas including silicon.

2. Experimental

Figure 1 shows a schematic diagram of PBIID system. RF pulse for plasma generation and negative high-voltage pulse for ion implantation were applied to a

sample through a single electrical feed-through. The RF pulse had the frequency of 13.56 MHz, the peak power of 300 W, the pulse duration of $\tau_{(RF)}$ = 50 μs and the repetition rate of f = 0.5 ~ 1 kHz. Plasma ions were implanted to the substrate and deposited film by the negative high-voltage pulse of V_b = 0 ~ -20 kV and the pulse duration of $\tau_{(HV)}$ = 5 μs. The precursor gases were CH_4, C_2H_2, $C_6H_5CH_3$, and organic metal compound gas including silicon.

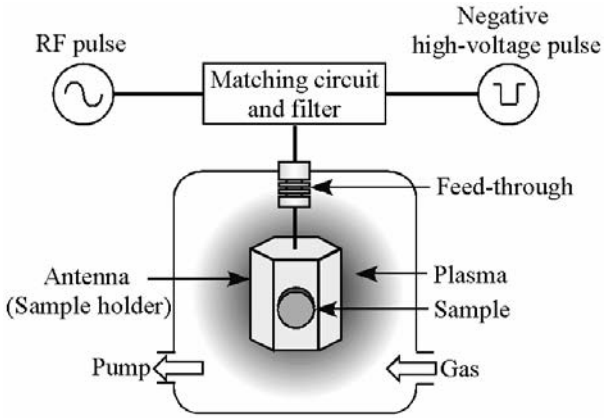

Fig. 1. A schematic diagram of plasma-based ion implantation and deposition system.

The preparation process of DLC film for measurement of residual stress, density, hydrogen content, and hardness was as follows: The first step was the sputter-cleaning process using the Ar plasma with the negative high voltage pulse (V_b = -10 kV, $\tau_{(HV)}$ = 5 μs, f = 1 kHz). In the second step, the ion implantation during deposition process using C_2H_2 or $C_6H_5CH_3$ plasma and the negative high voltage pulse (V_b = -10 kV, τ_{HV} = 5 μs, f = 1 kHz). The gas pressure was held at p = 0.5 Pa. Substrates used in the experiments were silicon wafer and quartz glass. The silicon samples were used for hardness, RBS analysis, and ERDA measurements. The quartz glass samples were used for residual stress measurements in DLC film. Adhesive strength of DLC film, prepared with 3 conditions as shown in Table 1 on SUS304 substrate (12 mm in diameter and 2 mm in thickness), was measured by the adhesion test.

The residual stress was determined from curvature of quartz glass plate (25 mm in length, 5 mm in width and 0.5 mm in thickness) after DLC film coating and thickness of DLC film using Stoney's equation[14]. The curvature and film thickness were measured by stylus profilometer (Dektak3, ULVAC). The density was determined from the area density measured by RBS. The hydrogen content was measured by ERDA. The hardness was measured by nano-indentation tester (ENT1100, ELIONIX). Depth profile of each element of DLC film and silicon wafer substrate was measured with Auger Electron Spectroscopy (AES, Model 255, PHI). An adhesion testing apparatus (Sebastian Five-A, Quad Group) was used to measure the adhesive strength of DLC film. An epoxy pre-coated aluminum stud (2 mmϕ

Table 1. Coating conditions for DLC preparation.

Conditions		Stage	Cleaning	Interlayer treatment				Deposition
(a)	As deposition	Gas	Ar					$C_6H_5CH_3$
		Pulsed voltage (kV)	-10					-5
		Process time (min)	30					120
(b)	C ion implantation and deposition	Gas	Ar	CH_4		C_2H_2		$C_6H_5CH_3$
		Pulsed voltage (kV)	-10	-20		-20		-5
		Process time (min)	30	30		30		120
(c)	C and Si ions implantation and deposition	Gas	Ar	CH_4	CH_4+Si	C_2H_2+Si	C_2H_2	$C_6H_5CH_3$
		Pulsed voltage (kV)	-10	-20	-5	-5	-20	-5
		Process time (min)	30	25	5	5	25	120

×12 mm) was vertically set to the sample. After curing at 150 degrees for 1 h, the sample was inserted into the machine platen and gripped. When applied, the stud was pulled down against the platen support ridge until failure occurred, and the tensile force required to cause failure was registered. All samples after adhesion test was observed with a CCD microscope (VH-8000, KEYENCE).

3. Results and Discussion

3.1 Properties of DLC

Figure 2 shows the compressive residual stress in DLC film prepared using C_2H_2 and $C_6H_5CH_3$ plasmas as a function of negative pulsed voltage, where $\tau_{(HV)}$ = 5 μs, f = 0.5 kHz, $\tau_{(RF)}$ = 50 μs, p = 0.5 Pa, and processing time T = 2 h. The compressive residual stress in DLC film prepared using C_2H_2 plasma is decreased with increasing negative pulsed voltage from about 0.47 GPa at V_b = 0 to 0.16 GPa at V_b = -20 kV. This reduction of compressive residual stress may be result from the local heating (thermal spike) by ion energy[8]. On the other hand, the compressive residual stress in DLC film prepared using $C_6H_5CH_3$ plasma is about 0.25 GPa at V_b = 0, and reduce to about several MPa at V_b = -5 ~ -7 kV. This is the same result as the C_2H_2 plasma. For negative pulsed voltage above about -10 kV, however, the compressive residual stress is increased up to 0.25 GPa. At this time, a strong optical emission around the substrate was observed at the same time as applied negative pulsed voltage[15], indicating the generation of glow discharge due to secondary electrons emitted by ion bonberdment to the substrate. Then, an increase in residual stress at V_b > -10 kV is ascribed to little ion implantation because of generation of glow discharge by negative pulsed voltage. In either case, the observed compressive residual stress in DLC film prepared using C_2H_2 or $C_6H_5CH_3$ plasma in present condition by PBIID system is at least two orders less than that of other methods.

Figure 3 shows the density, hydrogen content, and hardness of DLC film prepared using C_2H_2 or $C_6H_5CH_3$ plasma as a function of negative pulsed voltage, where f = 1 kHz, film thickness is 0.5 μm (density and hydrogen content) or 1 μm (hardness), and the other conditions

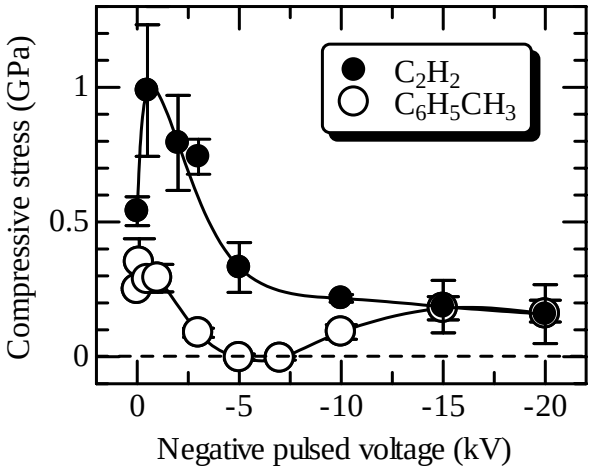

Fig. 2. Compressive residual stress of DLC film prepared with C_2H_2 or $C_6H_5CH_3$ plasma as a function of negative pulsed voltage for ion implantation.

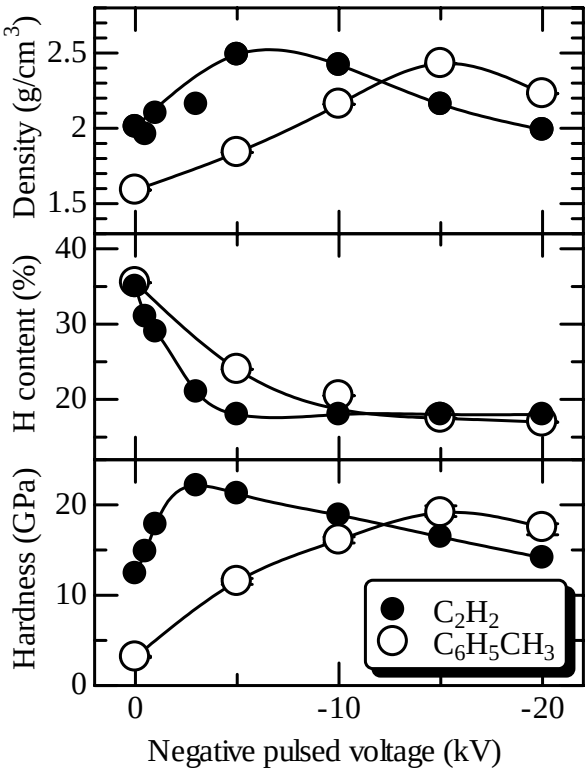

Fig. 3. Density, hydrogen content, and hardness of DLC film prepared with C_2H_2 or $C_6H_5CH_3$ plasma as a function of negative pulsed voltage.

were the same as Fig. 2. The density of DLC film prepared using C_2H_2 plasma ranges from 2.0 to 2.5 g/cm^{-3}, and has a peak at the negative pulsed voltage of -5 kV. For $C_6H_5CH_3$ plasma, the density ranges from 1.6 to 2.4 g/cm^{-3}, and has a peak at the negative pulsed voltage of -15 kV. As mentioned above, the effect of ion implantation is enhanced when the residual stress in DLC film is reduced by ion implantation during deposition. In other words, the density decreases when the effect of ion implantation is enhanced, indicating the thermal spike effect[16] is caused by ion implantation during deposition. The hydrogen content in DLC film decreases slightly with the increase of negative pulsed voltage, ranged from 17 to 37 %. The observed reduction of hydrogen content results from ion implantation during deposition. It is found that the hydrogen content in DLC film decreases with a little effect of ion implantation. The hardness of DLC film prepared using C_2H_2 plasma ranges from 12 to 22 GPa, and has a peak at the negative pulsed voltage of -3 kV. For $C_6H_5CH_3$ plasma, the hardness ranges from 3 to 19 GPa, and has a peak at the negative pulsed voltage of -15 kV. The higher density and the lower hydrogen content are, the higher hardness of DLC film is, indicating the hardness are dependent on the density and the hydrogen content. That is to say, the residual stress, density, hydrogen content, and hardness depends in good part on magnitude of ion implantation effect.

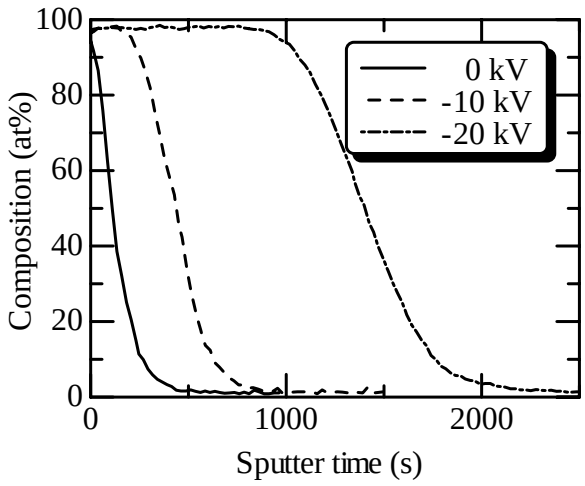

Fig. 4. AES depth profile of carbon in DLC film prepared with C_2H_2 plasma on a silicon substrate for various negative pulsed voltages for ion implantation.

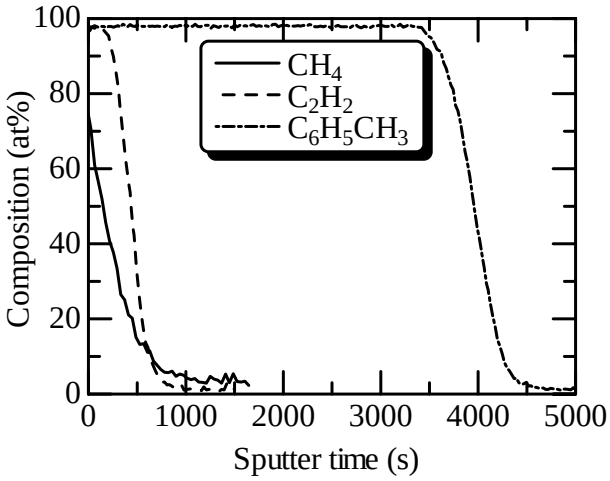

Fig. 5. AES depth profile of carbon in DLC film prepared with CH_4, C_2H_2, and $C_6H_5CH_3$ plasmas at the negative pulsed voltage of -10 kV.

3.2 Adhesive strength

Figure 4 shows AES depth profile of carbon in DLC film on a silicon wafer prepared with the C_2H_2 plasma for various negative pulsed voltages of V_b = 0, -10, -20 kV, where f = 1 kHz, T = 5 min, and the other conditions were the same as Fig. 2. As seen in Fig. 4, a carbon composition gradient, needed to improve the adhesive strength of DLC film, decreases with the increase of negative pulsed voltages. When applied negative pulsed voltage of -10 and -20 kV, carbon ions are implanted into the substrate and also deposited on the substrate, indicating the formation of a mixing layer of carbon and silicon. The deposition rate and the width of mixing layer are increased with increasing negative pulsed voltage. Figure 5 shows AES depth profile of carbon in the DLC film on silicon prepared using CH_4, C_2H_2, and $C_6H_5CH_3$ plasmas at the same conditions as those in Fig. 2 except V_b = -10 kV. As seen in Fig. 5, when using the $C_6H_5CH_3$ plasma, the deposition rate of DLC film increases approximately 10 times than that using the C_2H_2 plasma. For CH_4 plasma, carbon ions are mostly implanted into

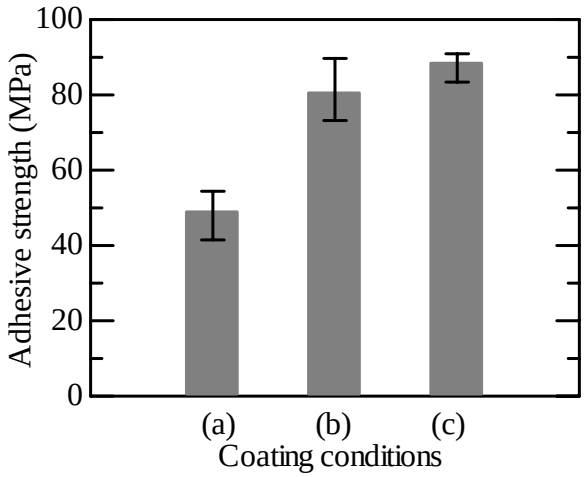

Fig. 6. Adhesive strength of DLC film prepared on SUS304 for various coating conditions, where (a) as deposition, (b) C ion implantation and deposition, and (c) C and Si ions implantation and deposition.

the substrate, but little deposition. A carbon composition gradient in DLC-coated silicon prepared using CH_4 plasma decreases than that of using C_2H_2 and $C_6H_5CH_3$ plasmas, indicating the use of CH_4 plasma can more deeper implant carbon ions to the substrate. Carbon ion implantation in the interlayer treatment step in the film preparation procedure using the CH_4 and C_2H_2 plasmas serves to produce an interfacial mixing layer between the DLC film and the substrate material. The use of $C_6H_5CH_3$ plasma leads to high speed deposition rate.

Figure 6 shows the adhesive strength of DLC film prepared on SUS304 substrate with the conditions in Table 1, where the error bar indicates the amount of scatter in measured values of 5 samples. Note the DLC films were prepared with the condition of the lowest residual stress. As seen in Fig. 6, the adhesive strength of about 49 MPa without ion implantation (condition (a)) increases to about 81 MPa with carbon ion implantation in the boundary region of DLC film and substrate (condition (b)). Furthermore, implantation of mixed carbon and silicon ions (condition (c)) leads to considerable enhancement of adhesive strength up to about 88 MPa which is larger than that reported by

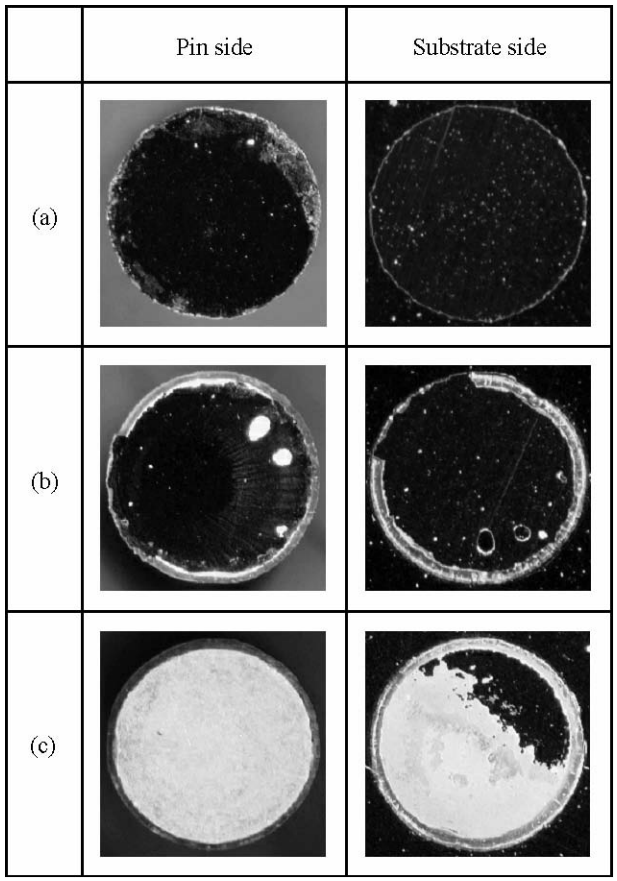

Fig. 7. Photograph of DLC-coated SUS304 and untreated SUS304 surfaces after tension test, where (a) as deposition, (b) C ion implantation and deposition, and (c) C and Si ions implantation and deposition.

Walter et al. [6].

Figure 7 shows the photograph of stud pin (left) and DLC-coated SUS304 (right) surfaces after tension test. DLC coating film prepared with the condition (a) is completely removed and with the condition (b) is mostly removed. With the condition (c), on the other hand, there is no delamination of DLC film, indicating that the adhesive strength of DLC film is enhanced above the strength of epoxy resin glue. The observed enhancement in adhesive strength by carbon ion implantation should be ascribed to the production of interface, graded in carbon composition, and the relaxation of residual stress in DLC film. Considerable enhancement in adhesive strength by implantation of mixed carbon and silicon

ions suggests the formation of chemical bonding such as SiC in the substrate.

4. Conclusions

DLC films were prepared by a hybrid process of plasma-based ion implantation and deposition using hydrocarbon gas plasmas and examined the effects of ion implantation on DLC preparation. Compressive residual stress in DLC film was considerably reduced to several MPa that was two orders less than that of conventional methods. Density, hydrogen content, and hardness are dependent on magnitude of ion implantation effect to a grate extent, ranged from 1.6 to 2.4 g/cm^{-3}, from 17 to 37 %, and from 12 to 22 GPa, respectively. Carbon ion implantation led to the formation of a mixing layer in the boundary region of DLC film and substrate. Adhesive strength is enhanced from 49 MPa without ion implantation to 81 MPa with carbon ion implantation. Furthermore, implantation of mixed carbon and silicon ions resulted in considerable enhancement of adhesive strength up to 88 MPa exceeding epoxy resign strength. Ion implantation to the film or substrate has an intense effect on properties and adhesive strength of DLC film.

Acknowledgements

This work was supported by the Cooperation of Innovative Technology and Advanced Research in Evolutional Area (CITY AREA).

References

[1] J. Robertson, Surf. Coat. Technol. 50 (1992) 185.

[2] D. R. McKenzie, D. Muller, and B. A. Pailthorpe: Phys. Rev. Lett., **67** (1991) 773.

[3] P. J. Fallon, V. S. Veerasamy, C. A. Davis, J. Robertson, G. A. J. Amaratunga, W. I. Milne, and J. Koskinen: Phys. Rev. B, **48** (1993) 4777.

[4] J. W. Ager III, S. Anders, A. Anders, and I.G. Brown: Appl. Phys. Lett., **66** (1995) 3444.

[5] J. G. Deng and M. Braun, Diam.: Relat. Mater., **4** (1995) 936.

[6] K. C. Walter, M. Nastasi, and C. Munson: Surf. Coat. Technol., **93** (1997) 287.

[7] Y. Oka, M. Tao, Y. Nishimura, K. Azuma and M. Yatsuzuka: Nucl. Inst. Methods in Phys. Res. B, **206** (2003) 700.

[8] M. M. M. Bilek, R. N. Tarrant, D. R. McKenzie, S. H. N. Lim, and D. G. McCulloch: IEEE Trans. Plasma Sci., **31** (2003) 939.

[9] R. J. Adler, S. T. Picraux: Nucl. Instrum. Methods Phys. Res. B, **6** (1985) 123.

[10] J. R. Conrad, J. L. Radtke, R. A. Dodd, F. J. Worzala, and N. C. Tran: J. Appl. Phys., **62** (1987) 4591.

[11] Y. Nishimura, A. Chayahara, Y, Horino, and M, Yatsuzuka: Surf. Coat. Technol., **156** (2002) 50.

[12] Y. Nishimura, Y. Oka, H. Akamatusu, K. Azuma and M. Yatsuzuka: Nucl. Inst. Methods in Phys. Res. B, **203** (2003) 696.

[13] Y. Oka, Y. Nishimura and M. Yatsuzuka: Vacuum, **73** (2004) 541.

[14] G. G. Stoney, Proc. Roy. Soc. A **82** (1909) 172.

[15] M. Onoi, E. Fujiwara, Y. Oka, Y. Nishimura, K. Azuma, and M. Yatsuzuka: Surf. Coat. Technol., **186** (2004) 200.

[16] C. A. Davis, Thin Solid Films 226 (1993) 30.

High Voltage Pulse discharge and Optical Emission Measurements in Plasma Base Ion Implantation and Deposition (PBIID) System

Etsuo Fujiwara, Michiharu Kirinuki, Keiichi Nishikawa, Masahiro Onoi, Yoshihiro Oka, Kingo Azuma, and Mitsuyasu Yatsuzuka

Dep. of Electrical Engineering and Computer Sciences, University of Hyogo
2167 Shosha, Homeji, Hyogo 671-2201, Japan

Keywords: Ion implantation, DLC, PBIID, Spectrum

The optical emissions in PBIID system were measured. CH (431 nm), H_α (656 nm), H_β (486 nm), and H_γ (434 nm) line spectra were observed from hydrocarbon gas plasma of acetylene and toluene. It was found that the deposition rate of DLC film was almost in proportion to the CH ($A^2\Delta \rightarrow X^2\Pi$, 431.4nm) line emission at measured various conditions for acetylene. The CH line emission intensity showed a peak near surfaces and decreased with distance.

1. Introduction

Plasma-based ion implantation is a technique developed in the late 1980s. The principle of operation is that the object to be ion-implanted is immersed in plasma and biased with a high voltage power supply. A sheath forms around the object and ions are accelerated across the sheath into the surface of the immersed object. The bias is pulsed to allow the plasma to replace depleted ions between the pulses. The low-density plasma sources for ion implantation are usually produced by glow discharge, thermal ionization, cathode arc discharge, and RF discharge.

Recently, the technique has been adapted to a RF discharge plasma. The RF pulse discharge electrode is the solid object itself, which generates isotropic low-density gas plasma around the solid object. The RF discharge pulses are applied during times between high voltage negative pulses. The plasma generation around the solid object and ion implantation by high voltage pulse is alternately repeated.

Plasma based deposition of carbon is a particularly interesting field due to the fact that the carbon films are typically harder, smoother, and more resistant to chemical attack than polymer films. Especially, DLC (diamond-like carbon) films are used as many mechanical parts because of their superior tribological properties of high mechanical hardness, high wear resistance and low coefficient of friction [1]. The advantage of PBIID (plasma-based ion implantation and deposition) process is small residual stress compared with conventional process [2,3]. For the hybrid system combined with the RF pulse and negative high voltage pulse, the deposition rates and the properties of deposited carbon films can be varied widely by changing the deposition parameters such as gas pressure of hydrocarbons and negative pulse voltage. In order to get some insight into the plasma processes for C2H2 gas plasma, we have used optical emission spectroscopy as a diagnostic tool.

In this paper, we report optical emission spectroscopy of C2H2 hydrocarbon plasma used for a-C:H deposition by PBIID (plasma-based ion implantation and deposition) process, and we also report optical emission distribution for a solid object with trenches.

2. Experimental setup

Figure 1 shows the experimental setup for the measurement of optical emission from hydrocarbon gas plasma such as acetylene and toluene plasmas in PBIID. In PBIID system, RF pulse for plasma generation and negative pulsed voltage for ion implantation were applied to a hexagonal sample holder through a single electrical feed-through. The RF pulse was the peak power of 300 W, the pulse duration of 50 μs, and the frequency of 13.56 MHz. The plasma ions were implanted to a substrate by negative pulsed voltage of 0 to –20 kV and the pulse duration of 5 μs.

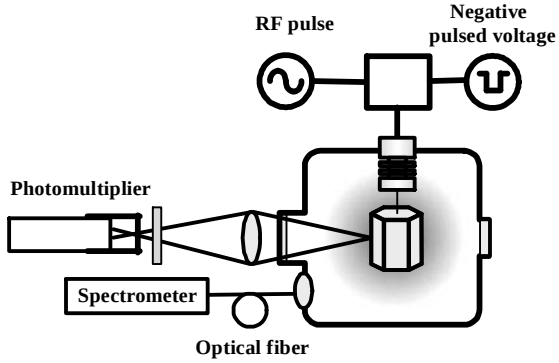

Fig. 1. PBIID process and experimental setup

Figure 2 shows the typical pulse shapes of RF pulse voltage of 50μs duration, negative pulsed voltage delayed 50us after end of RF pulse, and the high voltage current. The current in the Fig.2 shows the typical waveform of the plasma-based ion implantation, in which steeply rise and following decay current are due to growth of plasma sheath around objects.

Figure 3 is sample photographs of a golf driver head, a pipe, and trench objects in PBIID process. The thin plasma luminescence around solid objects was observed.

Optical emissions were measured by an optical multichannel analyzer (HAMAMATSU, C7460) and by a photo-multiplier (HAMAMATSU, R1463) with band-path filters. Deposition rate of DLC film was calculated by thickness of DLC film and by deposition time. A thickness of DLC film was measured with a stylus profilometer (Dektak3, ULVAC).

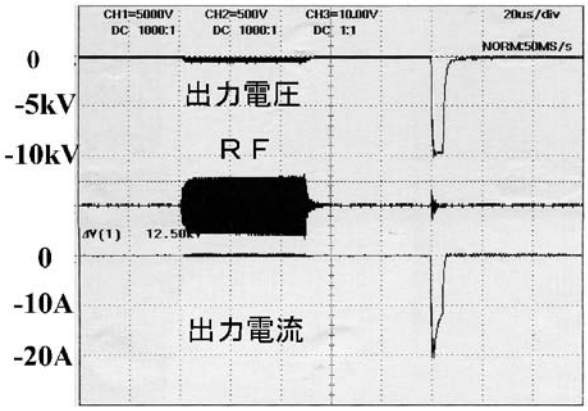

Fig. 2. Typical pulse shapes of RF pulse, pulse high voltage and current.

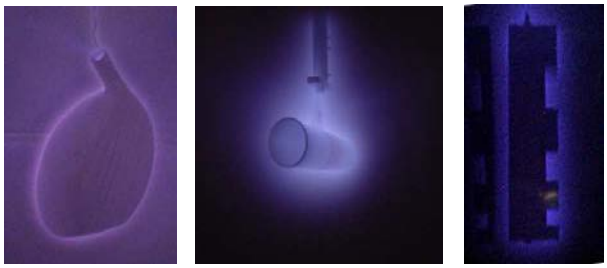

Fig. 3. Photographs of PBIID process of a golf driver head, a pipe, and trench objects

3. Optical emission measurements

Figure 4 shows the spectra of time integrated optical emission from acetylene for various negative pulse voltages. The main emission spectra were CH ($A^2\Delta \rightarrow X^2\Pi$) at 431.4 nm, H_α Balmer line at 656.28 nm, H_β at 486.13 nm, and H_γ at 434.05 nm. The same emission lines were observed for toluene plasma. The emission lines result either from dissociative excitation of the hydrocarbon molecules or from electron impact excitation of radicals and atoms.

Figure 5 shows high voltage pulse currents and optical emissions for various voltages in acetylene gas at pressure of 0.5Pa. The optical emission was measured by the photo multiplier without filter, and then all emissions from ultraviolet to near infrared spectra were integrated. The emissions seems that formation of excited atoms or molecules for emission need order of micro-second and also same order of time for decay. The emission intensity increased according to increase the pulse voltage.

If some lines of the optical emissions from the plasma can be in proportion to DLC deposition rate, it is very

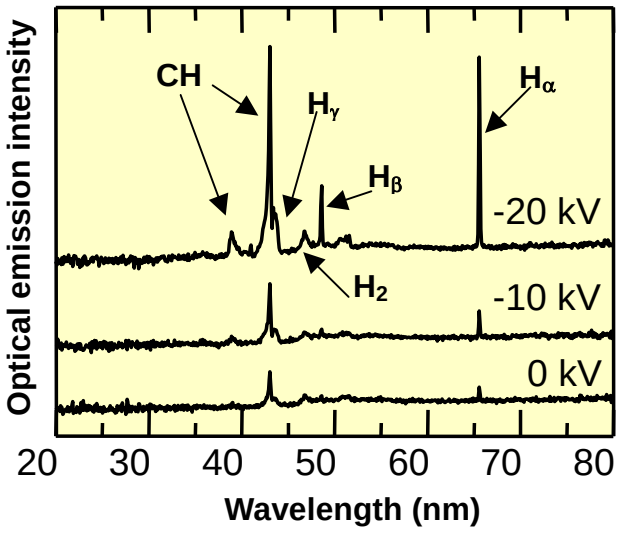

Fig. 4. Typical spectrum from acetylene plasma at various negative pulsed voltages.

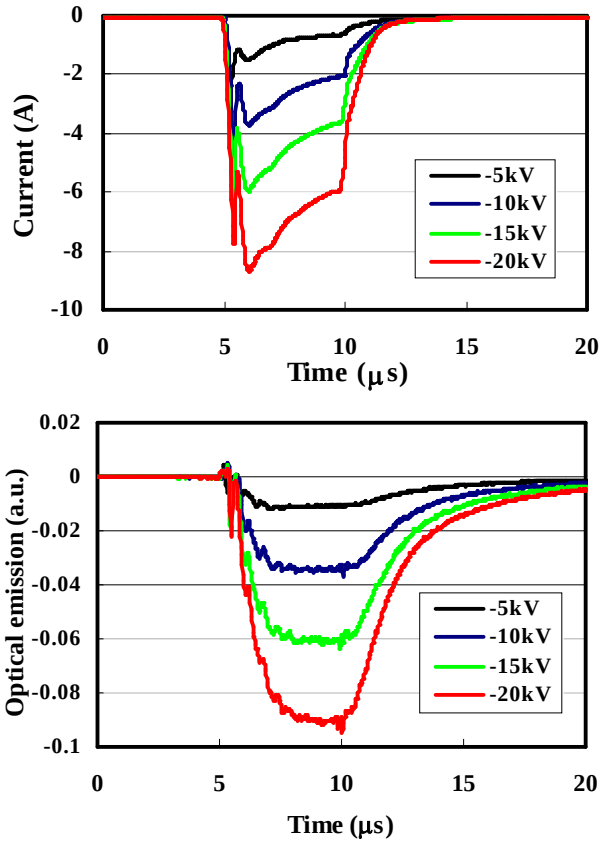

Fig. 5 High voltage pulse currents (a) and optical emissions (b) for various voltages in acetylene gas at pressure of 0.5Pa.

useful for controlling the thin film deposition. The emission lines from carbon plasma were not observed in conventional spectral range of 250nm to 900nm, which is important for the process monitoring. Then, we selected the other these bright lines, CH at 431.4 nm, H_α at 656.28 nm, and H_β at 486.13 nm for the monitoring. The hydrogen H_α, H_β, H_γ Balmer lines radiate to same lower energy level, then H_α, H_β lines are samples to study the Balmer lines.

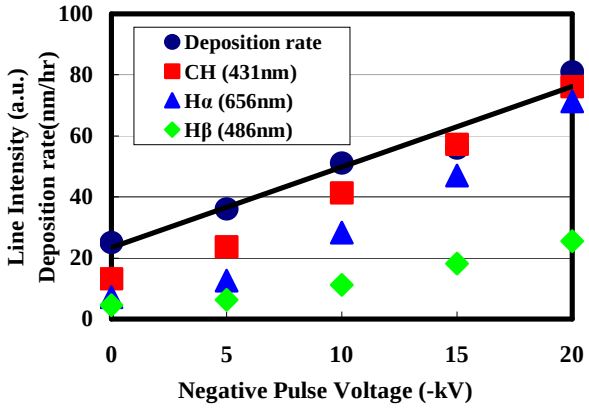

Fig.6 Emission intensity and DLC deposition rates at acetylene gas pressure of 0.5 Pa and repetition rate of 0.5kHz.

The CH emission and deposition rate of DLC film for acetylene plasma increased with straight lines for negative pulsed voltage. On the other hand, the H_α, H_β line intensities did not show linear correlation between the line intensities and deposition rate. The excitation of H Balmer lines may be complicated process, resulting in weak correlation.

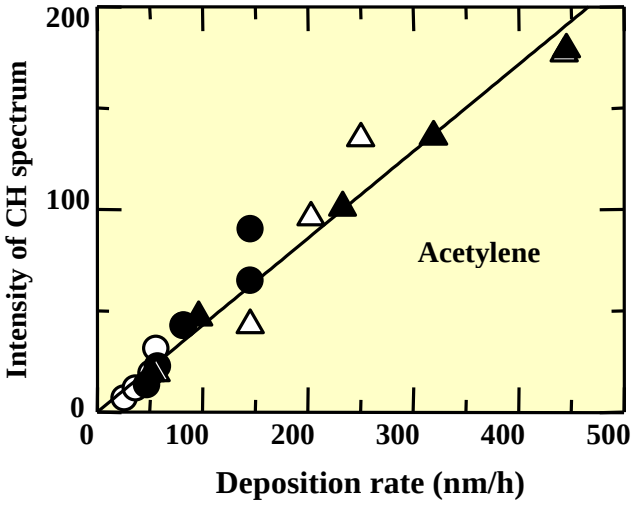

Fig. 7. Intensity of CH spectrum as a function of deposition rate of DLC film for acetylene plasma. ○：0.5kHz, 0.5Pa, HV(0 ~ -20 kV), ●：1.0 kHz, 0.5 Pa, HV(0 ~ -20 kV), △：–10 kV, 0.5 Pa, Freq.(0.5 ~ 4 kHz), ▲：–10 kV, 0.5 kHz, Pres.(0.5 ~ 3.0 Pa)

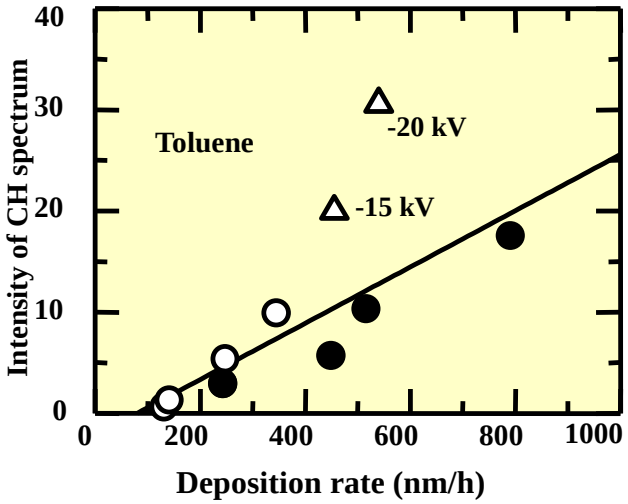

Fig. 8. Intensity of CH spectrum as a function of deposition rate of DLC film for toluene plasma. ○：0.5 kHz, 0.5 Pa ,H.V.(0~-10 kV), △：0.5 kHz, 0.5 Pa, H.V.(-15,-20 kV), ●：–5 kV, 0.5 Pa, Freq.(0.5 ~4 kHz)

Figure 7 and 8 show DLC deposition rate and CH emission intensity for acetylene and for toluene plasmas at pulse repetition rate of 0.5 to 4 kHz, gas pressure of 0.5 to 3 Pa, and negative pulsed voltage of 0 to –20 kV to confirm the correlation. The deposition rate of DLC film for acetylene seams in proportion to the CH emission in any conditions. On the other hand, the deposition rate of DLC film for toluene was not clear for the CH emission, especially for higher pulse voltage of more than –10kV in Fig.8. The voltage and current pulse shapes at the voltage of more than –15kV showed different waveforms compared with those of less than –10kV. The current pulse shapes suggested plasma discharge, resulting in different DLC deposition process.

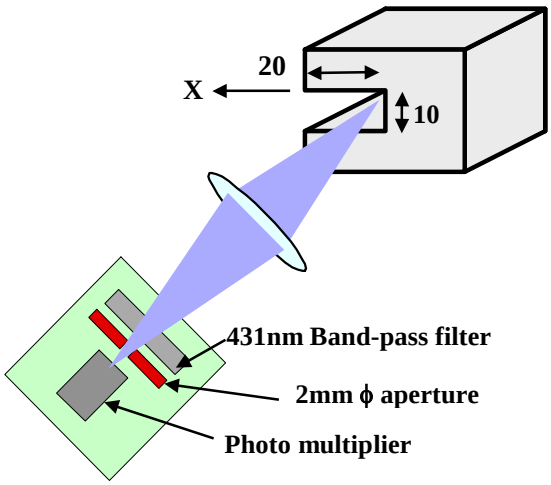

Fig.9 Measurements of emission distribution for trench solid sample.

The bright emission was observed for a trench structure in Fig. 3. We measured the optical emission distribution in space for a trench solid sample and for a flat sample as a reference. Figure 9 shows a setup for emission distribution measurements from plasma for a trench solid sample. The CH line emission of 431nm selected by the band-pass filter was measured by the photo multiplier. The space resolution was 2mm, which was limited by an aperture diameter in front of the photo multiplier. The measured points were 20mm in depth from the edge surface.

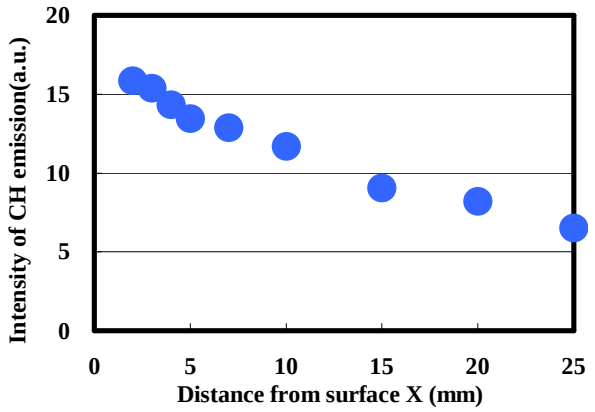

Fig.10 Emission distribution at right angle for flat surface. Negative pulse voltage of –10kV and acetylene pressure of 0.5Pa.

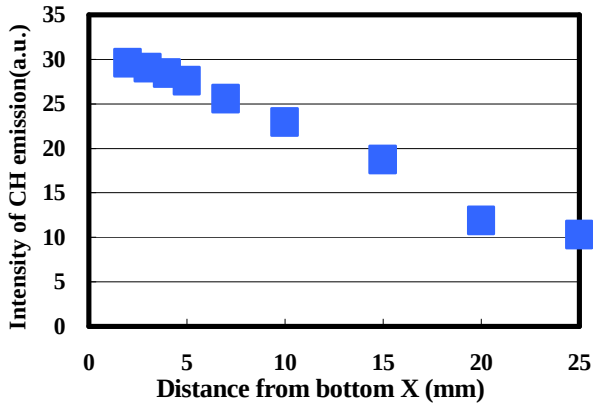

Fig.11 Emission distribution at right angle for trench. Negative pulse voltage of –10kV and acetylene pressure of 0.5Pa.

Figure 10 and 11 show the emission distribution at right angle for a flat and for a trench solid sample with the bottom width of 10mm, the depth of 20mm, and the length of 40mm, respectively. The conditions of the plasma operation were in the same way as negative pulse voltage of –10kV, pulse width of 5μs, acetylene gas pressure of 0.5Pa, and repetition rate of 0.5kHz. The CH line emission showed a peak near surfaces and decreased with distance, in which tendency of emission profile seemed almost in the same manner as the flat sample and as the trench sample. The optical emission had almost the same time history except intensity at the measured points for the flat sample and for the trench sample. It is interesting that the higher optical emission intensity was measured near the bottom surface in the trench than that near the flat surface. On the other hand, the electric field in a trench must be lower than a top surface as a common sense. Discharge in the trench seems to be the most probable, resulting in the bright emission.

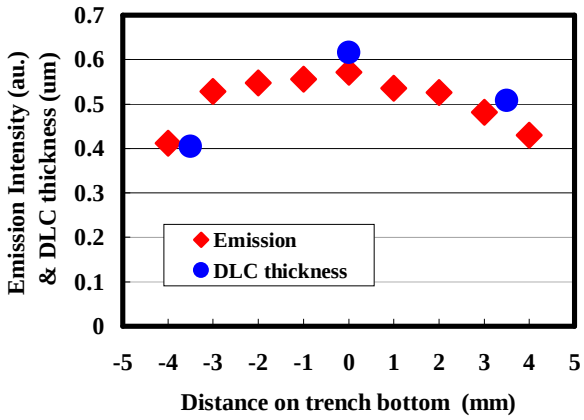

Fig.12 Emission distribution and DLC thickness on trench bottom. Negative pulse voltage of –10kV and acetylene pressure of 0.5Pa.

Figure 12 shows the CH line emission distribution and thickness of DLC deposition on the bottom surface of the trench solid sample. The optical emission and DLC thickness showed a similar tendency that those were lower intensity and thinner thickness at the corners than those at the center.

4. Conclusions

The optical emissions in PBIID system were measured. It was found that the deposition rate of DLC film was almost in proportion to the CH ($A^2\Delta \rightarrow X^2\Pi$, 431.4nm) line emission at measured various conditions for acetylene. It may be useful to control the deposition process by monitoring the optical emission of particular line spectrum. The CH line emission intensity showed a peak near surfaces and decreased with distance. The higher optical emission intensity was measured near the bottom surface in the trench than that near the flat surface.

Acknowledgement

This work was supported by the Cooperation of Innovative Technology and Advanced Research in Evolutional Area (CITY AREA).

References

[1] J. Robertson, Surf. Coat. Technol. 50 (1992) 185.

[2] M.Bilek, D.R.McKenzie, R.N.Tarrant, S.Lim and McClloch, Surf. Coat. Technol. 156 (2002) 136.

[3] Y.Oka, M.Tao, Y.Nishimura, et.al, Nucl. Instr. And Meth. In Phys. Res. B, 206 (2003)

Generation of Microplasma with pulsed discharge of an ethanol droplet in air

N.Shirai*, Y.Onaka, S.Ibuka, K.Yasuoka, and S.Ishii

Department of Electrical and Electronic Engineering
Tokyo Institute of Technology
2-12-1-S3-9 O-okayama, Meguro-ku, Tokyo, Japan

ABSTRACT

An ethanol droplet of 300μm in diameter is used to create a dense microplasma by pulsed discharge. The pulsed discharge took place simultaneously, when the droplet came into the space between miniature electrodes to which a dc high voltage was applied. Vaporization and dissociation of ethanol were confirmed in the discharge because the atomic line of hydrogen was observed in optical emission spectroscopy. Taylor cone is formed on the anode surface after the discharge, because the remaining ethanol on the anode is dragged to the cathode by electrostatic force. One can utilize the filament or electro-spray observed at the tip of the Taylor cone as an initial state of liquid for generating microplasmas.

(key word : microplasma, droplet, ethanol, electrospray, Taylor cone)

I. Introduction

Microplasma is attracting the interest of a number of researchers in these years, because it has a variety of applications such as plasma display panels (PDP), Micro Electro Mechanical System (MEMS), short wavelength light sources and micro chemical reactors. There are many ways to generate microplasmas [1-3]. We adopt a method in which electrical discharges are operated between electrodes, where a material with a small volume is placed [2]. We named it the “mass-limited mode", in which the volume of microplasmas is determined by that of the initial material and the separation of the electrodes, because there is no surrounding wall. As far as a spatially isolated small structure is obtainable, any state of matter such as solid, liquid or gas is applicable for the method. In the case of liquid, one can use droplet as the initial matter. Because the density of liquid is higher than that of gases, it is expected that dense microplasma is generated easily. However, most liquids are in molecular state, processes developing from discharge to plasma are more complicated than those for gases.

Chemical reactions often develop in the liquid phase. Consequently, the additional energy can be supplied to the reactions in the liquid phase through electrical discharges. Non-thermal reactions assisted by high energy electrons are expected. The discharge with liquid specimens is used to the analytical technique. Inductively coupled plasmas, ICP, powered by RF generators are widely used in a luminescence spectroscopic analysis of liquid material. The Processes that make specimens to be atomized and change them into plasma ate very important for the ICP method. Electrospray is also applied to the analytical technique on protein such as the

human genome that contains all of the biological information. The electrospray is created by applying high electric fields on the liquid. In mass spectrometry, atoms or molecule are ionized. Therefore the structure of DNA is destroyed in conventional ICP's methods. Electrospray ionization is used as a soft ionization method for chemical analysis of large biological molecules such as protein and DNA. It is called "soft" because the molecule being ionized does not fall apart or break up during the process [3-5]. In our droplet discharge, various shapes of liquid such as the Taylor cone, electrospray and filament were observed after the discharge. These structures of liquid are used as an initial state of the discharges. In this paper, we discuss the pulsed discharge of an ethanol droplet to create a dense microplasma between electrodes to which dc high voltage is applied in air.

II. Experimental Setup

Fig.1 shows the experimental set up for the discharge of ethanol droplet. The electrical discharge develops simultaneously when the droplet passes between the electrodes to which dc voltage is applied. The electrode system used is either a needle-to-needle one or a sphere-to-sphere one. The needle electrodes are made of stainless steel with a curvature radius of 40μm and the spherical electrodes are made of tungsten-carbide of 2mm in diameter. The pulsed discharge current is supplied by a capacitor connected to the electrodes in parallel. The ethanol droplet was generated by a micro dispenser (MJ-020 by MECT Co.). The spherical droplet with a diameter of 300μm and a volume of 10nl was dropped into the discharge space from the dispenser head. The light emitted from the discharge was observed with a PIN photodiode (DET200 by Thorlab Co.) and was analyzed by a multi-channel optical spectrometer (EPP2000C by Stellar Net Co.). The temporal and spatial behavior of the droplet was observed with a high-speed video camera (FASTCOM -512PCI by Photoron Co.). Early stage of the discharge was observed with a fast ICCD camera (DH734-18U-03 by Andor technology Co.)

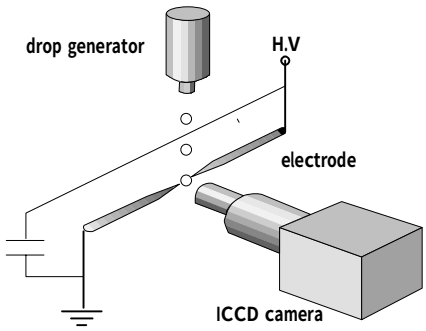

Fig1. experimental setup

III. Results and Discussion

Breakdown voltage dependence on the electrode separation with and without the ethanol droplet was examined using the needle or sphere electrode systems in air. Fig.2 shows the breakdown voltage characteristics for the electrode separation ranging from 100μm to 900μm. When the droplet was placed between the electrodes, the breakdown voltages were less than half of those without the droplet. The breakdown voltage was not affected by the shape of electrodes. The discharge takes place when the droplet is going to pass between the electrodes. One can easily set up a pulsed high current discharge using a capacitor that is connected to the electrodes in parallel. Any switching device is unnecessary to power the pulsed discharge because the discharge is initiated simultaneously when the droplet is placed between the electrodes. Fig.3 shows the voltage and current waveforms observed in the discharge with a capacitor of 200nF charged to 2kV. The rate of current rise of 2.46×10^{10}A/s is obtained as a result of small residual inductance, although no switching device is used in the discharge circuit.

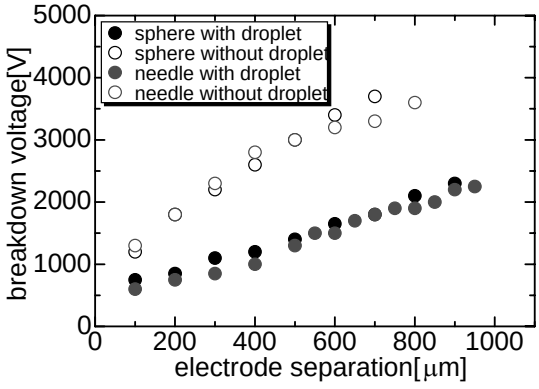

Fig2. breakdown characteristics with and without the droplet

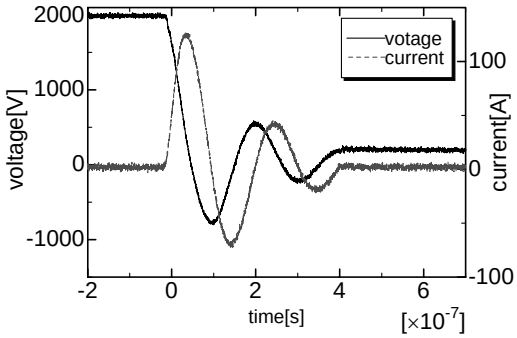

Fig.3 Current and voltage waveforms for the discharge with a capacitor of 2.2nF

Fig.4 shows the temporal change of visible light emission detected with the PIN photodiode. The peak of visible light intensity appears during the first half cycle of the discharge current and after then the intensity decays. Light intensity increases with increasing capacitance and capacitor voltage.

Fig.5 shows a photograph of early stage of the discharge taken with the fast ICCD camera. It was taken at 50ns after the discharge took place with an exposure time of 30ns. Although the discharge develops between the electrodes, the droplet keeps its shape. Breakdown of air precedes the droplet discharge that includes complicated processes such as boiling and vaporization phase before ionization. Fig.6 is an electric field profile near the electrodes, which wad obtained using a commercially available software for the field calculation. In the analysis, we set that the electrode separation was 500μm and the applying voltage was 2kV. The enhanced electric field around the droplet induces gas breakdown.

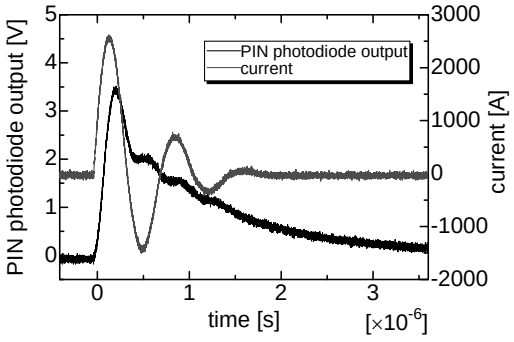

Fig.4 The current and total light emission

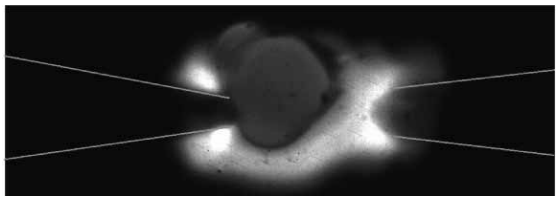

Fig.5 The early stage of droplet discharge observed with the fast ICCD camera

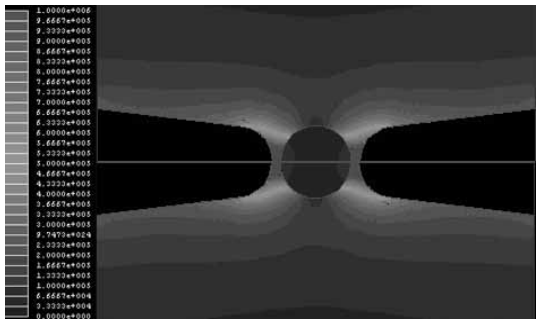

Fig.6 Calculated electric field profile near the electrodes with the ethanol droplet

Fig.7 is time-integrated optical emission spectra of the discharges. Two significant lines are hydrogen atomic line, H_α and a nitrogen atomic line. The nitrogen line is originated in the discharge in air. The H_α line gives evidence of the vaporization of ethanol. The intensity of H_α line increases with increasing the capacitor energy from 4.4mJ to 400mJ. The ratio of the intensity of H_α line to that of the nitrogen line also increases, because dissociation of ethanol is enhanced. Fig.8 shows the temporal behavior of the discharge including current and the spectral lines. The peak of nitrogen line appears immediately after the current start to rise. The maximum of the H_α line is delayed by 1μs from the peak of the nitrogen line. The result confirms that air breakdown occurs between the electrodes initially and then the discharge of ethanol droplet develops. This agrees also with the photograph taken using the fast ICCD camera shown previously in fig.5. When a droplet of sodium chloride solution was used, an atomic line of sodium was observed in the time-integrated emission spectra of discharges. Utilizing the emission spectra, the droplet discharge is applied to analytical technique.

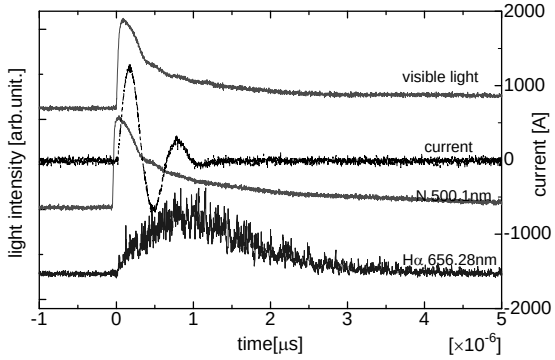

Fig.7 Temporal change in nitrogen and hydrogen lines

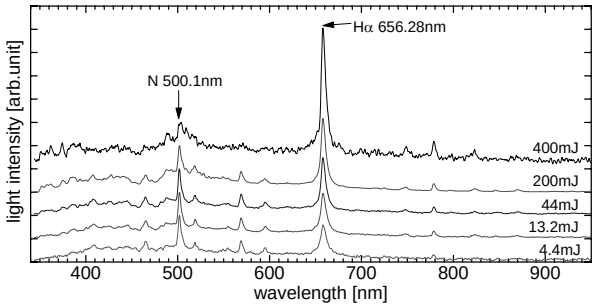

Fig.8 Time integrated optical emission spectra of ethanol discharge

Macroscopic behavior of the droplet before and after the discharge was observed using the high-speed video camera with a frame rate of 16000fps. Fig.9 shows ten frames of the video camera for the discharge with a stored energy of 13.2mJ. In the first three frames, a free-falling ethanol droplet is recorded. The discharge takes place in the fourth frame. The deformation process is seen from the fifth frame where a part of the droplet remains its original shape. When the capacitor energy is increased to 200mJ, the droplet loses its shape after the discharge and it is exploded with a shock wave as shown in Fig.10. Fig.11 show the complete evaporation of the droplet during the discharge, when the energy is increased further up to 400mJ. The evaporation of the droplet is observed more clearly in Fig 12, which is a shadow-graph image illuminated by a He-Ne laser. The image was recorded through an interference filter that is transparent to the laser light.

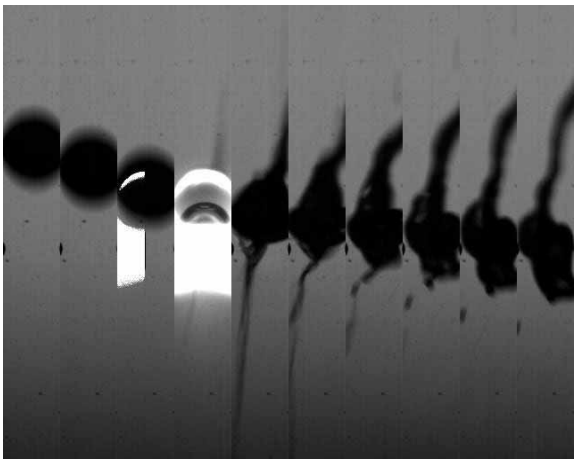

Fig.9 High speed video frames of the discharge with energy of 13.2mJ

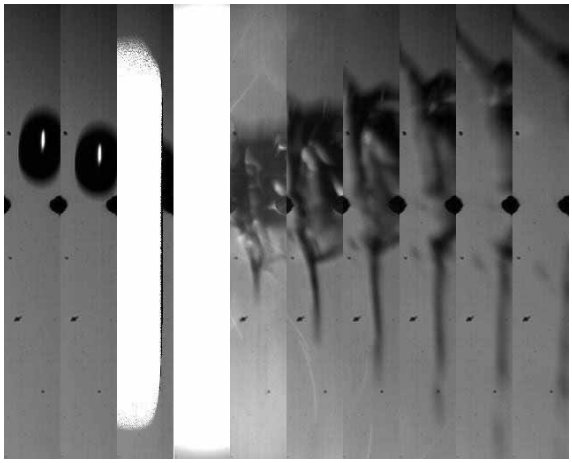

Fig.10 High speed video frames of the discharge with energy of 200mJ

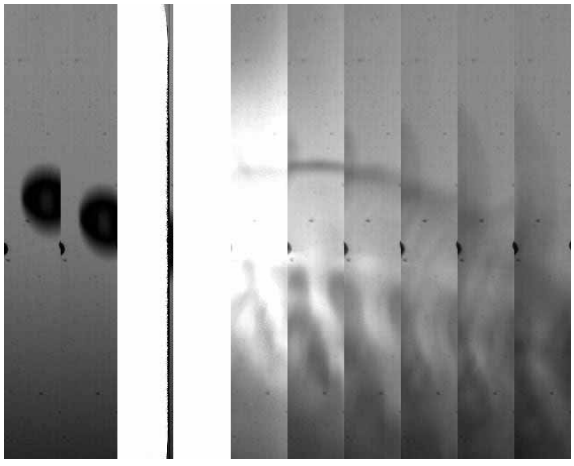

Fig.11 High speed video frames of the discharge with energy of 400mJ

A small amount of ethanol existed on the surface of the electrode after the discharge. The remaining ethanol on the anode is dragged to the cathode by electrostatic force. When the electrode separation is over 700μm, the Taylor cone is formed on the anode surface. Fig13 is a photograph of formation of a filament of ethanol protruding from the tip of the Taylor cone observed in the sphere-to-sphere electrode system. When an electric field is higher, the electrospray is formed at the tip of the filament in the needle-to-needle electrode system. One can utilize the filament or electro-spray as an initial state of liquid for generating microplasmas.

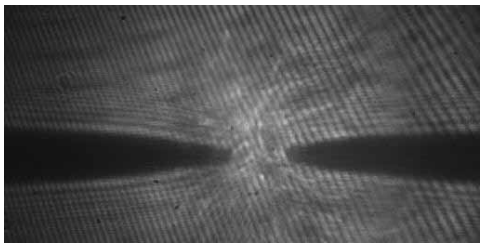

Fig12. Evaporating ethanol droplet between the electrodes

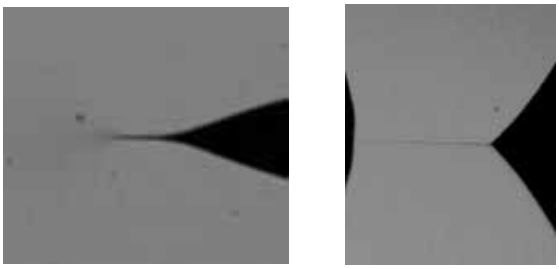

Fig13. Formation of Taylor cone with electrospray (left) or filament (right)

Ⅳ. Conclusion

We have made microplasma with the ethanol droplet by electrical discharge in air. The generation of microplasma with the “mass-limited mode” using liquid shows a number of features that are specific to the microplasma. Pulsed discharges are obtained without any high-voltage pulse generator, because the discharge starts as soon as the droplet comes into between the electrodes.

The formation of the Taylor cone is useful as a viewpoint of microplasma generation. One can utilize the filament or electro-spray observed at the tip of the Taylor cone as an initial state of liquid for microplasmas.

Acknowledgment

This work was supported by a Grant-in-Aid for Scientific Research from the Ministry of Education, Culture, Sports, Science and Technology.

References

[1] Kunihide Tachibana, Kaname Mizokami, Naoki Kosugi, Tetsuo Sakai: “Three-dimensional diagnostics of dynamics behaviors of exited atoms in microplasmas for plasma display panels", IEEE Transactions on Plasma Science, Vol.31 (2003) p.68-73

[2] Takuma Yokoyama et al, “DC Discharge Characteristics in Microplasma with Miniature Gas flow”, The paper of Technical Meeting on Pulsed Power Technology, IEE Japan (2004) PTP-04-51

[3] Takuma Yokoyama,Takuya Kuraoka, Kazuya Takano, Shinji Ibuka, Koichi Yasuoka, Shozo Ishii, “Early Stage of Pulsed HighCurrent Discharge with Copper Powder”, IEEJ Transactions on Fundamentals and Materials,v 123,n 1,(2004)

[4] N.shirai, Y.Onaka, S.Ibuka, K.Yasuoka, S.Ishii “Generation of micro plasma that used electrical discharge of ethanol droplet”, The paper of Technical Meeting on Plasma Science and Technology, IEEE Japan (2004) PST-04-29

[5] Fenn, John B,"Electrospray wings for molecular elephants (Nobel lecture)",Angewandte Chemie - International Edition, v 42, n 33, (2003) p 3871-3894

[6] R. Juraschek, F.W. Rollgen “Pulsation phenomena during electrospray ionization” International Journal of Mass Spectrometry 177, (1998) p.1-15

[7] A. L. Yarin, S. Koombhongse, D. H. Renekera “Taylor cone and jetting from liquid droplets in electrospinning of nanofibers” Journal Of Applied Physics v.90, n9, (2001) p4836-4846

Efficient generation of copper particle microplasma with a fast pulsed discharge current

S.Hamada*, T.Amano, S.Ibuka, K.Yasuoka, and S.Ishii

Department of Electrical and Electronic Engineering
Tokyo Institute of Technology
2-12-1 O-okayama, Meguro-ku, Tokyo, Japan

ABSTRACT

We examined the early phase of pulsed discharges with a copper particle of 100μm in diameter, where solid copper is vaporized and ionized, to generate dense microplasmas. Electrical energy has to be delivered to the particle efficiently during the phase transition. We built a low-inductance discharge system to obtain a fast rate of current rise. The discharges were observed using a fast ICCD camera and laser shadowgraph technique. Vaporization of particle copper takes place at the contact region between the particle and the electrode. Vaporization and ionization do not take place in the whole part of the particle. However, the input energy to the particle is 7.5mJ during the phase transition, which is larger than that obtained using the power supply with slower current rise.

Keyword: Copper, Powder particle, Microplasma, Pulsed discharge

Ⅰ.Introduction

Microplasmas are utilized in a variety of applications such as plasma display panels, microelectromechanical systems, short wavelength light sources, and micro-reactors in chemistry. We proposed and examined generation of dense microplasmas with solid powder particles. Fiber pinches and exploding wires are well known plasmas created with solid materials. These plasmas are powered by high voltage or high current pulse generators. In this study, we used a copper particle with a diameter of 100μm and capacitor discharge with a peak current of 2-5kA. Applications of the microplasma are micro-metallization, microscopic plasma processes, and thin film formation in very small areas. In previous study, we showed that microplasmas were generated with the cooper particle that was heated and vaporized by pulsed discharges. However, the phase transition from solid to gas did not take place uniformly in the particle, because of slow current rise. We examined the influence of the rate of current rise on the discharge development from solid copper. We designed and built a low inductance discharge system to establish faster discharge as compared with the previous experiments.

Ⅱ.Experimental apparatus

We used a spherical copper particle with a diameter of 100μm as initial material. Reproducibility of the pulsed discharge is highly expected and handling of the small material is easily conducted because the powder is sphere. Taking application into account, the generation of microplasma with the copper particle was carried out in air. The ratio of electrostatic force to gravitational force acting on the particle increases with decreasing the particle radius. This enables us to control the particle with electrostatic force. The particle was easily attached to the surface of electrodes electrostatically. Manipulation of placing the particle between electrodes was conducted by observing under an optical magnifying system with the combination of lenses and a CCD camera.

A pulsed current flows through the particle, whose temperature increases by Joule heating, because the particle is made contact with electrodes initially. The particle becomes plasmas from solid state through the phase transition processes of fusion, vaporization and ionization. The rate of current rise has to be high enough for the electrical energy to be delivered to the particle during the phase transition. The initial resistance of particle is so small that efficient power transfer from the power supply to the discharge load is difficult during this phase transition. Copper has often been used as an initial material in the experiments of exploding wire and fiber pinches. Therefore, there are a lot of reporting on material properties at each phase and discharge characteristics of copper are well known.

Fig.1 is the schematic of discharge circuit. A small capacitor bank of 200nF is charged to 3kV with a stored energy of 0.9J and is discharged by a spark-gap switch that is triggered by a ultra-violet light pulse. To make the current rise as fast as possible, we designed the discharge circuit to have low residual inductance. The switch is directly connected to the discharge electrodes made of tungsten, around which the capacitors are located symmetrically. Making the length of thin electrode region to be short, inductance of the discharge electrodes with a diameter of 300μm is reduced.

Temporal behavior of the discharge development was observed using a fast ICCD camera and a laser shadowgraph technique, in which second-harmonic wavelength of 532nm of a Nd:YAG laser with a pulsewidth of 6ns was used. Optical emission spectroscopic measurement was conducted using an optical mulch-channel analyzer to examine excitation and ionization of copper atoms.

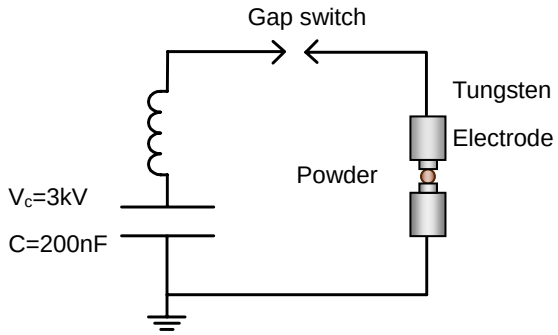

Figure.1. Schematic of discharge circuit.

Ⅲ.Results and discussion

1. Measurement of voltage and current

Fig.2 is a discharge current, of which peak is 3.5kA and reaches at 185ns. The rate of current rise is 2.97×10^{10}A/s, which is eight times larger than that for the previous experiments, where the current peak of 2.3kA reaches at 960ns. The current density is 4.5×10^{7}A/cm^2, which is comparable to that of high energy fiber pinches.

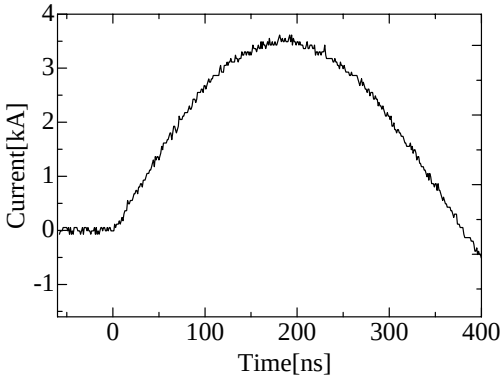

Fig.2. Discharge current with a copper particle at charging voltage of 3kV.

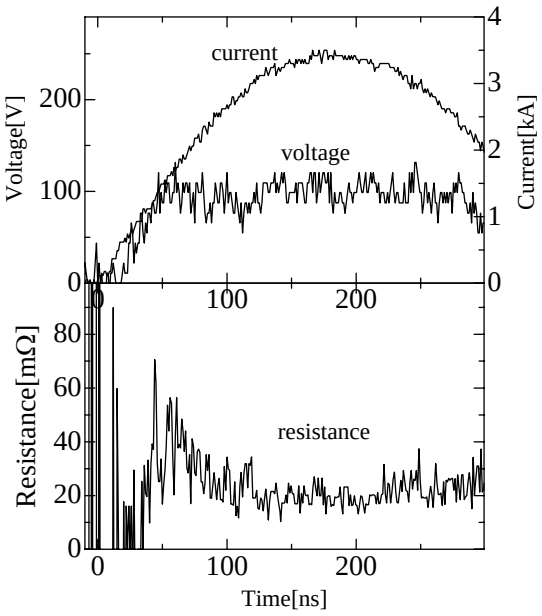

Fig.3. Temporal change of voltage, current, resistance of the discharge.

Although the discharge current is sinusoidal, the electrode voltage increases linearly and stays constant at 100V after 50ns as shown in Fig.3. The voltage is obtained from the measured one by eliminating inductive component and voltage drop in the electrodes. The effective resistance between electrodes increases steeply and reaches to approximately 20mΩ at t=75ns, which is much larger than the initial value of 0.15mΩ. When the discharge is initiated, temperature of the copper particle increases. It goes through from melting point to boiling point. Vaporization of the copper develops at the boiling point and ionization also develops at the same time. The constant resistance of 20mΩ means that electrons and copper ions exist between the electrodes.

2. Optical emission Spectroscopy

Fig.4 shows time-integrated spectral profiles of the atomic and ionic lines of copper from the discharges. The copper atomic lines, Cu I of 510.55nm, 515.32nm, 521.82nm, and 529.25nm are observed. The copper ionic line, Cu III of 437.71nm is also observed. Any spectral lines of tungsten, oxygen, and nitrogen do not appear. Consequently, melting of tungsten electrodes and ionization of air surrounding the copper particle are negligible. Ionization of air does not develop, because the electric field is 1MV/m between the electrodes.

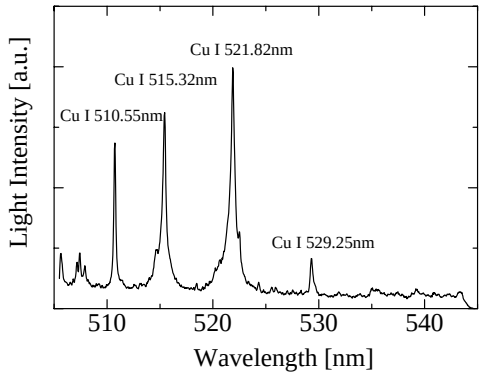

(a) Copper atomic lines

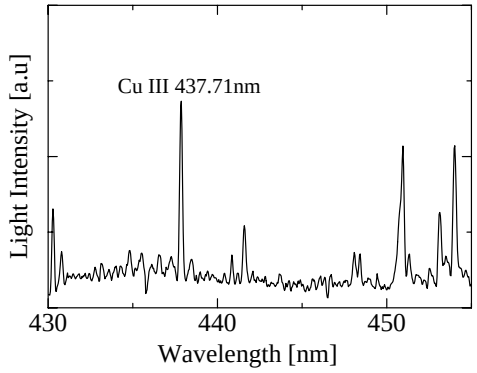

(b) Copper ionic lines

Fig.4. Time-integrated spectral profiles of the copper atomic lines and ionic lines.

Fig.5 summarizes the temporal change in discharge current, electrode voltage, visible light emission, copper atomic line, and copper ionic line. Intensities of both the copper atomic and ionic lines increases from t=75ns, where the electrode voltage reaches its constant value of 100V. The result that these lines appear at the same time shows that vaporization and ionization of the particle develops simultaneously. In the present experiments, both atoms and ions of copper exist at the beginning of

vaporization phase, because uniform phase transition from liquid to gas does not take place spatially. Higher capacitor energy is necessary to establish uniform vaporization of the particle. The timing in which the spectral lines appeared fluctuated shot by shot. This was caused by the difference in contact condition between the particle and the electrode surface, which affects current distribution in the particle.

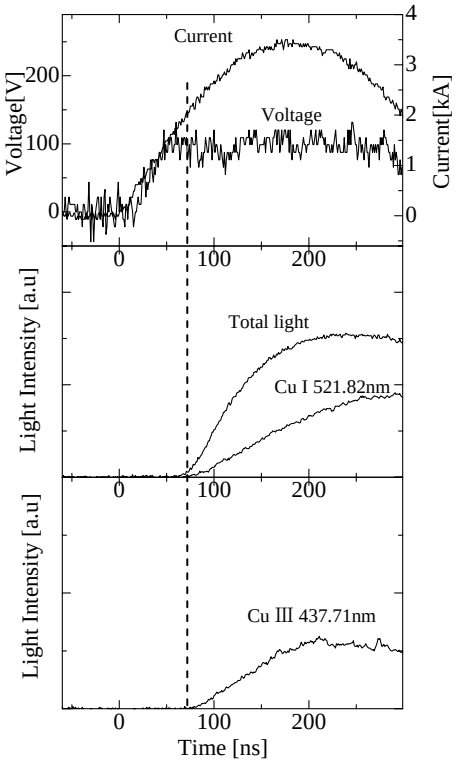

Fig.5. Temporal change of spectral lines.

3. Measurement of ICCD camera

Fig.6 shows visible light photographs of the discharge recorded using the fast ICCD camera with an exposure time of 2ns. Each photograph is taken for different discharge. Weak light emission appears at the contact regions between the particle and electrode at t=24ns. The emission expands to wide area between the electrodes at t=35ns. The emitted light is from the high temperature copper vapor. However, the intensity is not observed in the signal shown in Fig.5. This is because of the difference in the dynamic-range of sensitivity of the ICCD camera and the photo-multiplier. Intense emission appears at the contact region, where current density is extremely high. The shape of particle clearly recorded. At t=75ns, copper vapor expands further and the particle is concealed by the emission.

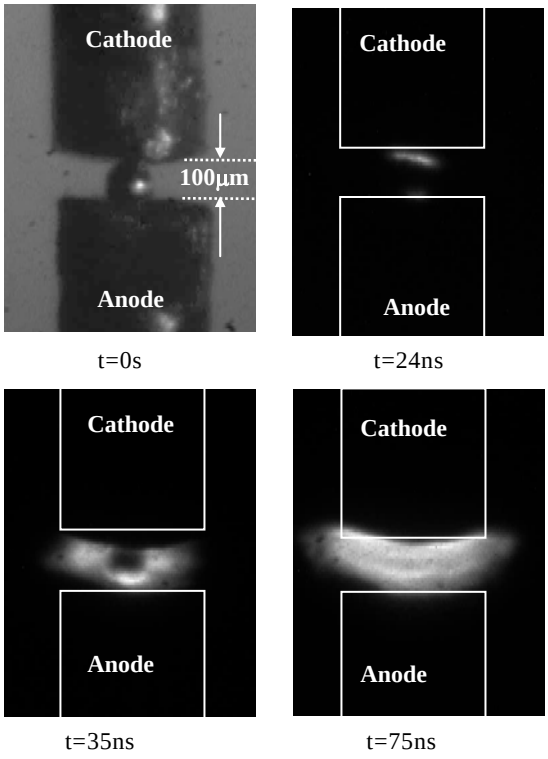

Fig.6. Snapshots of the discharge taken with the ICCD camera.

4. Laser shadowgraph observation

Visible light photography is not suitable to observe spatial change of the particle. Fig.7 is images observed with the laser shadowgraph method. Deformation of the particle begins at t=75ns development of vaporization is observed near the anode. Vaporization appears remarkably at the contact region of the particle and the anode, where current density is very high as shown in Fig.7(a),(b). Afterward, copper vapor expands between the electrodes. The temperature at the surface of the particle reaches more than 2600℃. The particle has not touched the electrode surface in these images judging by the data of Fig.3 in which voltage and resistance stay constant. Compared with previous results, the rate of current of rise affects characteristics of the early stage of the discharge.

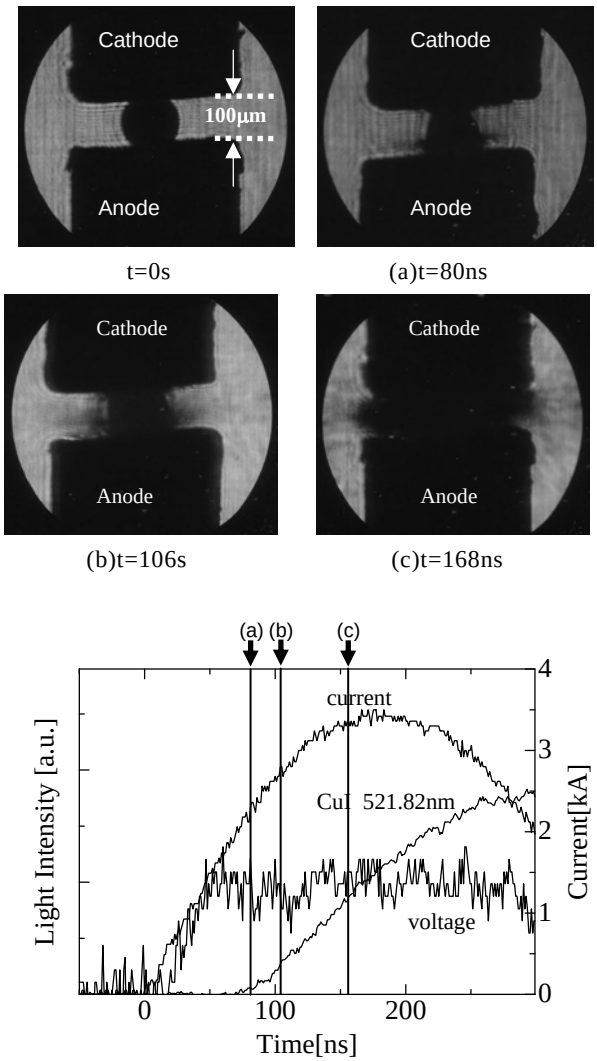

Fig.7. images observed with the laser shadowgraph method.

5. Characterization of energy input

Transition point and required energy for transition of the copper particle of 100mm in diameter are summarized in Table.1. Temporal change of energy delivered to the particle is calculated using the current and electrode voltage waveforms. Energy delivered to the particle up to t=75ns is 7.5mJ, which is larger than 0.94mJ obtained in the previous experiment. Energy input at the early phase of discharge in which the phase transition takes place is affected by the rate of current rise remarkably. Therefore, a fast pulsed power supply is required to generate the microplasma with powder particles efficiently. In the present experiment, the delivered energy of 7.5mJ is not large enough to the energy of 28.5mJ, which is necessary to vaporize the particle completely. The whole part of the copper particle is not vaporized and the phase transition does not develop uniformly, because the energy is inadequate.

Table.1. Transition points and energy required for transition of the copper particle with a diameter of 100μm.

Melting Temperature	1083℃
Boiling Temperature	2580℃
Melting Energy	3.08mJ
Boiling Energy	28.5mJ
Ionization Energy	83.3mJ
Energy Deposited	7.5mJ
Percent of Vaporization Energy	26%

6. Conclusion

In the copper particle discharges in air, copper atoms are mainly ionized and ionization of oxygen and nitrogen is negligible. Vaporization of the copper takes place at the contact region between the particle and the electrode, where discharge current density is high. Energy input up to vaporization of the particle is affected by the rate of current rise. Fast pulsed discharge current is necessary to generate micorplasma with small solid particle efficiently. However, the electrode voltage must be kept lower than breakdown voltage of air for the discharge current to be sustained by electrons and copper ions.

References

[1]T,Amano,S.Hamada,S,Ibuka,K.Yasuoka,S,Ishii, "Efficient Energy Delivery in a Copper Particle Microplasama", The paper of Technical Meeting on Plasma Science and Technology, IEEE Japan(2004), PST-04-97

[2]C. E. Wen et al "Processing of fine-grained aluminum foam by spark plasma sintering", Journal of Materials Science Letter, v.22 (2003), pp.1407-1409
[3]Keyser, C et al, "Studies of high-repetition-rate laser plasma EUV sources from droplet targets", Applied Physics A: Materials Science and Processing, v.77, n.2 (2003), pp. 217-221
[4]M.G.Haines et al, "The past, present, and future of Zpinches", Physics of Plasmas, v.7 (2000), n.5, pp.1672-1680
[5]K.M.Chandler et al, "The Relationship Between Exploding Wire Expansion Rate and Wire Material Properties Near the Boiling Temperature", IEEE Transaction On Plasma Science ,v.30 n.2 (2002), pp577-587
[6]D.A.Hammer,D.BSinars, "Single-wire explosion experiments relevant to the initial stage of wire array Z pinch, Laser and Particle Beams, v19 n3(2001), pp577-391

Enhancement of Perpendicular Velocity Component of An Intense Relativistic Electron Beam Using Magnetic Cusp Field

Akihiro Osawa, Naru Tomisawa, Ritoku Ando and Keiichi Kamada

Graduate School of Science and Technology, Kanazawa University, Kanazawa, 920-1192

An electron beam with energy of 500-700 keV, current of 3 kA and duration of 200 ns was injected into magnetic cusp field with magnitude of 3-8 kG in order to increase the azimuthal velocity component of electrons. The change of the velocity along the axis of the magnetic field was measured in front of and behind the cusp field. The axial velocity was reduced as the magnitude of the magnetic field increased. As the energy was conserved in the static magnetic field, the azimuthal velocity was increased. However, the beam current passing through the magnetic cusp field was decreased as the magnitude of the magnetic field and/or the radius of the beam increased. A particle-in-cell simulation code KARAT was used to estimate the practical transition width and the current passing through the magnetic cusp field.

Keywords: Intense electron beam, electromagnetic wave, superradiance, cusp, azimuthal velocity

1. Introduction

Intense electromagnetic radiation sources are developed for applications in nuclear fusion, particle accelerators, radars, etc. Nearly continuous power output of ∼1 MW is achieved by Gyrotron etc. On the other hands, the microwave devices with output power over 1GW are still in an experimental stage. An intense relativistic electron beam (IREB) is used as a convenient energy source. Usually, the conventional mechanisms for microwave radiation applied to the low power devices are employed to obtain the intense microwave radiation. Though an IREB with duration of several hundred nano second is utilized, the breakdown caused by the strong electric field of the radiated microwave limits the microwave duration less than 100 ns, and the radiation efficiency decreased dramatically. One of the solutions for the breakdown is to develop new mechanisms of short-pulsed electromagnetic radiation with high efficiency. Stimulated emission from extended electron bunches - superradiance (SR) [1] can be considered as effective mechanism of generation of ultra-short intense electromagnetic pulses with output power over 1 GW. Different types of SR emission (bremsstrahlung, cyclotron, Cherenkov) were studied theoretically and were observed experimentally [2-4].

We found out a new mechanism of SR. An IREB whose azimuthal velocity is the same as the axial velocity and the magnetic mirror field were utilized. When the magnetic mirror field reflected the IREB, the new SR could be expected. The radiated frequency was around the cyclotron frequency. We used particle-in-cell simulation code KARAT[5] and obtained the results as shown in Fig. 1. The beam parameters used in the simulation were nealy equal to those of the beam source mentioned in this paper except the beam duration. Monochromatic frequency radiation was expected and the duration of the radiation was found to be very short with high intensity. More detail of the radiation is now studied theoretically. We started to realize the new SR device with an IREB. As the beam duration should be changed by multi-stage autoacceleration method [6], an axial velocity dominant hollow beam must be used at the initial beam injection stage. To increase the azimuthal velocity component of the beam, we use magnetic cusp field behind the multi-stage autoacceleration apparatus.

The behavior of the electron beam passing through magnetic cusp field was studied extensively in 1970s to obtain electron ring [7-11]. In

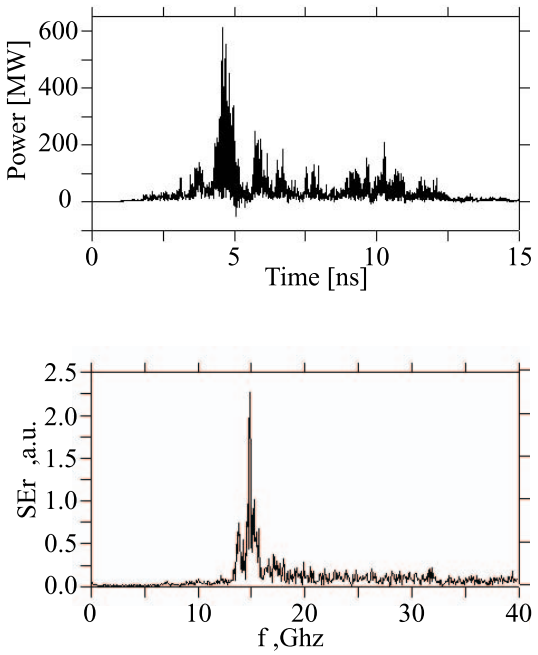

Figure 1: Simulated frequency spectrum and power output of new SR.

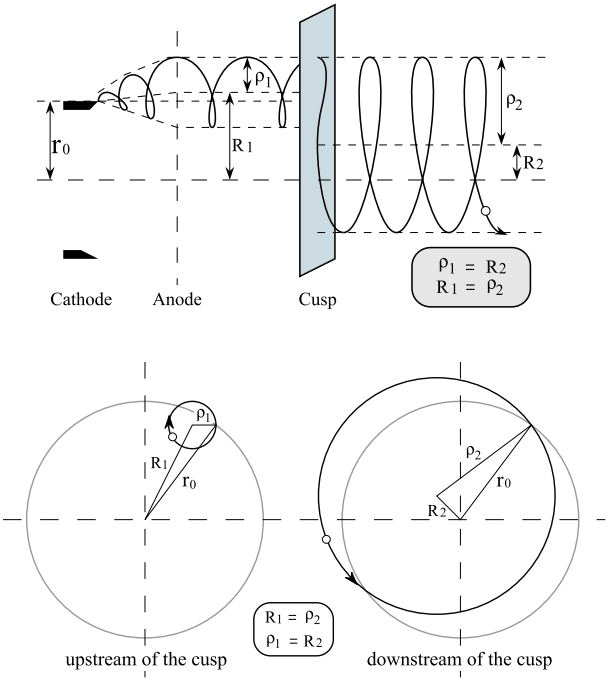

Figure 2: The schematic of the particle orbit through the idealized magnetic cusp field. Up: electrons are injected from an annular cathode. Down: cross section of the orbits.

this paper, we use a magnetic cusp field to increase and control the azimuthal velocity component of the electron beam for new SR described above.

2. Single Particle Motion

A hollow electron beam emitted from an annular cathode with radius r_0 centered on the axis of the magnetic cusp field. It is assumed that an ideal magnetic cusp field has only constant axial component B_z and its direction turns to opposite $-B_z$ at $z = z_0$. In this paper, we call $|B_z|$ the magnitude of the magnetic field. Using the Lagrangian for the motion of relativistic electrons in an external axisymmetric magnetic field, motion of an electron passing through an idealized cusp field configuration described above is obtained[7]. Electrons move along helical orbits with Larmor radius ρ_1 with the radial length of centers of gyration R_1 (Fig. 2) and are injected into the magnetic cusp field at $z = z_0$. The Larmor radius and centers of gyration change to ρ_2 and R_2, respectively, at the downstream side of the cusp. The relation among Larmor radii and the centers of gyrations is written as,

$$\rho_2^2 = r_0^2 + \rho_1^2 = R_1^2 \quad (1)$$

$$R_2^2 = \rho_2^2 + r_0^2 = \rho_1^2. \quad (2)$$

The Larmor radius in the downstream side, ρ_2, is equal to the distance of the center of gyration from the center axis in the upstream side, R_1. The schematic of the particle orbits is shown in Fig.2. The total electron velocity in the static magnetic field is a constant of the motion and it is written as

$$v_0^2 = v_{z1}^2 + \rho_1^2\omega_c^2 = v_{z2}^2 + \rho_2^2\omega_c^2, \quad (3)$$

where v_0 is the initial velocity, v_{z1} and v_{z2} are the axial velocities in upstream and downstream side of the cusp, respectively, and ω_c is the Larmor frequency. The azimuthal velocity of electron is increased in the downstream side, as the Larmor radii ρ_2 is increased as shown in Fig. 2.

Calculated square of the velocities are shown in Fig. 3 as a function of magnitude of the magnetic field using r_0= 5 mm, initial energy = 700 keV. The azimuthal velocity increases as

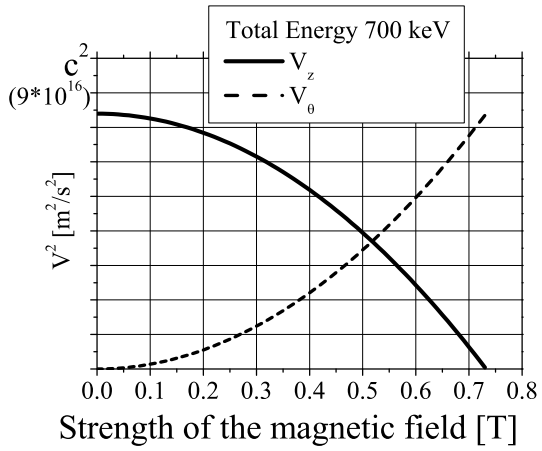

Figure 3: Calculated square velocities. Solid line indicate the calculated result using equation of motion for a single electron.

the axial velocity decreases. The electron cannot pass through the cusp magnetic field when the magnitude of the magnetic field is larger than about 0.7 T. The maximum magnitude of the magnetic cusp field that electrons can pass through increases as the initial electron energy increases and /or the R_1 decreases.

The single electron estimation shows that the magnitude of 0.5 T is enough to obtain electrons whose azimuthal velocity is nearly equal to the axial one. The magnetic cusp field can enhance the azimuthal velocity of an electron. In the experiment, space charge effect of the intense electron beam and non-idealized cusp magnetic field might make the situation difficult.

3. Experimental Setup

The experimental configuration is shown in Fig.4. A hollow electron beam with energy of 550-800 keV, current of 3 kA and duration of 180 ns was injected from an annular cathode with diameter of 10 or 15 mm into a drift tube with inner diameter of 30 mm. Two opposing solenoid coils are used to form a magnetic cusp field. Two coils had an equal size and generated the same magnitude up to 0.8 T but opposite direction of the magnetic field. A soft iron plate was placed between the coils to narrow the cusp length. The magnitude of the axial magnetic field along the axis is shown in Fig. 5. The transition width of the cusp was about 10 cm

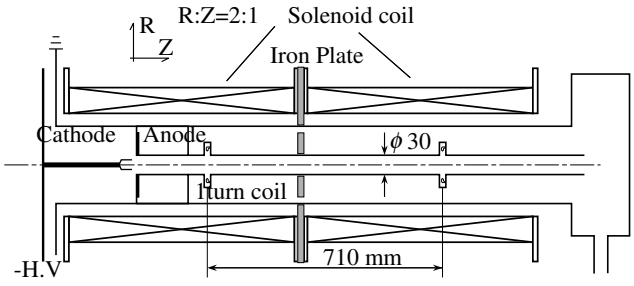

Figure 4: Experimental configuration.

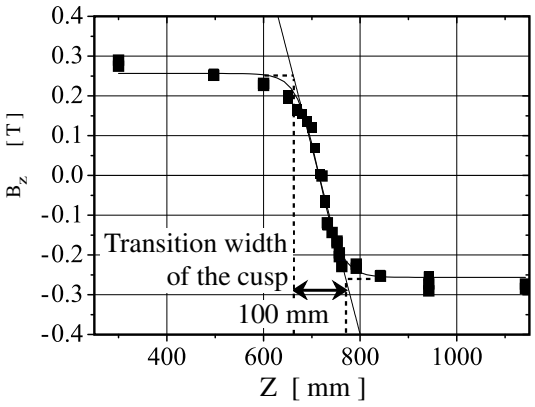

Figure 5: The magnitude of the axial magnetic field along the center axis measured by an one turn magnetic probe. The transition width of the magnetic cusp field is about 10 cm.

as shown there. A movable beam detector and fixed magnetic probes were used to observe the beam current.

3. Experimental Results

The shape of the cross section of the beam was observed by a damage pattern on the brass plate. The cathode with diameter of 10 mm was used. Though the inner diameter was about 9 mm at both side of the cusp, the outer diameter was a little decreased at the downstream side of the cusp, as shown in Fig. 6.

The axial velocity of electrons in the downstream side of the cusp was measured by the time-of-flight method. The square of the axial velocity is plotted against the magnitude of the magnetic field in Fig. 7. The axial velocity of electrons decreased by the magnetic cusp field. As the kinetic energy of electrons is conserved in the static magnetic field, the az-

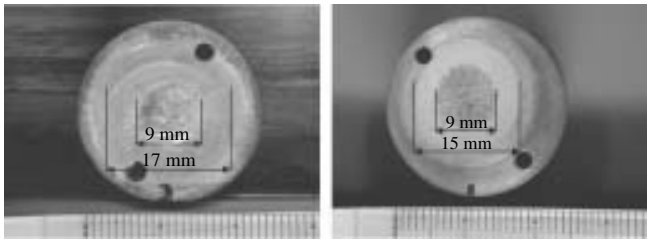

Figure 6: Damage patterns in the upstream and downstream sides of the cusp. The outer radius of the damage was decreased at the downstream side of the cusp field.

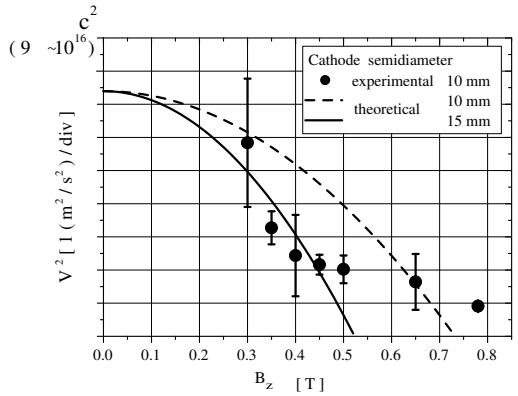

Figure 7: The square of the axial velocity are plotted against the magnitude of the magnetic field. Solid line indicates the calculated result using the equation of motion for a single electron.

imuthally velocity should be increased. Solid and dotted lines in Fig. 7 indicate the calculated results for a single electron. The decrease of the square velocity through the cusp is larger than the calculated result for the cathode with diameter of 10 mm. It is not clear yet that the difference between experimental results and the calculated results for a single electron comes from the space charge effect, the presence of the transition width of the magnetic cusp field and/or the thickness of the beam.

The beam current detected at the downstream side of the cusp was smaller than the injected beam current. In Fig. 8, the waveforms of the beam current observed at the upstream and downstream side of the cusp are shown. The beam current passing through the cusp was decreased as the magnitude of the magnetic field was increased. The ratio of the

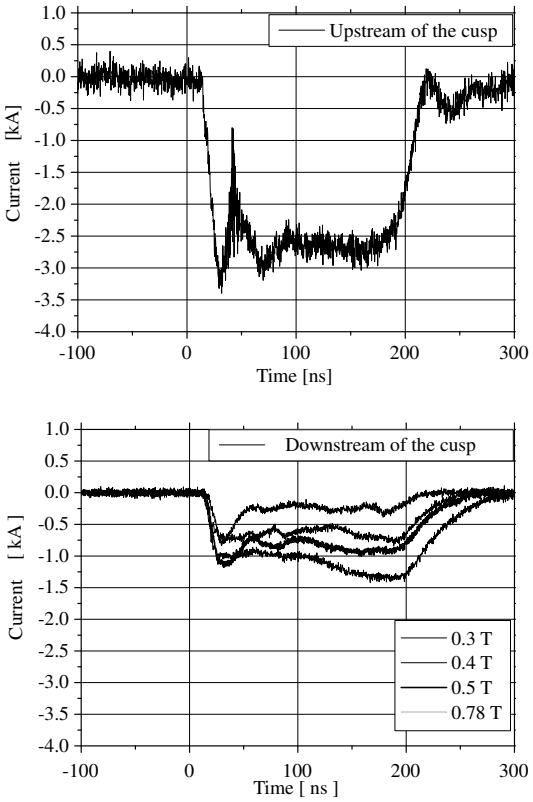

Figure 8: The waveforms of the beam current observed at the upstream (up) and downstream (down) side of the cusp.

passing current to the injected one is plotted against the magnitude of the magnetic field in Fig. 9. The injected current is not so changed by the electron energy. Note that the axial magnetic field more than 0.3 T was necessary to propagate the beam for long distance. The diameter of the cathode affected strongly to the beam current passing through the cusp field. The transition width of the cusp that electrons experienced increases as the distance from the center axis increases. As shown in Fig. 6, the outer diameter of the beam cross section was decreased. The inner wall of the drift tube was damaged at the cusp. Therefore, the electrons located outside of the beam cross section were considered to be lost.

4. Discussions

The azimuthal velocity of electrons was increased by the magnetic cusp field. However, the passing current through the magnetic cusp field was decreased. In order to obtain more

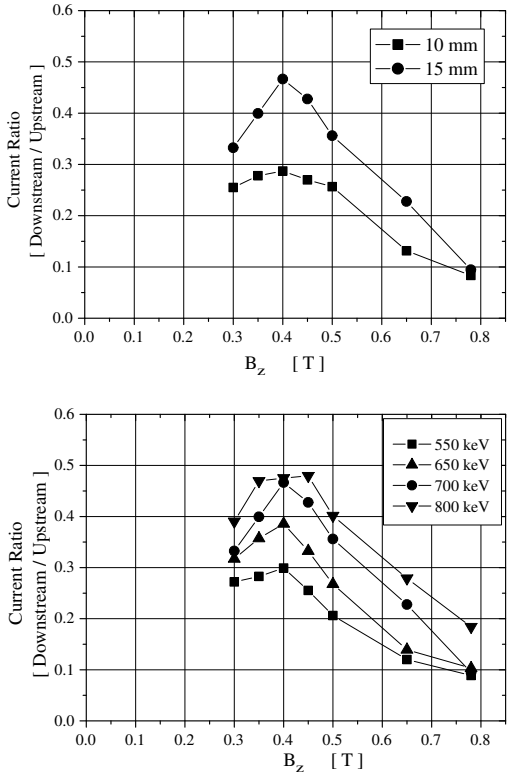

Figure 9: The ratio of the transmitted current to the injected one is plotted against the magnitude of the magnetic field. Up: the diameter of the cathode is changed. Down: Energy of electrons is changed.

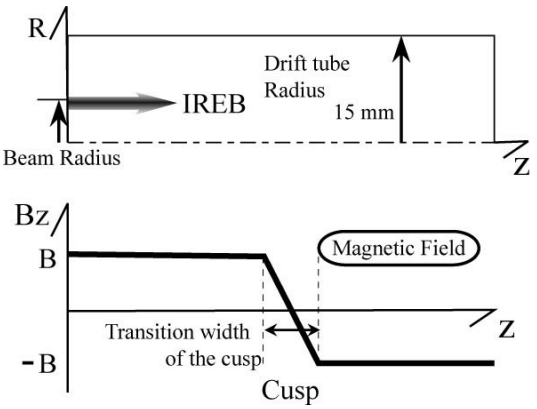

Figure 10: The geometry of the simulation.

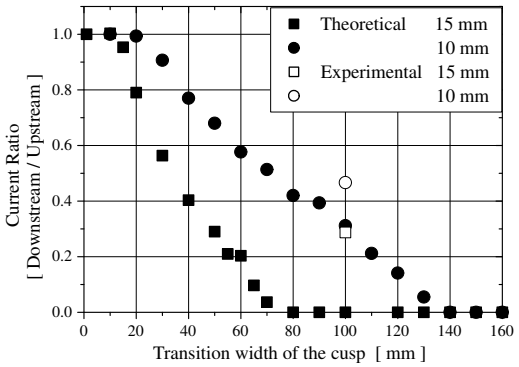

Figure 11: The ratio of the current passing through the cusp to the injected current is plotted against the transition width of the cusp. Simulated results are depicted by filled symbols. Experimental results with transition width of 10 cm are indicated by open symbols.

current passing through the cusp field, we use the particle-in-cell simulation code KARAT to investigate the effect of the transition width. The geometry used in the simulation is shown in Fig. 10. An electron beam with energy of 700 keV and current of 3 kA was injected from left hand side of the figure. The diameter of the beam was set to be 10 or 15 mm with thickness of 1 mm. The transition width of the cusp was changed from 1 to 160 mm. The magnitude of the magnetic field was 0.3 T.

The simulated results indicates that the transition width of the cusp strongly affect to the current passing through the cusp as shown in Fig. 11. The more electrons injected from the cathode with diameter of 10 mm were obtained than those from the 15 mm cathode as observed in the experiment. The difference between the experimental and simulated results was suspected to be caused by the wider beam thickness in the experiment. In the experiment, small fraction of electrons was observed near the center axis. Practical transition width in the experiment that we can make might be 5 cm, so that it is expected that we can make the beam current passing through the cusp field with required azimuthal velocity twice larger than those we now obtained. In Fig. 12, the positions of electrons at 10 ns later from the injection time are shown. A part of electrons went away to the wall at the cusp field.

The simulated azimuthal velocity of electrons is plotted against the axial position in Fig. 13. The electrons obtain azimuthal energy at the cusp field. Though the current passing through cusp field decreased as the tran-

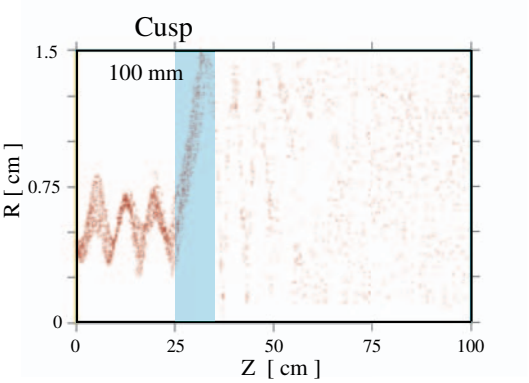

Figure 12: The simulated electron position at 10 ns later from the beam injection.

sition width increased, the azimuthal velocity at downstream side of the cusp field show only small difference between transition widths of 10 and 100 mm.

5. Conclusion

The azimuthal velocity of electrons can be enhanced by using a magnetic cusp field. When the requested ratio of azimuthal to axial velocity is around 1, the magnetic cusp field is effective to control the ratio. It is necessary to make the transition width of the cusp field as short as possible to reduce the loss of electrons at the cusp.

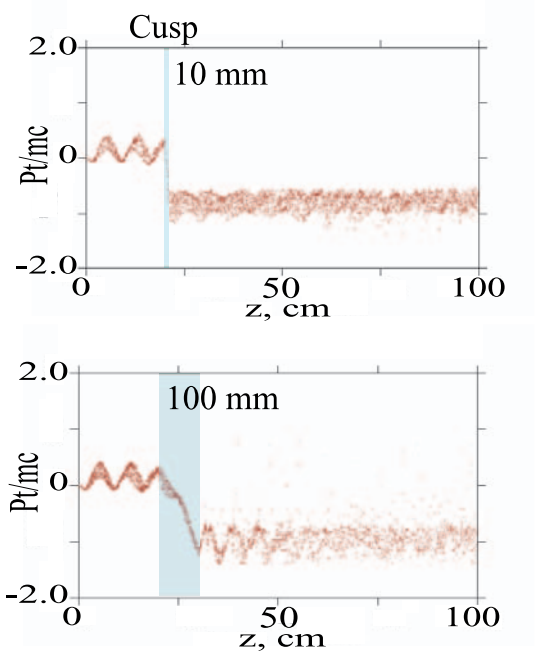

Figure 13: The simulated azimuthal velocity is plotted aginst the axial position.

References

[1] N. S. Ginzburg, I. V. Zotova, Sov. Tech Phys. Lett., 15, 573, 1989.
[2] N. S. Ginzburg, I. V. Zotova A. S . Sergeev I. V. Konoplev A. D. R. Phelps A. W. Cross S. J. Cooke, V. G. Shpak, M. I. Yalandin, S. A. Shunalinov, and M. R. Ulmaskulov, , Phys. Rev. Lett., 78, 2365, 1997.
[3] M. I. Yalandin, V. G. Shpak, S. A. Shunailov, M. R. Ulmaskulov, N. S. Ginzburg, I. V. Zotova, A. S. Sergeev, A. D. R. Phelps, A. W. Cross, K. Ronald, S. M. Wiggins, IEEE, vol. 28, 1615. 2000.
[4] S. M.Wiggins , D. A. Jaroszynski, B. W. J. McNeil, G. R. M. Robb, P. Aitken, A. D. R. Phelps, A. W. Cross, K. Ronald, V. G. Shpak, M. I. Yalandin, S. A. Shunailov , M. R. Ulmaskulov, N. S. Ginzburg, Phys. Rev. Lett., vol. 84, 2393. 2000.
[5] V. P. Tarakanov, "Users manual for code KARAT", ver. 7.09, 1999.
[6] D. Hasegawa, K. Kamada, K. Shimizu, R. Ando and M. Masuzaki, IEEE Trans. Plasma Sci., vol. 28, 1648, 2000.
[7] M.J.Rhee and W.W.Destler, Phys. Fluids, vol. 17, p. 1574, 1974 .
[8] W.W.Destler, P.K.Misra and M.J.Rhee, Phys. Fluids, vol. 18, 1820, 1975 .
[9] W.W.Destler, D.W.Hudgings, R.A. Kehs, P.K.Misra and M.J.Rhee, IEEE TRANS. Nucl. Sci., vol. NS-22, 995, 1975.
[10] M.Friedman, Phys. Rev. Lett., 1098, 1970.
[11] T.Mizuno, H.Sekita, M.Kitora, Y.Naito, H.Saito, and T.Sekiguchi, Jpn. J. Appl. Phys. 2, vol. 30, L-128, 1991.

Particle-in-Cell Simulation of Large Orbit Gyrotron

Keisuke Naito , Weihua Jiang, and Kiyoshi Yatsui[1]
Extreme Energy-Density Research Institute, Nagaoka University of Technology

Masaki Kamada and Toshitaka Idehara
Research Center for Development of Far Infrared Region, University of Fukui
3-9-1 Bunkyo, Fukui-shi, 910-8507 Japan

Abstract

This paper reports particle-in-cell simulations of large orbit gyrotron (LOG). We have performed simulations for LOG by dividing it into two portions, the electron-beam diode and the interaction cavity. The electron-beam parameters obtained by two-dimensional simulations of the electron-beam diode are used as the boundary conditions for the three-dimensional simulations of the cavity. This paper reports the simulation results of the electron beam diode and propagation tube.

Keyword: large orbit gyrotron (LOG), particle-in-cell (PIC) simulation, high-power microwaves, relativistic electron beam

1. Introduction

High power microwave (HPM) sources have various applications in thermal nuclear fusion, pulsed radar, particle acceleration, wireless power transmission, and other industrial and military fields. Among many kinds of HPM generators, gyrotron has advantages in high efficiency and high frequency. (1)

Gyrotron is a microwave oscillator that makes use of the electron cyclotron motion in a magnetic field. The oscillation happens when the electron-beam bunching occurs at the resonant frequency. For this reason, the oscillation frequency depends on the strength of the applied magnetic field.

Gyrotron is considered to be a potential source for powerful radiation in far-infrared region.(2) Electromagnetic waves in this frequency range are expected to have many applications in new-material development, advanced analysis, and plasma diagnostics. The challenge of using gyrotron for generation of far-infrared radiation is achieving high frequency and mode control.

For example, the electron cyclotron frequency in THz range corresponds to a magnetic field on the order of tens of Teslas, which is very difficult to obtain experimentally. A practical method to multiply the oscillation frequency without increasing the magnetic field is making use of the higher harmonic modes. However, due to strong mode competition, the experimentally obtained efficiency for higher harmonics is usually very low for conventional gyrotrons.

Large orbit gyrotron (LOG) is a special type of

gyrotron, where the electron cyclotron radius equals the beam radius. Due to this unique property, it is theoretically expected that the mode competition can be effectively controlled so that the higher harmonic wave efficiency can be significantly increased.

In this paper, a LOG is studied by simulation code "MAGIC",[3] which is a fully electromagnetic, relativistic, particle-in-cell simulation code widely used for plasma and particle beam studies. The simulations are carried out for electron-beam parameters of pulsed power generator "ETIGO-IV", i.e., diode voltage of 400 kV, diode current of 13 kA, and pulse width of 120 nsec.

In the simulation, the LOG is divided into two portions, an electron-beam diode and an interaction cavity. The diode is studied by using two-dimensional simulations. This paper reports our recent simulation results of the electron beam didoe and the propagation tube.

2. Structure of large orbit gyrotron (LOG)[5]

The general view of LOG under present development is shown in Fig. 1. A CW coil generates magnetic field for forming the helical electron beam and a pulsed coil provides strong magnetic field for the cavity. When a high voltage is applied between the anode-cathode gap, an electron beam is extracted from the cathode and accelerated toward the anode. Since the cathode is in a cusped magnetic field, the electrons have large component of momentum perpendicular to the magnetic field when they reach the anode. The gradient of the axial magnetic field between the anode and the cavity further increases the perpendicular component of the electron momentum and compresses the electron beam diameter. The ideal situation at the cavity entrance is a thin electron beam having a cyclotron radius that equals to the beam radius and a cyclotron frequency that resonates with the cavity.

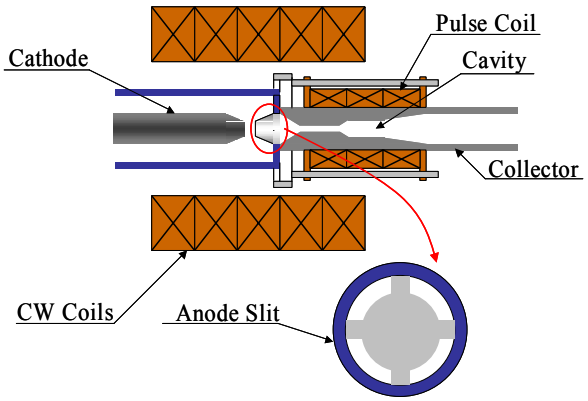

Fig. 1 The general view of LOG

3. Particle-in-cell simulation

The simulation model of the electron diode is shown in Fig. 2. It is axially symmetric and the simulation is carried out in 2.5-dimensional cylindrical coordinate. Across the anode slit, an aluminum foil of 0.1 μm in thickness is used in order to define the electrical potential of the inner part of the anode. Electrons are emitted from the cathode surface facing the anode. Both electrodes are considered as perfect conductors.

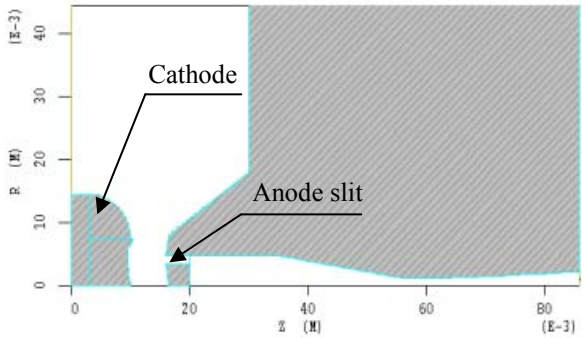

Fig. 2 The simulation model of the electron beam diode.

The applied voltage is 400 kV, which is the maximum output voltage of "ETIGO-IV". However, for simplicity, a constant voltage is used (as shown in Fig. 3) instead of the real waveform. The cell size is 0.1 × 0.1 mm and the simulation time is 5 ns. The applied magnetic field on the center axis is that shown in Fig. 4.

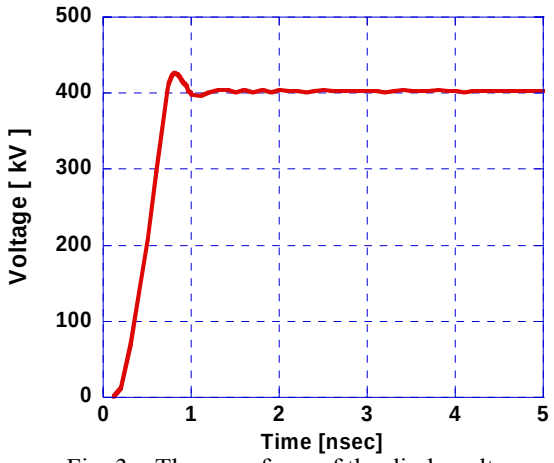

Fig. 3 The waveform of the diode voltage.

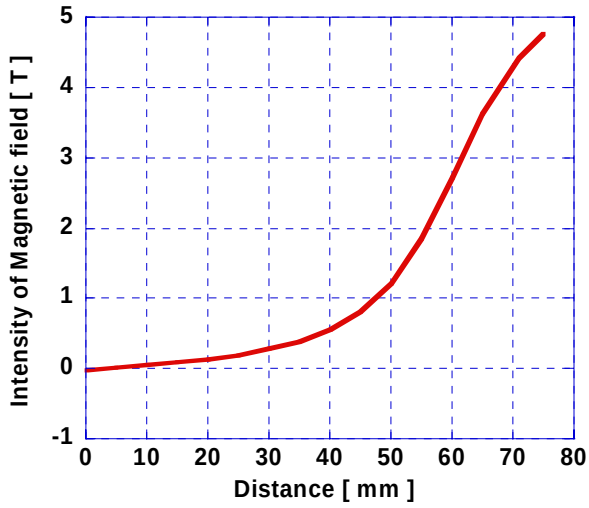

Fig. 4 The intensity of the applied magnetic field.

The electron map obtained from the simulation is shown in Fig. 5. From Fig. 5, it is seen that the electrons are emitted from cathode and only a small portion of them can pass through the anode slit. However, the annular beam that passed through the anode exhibits large energy spread which is considered to be caused by the anode foil. Therefore, for the following simulations, it is assumed that an electron beam is injected at the position of the anode.

The kinetic energy distribution of the electron beam obtained from the simulation result of the diode is shown in Fig. 6 and Fig. 7. As a result, the electron momentum parallel to the magnetic field ($P_{\parallel}$) is 4.34×10^{8} [γm/s], and that perpendicular to the magnetic field ($P_{\perp}$) is 0.045×10^{8} [γm/s], at the position of the anode foil.

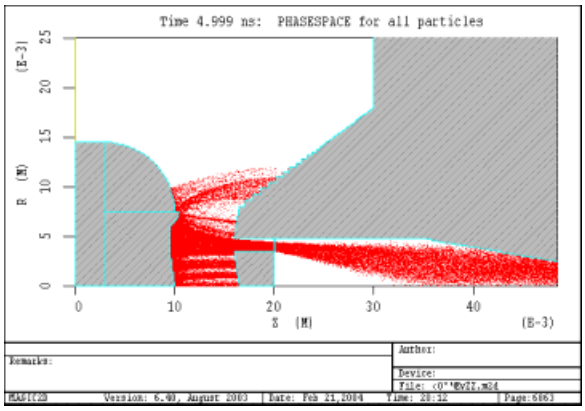

Fig. 5 The electron map obtained by the simulation

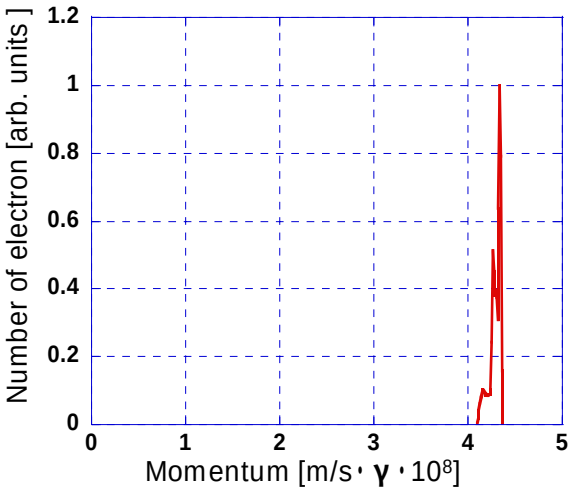

Fig. 6 Electron momentum parallel to the magnetic field ($P_{\parallel}$)

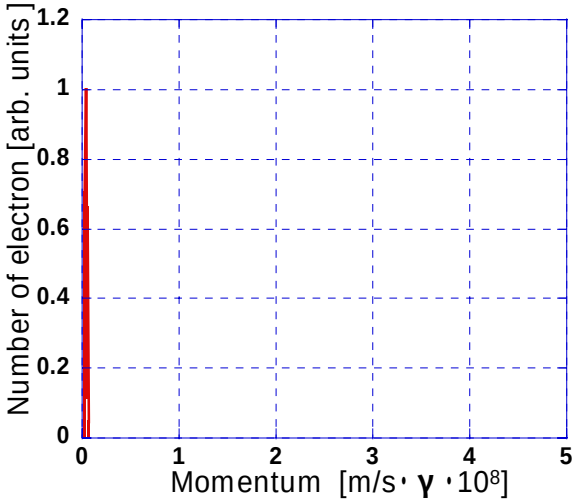

Fig. 7 Electron momentum perpendicular to the magnetic field ($P_{\perp}$)

The simulation model for electron beam propagation is shown in Fig. 8. An electron beam with parameters shown in Figs. 6 and 7 is injected at the left boundary.

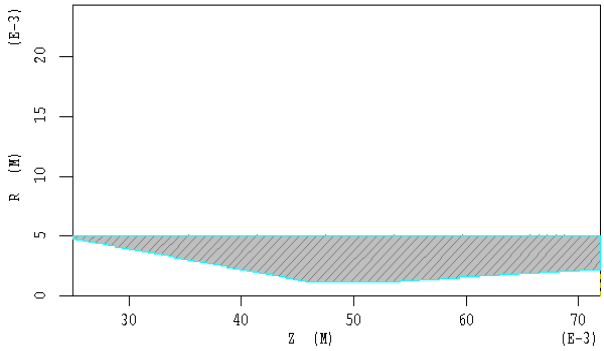

Fig. 8 The simulation model for electron beam propagation.

The electron trajectory obtained from the simulation results is shown in Fig. 9. It is seen that the electron beam is compressed in diameter while keeping its thickness, which is very important to LOG. The electron beam current and kinetic energy distribution are shown in Fig. 10, 11 and 12. It is obtained that $P_{\parallel} = 3.68\times10^{8}$ [γm/s], and $P_{\perp} = 2.21\times10^{8}$ [γm/s], at the entrance of the cavity.

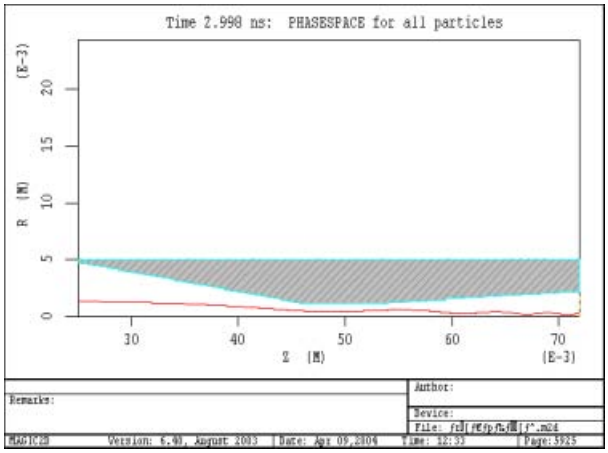

Fig. 9 The trajectory of the electron beam

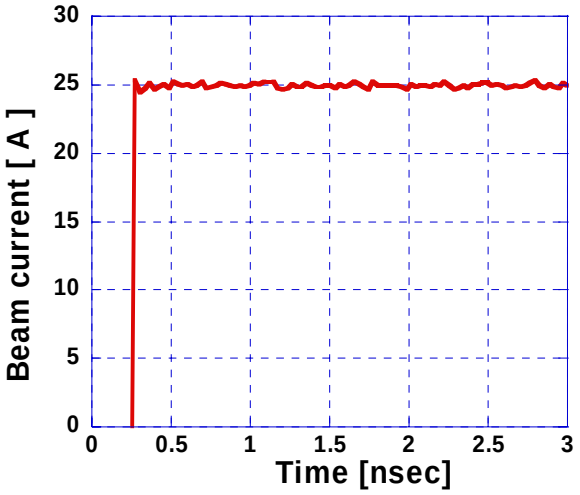

Fig. 10 The current waveform of the electron beam.

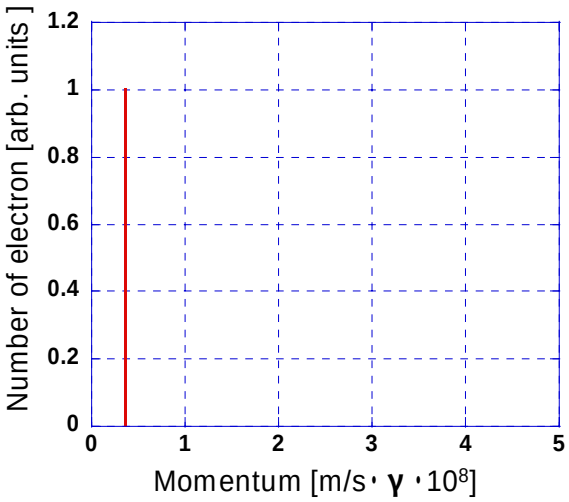

Fig. 3-10 Electron momentum parallel to the magnetic field ($P_{\parallel}$)

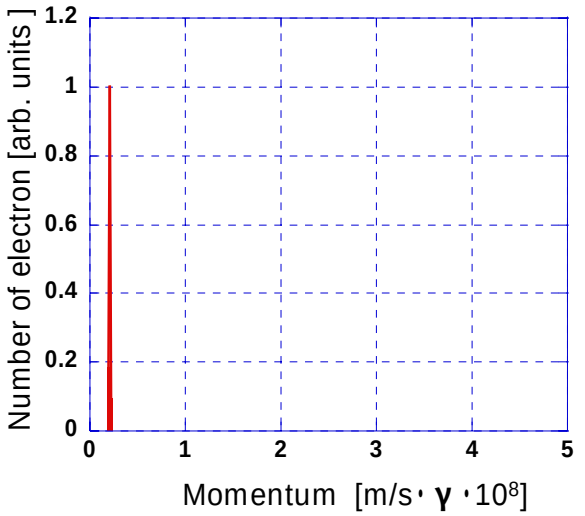

Fig. 3-11 Electron momentum perpendicular to the magnetic field ($P_{\perp}$)

4. Conclusions

Numerical simulations are carried out for large orbit gyrotron (LOG). The simulation model divides the LOG into two portions, the electron diode and the interaction cavity. This paper reports the simulation results on the diode and the propagation tube. As a result, $P_{\parallel} = 3.68\times10^{8}$ [γm/s], and $P_{\perp} = 2.21\times10^{8}$ [γm/s] have been obtained as the electron beam parameters at the entrance of the cavity. In addition, the electron beam keeps a small value thickness while being compressed by the magnetic field in the propagation tube.

References

(1) Steven H. Gold , Gregory S. Nusinovich : “ Review of high power microwave source research ” , Rev. Sci. Instrum., Vol.68 , No.11 , 3945-3974 (1997)

(2) Y. Itakura , T. Idehara , Y. Yasuoka : “ Modern technologies in the far infrared region ” , IEEJ Trans. FM [in Japanese], Vol. 123 , No. 10 , 949-954 (2003)

(3) L. Ludeking , D. Smithe , M. Bettenkausen , S. Hayes :“ MAGIC USER’S MANUAL ” , Mission Research Co. (1999)

(4) A. Tokuchi , N. Ninomiya , W. Jiang , K. Yatsui : “ Repetitive Pulsed-Power Generator “ ETIGO- ” , IEEE Trans. Plasma Science , Vol. 30 , No. 5 , 1637-1641 (2002)

(5) T. Idehara , V.N. Manuilov , O. Watanabe , M. Kamada , La Agusu , K. Yatui , Wiehua Jiang : “ Electron gun for powerful large orbit gyrotron “ , Fukui university , FIR center report , FIR FU-41

Beam illumination and implosion simulation in inertial confinement heavy ion fusion

T.Someya, K.Miyazawa, T.Kikuchi and S.Kawata

Utsunomiya University

Abstract

Three-dimensional computer simulations are performed for a heavy ion beam (HIB) irradiation onto a direct-driven spherical fuel pellet in heavy ion fusion (HIF). In addition, the non-uniformity growth due to a little pellet displacement from a reactor chamber center is investigated. The calculation results demonstrate that we can realize a rather low non-uniform energy deposition: for example, less than 2.0 % even for a 32-beam irradiation system. Moreover we develop hydrodynamic simulation code to calculate a target implosion.

Keywords: Heavy ion fusion, implosion, beam illumination, hydrodynamics code

1. Introduction

Key issues in heavy ion beam (HIB) inertial confinement fusion (ICF) include an accelerator design for intense HIBs, efficient HIB transport, a HIB-target interaction, a reactor design and so on [1-4]. In this study, we focus on a HIB-target interaction in ICF. In HIB ICF, the beam irradiation non-uniformity on a direct-driven fuel pellet must be suppressed under a 2~3 % in order to achieve a symmetric fuel pellet implosion [5]. Therefore a multi-HIB illumination is required to achieve a low beam non-uniformity in the pellet implosion. On the other hand, the total HIB number should be restricted to a realistic number. Therefore, in this study, we simulate a HIB illumination on the spherical direct-driven target using 12, 20, 32, 60, 92 and 120-beam irradiation systems. In an ICF power plant, a position of fuel pellet may shift from a reactor center, because a pellet may be injected from a pellet injection port at a reactor wall. The HIB illumination non-uniformity may be influenced by a little pellet displacement from the chamber center. In this paper we also investigate the relation between the pellet displacement and the HIB illumination non-uniformity. For the evaluations of the illumination non-uniformity on the target, we compute the root mean square (RMS) non-uniformitiy on the target. In addition, we also perform mode analyses of the HIB deposition energy on the spherical fuel target using the Legendre polynomial and the Fast Fourier Transfer (FFT).

Moreover we develop hydrodynamics code in order to calculate target implosion.

2. Simulation Model

HIBs may be one of promising energy-driver candidates in ICF. In this study, we use a lead (Pb^+) beam with the Gauss distribution as a HIB in ICF. The beam parameters are as follows: the mean particle energy is 8.0 GeV, the beam temperature is 100 MeV, the transverse beam emittance is 5.0 mm-mrad, and the maximal initial beam density is 1.3×10^{11} cm^{-3}. The mean HIB radius is 3.3 mm. The chamber radius is 5.0 m. In our study we use 12, 20, 32, 60, 92 and 120-beam irradiation systems. Moreover we use Al+Pb layer target as shown in Fig. 1. The Al layer thickness and mass density are 0.97 mm and 2.69 g/cm^3, and Pb layer is 0.03 mm and 11.3 g/cm^3, respectively.

In our study, we calculate the HIB energy deposition using a stopping power. Moreover we employ the widely-used expression of the HIB

particle effective charge and calculate the effective charge of the HIB particles traveling through the target. The stopping power in the target is considered to be the sum of the energy deposited in a target nuclei, target bound, free electrons, and target ions [6]: Estop = Enuc + Efree + Ebound + Eion, where Estop is the deposition energy in the target, Enuc is the deposition energy by the nucleus scattering, Efree is by the free electron, Ebound is by the bound electron, and Eion is by the target ion.

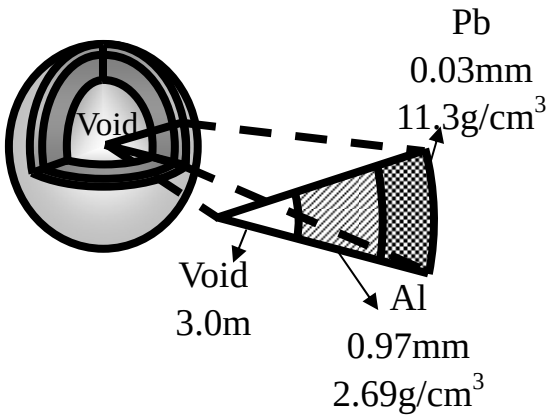

Fig. 1. Target structure

In order to achieve an effective pellet implosion, the deposition energy non-uniformity must be suppressed under few %. Therefore, in our study, we evaluate the energy non-uniformity at the target. In HIB ICF the Bragg peak deposition area plays the most important role for a target implosion. Therefore we define the total relative root-mean-square (RMS) non-uniformity as follows:

$$\sigma_{RMS} = \sum_{i}^{n_r} w_i \sigma_{RMSi}$$

$$\sigma_{RMSi} = \frac{1}{\langle E \rangle_i} \frac{\sqrt{\sum_j \sum_k \left(\langle E \rangle_i - E_{ijk} \right)^2}}{n_\theta n_\phi}$$

$$w_i = \frac{E_i}{E}$$

Here, σ_{RMS} is the RMS non-uniformity. σ_{RMSi} is the RMS non-uniformity on i-th (r = constant) surface of deposition. ω_i is the weight function in order to include the Bragg peak effect or the deposition profile. n_r, n_θ and n_ϕ are mesh numbers in each direction of the spherical coordinate. $<E>_i$ is the mean deposition energy on the i-th surface, E_i is the total deposition energy on the i-th surface, and E is the total deposition energy. We also performed mode analyses on the spherical fuel target by using the spherical harmonic function and FFT. In order to include the Bragg peak effect we calculate the spectrum of the deposition energy at the Bragg peak layer and we also calculate the global energy-spectrum using the weight function ω_i. Moreover, in this study, the summation of the energy spectrum amplitude is normalized to be 1.0.

In our developing implosion code, to use the computational resource effectively, we adapt the ALE for the radial mesh. We also employ the R-CIP method for the advection term to archive an effective calculation. To capture the several materials during the hydrodynamic motion, we employ the color function. In our implosion code, three temperature (ion, electron and radiation temperature) is used. Moreover we adapt the ADI method for heat conduction in order to calculate effectively at the three dimensional case.

3. Simulation Results

Figure 2(a) shows the deposition energy of beam particles at each surface without the beam temperature effect, 32-beam system, and the Gauss distribution. In Fig. 2(a), we can see the Bragg peak at the middle layer of the energy absorption region, and the RMS and non-uniformity is low at the Bragg peak layer. At the end of the beam particle stopping region, the deposition energy is much small compared with the Bragg-peak-layer's one. In actual the pressure peak generated by the HIBs deposition at the Bragg peak region drives the inner fuel to the implosion with a high speed

(typically ~ $3x10^7$cm/s). Based on this reason and on results of the implosion studies previously performed, it is known that the HIBs deposition energy in the Bragg peak region contributes mainly to the implosion. Therefore, in this paper, we calculated total RMS non-uniformity using the weight function w_i in order to include the Bragg peak effect. The RMS non-uniformity is evaluated σ_{RMS}=5.95 %. Figure 2(b) shows the energy deposition in the case of 32-beam system, the Gauss distribution including the longitudinal beam temperature of 100MeV and the transverse beam radial emittance of 5.0 mm mrad. In Fig. 5(b) we can see that the Bragg peak moves slightly outward in the radial direction and the RMS non-uniformity becomes σ_{RMS} =1.86 %. The HIB illumination non-uniformity in the realistic case including the beam temperature or the beam divergence becomes small compared with that in the case with the zero-temperature HIB. This result presents that the HIB illumination non-uniformity can be smoothed and suppressed due to the beam temperature or the transverse emittance.

We also calculate the deposition-energy spectra at the Bragg peak layer for the zero-temperature beam (r=3.79 mm) and for the case with the beam temperature of 100 MeV (r=3.87 mm) as shown in Figs. 3(a) and (b). Figures 3(c) and (d) are the global non-uniformity spectra using the weight w_i for the zero-temperature beam and for the case with the beam temperature of 100 MeV. In Fig. 3, (n, m) and s_m^n are the mode numbers and the amplitude of spectrum, respectively. If the deposition energy is distributed in complete spherically symmetric, the amplitude of spectrum is set to 1.0 in the mode (n, m)=(0, 0) in our study. In order to achieve a symmetric energy deposition in the direct-drive HIB ICF, the most spectrums should be concentrated on the mode (n, m)=(0, 0), and the amplitude of the mode (n, m)=(0, 0) has a large value near 1.0 in our simulation results, compared with those for other modes. For this reason, in this paper, we focus on the amplitudes of spectrum modes except the mode (n, m)=(0, 0). Therefore our calculation results shown in spectrum figures present the spectrum without the mode of (n, m)=(0, 0). In Fig. 3 the amplitude of the spectra in the case of the Bragg peak layer is small compared with that for the global non-uniformity. This result means that the deposition energy at the Bragg peak layer is more uniform compared with the deposition energies at other layers. This is also confirmed by the results in Fig. 3. In HIB ICF the Bragg peak area plays an important role for the symmetric target implosion. Therefore we expect that we may realize an effective compression of target and efficient target implosion. We also confirm that the amplitude in the case including the beam temperature becomes small compared with that in

(a) Without beam temperature

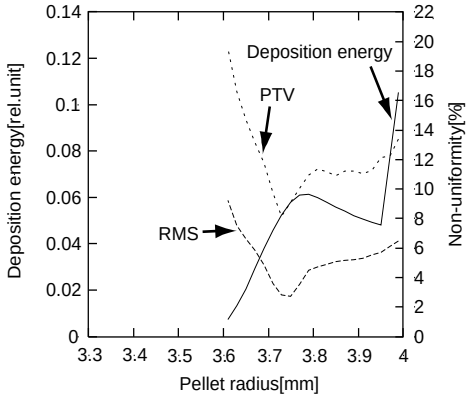

(b) With beam temperature

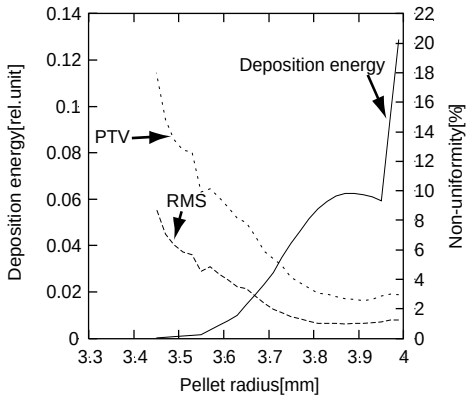

Fig.2 The deposition energy and non-uniformities in the cases (a) without the beam temperature effect and (b) with the temperature.

(a) Bragg peak (r=3.79mm), zero-temperature beam

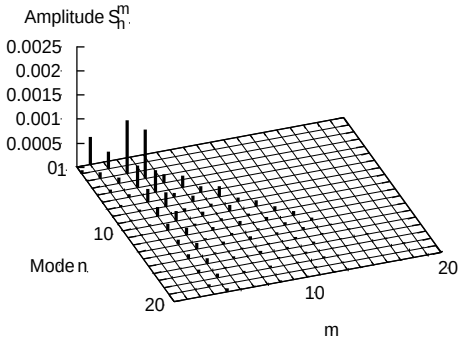

(b) Bragg peak (r=3.87mm), with beam temperature

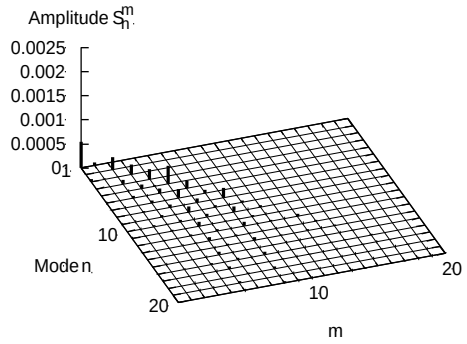

(c) Global, zero-temperature beam

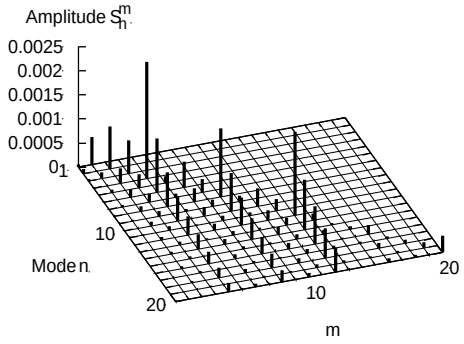

(d) Global, with beam temperature

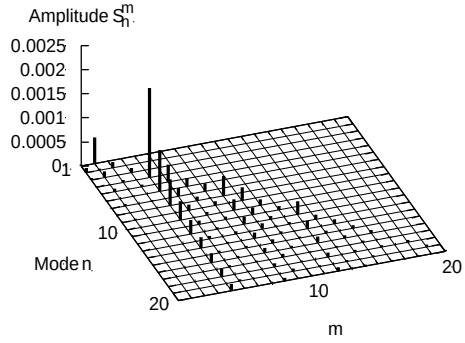

Fig.3 The energy spectra at the Bragg peak layer (a) for the zero-temperature and (b) with the beam temperature. The global non-uniformity spectra for the (c) zero-temperature beam and (d) with the beam temperature.

the amplitude of the deposition-energy spectrum at the mode (n, m)=(0, 0) is 0.97 in the case with the zero beam temperature, and the amplitude of the energy spectrum at the mode (n, m)=(0, 0) is 0.99 in the case including the beam temperature.

Figure 4 shows the RMS non-uniformity versus the HIB total number. The marked circles and crosses mean the results in the cases of with and without the temperature effect, respectively. From this figure, we confirm that even 32-beam system including the HIB temperature, the RMS non-uniformity is less that 2.0 %.

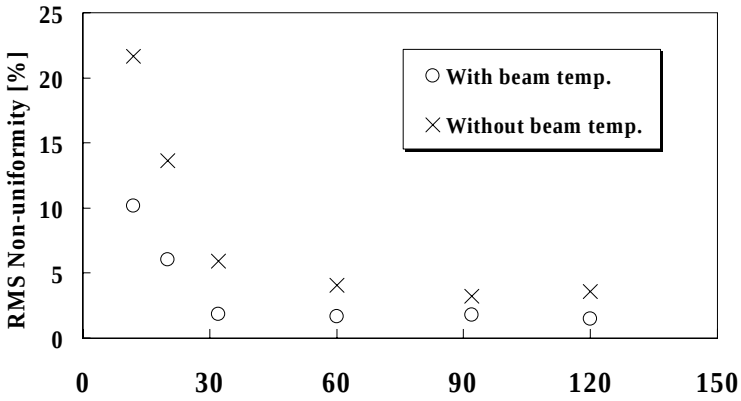

Fig.4 RMS non-uniformity v.s. HIB total number.

In the above subsections, all calculations were performed with the assumption that a pellet is set just to the chamber center. Such the requirement is difficult to be realized in practice. Therefore a little pellet displacement from the reactor chamber center is evaluated in this subsection. We assume that the pellet is injected into the chamber vertically, and simulate the effect of a little displacement dz as shown in Fig. 5. Our illumination pattern is a basically spherically symmetric pattern. So the vertical displacement of dz may be sufficiently general for our present purpose. The results for the HIB irradiation systems investigated are plotted in Fig. 5 in the case of the Gaussian beam including **the beam temperature. From the Fig. 5, we can confirm that the HIB irradiation non-uniform**ity is

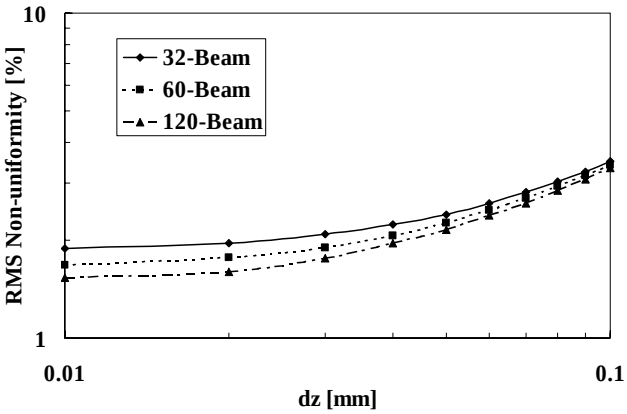

Fig.5 Pellet displacement v.s. the RMS non-uniformity.

sensitive to the pellet position displacement in the both cases. This result means that the pellet displacement may be a serious problem in HIB ICF.

In order to analyze the target plasma hydrodynamics, we develop a three dimensional implosion code. Figure 6 show the hydrodynamic calculation results. In Figs. 6 (a)-(c) show the color function and (d)-(e) are target material mass density. In this case, we employ the spherical coordinate and include a 20 % non-uniformity in the theta direction. In Figs. 6 (a)-(c), the number 1, 2, and 3 shows the DT fuel, the Al pusher, and the Pb tamper, respectively. From these figures, we can confirm that the three materials are captured clearly with time progress in the computational scheme. From Figs. 6 (d)-(e), we can see that the DT fuel is compressed non-uniformly during hydrodynamic motion. The calculation is performed in stable with a high non-uniformity (20 %).

4. Summary

In this paper, we studied the HIB deposition non-uniformity in a direct-driven HIB-ICF pellet. For various beam parameters and different reactor chamber radii we investigated the energy deposition non-uniformity using 12, 20, 32, 60, 92 and 120-beam irradiation systems. The HIB diverges slightly by the beam temperature. We include the effect of a beam longitudinal temperature and the beam transverse emittance. In our simulation results we confirm that the HIB illumination non-uniformity is 1.86 % in the case of the Al+ Pb target structure, the beam temperature of 100MeV, the 32-beam system, and the Gaussian particle

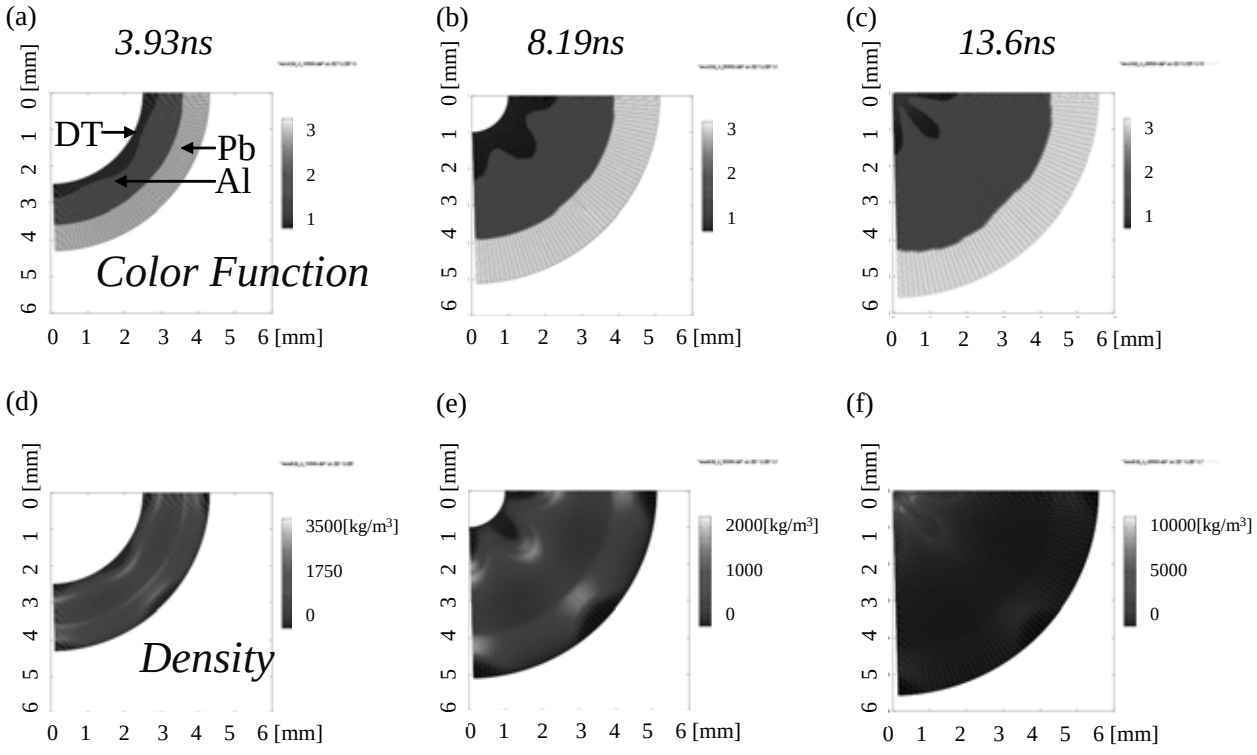

Fig.6 Hydrodynamics calculation results with a time dependent. (a)-(c) show the color function and (d)-(e) plasma density.

density distribution. On the other hand, the RMS non-uniformity using the Gaussian beam without the beam temperature is 5.95 %. From these results, we expect that the fuel can be successfully imploded and the fusion energy can be released from a direct-driven fuel pellet in HIB ICF using the Gaussian HIBs. Moreover we analyzed the spectrum of the HIB illumination non-uniformity in the spherical target. As a result, the deposition energy non-uniformity in the target includes higher modes with sufficiently low amplitudes. Therefore the mode analyses also demonstrate that by using an appropriate illumination pattern and the selected HIB illumination parameter values the sufficiently low non-uniformity can be realized. We also investigated the non-uniformity growth due to the little pellet displacement of the pellet position from the chamber center. The calculation results demonstrated that the pellet displacement is a serious problem in HIF. We are also developing a target hydrodynamic computer code. In the near future we can calculate a realistic target hydrodynamics stably with the realistic beam illumination non-uniformity. In order to investigate a dynamic HIB illumination non-uniformity, hydrodynamic implosion simulations coupled with our 3-D HIB illumination code should be performed, and this work should be done in the near future as the next step.

Acknowledgements

This work is partly supported by JSPS (Japan Society for the Promotion of Science) and MEXT (Ministry of Education, Culture, Sports, Science and Technology). We would like also to present our thanks to colleagues in the Japan and US HIF VNL research groups for their fruitful discussions on this subject.

References

[1] M.Tabak and D.Callahan-Miller, Phys. Plasmas 5, 1895 (1998).

[2] W.J.Hogan, R.Bangerter, and G.L.Kulcinski, Phys. Today 45, 42 (1992).

[3] T.Someya, S.Kawata, et al., Fusion Science and Tech. 43, 282 (2003).

[4] T.Someya, A.Ogoyski, et al., Phys. Rev. STAB. **7** 044701 (2004).

[5] S.Kawata and K.Niu, J. Phys. Soc. Jpn. 53, 3416 (1984).

[6] T.A.Mehlhorn, Sandia National Laboratories, SAND80-0038, (1980).

Beam instability during high-current heavy-ion beam transport

T. Kikuchi, T. Someya*, S. Kawata*, M. Nakajima**, and K. Horioka**

Department of Electrical and Electronic Engineering, Utsunomiya University, Utsunomiya 321-8585, Japan
*Department of Energy and Environmental Science, Utsunomiya University, Utsunomiya 321-8585, Japan
**Department of Energy Sciences, Tokyo Institute of Technology, Yokohama, 226-8502, Japan

Abstract

In driver system for heavy ion inertial fusion, beam dynamics is investigated by particle-in-cell simulations during final beam bunching. The particle simulations predict that the beam is transported with the localized transverse charge distribution induced by the strong space charge effect. The calculation results also show that the emittance growth during the longitudinal bunch compression for various particle distributions at the initial conditions and with two types of transverse focusing model, which are a continuous focusing and an alternating gradient focusing lattice configurations.

Keywords: Final Beam Bunching, Space Charge Dominated Beams, Beam Dynamics, Particle Simulation, Heavy Ion Inertial Fusion

1 Introduction

Physics of space-charge-dominated beams is crucial in heavy ion inertial fusion (HIF) [1]. In the HIF, energy of several MJ should be injected as a short time pulse to a fuel pellet. The target pellet illuminated by the energy driver is rapidly imploded. The implosion can cause a high energy density state at the center of the pellet, and thermonuclear reactions can produce the high-temperature dense plasma. The intense heavy-ion beam (HIB) is one influential candidate as the energy driver.

Required parameter values of HIB are several GeV particle energy, ∼100 kA total current, and ∼10 ns short pulse duration [2], and the beam parameters are far from those of conventional particle accelerator system. Therefore the beam dynamics and control are important research issues in HIF. At the final stage (see Fig. 1), the beam pulse must be longitudinally compressed from ∼100 to ∼10 ns.

Induction voltage modulators, which have a precise waveform controllability, are useful devices for this purpose [3]. For an effective pellet implosion, we should transport and compress the bunch of HIB with a low emittance growth. A final focus and beam illumination are crucial, but a large emittance interferes the focusing to the small fuel pellet [4, 5]. For this reason, the final beam bunching and the final focusing are a key technology in the HIF driver system. In these regions, the intense HIB is in the space-charge-dominated state, and beam instabilities occur during the beam transport. Dilution of particle distribution can also cause the emittance growth, because nonequilibrium particle distribution will approach to a thermal equilibrium state [6].

In our previous studies [7, 8, 9], the beam instability excited by the strong space charge effect was observed using multiparticle numerical simulations during the final beam bunching. The final beam bunching was carried out by the beam transport using the alternating focusing lattice system. In this study, we also investigate the beam dynamics during the bunch compression with the continuous focusing system. The particle-in-cell (PIC) [10] simulation with a longitudinal bunch compression model [11] is carried out to investigate transverse particle behaviors. The transverse charge distribution and rms emittance are shown in the beam transport with the continuous and the alternating gradient focusing lattice models.

2 Simulation model and beam parameters

The high-energy particle beam is transported by using a magnetic quadrupole focusing channel as a

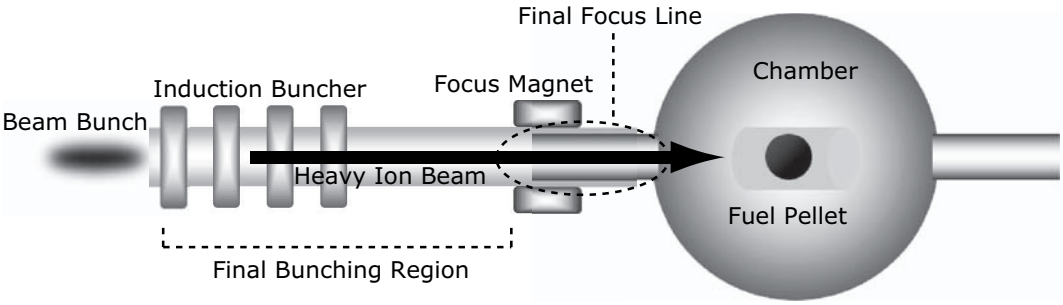

Figure 1: Final stage of HIF driver system. The beam bunchers by induction voltage modulators longitudinally compress the beam bunch. After the final beam bunching, the beam is transversely focused onto the target pellet.

unit of focus-drift-defocus-drift (FODO) lattice [12]. Generally, the beam transport by the FODO lattice causes a non-axisymmetric behavior in the beam cross-section. We are interested in such beam dynamics with a longitudinal bunch compression. For the above reasons, the fully three-dimensional numerical scheme is essentially required by the beam dynamics simulation. From the viewpoint of the computational cost, the full calculations are difficult. While the longitudinal bunch length is of the order of meter, the scale of the transverse cross section is only a few cm in the stage of final beam bunching [13]. Consequently, the small-scale phenomena by the space charge structure will be dominated by the transverse beam dynamics.

We deal with the particle dynamics in the transverse cross section of the beam by multi-particle simulations, and the effect of longitudinal compression is introduced as the beam current increases. The linear current increase model causes the most serious influence in the particle dilution in the phase space. From the viewpoint of the beam physics study, the history of linear current increase is assumed as model of the longitudinal bunch compression.

We use the PIC method for descriptions of the transverse behavior with the longitudinal compression, the effect of which was evaluated by assuming linear increase in the beam current. For the particle positions x_p and y_p of index p, the equations of motion along the transport distance s are written as[8]

$$\frac{d^2 x_\mathrm{p}}{ds^2} = -k_x\, x_\mathrm{p} - \frac{qe}{\gamma^3\, m_0\, v_\mathrm{z}^2}\frac{\partial \phi}{\partial x}, \tag{1}$$

$$\frac{d^2 y_\mathrm{p}}{ds^2} = -k_y\, y_\mathrm{p} - \frac{qe}{\gamma^3\, m_0\, v_\mathrm{z}^2}\frac{\partial \phi}{\partial y}, \tag{2}$$

where k_x and k_y are the transverse confinement forces, q is the charge state of the beam ion, e is elementary charge, m_0 is the rest mass of the beam ion, γ is the relativistic factor at the center of longitudinal beam position, v_z is the longitudinal beam velocity, and ϕ is the self-electrostatic potential of the beam, respectively. In this study, we simply assume the effect of the self-magnetic field as factor of $1/\gamma^2$ [14]. The self-electrostatic potential is calculated by

$$\frac{\partial^2 \phi}{\partial x^2} + \frac{\partial^2 \phi}{\partial y^2} = -\frac{\rho}{\epsilon_0}, \tag{3}$$

where ρ is the (area) charge density given by the beam particle positions and ϵ_0 is the permittivity of free space, respectively. The charge and mass of the super particles are re-weighted with the beam transport [11]. The quadrupole occupancy is fixed at 0.5, and the one lattice period is 3 m.

The beam parameters are assumed as Table 1 [2]. The initial generalized perveance is assumed to 3.58×10^{-6}. The initial undepressed and depressed phase advances are $\sigma_0 = 72$ deg and $\sigma = 65.2$ deg. The transverse calculation region is fixed at the square of 10 cm $\times$ 10 cm, and the outer boundary condition is given as a conductor wall. The initially rms matched Kapchinskij-Vladimirskij (KV), waterbag (WB), Gaussian (GA), Parabolic (PA) [15],

Table 1: Beam parameters for final beam bunching in HIF.

Ion species	Pb^{1+}
Number of ions	6.25×10^{14}
Particle energy [GeV]	10
Initial beam current [A]	400
Final beam current [kA]	10
Initial pulse duration [ns]	250
Final pulse duration [ns]	10

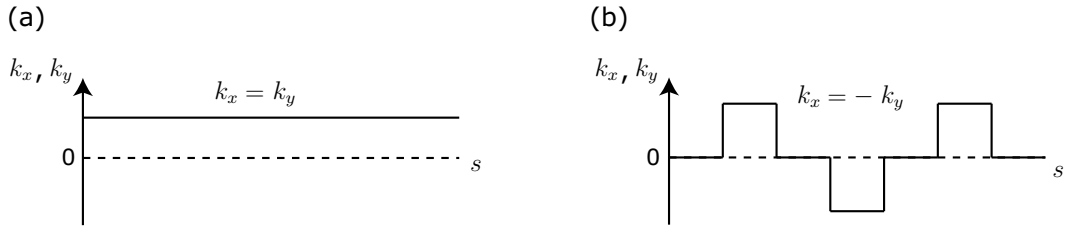

Figure 2: Calculation model of transverse focusing lattice system, (a) for continuous focusing (CF) lattice case, (b) for alternating gradient (AG) focusing case (FODO).

and semi-Gaussian (SG) [11] beams are chosen as the initial particle (non-stationary) distribution.

The ratio Δ/λ_D of the grid zone length Δ to the Debye length λ_D is evaluated by rms emittance ϵ_f after the final beam bunching. Since the behavior likes a quasi-neutral plasma, the Debye shielding is important issue in this region. The grid size of $0.23\lambda_D$ is used to satisfy the Debye shielding effect and the calculation cost [10]. For the validation of the numerical convergence, we also tried to check the calculation results using the different numbers of grids and super particles. The mesh number is varied from 64×64 to 1024×1024, and the super particle number is changed from 1×10^5 to 3×10^6. As mentioned earlier, we tried to check the many test calculations to change the numbers of particles and cells used. Consequently, we use the mesh number of 512×512 for the accurate calculation in this study.

We study the emittance growth mechanism with two types of the transverse focusing lattice system, i.e. an alternating gradient (AG) focusing and a continuous focusing (CF) configurations. Figure 2 shows the focusing models during the beam transport. The transverse focusing coefficients k_x and k_y are constant for the continuous focusing model, and are given as the alternate values for the AG focusing model as shown in Fig. 2.

3 Numerical Simulation Results

According to the calculation conditions described in the previous section, we simulate numerically the beam dynamics during the final beam bunching with the CF and AG focusing models. Figure 3 shows the normalized charge distribution in the initial KV beam using the CF lattice during the final beam bunching. The charge density is normalized by the maximum value at each map. The beam radius is extended with the beam current increase due to the longitudinal bunch compression. The localized charge distribution is indicated during the final beam bunching as shown in Fig. 3, and it caused by the beam instability excited due to the strong space charge effect [8].

The emittance value is used for the evaluations of beam transport quality. We define the average of unnormalized transverse rms emittance ϵ as

$$\epsilon = \frac{\epsilon_{x,rms} + \epsilon_{y,rms}}{2}, \tag{4}$$

where $\epsilon_{x,rms}$ and $\epsilon_{y,rms}$ are the unnormalized rms emittances for horizontal and vertical directions given by

$$\epsilon_{x,rms} = \left[\langle x^2\rangle\langle x'^2\rangle - \langle xx'\rangle\right]^{1/2}, \tag{5}$$

and

$$\epsilon_{y,rms} = \left[\langle y^2\rangle\langle y'^2\rangle - \langle yy'\rangle\right]^{1/2}, \tag{6}$$

respectively. The initial emittance is assumed at $\epsilon_i = \epsilon_{x,rms} = \epsilon_{y,rms}$ =10 mm mrad. At each initial distribution, the evolution of the emittance growth ϵ/ϵ_i, which indicates the ratio of the average emittance to the initial one at each lattice period, is shown in Fig. 4. The beam instability is observed in case for the KV beam transport with the CF and AG focusing lattice configurations. However the instability contributes hardly the rms emittance growth in the KV beam transport with the CF lattice. Although the beam instability with the abrupt emittance growth can be induced for the WB beam transport with the AG focusing model, the rms emittance growth without the beam instability is caused in the WB beam transport with the CF lattice system. On the other hand, the initial GA, PA, and SG beams cause the gradual emittance growth in the transport with the CF and AG focusing lattices. Also the emittance growth histories are almost same in the GA and PA beam transport with the CF and AG focusing lattice models.

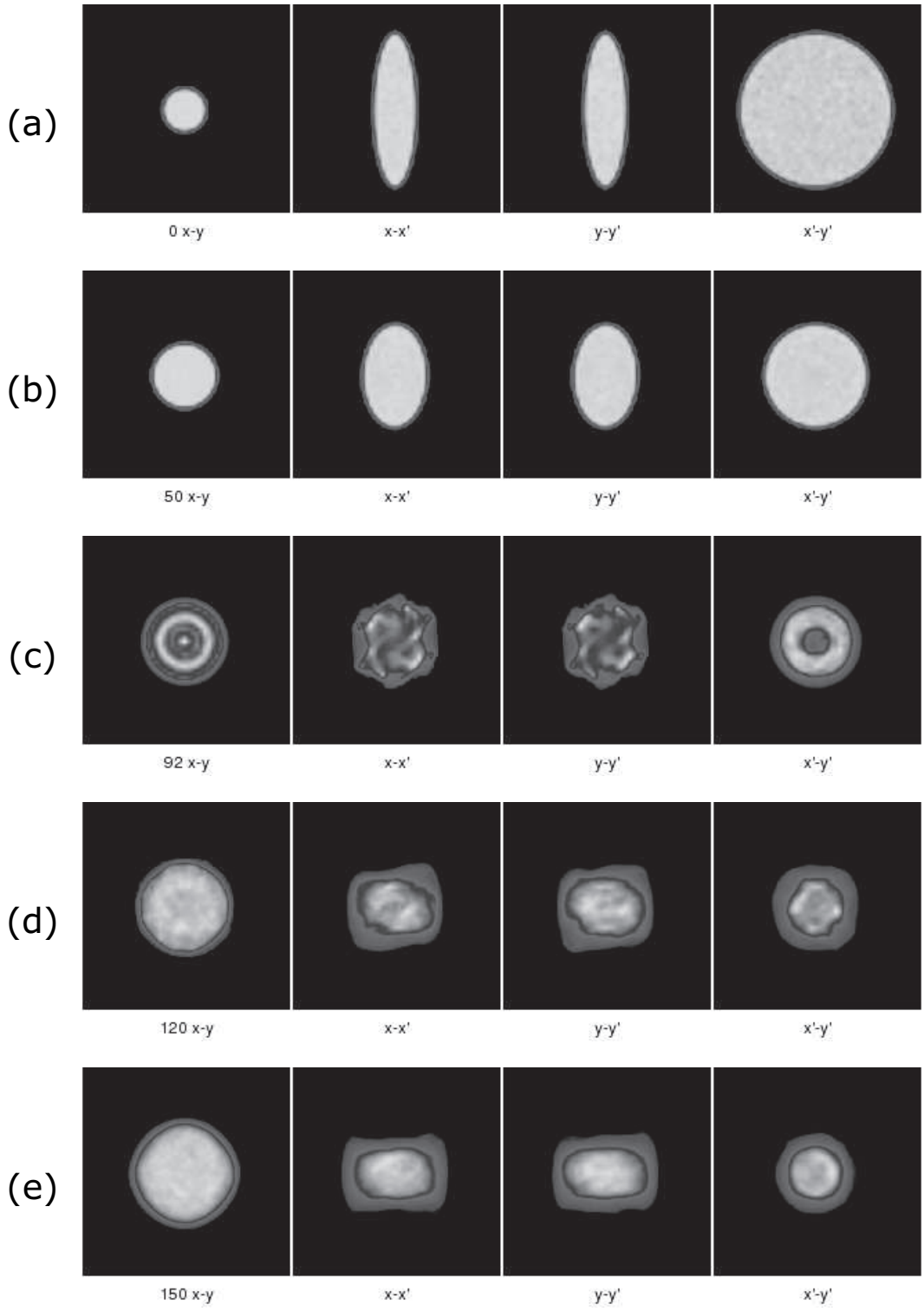

Figure 3: Normalized charge distribution in real and phase spaces with initial KV beam using CF lattice, (a) at initial condition, (b) at 50 lattice periods, (c) at 92 lattice periods, (d) at 120 lattice periods, and (f) at 150 lattice periods, respectively.

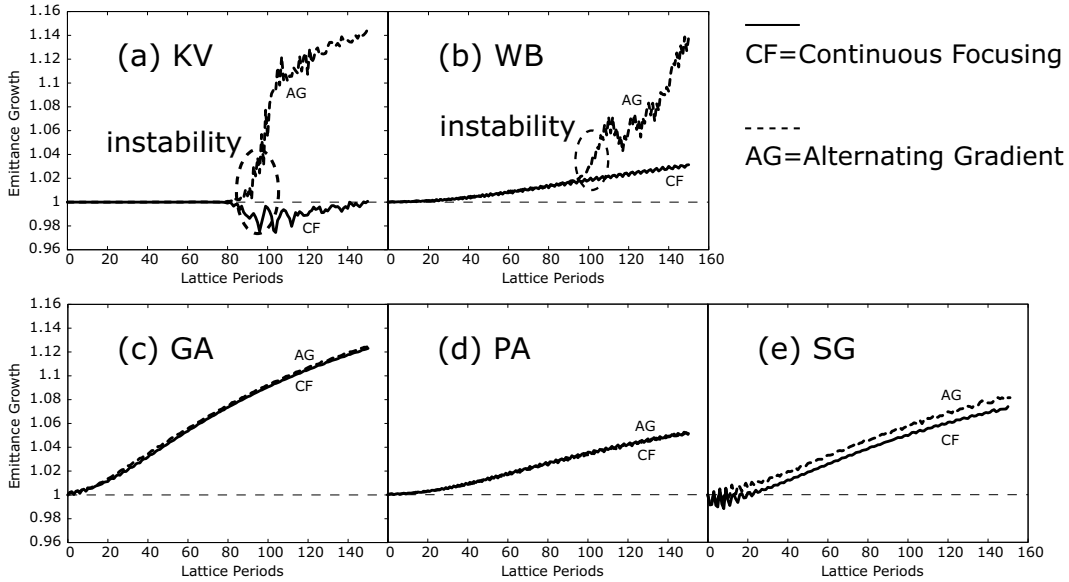

Figure 4: Evolution of the rms emittance during the final beam bunching, (a) for KV, (b) for WB, (c) for GA, (d) for PA, and (e) for SG beams, respectively. Solid curve shows the emittance growth for CF lattice, and the dashed line indicates one with AG focusing lattice.

4 Conclusions

The transverse beam dynamics was investigated during the final beam bunching in the HIF driver system. The PIC simulation with the beam current increase, as a model of the longitudinal bunch compression, was carried out for the study of beam transport under the strong effect of space charge oscillations.

The initial KV beam transport caused the localized particle distribution due to the space charge effect during the final beam bunching. For the KV beam transport with the CF and AG focusing lattice configurations the beam instability was observed, however the beam transport was carried out without the emittance growth in the CF lattice model. The beam instability was caused in the WB beam transport with the AG focusing lattice, while could not be induced in case with the CF lattice. In the cases of GA, SG, and PA beams, it is expected that the instability induced by the space charge effect did not contribute to the emittance growth.

Acknowledgments

This work was carried out under the collaborating research program at National Institute for Fusion Science. This work was partly supported by JSPS (Japan Society for the Promotion of Science) and MEXT (Ministry of Education, Culture, Sports, Science and Technology). We would like to thank Drs. S.M. Lund, T. Katayama, and E.A. Startsev for useful advices. We also thank to Ms. Y. Nakajima for the preparation of this manuscript.

References

[1] J.J. Barnard, J. Fusion Energy **17**, 223 (1998).

[2] J.J. Barnard, R.O. Bangerter, A. Faltens, T.J. Fessenden, A. Friedman, E.P. Lee, B.G. Logan, S.M. Lund, W. Meier, W.M. Sharp, and S.S. Yu, Nucl. Instrum. Methods in Phys. Res. **A415**, 218 (1998).

[3] K. Horioka, M. Nakajima, M. Watanabe, M. Honda, E. Hotta, M. Shiho, M. Ogawa, J. Hasegawa, J. Kishiro, and K. Takayama, Laser Part. Beams **20**, 609 (2002).

[4] T. Someya, A.I. Ogoyski, S. Kawata, and T. Sasaki, Phys. Rev. ST Accel. Beams **7**, 044701 (2004).

[5] A.I. Ogoyski, S. Kawata, T. Someya, A.B. Blagoev, and P.H. Popov, J. Physics D **37**, 2392 (2004).

[6] S.M. Lund, J.J. Barnard, and J.M. Miller, Proceedings of the 1995 Particle Accelerator Conference, Dallas, May 1995, p.3278.

[7] T. Kikuchi, M. Nakajima, and K. Horioka, J. Plasma Fusion Res. **79**, 105 (2003).

[8] T. Kikuchi, M. Nakajima, K. Horioka, and T. Katayama, Phys. Rev. ST Accel. Beams **7**, 034201 (2004).

[9] T. Kikuchi, T. Someya, S. Kawata, M. Nakajima, K. Horioka, and T. Katayama, *to be published in* Nucl. Instrum. Methods in Phys. Res. (2005).

[10] R.W. Hockney and J.W. Eastwood, *Computer Simulation Using Particles*, McGraw-Hill, New York, (1981).

[11] S.M. Lund, O. Boine-Frankenheim, G. Franchetti, I. Hofmann, and P. Spiller, Proceedings of the 1999 Particle Accelerator Conference, New York, March 1999, p.1785.

[12] M. Reiser, *Theory and Design of Charged Particle Beams*, Wiley, New York, (1994).

[13] T. Kikuchi, M. Nakajima, and K. Horioka, Laser Part. Beams **20**, 589 (2002).

[14] S. Machida and M. Ikegami, Proceedings of the Workshop on Space Charge Physics in High Intensity Hadron Rings, AIP Conf. Proc. No.448 (AIP, New York, 1998), p.73.

[15] Y.K. Batygin, Proceedings of the Computational Accelerator Physics Conference, Los Alamos, 1993, AIP Conf. Proc. No. 297, (1994) p.419.

Direct Extraction of Ions from Expanding Laser Ablation Plasma

Mitsuo Nakajima, N. Kobayashi, and K. Horioka
Tokyo Institute of Technology, Energy Sciencies

J. Hasegawa and M. Ogawa
Tokyo Institute of Technology
Research Laboratory for Nuclear Reactors

Ions are extracted directly from the expanding plasma ablated on small spots and linear without a drifting space. We investigate behaviors of the emitting surface by measuring ion beam current and its image. In the experiment of the small laser spot, a matching-like operation was founded in which the emitting boundary didn't move so much and the current had a flat-topped waveform under suitable conditions. We obtained copper ion current of 80 mA with $\varepsilon_n = 0.25\pi\text{mm}\cdot\text{mrad}$, fast rising of 40 ns and flat-top waveform. In the long linear spot, the divergent angle was decreased. Based on the experimental results, some indication of the possibility of large area laser ion source with direct extraction is obtained.

I. INTRODUCTION

Heavy ion fusion(HIF) requires high-current(A) and high-brightness($\varepsilon_n < 1\pi\text{mm}\cdot\text{mrad}$) heavy ion beams. However, current density is severely restricted by breakdown and beam radius(a) by the emittance scaling($\varepsilon_n \propto a\cdot(T_i/M)^{1/2}$) . Beams are dominated by space charge force, so the charge state must be low($1^+ - 3^+$) and rectangular current pulses are demanded.[1]

In the case of high current ion sources, the efficiencies of the source gas consumption and its ionization must be low, so gaseous discharge type ion sources may be difficult to use. Thermonic sources offer high brightness beams with a charges state limited to 1^+, but flux levels are relatively low[2].

A pulsed solid vapor type such as a vacuum arc source or laser ion source is one of possible candidates. The matching problem which the plasma meniscus changes temporally with a balance of the extraction current and the supply current (as shown in fig.1) is severe for pulsed ion sources due to a fluctuation of plasma supply. The vacuum arc ion source has been overcoming these two problems namely beam noise and poor reproducibility. Recently, up to 17 mA/cm^2 of Gd ions ware produced with about 85% of the ions in 3^+ state, a pulse rise-time close to $1\mu s$ and beam fluctuation level of less than 3% rms[3].

To avoid pre-fill of plasma in the extraction gap and to solve the matching problem, a grid control method is effective[4, 5]. Since the extractor operates in a space-charge-limited mode, a plasma fluctuation doesn't affect the beam current if the ion flux from the plasma exceeds the space-charge-limited flow. Flat-topped current beam waveforms with fast current risetimes are obtained. However, the confinement grid increase the risk of breakdown. Laser irradiation is well-suited to make a dense and low temperature plasma effectively. And there is no random plasma fluctuation like the vacuum arc discharge plasma. It is well known that ablation plasma has high drift velocity(v_d) up to 100 eV comparing with plasma temperature even though low irradiation[6, 7]. Because the ion drift velocity is considerably faster than the ion acoustic velocity($v_a = (kT_e/M)^{1/2}$), the pre-sheath acceleration is not needed. In the case of drifting plasma source, a supply current density is represented as $\sim nqv_d$ not the Bohm current density($\sim nqv_a$) and it has sufficient supply capacity.

Conventionally, powerful lasers have been used for generating of highly charged ions with a long drifting space. If low charge states of ion, especially a pure single charge state considered to be easy to make, are desirable the laser fluence must be just above the threshold of plasma ablation and naturally a plasma expansion length must be short.

We propose an ion extraction scheme, where ions are directly extracted from an ablating plasma made by large area, low-fluence laser irradiation. This scheme is expected to have the following characteristics. It facilitates the generation of a pulsed beam with a fast current rise-time due to a rapid plasma generation without adding another electrode. Secondary, as schematically shown in

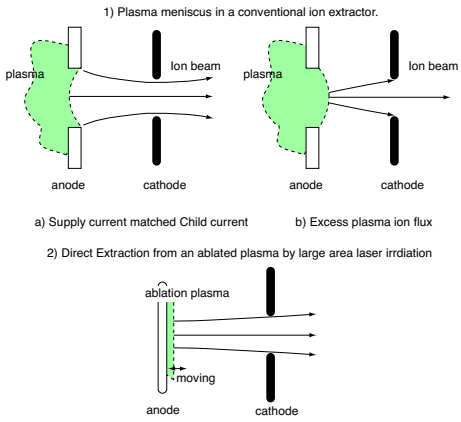

FIG. 1: A conventional extractor and a direct extractor from an ablation plasma

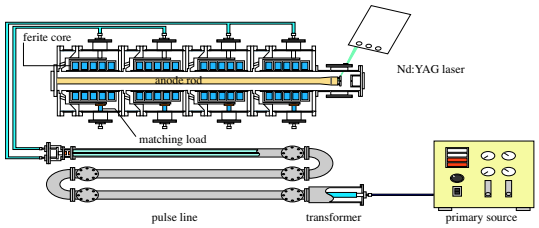

FIG. 2: A Schematic view of the induction accelerator and the laser ion source

fig.1, the shape of the emitting surface does not vibrate with plasma fluctuation like a conventional ion extractor but the boundary can move. Since laser plasmas have no random fluctuation as seen in a vacuum arc discharge plasma, we can expect to make the state where plasma ion flux almost matches, so the emitting boundary does not move so much with time. However, dynamics of the emitting surface may exert a bad influence upon beam optics.

II. EXPERIMENTAL APPARATUS

A schematic diagram of experimental apparatus is shown in fig.2. Four induction cavities made of ferrite cores, connected to a pulse forming line, can generate voltages up to 50kV during 400 ns. Four cavities were stacked in a voltage adder configuration. In our experiments, extraction voltage was about 120 kV with 400 ns duration.

We used a frequency doubled Nd:YAG laser with pulse duration of 5-7 nsec for copper rods and an excimer laser for zinc rods. The small spot size of laser evaporation was $1.6 \times 0.5\text{mm}^2$ and the linear size was $0.5 \times 10\text{mm}^2$.

Electrodes were made of SUS plates and the extraction hole was 10 mm in diameter. The gap length was 20 mm. This configuration of extraction was not optimized for the beam optics to see the emitting surface behaviors more clearly.

We performed the experiments under a background pressure of the order of 10^{-6} torr. To avoid contaminations, we shot the laser four times per one measurement with a few Hz and the last one was used for the source plasma.

As shown in fig.3, we observed beam images through a pepper-pot plate of 100 μm thickness made of tantalum which has 90 μm holes with 1mm intervals. Images were visualized by a multi-channel-plate(MCP) + phosphor screen opened during 50-300 nsec with a cable gate pulser. The pepper-pot plate was located behind the cathode electrode and the MCP was placed15.2 mm from the pepper-pot plate.

Beam current was measured with a Faraday cup which has an aperture of 17 mm and also located behind the cathode. This means all of extracted ions were captured.

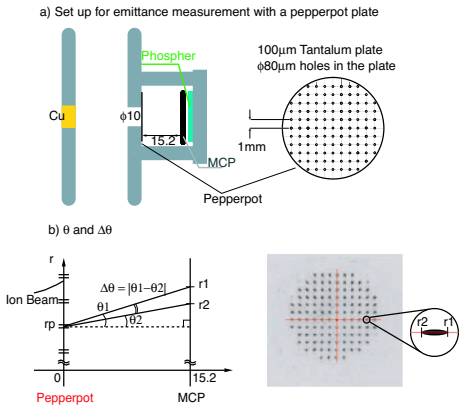

FIG. 3: A schematic apparatus of measuring beam emittance

III. RESULTS AND DISCUSSION

A. Experiment in small spot irrdiation

Figure 4a) shows typical beam waveforms and pepper-pot images in the case of a direct extraction as a function of the time delay of voltage application from a laser pulse t_d. The gate of MCP was opened between 100 to 400 ns after gap voltage application. In the case of 0-200 ns delay, the current waveforms increases and beam images expands. Obviously, the ion supply current is in excess and the emitting surface moves forward.

At 400 ns delay, there is a small spike in the current waveform. This is caused by plasma pre-fill in the gap since the front of ablation plasma, although it is low density by the diffusion, can approach the cathode. The current waveform is similar to that of a plasma opening switch.

Between 200 to 400 ns delay, current waveforms are flat-top and beam patterns also become a dot-like shape. Because the effective gap length becomes short and the space charge limit current increases with time, the ion supply current becomes to match the extracted current.

As shown in fig.4b), when the laser output energy downs to 28 mJ, it becomes easy to obtain a flat current waveform, and the beam pattern is also improved. It means the emitting surface doesn't move so much.

In order to estimate rough position and shape of the emitting surface, we drew straight lines that connect the dots of screen image and pepper-pot holes as shown in fig.6. Figure 5 shows that the extension of each lines intersected in the small point in the all conditions. As shown in fig.6, we can understand that dot patterns deform in elliptical shape at the outer side. While in the case of excess supply, the intersection moves with the plasma drift velocity. It means that we can consider the emitting surface as a point ion source for small spot irradiation in our extraction configuration. It may be supported by electric field distortion with plasma expanding.

Figure 7 shows the position of the intersection that

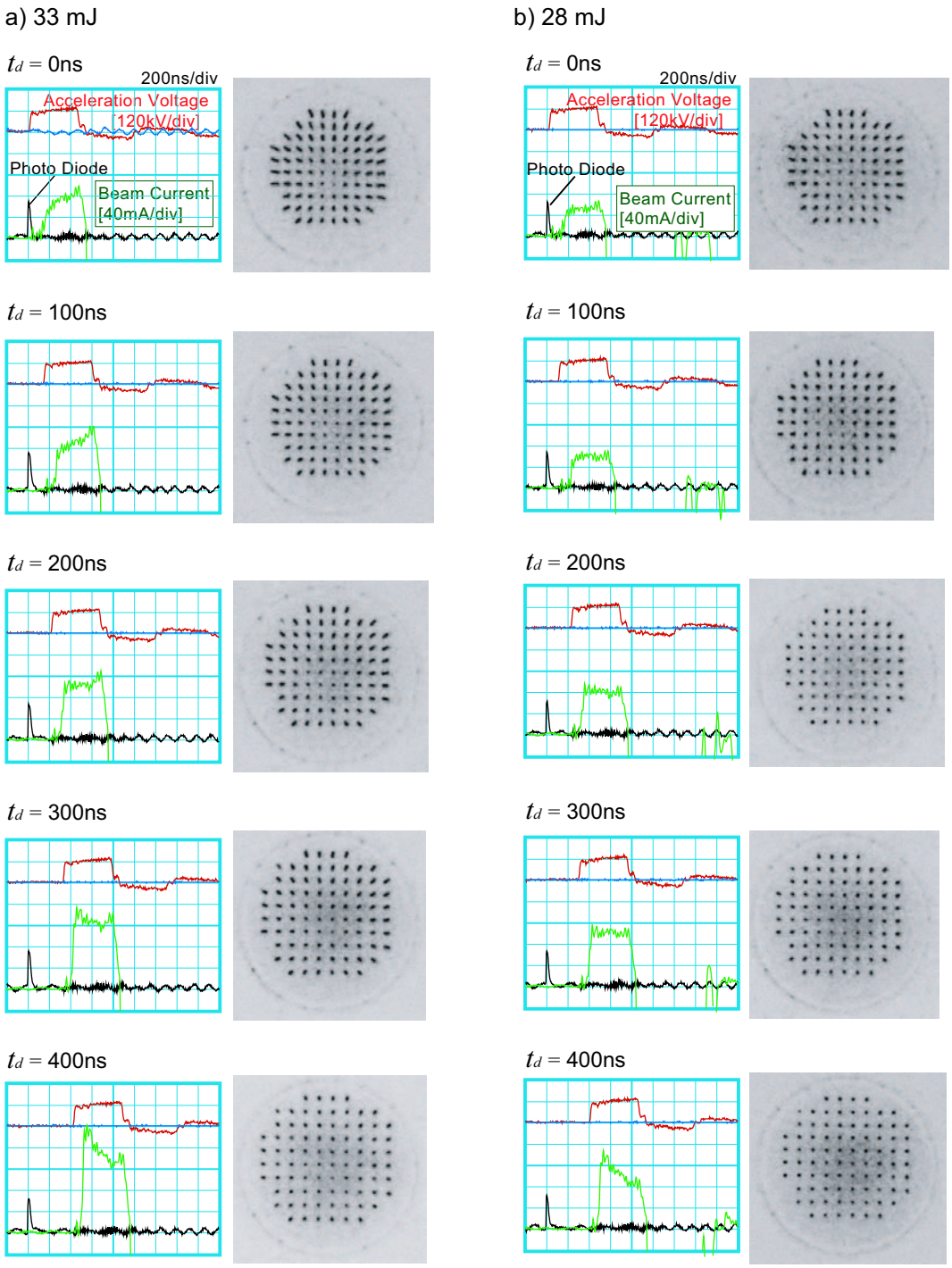

FIG. 4: Current waveforms and beam images with direct extraction from ablating plasma of Cu target at laser energies of a) 33 mJ and b) 28 mJ. t_d represents time delay of voltage application after laser irradiation. The MCP gate was opened between 100 to 400 ns after gap voltage application.

means the position of emitting surface. As one expected, the emitting surface goes forward when excess supply and come back when insufficient supply. However, in the case of 26.1mJ , a matching condition which the emitting surface doesn't move so much is observed.

B. Experiment in line irradiation

A point source leads to high brightness but divergent beam. We made line plasma in a vertical direction to improve the divergence. In a horizontal direction, the

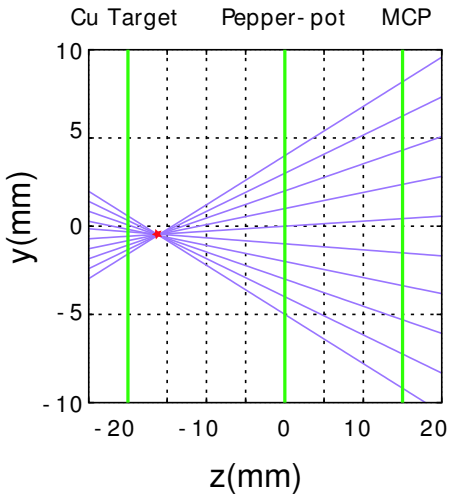

FIG. 5: This is an example that each lines intersects in a small point.

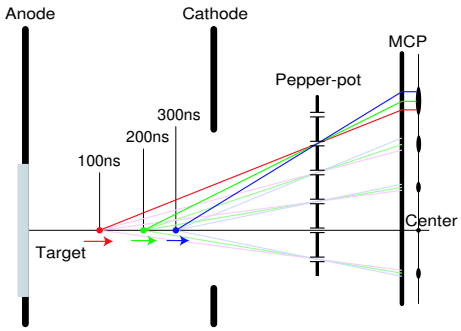

FIG. 6: We can explain the beam pattern with a moving point ion source.

straight lines connecting images and pinholes intersected in a small point again like a small spot irradiation. So we can estimate the position of the emitting surface.

Figure 8 shows envelopes at the positions of the emitting surface estimated from horizontal direction. The length of envelope was a few mm since the uniformity of laser irradiation was a few mm. It decreased as expanding. It seems the emitting surface becomes to curve. Uniformity of laser irrdiation is important.

As shown fig.9, as for the horizontal direction, divergent angles are still large. However, in the vertical direction, especially in near the center, the divergent angles become small for 0-100nsec.

If laser beam irradiates uniformly, the emittance will improve to 0.15 πmm $\cdot$ mrad which is estimated from the center.

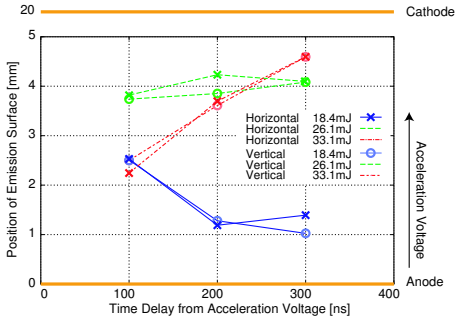

FIG. 7: In the case of excess plasma supply, the emitting surface moved forward with plasma drift velocity. In insufficient supply, it moved back. In matching, it didn't move.

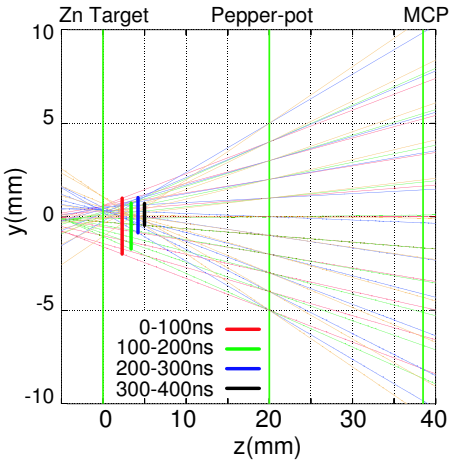

FIG. 8: Current waveforms and beam images with direct extraction from ablating plasma of Cu target at laser energies of a) 33 mJ and b) 28 mJ. t_d represents time delay of voltage application after laser irradiation. The MCP gate was opened between 100 to 400 ns after gap voltage application.

IV. SUMMARY

We have proposed a new scheme for high-flux ion sources, which utilize direct injection of laser ablation plasma into the acceleration gap. From the proof-of-principle experiments, we could point out that main cause of emittance degradation is the space charge potential in front of the point-like, moving emission surface of the drifting plasma, and when the ion supply of the source plasma is close to the space charge limited current of the effective acceleration gap, the drift of injected plasma is counterbalanced.

When we operate it at proper condition with low-fluence laser small spot irradiation on Cu target , high flux ions are extracted with current density of 100 mA/cm^2, flat-top waveform, fast rising time of less than 40 nsec, and with emittance of less than 0.35 πmm $\cdot$ mrad.

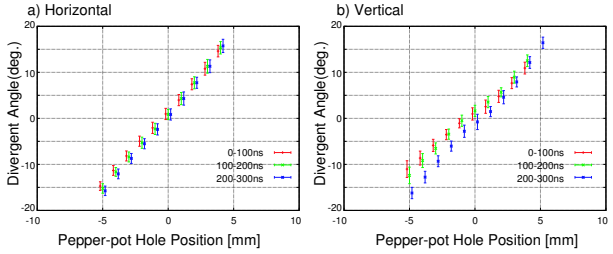

FIG. 9: Divergent angle of a) horizontal and b) vertical direction. In horizontal direction, it was the same as in the case of small spot irradiation.

Based on the obtained results, we can conclude that if we increase the ablation area using a high energy laser, the direct injection scheme will be able to additionally improve not only ion current level but also the beam quality as well.

[1] E.P. Lee, J. Hovingh, AIP Conf. Proc. No.249 PT.2 (1992)1713-24

[2] F.M. Bieniosek, J.W. Kwan, E. Henestroza, C. Kim, Nucl. Instrum. Methods Phys. Res. A464(2001)592-8

[3] N. Qi, J. Schein, R.R. Prasad, M. Krishnan, A. Anders, J. Kwan, I.Brown, Nucl. Instr. and Meth. A464(2001)576-81

[4] L.K. Len, S. Humphries Jr. C. Burkhart, AIP Conf. Proc. 152(1986)314-22

[5] M. Yoshida, J. Hasegawa, J.W. Kwan, Y. Oguri, M. Nakajima, K. Horioka, M. Ogawa Jpn. J. Appl. Phys. 42(2003)5367-71

[6] G.C. Tyrrell, L.G. Coccia, T.H. York, I.W. Boyd, Appl. Surf. Sci. 96-98(1996)227-32

[7] J.G. Lunney, Appl. Surf. Sci. 86(1995)79-85

[8] G.P. Bazhenov, O.B. Ladyzhensky, E.A. Litvinov, S.M. Chesnokov, Zh. Tekh. Fiz. 47(1977)2086-91

[9] R.W. Dreyfus, J. Appl. Phys. 69(3)(1991)1721-9